Volcanic processes during eruption and unrest: combining satellite and ground-based monitoring at Galeras and Santorini volcanoes

by

Michelle M. Parks

Thesis submitted to the University of Oxford for the degree of Doctor of Philosophy in Earth Sciences

Department of Earth Sciences and St Edmund Hall

University of Oxford

Trinity 2013

Supervised by Dr. T.A. Mather, Dr. J. Biggs and Prof. D.M. Pyle

Abstract

Volcanic processes during eruption and unrest: combining satellite and ground-based monitoring at Galeras and Santorini volcanoes

Michelle M. Parks

St Edmund Hall, University of Oxford

Doctor of Philosophy, Trinity 2013

This dissertation explores the combination of Interferometric Synthetic Aperture Radar (InSAR) results with field data to provide additional constraints on the processes controlling deformation signals observed at Galeras volcano (Colombia) and Santorini volcano (Greece).

InSAR measurements during 2007-2008 at Galeras reveal a subsidence signal on its northeast flank. I model InSAR and gravity data to determine the best-fit parameters for the subsidence source and suggest this signal was caused by deflation of the magma chamber associated with the January 2008 eruption.

In January 2011, Santorini volcano entered a period of unrest characterised by earthquake swarms and caldera-wide uplift. I analyse satellite data over a period incorporating both the preceding phase of quiescence (1993-2010) and the phase of unrest (2011-2012). A subsidence signal is confirmed on the intra-caldera island of Nea Kameni during 1993-2010. I investigate several possible scenarios for its source, with my preferred explanation being a combination of cooling and contraction of historic lava flows, and loading from these flows inducing relaxation of the substrate. I also use

a joint InSAR/GPS inversion technique to model the caldera-wide uplift observed during 2011-2012. I determine the optimal parameters for the deformation source and the temporal variation in volume change within the shallow magma chamber. The renewed activity offered an opportunity to observe how soil-gas emissions would respond to an influx of magma to a shallow reservoir. I employ a new approach (^{222}Rn-δ^{13}C systematics) to identify and quantify the source of diffuse degassing at Santorini during the period of unrest.

Finally, I present a new high-resolution merged LiDAR-Bathymetry grid, enabling detailed mapping of both onshore and offshore historic lava flows emplaced in the centre of Santorini caldera. Updated lava volumes provide new extrusion rate estimates and a means of estimating both the size and duration of future dome-building eruptions at Santorini.

Extended abstract

Establishing a time series of deformation is one of the keys to understanding and predicting the magmatic behaviour of active volcanoes. Satellite techniques represent an increasingly useful tool for measuring volcanic deformation over timescales spanning days to decades. This dissertation explores the combination of Interferometric Synthetic Aperture Radar (InSAR) measurements with complementary field data to provide additional constraints on the processes controlling the deformation signals observed in two distinct volcanic settings: i) Colombia and ii) Santorini volcano.

Colombia contains numerous young or active volcanoes, many of which are inaccessible. I use L-band (23.6 cm wavelength) radar data acquired between 2006 and 2009, to survey 15 active volcanoes along the Colombian segment of the Northern Volcanic Zone. Analysis of 100 interferograms showed that the majority of volcanoes were not deforming. However, independent interferograms display an average subsidence of 3 cm on the northeast flank of Galeras, coinciding with the January 2008 eruption. I combine InSAR, field measurements and source modelling to determine the origin, size and location of the source of subsidence at Galeras. The results suggest that this signal was caused by deflation of the magma chamber associated with the January 2008 event. Modelling provides insight into the depth to source (~ 2 km) and a volume change (-6.5×10^{5} m^{3}) which is consistent with that derived from modelling contemporaneous tilts and the volume of material erupted. I also demonstrate that a historic gravity anomaly (observed between 1997-1999) may be modelled using the same depth and location derived from modelling the 2007-2008 InSAR displacements. This observation supports the existence of a recurrent magma chamber beneath the northeast flank of Galeras volcano.

Santorini Volcano, the site of the catastrophic Minoan eruption in Greece, exhibits two distinct eruptive styles: small, effusive eruptions occur relatively frequently and build shields and domes of lava, whereas large explosive eruptions occur rarely, at intervals of 10,000–30,000 years. Both types of eruption were thought to incubate in a shallow magma chamber that is continually charged by small batches of melt injected into the chamber from below. However, petrological work suggests that at least 15% of the material ejected during the Minoan explosive eruption arrived in the magma chamber less than 100 years before the eruption. Here I use InSAR and Global Positioning System (GPS) measurements of surface deformation at Santorini to show that 10–20 million m^3 of magma were intruded beneath the volcano during the period of unrest from January 2011 to April 2012. This volume is equivalent to 10–50% of the volumes of recorded dome-forming eruptions. GPS and triangulation data show that this is the only volumetrically significant intrusion to have occurred since 1955, shortly after the last eruption. My observations imply that whether Santorini is in an explosive or dome-forming phase, its shallow magma chamber is charged episodically by high-flux batches of magma. The durations of these events are short in comparison with the intervening periods of repose and their timing is controlled by the dynamics of deeper magma reservoirs.

In light of this renewed activity, I analyse satellite data over an extended period incorporating both the phase of quiescence (1993-2010) and the phase of unrest (2011-2012). Mean line of sight velocity maps from 1993-2010 reveal a persistent slow subsidence signal on the intra-caldera island of Nea Kameni with an average rate of ~ -6 mm/yr. I investigate several possible scenarios for the source of this subsidence, with my preferred explanation being a combination of the cooling and contraction of historic lava flows, and loading of the 1866-1870 lava flows inducing viscoelastic relaxation of the substrate. I also employ a joint InSAR/GPS inversion technique to model the caldera-wide uplift observed during 2011-2012 and derive new information on the rate of volume change within the shallow magma chamber. This method determines the temporal evolution of source parameters by converting both InSAR and GPS observations into a time series of sub-surface volume change, treating the displacements as arising from a pressure variation at depth within an elastic crust. The best fitting parameters derived from the combined InSAR-GPS inversions suggest that there is a spherical source with an effective volume of order ~ 14–23 million m^3, centred slightly to the north of Nea Kameni at an average depth of ~ 4 kilometres beneath the surface.

The time series of sub-surface volume change reveals two distinct pulses during the period of unrest. These pulses may be explained by either batches of melt being delivered to the shallow chamber, or they may represent episodes of vesiculation, or possibly a combination of both. A lag response is identified between the cessation in micro-seismicity within the caldera (in late January 2012) and a significant decline in the rate of sub-surface volume change (several months later). I investigate whether the viscoelastic rheology of a shell (representing a ductile aureole) surrounding the magma chamber may account for the observed variation in cumulative volume change and explain the apparent delay. The derived model is consistent with both seismicity and deformation observations and suggests that melt supply to the shallow magma chamber ceased prior to late January 2012.

The 2011-2012 period of unrest offered an opportunity to observe how the soil-gas emissions would respond to an influx of new magma to a shallow reservoir. I employ a new approach using ^{222}Rn-δ^{13}C systematics to identify and quantify the source of diffuse degassing at Santorini during the period of renewed activity. Soil CO_2 flux measurements were made across a network of sites on Nea Kameni between

September 2010 and January 2012. Gas samples were collected in April and September 2011 for isotopic analysis of CO_2 ($\delta^{13}C$), and radon detectors were deployed during September 2011 to measure (^{222}Rn). My results reveal a change in the pattern of degassing from the summit of the volcano (Nea Kameni) and are suggestive of an increase in diffuse CO_2 emissions between September 2010 and January 2012. High-CO_2-flux soil gas samples have $\delta^{13}C \sim 0‰$. Using this value and other evidence from the literature I conclude that these CO_2 emissions from Santorini were a mixture between CO_2 sourced from magma, and CO_2 released by the thermal or metamorphic breakdown of crustal limestone. I suggest that this mixing of magmatic and crustal carbonate sources may account more broadly for the typical range of $\delta^{13}C$ values of CO_2 (from ~ -4‰ to ~ +1‰) in diffuse volcanic and fumarole gas emissions around the Mediterranean, without the need to invoke unusual mantle source compositions. At Santorini a mixing model involving magmatic CO_2 and CO_2 released from decarbonation of crustal limestone can account for the $\delta^{13}C$ and (^{222}Rn)/CO_2 characteristics of the ‘high-flux’ gas source. This model suggests ~ 60% of the carbon in the high-flux deep CO_2 end member is of magmatic origin. This combination of $\delta^{13}C$ and (^{222}Rn) measurements has potential to quantify magmatic and crustal contributions to the diffuse outgassing of CO_2 in volcanic areas, especially those where breakdown of crustal limestone is likely to contribute significantly to the CO_2 flux.

The ability to accurately map the thickness and extent of historic lava flows at Santorini volcano provides valuable insight into the relationships between pre-eruption interval, eruption duration and the volume of lava extruded during historic dome-building events. I present a new high-resolution merged LiDAR-Bathymetry grid, which has enabled detailed mapping of both onshore and offshore historic lava flows emplaced in the centre of the Santorini caldera since 46 AD. The new merged dataset

reveals a wealth of interesting morphological features, providing an insight into flow emplacement and evolution of the flow field. Two separate submarine flows are identified to the east of Nea Kameni (NK East and Drakon). The age of these lava flows is presently unknown. A third submarine flow is located to the north of Nea Kameni, which appears to predate the 1925-1928 lava flows but was emplaced subsequent to the 1707-1711 lava flows.

Yield strength estimates derived from the morphology of the 1570/1573 submarine flow suggest that submarine lava strengths are approximately three to four times greater than those derived from the onshore flows. To our knowledge this is the first documented yield strength estimate for submarine flows. This increase in strength is likely related to cooling of the dacite lava flows as they enter the ocean. The updated lava volume estimates derived from the merged LiDAR-Bathymetry grid suggest an average lava extrusion rate ~ 2 m^3s^{-1} during four historic eruptions on Nea Kameni (1707-1711, 1866-1870, 1925-1928 and 1939-1941). They also reveal a linear relationship between the pre-eruption interval and the volume of extruded lava. This may be used to infer the size of future dome-building eruptions at Santorini volcano, based on the time interval since the last significant eruption.

The new results presented in this dissertation highlight the potential of InSAR for measuring displacement rates at active volcanoes. In particular, they demonstrate that the combination of InSAR results with complementary field data may provide additional information on the processes controlling the observed deformation, as well as the underlying causes of volcanic unrest.

Acknowledgements

I would like to thank my supervisors (Tamsin, Juliet and David) for their guidance, inspiration and constant support throughout my DPhil. I would also like to thank Philip England for his useful discussions and collaboration working on Santorini. Without the friendship and support of my Greek colleagues (especially Evi Nomikou and Costas Raptakis), my Italian colleagues (Giovanni Chiodini and Stefano Caliro) and my hard-working field assistants (Sarah Dodd and Rebecca Neely) much of the work I present here would not have been possible. I am extremely grateful to the Nomikos Foundation and Boatmen Union of Santorini who kindly provided transport during my fieldwork on Santorini, despite the incredibly high fuel prices and to the Natural Environmental Research Council who funded my studentship and supported much of my work on Santorini through an urgency grant NE/J011436/1.

I would like to thank Marta Calvache for her collaboration and being so generous with her time during my visit to Colombia. I also thank Patricia Ponce, Diego Gómez, Lourdes Narváez, Gloria Cortés and Milton Ordoñez for their useful discussions and wonderful hospitality and Adelheid Weise for providing data from his 1998-2000 gravity campaigns.

Finally, I would like to thank my family, Jill and Roger (for their encouragement and support) and my husband (for his unconditional love, support, patience and understanding, regardless of my decision to leave an established career in the oil industry to pursue my dream). I dedicate this dissertation to him.

Contents

Chapter 1

Introduction

There are over 1500 sub-aerial volcanoes around the world that are regarded as ‘active’ or ‘potentially active’ (Smithsonian Institution, 2013). Of these, on average 50 – 70 erupt in any year, so most volcanoes spend the majority of their time in between eruptions. Globally, there are approximately 70 volcano observatories charged with monitoring (www.wovo.org), meaning that many of the potentially active volcanoes of the world are only sparsely monitored, if at all.

Recent decades have seen a considerable growth in the use of remote-sensing approaches to monitor volcanoes around the world (e.g., Fournier et al., 2010; Hooper et al., 2012; Sparks et al., 2012). Developments in satellite instruments able to detect volcanic gas and ash plumes has transformed our capacity to monitor eruptive activity globally (Theys et al., 2009; Flentje et al., 2010; Rix et al., 2012); while developments in the remote-sensing of ground deformation are beginning to transform our understanding of what happens beneath volcanoes both during eruptions, and during quiescence (Lu & Dzurisin, 2010; Sigmundsson et al., 2010; Solaro et al., 2010; Bathke et al., 2011). Comparison of long term deformation measurements with contemporaneous field datasets, (such as micro-seismic earthquake activity and volcanic degassing measurements) is crucial to understanding the characteristic behaviour of volcanoes in either state. Joint analysis of multiple data streams may provide insight into the origin of any observed ground displacements (e.g., hydrothermal or magmatic) as well as aid in the identification of key transitional phases (e.g., from quiescence to unrest). This thesis explores the combination of satellite remote sensing of ground deformation with other data streams from ground-based measurements in order to advance our understanding of volcanic processes both during eruption and unrest.

1.1 Volcanic processes

Satellite techniques combined with ground-based monitoring systems provide a powerful tool for observing numerous volcanic processes in real-time or near real-time. Pre-eruptive, co-eruptive and post-eruptive observations are key to identifying these various processes and gaining insight into the magmatic plumbing system. Pre-eruptive processes may include magmatic intrusions, degassing, cooling & crystallisation of subsurface magma bodies and changes in hydrothermal activity. Each of which may produce observable ground deformation at the surface. Examples include the huge topographic bulge on the north flank of Mt St Helens that became evident ~ 6 weeks prior to the May 1980 eruption (Lipman et al., 1981; Walter, 2011); caldera-wide uplift detected at Rabaul volcano (Papua New Guinea) some 23 years prior to the 1994 eruption (McKee et al., 1985) and the horizontal and vertical displacements which accompanied a series of magmatic intrusions at Eyjafjallajökull, in 1994 (Pedersen & Sigmundsson, 2004), 1999 (Pedersen & Sigmundsson, 2006) and 2009 (Sigmundsson et al., 2010).

A magmatic intrusion often triggers micro-seismic earthquakes as the melt pushes its way through the crust; related to either the migration of the magma itself, or consequent changes in the local stress regime. Several examples include precursory swarms of volcano-tectonic (VT) earthquakes observed at El Hierro volcano (Canary

Islands) prior to the 2011-2012 eruption (López et al., 2012) and swarms of long-period events identified prior to explosions at Redoubt volcano (Alaska) during the 1989-1990 and 2009 eruptions (Chouet et al., 1994; Buurman et al., 2013).

As the melt rises within the crust volatiles are released from the magma and migrate through open fracture pathways towards the surface. Pre-eruptive variations in gas emissions have been measured at multiple volcanoes, including an increase in CO_2 emissions at Usu volcano, Japan (Hernandez et al., 2001) prior to the March 2000 eruption. The recent submarine eruption at El Hierro was preceded by an increase in helium emissions (Padrón et al., 2013) and on Stromboli (Italy), increases in CO_2 and CO_2/SO_2 ratios were observed prior to explosions in 2006 and 2007 (Allard, 2010).

Co-eruptive processes include (but are not limited to) explosions, ash and gas emissions, depressurisation of the magmatic plumbing system, dome extrusion, pyroclastic flows and lava flows. Satellite instruments such as AVHRR and GOES have enabled measurements of volcanic ash clouds since the late 1980s (Prata, 1989; Pyle et al., 2013) and sulphur dioxide plume measurements since 1982 (Krueger, 1983; Pyle et al., 2013), while recent advances in this field have permitted detection of other volcanic gases and plume height estimates (e.g., Rix et al., 2012). Co-eruptive subsidence (related to the depressurisation of the shallow plumbing system) was detected at Lascar volcano, Chile in 1995 (Pavez et al., 2006), and during the 1998 eruption at Cerro Azul (Amelung et al., 2000), while episodes of dome growth and collapse have been recorded using ground-based radar and time-lapse imagery (e.g., Wadge et al., 2008; Walter et al., 2013). Pyroclastic flow deposits have been mapped at Montserrat, using TerraSAR-X radar images (Wadge et al., 2011) and the advancement of lava flows have been monitored at Bagana volcano, Papua New Guinea (Wadge et al., 2012).

Post-eruptive processes include depressurisation of the magmatic plumbing system resulting from magma withdrawal (e.g., Delaney and McTigue, 1994; Bathke et al., 2011); changes in the hydrothermal system (e.g., Waite & Smith, 2002; Chiodini et al, 2012); compaction of lava flows (Briole et al., 1997; Ebmeier et al., 2012); flank destabilisation (e.g., Kerle & Van Wyk De Vries, 2001; Walter et al., 2005); cooling and crystallisation of remnant intrusions (de Zeeuw-van Dalfsen et al., 2013) or gravitational loading (e.g., Dzurisin et al., 2002).

1.2 Volcano monitoring

The key geophysical/geochemical techniques employed by both observatories and research institutions for observing active volcanoes can be broken into 7 main categories: seismicity, deformation, gas, thermal, gravimetry, electromagnetic and infrasound. Routine volcano monitoring commenced in 1845 with the completion of the Vesuvius volcano observatory (Sparks et al., 2012) and in 1856, Luigi Palmieri installed his "sismografo elettro-magnetico" at the observatory for monitoring earthquakes (INGV, 2013). Since this time, volcano seismology has played a major role in detecting changes in volcanic activity and is still the leading technique in terms of real-time monitoring and its potential for making short-term eruption forecasts (Cornelius & Voight, 1994; Kilburn & Voight, 1998). It does however rely on the ground-based deployment of an instrument (or better a network of instruments) local to the volcano. Since the early 1990s there have been major advances in remote sensing techniques, which are now routinely employed to monitor volcanic deformation, gas emissions and thermal anomalies, and have the advantage of offering potentially global coverage including otherwise inaccessible or unmonitored volcanoes.

Volcano seismology continues to play a major role in the monitoring of active volcanoes (e.g., Chouet & Matoza, 2013). Networks of seismometers are used by volcano observatories to determine the hypocentre locations of volcanic earthquakes (e.g., Waldhauser & Ellsworth, 2000; McNutt, 2005) and graphs of real-time seismic amplitude measurements (RSAM) (e.g., Endo & Murray, 1991; Voight & Cornelius, 1991) or number of VT events against time (e.g., Kilburn, 2003), is often employed for short-term eruption forecasting.

Surface deformation at volcanoes has been monitored using triangulation, levelling, electronic distance measurements (EDM), Global positioning system (GPS) satellites, Synthetic aperture radar interferometry (InSAR), Light detection and ranging (LiDAR) and time-lapse photogrammetry. In the early years of volcano geodesy, triangulation, levelling and EDM were the core ground deformation monitoring techniques (e.g., Lipman and Mullineaux, 1981; Archbold et al., 1988; Dvorak and Dzurisin, 1997).

Variations in gas emissions have been monitored using soil gas surveys (e.g., Baubron et al., 1991; Chiodini et al., 1998), permanent continuous monitoring stations (e.g., Carbone et al., 2003; Zimmer & Erzinger, 2003), multi-gas detectors (e.g., Witt et al., 2008) and direct field sampling of volcanic plumes (Chiodini et al., 2011), hydrothermal springs and fumaroles (e.g., Fischer et al., 1997). Remote sensing techniques are becoming more widely used to monitor SO_2 emissions at volcanoes (e.g., Carn et al., 2003) and future advancements in retrievals from the Greenhouse Gases Observing Satellite (GOSAT) (e.g., Yokota et al., 2009; Butz et al., 2011) may enable the monitoring of CO_2 and $CH_{4.}$

Infrared image analysis has been used to determine heat and mass fluxes at active lava lakes (e.g., Harris et al., 1999), cooling rates of lava flow fields (Oppenheimer, 1991) and to monitor the growth of lava domes (e.g., Kaneko et al., 2002; Walter et al., 2013). Satellite data acquired by the Moderate Resolution Imaging Spectroradiometer (MODIS) have been used for the near-real-time monitoring of thermal anomalies at volcanoes (Wright et al., 2002) and Landsat 7 Enhanced Thematic Mapper data has been used to determine the evolution of lava flows (Wright et al., 2001).

Other major ground-based techniques fall into the categories of gravimetry, electromagnetic and infrasound. Local variations in the Earth's gravitational field and electromagnetic disturbances have been associated with the intrusion of melt beneath volcanoes and can be detected using gravimetry or electromagnetic (EM) methods. Gravity anomalies have been detected beneath the edifice of many volcanoes including Mt Etna (Budetta et al., 1999), Campi Flegrei (Italy), Rabaul (Papua New Guinea) and Krafla (Iceland) (Berrino et al., 1992 and references therein). Self-potential anomalies have been observed at several volcanoes including Piton de la Fournaise (Réunion island), Mt Unzen (Japan) and Kilauea (Hawaii) (Johnston et al., 2001; Revil et al., 2003). Infrasound is a relatively new approach to volcano monitoring but has been employed at Mt Erebus (Antartica), Fuego (Guatemala), and Villarrica (Chile) to provide insight into conduit processes (Johnson et al., 2004).

This thesis explores the combination of satellite measurements of ground deformation at volcanoes using synthetic aperture radar interferometry (InSAR) with several different ground-based techniques: global positioning system (GPS) monitoring, light detection and ranging (LiDAR) measurements, tilt measurements, gravimetry, soil gas monitoring and seismic monitoring. An overview of the various monitoring techniques and data utilised in this dissertation are discussed in the following sections.

1.2.1 Synthetic aperture radar interferometry (InSAR)

Synthetic aperture radar (SAR) images contain both amplitude and phase component data. Any ground deformation that takes place between two separate SAR acquisitions results in a phase shift (or path difference from the ground to the satellite). This phase shift can be detected by computing an interferogram, which involves multiplication of the first SAR image by the complex conjugate of the second SAR image (Massonnet and Feigl, 1998; Bürgmann et al., 2000; Rosen et al., 2000).

The phase of the derived interferogram is equal to the difference in the phase component of the two SAR images. The observed phase change arises from a combination of differences in the position of the satellite, topography, ground deformation, atmospheric delay and the scattering properties of the ground (equation 1.1).

$$\Delta\varphi_{int} = \Delta\varphi_{geom} + \Delta\varphi_{def} + \Delta\varphi_{atm} + \Delta\varphi_{pixel} \tag{1.1}$$

$\Delta\varphi_{int}$ is the phase of the interferogram, $\Delta\varphi_{geom}$ is the combined phase contribution derived from differences in the satellite's position overhead between the two image acquisitions and a perspective effect on topography, $\Delta\varphi_{def}$ results from ground deformation, $\Delta\varphi_{atm}$ from atmospheric delay caused by differences in atmospheric conditions on the different acquisition dates (e.g., interactions in the ionosphere and variations in temperature, pressure and water vapour in the troposphere), and $\Delta\varphi_{pixel}$ is the phase contribution due to individual scatterers within a pixel.

If the scattering properties of the ground remain largely unchanged during the repeat period of the satellite, then the phase contribution from $\Delta\varphi_{pixel}$ is mostly negligible. $\Delta\varphi_{geom}$ is corrected for during the processing, using an accurate digital elevation model (DEM) and precise satellite orbits, however $\Delta\varphi_{atm}$ remains a significant impediment to the measurement of small scale deformation (< 10 cm) at volcanoes, especially in tropical regions where water vapour has a considerable effect (Zebker et al. 2000; Hanssen, 2001; Heleno et al., 2010).

If atmospheric delay over the target region is small, then the $\Delta\varphi_{atm}$ term is often ignored. Otherwise attempts are made to reduce the atmospheric phase contribution, either via interferogram stacking to enhance the signal to noise ratio (e.g. Biggs et al., 2007), or by making direct comparisons between elevation and interferometric phase in a non-deforming area, to assess the likely occurrence of phase variations related to stratified water vapour (e.g. Wicks et al., 2002). Where appropriate, data from optical satellites, GPS instruments or numerical weather model outputs may be employed, to correct interferograms for differences in water vapour and atmospheric pressure respectively (e.g. Jolivet et al., 2011; Walters et al., 2013).

Once the remaining phase components in equation 1.1 have been removed, the phase contribution resulting from deformation alone ($\Delta\varphi_{def}$) can be determined and converted into displacement (Δd) in the satellite's line-of-sight (LOS), using equation 1.2:

$$\Delta\varphi_{def} = -\frac{4\pi}{\lambda}\Delta d \tag{1.2}$$

where Δd is the LOS displacement, λ is the wavelength of the transmitted radar pulse and $\Delta\varphi_{def}$ is the phase contribution from deformation.

The phase component for each pixel within an interferogram is the coherent sum of the radar returns from multiple scatterers. Relative movement of these scatterers during the repeat pass of the satellite results in a random phase return, referred to as temporal decorrelation (Zebker and Villasenor, 1992). Multi-temporal InSAR (MT-InSAR) techniques are often employed to overcome decorrelation problems associated with conventional InSAR processing. There are two primary MT-InSAR methods, both of which involve the processing of multiple interferograms spanning various time periods to generate a time series of deformation. The first of these is known as the persistent scatterer (PS) method, the second is referred to as the small baseline (SB) method.

PS methods involve the generation of a series of two-pass interferograms with respect to a common master image (or first image). Common pixels are identified throughout the series of images, whereby the radar return for that pixel is consistently dominated by a single bright scatterer - such that the overall phase remains relatively constant in time (e.g., Feretti et al., 2001) or space (e.g., Hooper et al., 2004). SB methods (e.g., Berardino et al., 2002; Schmidt and Bürgmann, 2003; Hooper, 2008) combine subsets of two-pass interferograms with small perpendicular and temporal baselines, to target pixels that remain relatively stable over short time periods after spectral filtering in range and azimuth. Hooper (2008) refers to these pixels as slowly-decorrelating filtered phase (SDFP) pixels (Hooper, 2008). Both methods have their advantages and disadvantages, but the success of either technique depends on the inherent ground scattering properties of the target area and the frequency of SAR acquisitions.

1.2.2 Global positioning system (GPS) monitoring

GPS satellites were originally designed and launched by the U.S. Department of Defense for military purposes, but are now routinely used by scientists to monitor volcanic deformation. This earth-orbiting navigation system comprises a constellation of 24 satellites, which have been fully operational since 1994 (Beutler et al., 1999). The satellites orbit the earth twice a day at an altitude of 20,200 km (Dana, 1997), transmitting signals at two known frequencies 1.57542 and 1.22760 GHz; referred to as L1 and L2 carriers respectively (Beutler et al., 1999). Transmissions in the L1 frequency band are intercepted by commercial GPS receivers, which automatically calculate the range to the satellites and enable precise positioning of the receiver via triangulation. At least four satellites must be visible in the sky to determine the receiver's latitude, longitude and elevation. However, a lock on additional satellites is desirable as this improves the accuracy of the measurements. There are two main types of GPS measurements undertaken at volcanoes: campaign GPS measurements and continuous GPS (cGPS) measurements.

i) Campaign measurements are made by undertaking multiple repeat surveys (for example, every six months) at the same GPS site. During each survey, measurements are made at a series of GPS sites, with one measurement typically recorded every 15 seconds for short period occupations (lasting several hours) or every 60 seconds for longer period occupations (lasting several days). This usually consists of reoccupying GPS benchmarks (brass pins) cemented into bedrock, although triangulation monuments/pillars may also be used – an example of both is displayed in Figure 1.1. GPS receivers are typically mounted on either a tripod or a spike mount, however the use of pillar plates is preferable for reoccupation of monuments.

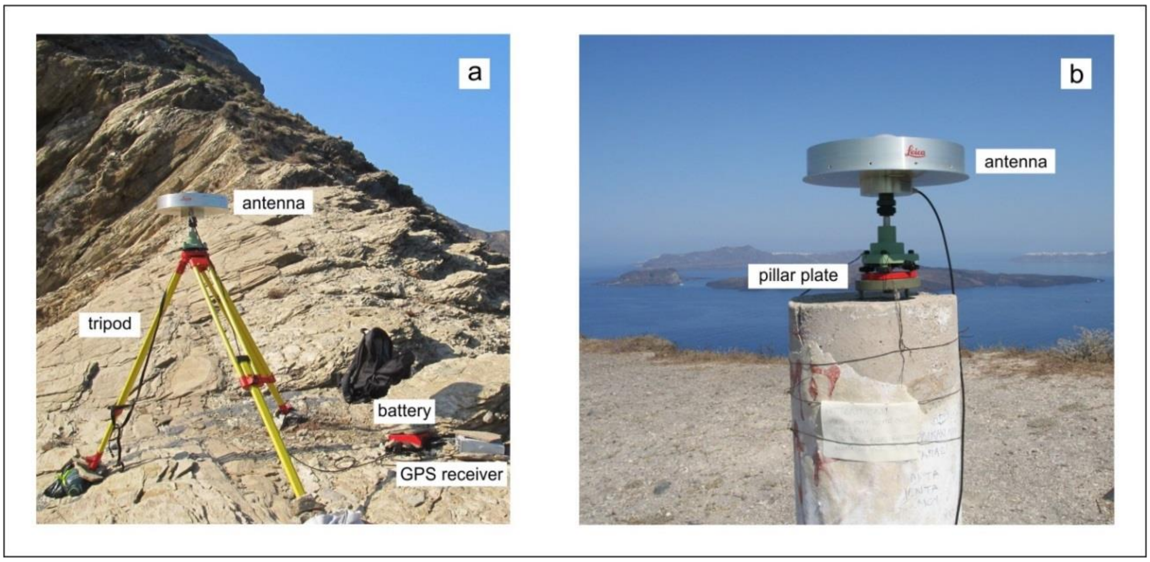

***Figure 1.1:** Campaign GPS equipment. **(a)** Leica choke ring antenna mounted on a tripod. **(b)** Leica choke ring antenna mounted on a pillar plate on top of a concrete triangulation monument. Photo credit: Emily Warren-Smith.*

ii) Continuous GPS (cGPS) sites are permanent installations capable of storing and transmitting a continuous stream of position measurements. The ability of this technique to provide continuous deformation measurements is invaluable during periods of volcanic unrest. During the summer of 2011, the University of Oxford and the National Technical University of Athens installed three additional cGPS sites at Santorini, including one on the intra-caldera volcano Nea Kameni (site MKMN – Figure 1.2). At this site we installed a Trimble Zephyr geodetic antenna, connected to a Trimble NetRS receiver powered by a 12V battery and 235Wp solar panel (Figure 1.2(a)). A radio link connected to the receiver and a separate Yagi antenna (positioned to enable direct line of sight to the main island of Thera - Figure 1.2(b)) were used to transmit the data daily from the MKMN site on the volcano to the Nomikos Conference Centre on Thera (with a direct uplink to the internet). The battery and solar panel were connected to a power regulator, which in turn was connected to the receiver and radio link, in order to control the power supply to these instruments. Position measurements were recorded at this site every 30 seconds. The daily data files were stored on the receiver's internal hard disk and transmitted once daily.

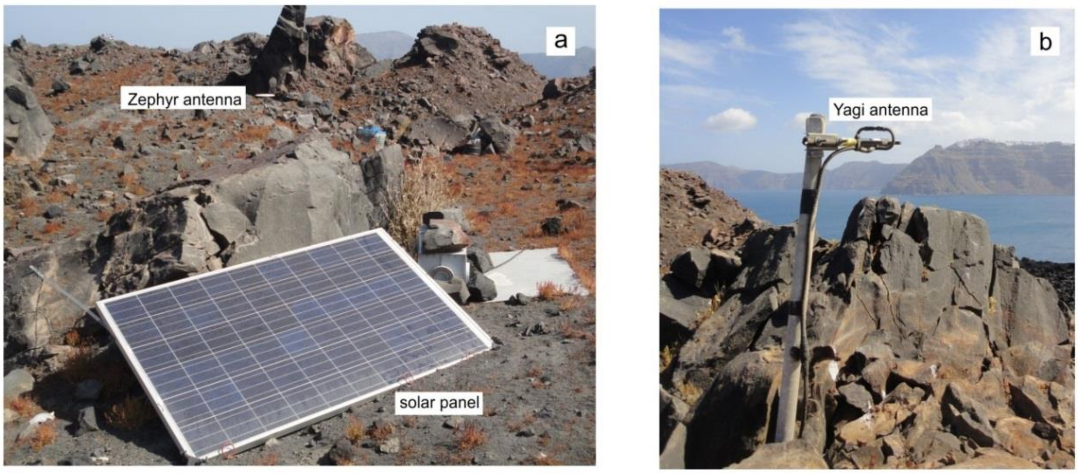

Figure 1.2: *Continuous GPS equipment setup at site MKMN on Nea Kameni, Santorini.* ***(a)*** *Solar panel and geodetic Zephyr antenna setup.* ***(b)*** *Yagi antenna with direct line of site to the main island of Thera (Santorini) used to transmit daily measurements from the site MKMN on the intra-caldera volcanic island of Nea Kameni.*

1.2.3 Light Detection and Ranging (LiDAR) measurements

LiDAR is becoming a more widely used technique in geodetic studies for producing high resolution (1-2 m) digital elevation models and monitoring deformation via the differencing of point cloud data acquired throughout repeat LiDAR surveys (Borsa and Minster, 2012; Nissen et al., 2012). In volcanic studies airborne LiDAR has been used to map the morphological and volumetric changes associated with historic eruptions (e.g., Pyle and Elliott, 2006; Neri et al., 2008); identify different volcanic deposits (e.g., Fornaciai et al., 2010) and determine emplacement mechanisms and rheological properties of lava flows (e.g., Pyle and Elliott, 2006; Ventura and Vilardo, 2008).

Airborne LiDAR systems comprise 3 primary components: (1) a near-infrared laser scanning unit which emits and records the backscattered radiation; (2) a differential GPS unit, used to determine the position of the aircraft and (3) an inertial measurement unit (IMU), attached to the laser scanner, used to determine the roll, pitch and yaw (Reutebuch et al., 2005). The recorded return travel time of each laser pulse enables computation of the range from the scanner to the ground. This information is combined with the precise position of the scanning unit (derived from the GPS and IMU) to calculate the coordinates for each reflection point on the ground (Baltsavias, 1999; Reutebuch et al., 2005).

1.2.4 Tilt measurements

Electronic tiltmeters are high precision instruments capable of recording continuous tilt measurements with a high temporal resolution. The apparatus consists of a glass vial containing a bubble immersed in a conducting fluid (Westphal et al., 1983). Ground displacements result in a shift in the location of the bubble with respect to two electrodes. This shift produces an electric current which is amplified and converted to a tilt measurement in microradians. Due to their sensitivity to changes in temperature and pressure they are often installed in boreholes on the flanks of volcanoes. Tiltmeters have recorded remarkable deformation measurements at a series of volcanoes providing insight into diverse volcanic processes, including an episode of aseismic slip on the south flank of Kilauea volcano in November 2000 (Cervelli et al., 2002a), tilt cycles related to magma pressurisation at the Soufrière Hills volcano from 1996 -1997 (Voight et al., 1998), and dyke emplacement prior to the July 2001 eruption at Mt Etna (Bonaccorso et al., 2002).

1.2.5 Gravimetry

Gravity surveys are capable of detecting subtle variations in the Earth's gravitational field that result from changes in surface height and the distribution of mass at depth. At volcanoes, these changes could result from a number of processes, including the subsurface influx or withdrawal of melt, the cooling and crystallisation of a magmatic intrusion (e.g., Rymer at el., 1998; Battaglia et al., 1999) and the migration of magmatic fluids and their associated hydrothermal systems (e.g., Gottsmann et al., 2005; Todesco et al., 2010).

Gravimeters fall into two main categories: absolute free-fall gravimeters and spring-based relative gravimeters. The absolute gravimeters calculate the acceleration due to gravity from the time it takes for a falling weight to pass through certain fixed points within a vacuum (http://www.microgsolutions.com). Relative gravimeters consist of a weight suspended on a metal or quartz spring (e.g., Budetta & Carbone, 1997). Local variations in gravity are calculated by measuring changes in the length (or stretching) of the spring at different site locations. Spring-based gravimeters are commonly used for field surveys as they are more durable and portable; however absolute gravimeters are used to establish national and international gravity base station networks and to "tie-in" a relative gravity survey. They can also be used in continuous mode at a fixed location to monitor height and/or mass changes, for example, prior to, during and following an eruption.

A combination of several permanent gravity stations recording continuous measurements and a series of denser campaign style measurements is typically employed during volcano monitoring to obtain greater temporal and spatial resolution (Carbone et al., 2003). However the utility of measurements relies on the accuracy of a series of corrections to compensate for instrumental drift, solid Earth tides and surface height changes (with respect to the geoid). Modern gravimeters such as the Scintrex CG-5 (http://scintrexltd.com/) contain an internal GPS receiver and electronic tilt sensors enabling automated tidal and tilt corrections and real-time free-air and Bouguer corrections. The equipment has a measurement resolution of ~ 2 microGal which corresponds to a height change of ~ 0.6 cm.

1.2.6 Soil gas monitoring

Monitoring gas emissions at active volcanoes has proved to be an increasingly useful tool for determining changes in the behaviour of a volcano (e.g., Hernandez et al., 2001; Inguaggiato et al., 2011). Degassing occurs during both eruptive phases and periods of quiescence - therefore, gaining a better understanding of background emissions may facilitate the identification of transitional periods. At Santorini I analysed carbon-dioxide (CO_2) and radon (^{222}Rn) soil gas measurements prior to and during the recent 2011-2012 period of unrest. A schematic summarising the various sources of these gas emissions at Santorini volcano is displayed in Figure 1.3. A photograph of the equipment used to measure CO_2 soil gas emissions is presented in Figure 1.4.

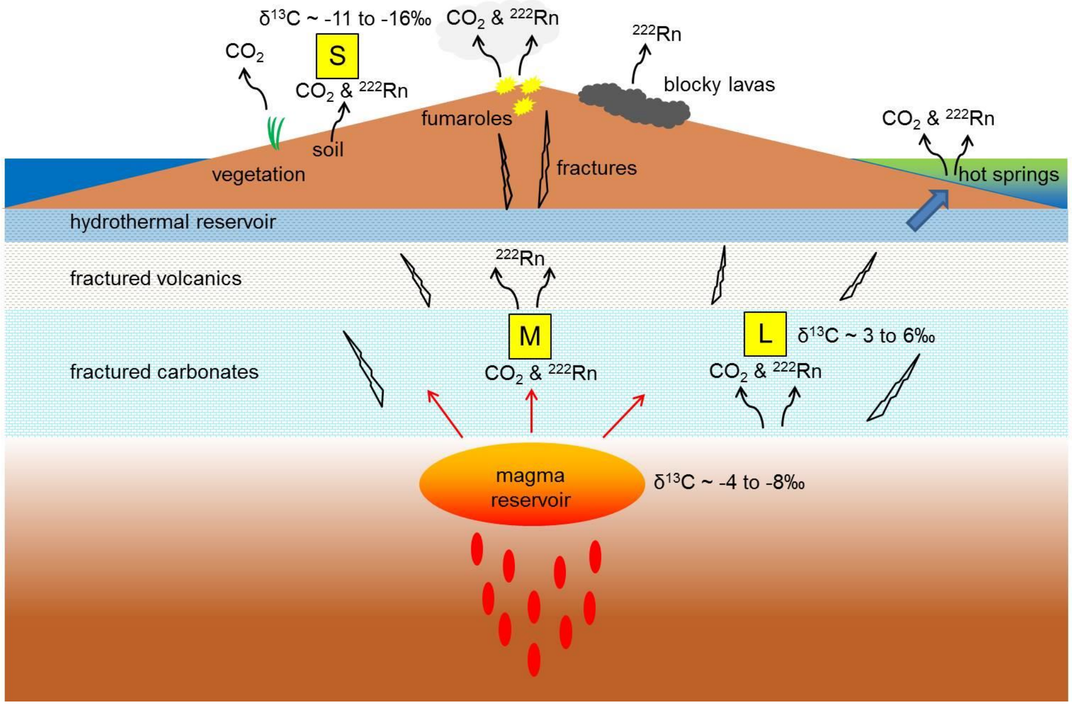

Figure 1.3: *Various sources of CO_2 and ^{222}Rn gas emissions at Santorini volcano. The $\delta^{13}C$ values represent the typical endmember carbon isotopic compositions of the CO_2 gas released from magma (M), limestone (L) and soils (S). These are discussed in detail in Chapter 6.*

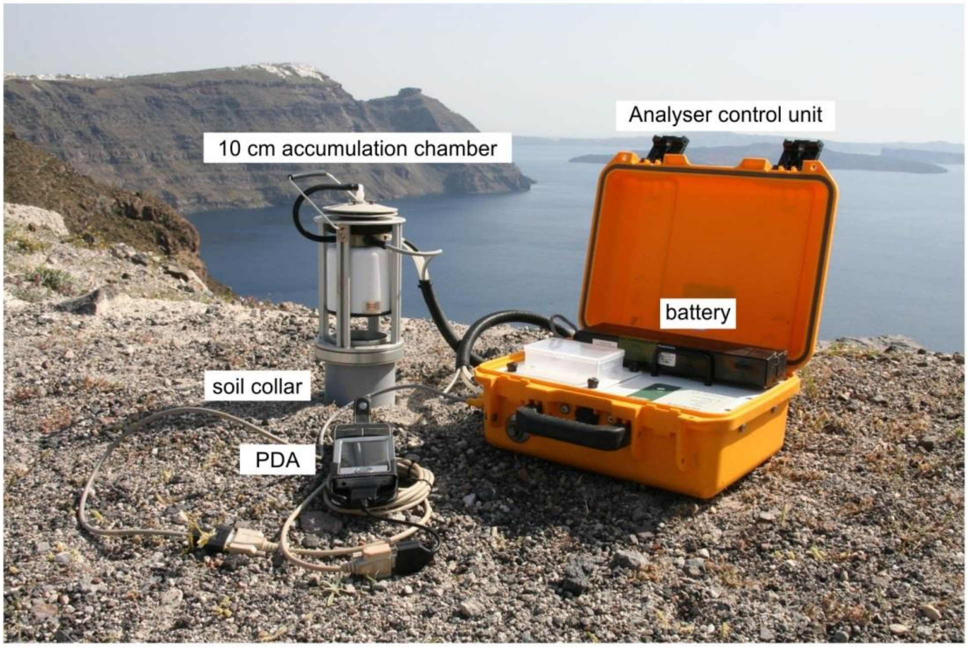

Figure 1.4: *Soil* CO_2 *monitoring equipment. The equipment consists of an Analyser control unit which houses the Infrared gas analyser (IRGA), a series of air filters and a rotary pump. The equipment is powered by 12V rechargeable batteries. The 10 cm gas accumulation chamber sits on top of a PVC soil collar which prevents lateral diffusion of gases. Data can be stored on the instruments hard drive or internal compact flash card. The personal data assistant (PDA) is used to set up parameters and control the measurements.*

1.2.7 Seismic monitoring

Seismometers essentially comprise of a weight suspended from a spring, attached to a rigid frame. The ground motion accompanying an earthquake can be measured by recording the voltage induced by the relative movement between the stationary weight and the moving frame (coupled to the earth), while accurate internal clocks are used to record the precise timing of events. Seismometers fall into a number of categories based on their dynamic range and whether they are capable of detecting vertical/horizontal motions: short-period (SP) seismometers are only sensitive to high frequency motions between 1-10 Hz (periods between 1 to 0.1 sec); long-period (LP) seismometers are sensitive to frequencies between 0.01-0.1 Hz (periods between 100 to 10 sec) (Lowrie, 1997); broadband seismometers (also referred to as force-feedback seismometers) incorporate a damping mechanism which provides a larger dynamic range - between ~ 0.03 to 50 Hz (33 to 0.02 sec) (http://www.guralp.com/product-range/seismometers/); single component instruments can only detect vertical motions, whereas 3-component instruments are capable of detecting movement in all directions. Broadband 3-component seismometers (such as the Güralp 40T) are optimal for deployment at volcanoes, however the higher cost associated with these instruments often dictates that a combined network comprised of broadband and SP seismometers is typically deployed.

1.3 Field areas

1.3.1 Background

This dissertation focusses on the application of the InSAR technique to monitor ground deformation in two distinct volcanic settings (the Northern Volcanic Zone of the Andes and the South Aegean Volcanic Arc). I explore the benefits of combining InSAR with complementary volcano monitoring techniques (including GPS, gravity and soil gas monitoring) to obtain additional insight into the source of any observed deformation and the evolution of causative volcanic processes. Two distinct study areas were chosen:

1) The Colombian segment of the Northern Volcanic Zone: to determine whether modelling a combination of co-eruptive InSAR measurements and historic gravity measurements may provide additional constraints on the source and location of the deformation observed at Galeras volcano during the 2008 eruption and a gravity

anomaly detected 10 years earlier. An additional secondary benefit was that this field area allowed us to assess the benefit of using L-band (23.6 cm wavelength) satellite data to improve interferogram coherence at the often highly vegetated, steep sloped and occasionally snow-clad stratovolcanoes.

2) Santorini Volcano, South Aegean Volcanic Arc: to enable joint analysis of InSAR, GPS and gas measurements at a non-erupting (and initially quiescent) caldera volcano; also to derive a time series of deformation and soil gas emissions and obtain an improved understanding of the evolution of caldera-forming systems.

An overview of the studies I have undertaken in both volcanic regions is provided in the following section.

1.3.2 Northern Volcanic Zone, Colombia

The Colombian segment of the Northern Volcanic Zone (NVZ) extends for over 500 km (Figure 1.5) and is associated with the subduction of the Nazca plate beneath South America at a rate of 58 mm/yr (Trenkamp et al., 2002). Colombia is dominated by large andesitic–dacitic stratovolcanoes. These account for 13 of the 15 active volcanoes. Several significant eruptions have occurred at Colombian volcanoes within the historical record. In recent years, the most notable events have included the 1985 eruption at Nevado del Ruiz and the 1993 eruption at Galeras. The inaccessibility of sites for field based monitoring and the high risk of exposure to hazards make InSAR ideally suited to make a significant impact on the monitoring and understanding of volcanic activity in Colombia.

Interferograms were analysed from an area covering 15 active Colombian volcanoes, utilising L-band data from the Japanese Satellite ALOS. The main observation from this study was a subsidence signal detected on the northeast flank of Galeras volcano. 2D modelling of averaged interferograms, error analysis, comparison with contemporaneous tiltmeter measurements and gravity modelling was undertaken at Galeras volcano, to determine the origin and optimal parameters for the source of deflation. In addition, my results confirm that L-Band InSAR is successful in producing coherent interferograms at the majority of Colombia's historically active volcanoes. This improvement in coherence has provided insight into the magmatic plumbing beneath Galeras volcano through the interpretation and modelling of a co-eruptive subsidence signal associated with the January 2008 eruption.

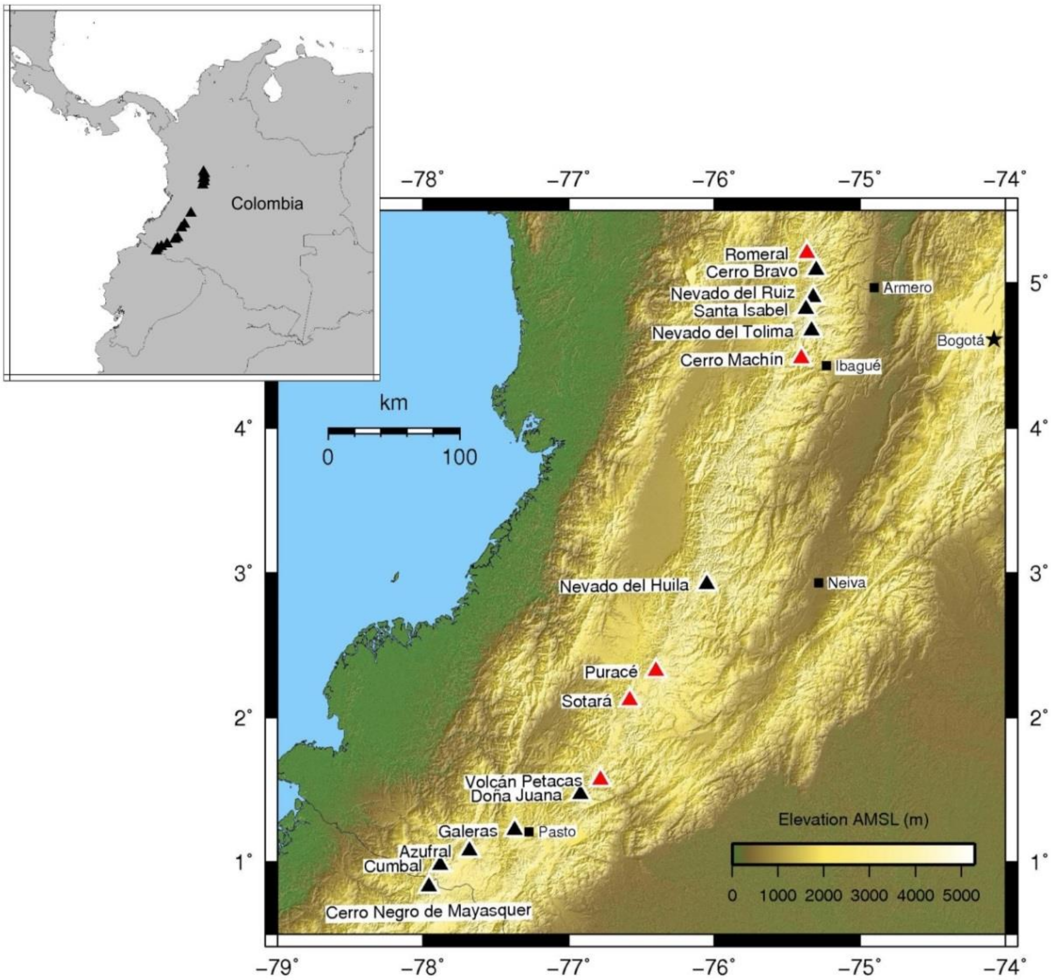

Figure 1.5: *Digital elevation model of Colombia displaying the location of the 15 active volcanoes (triangles) within the Colombian segment of the Northern Volcanic Zone. Red triangles represent volcanoes where new data was processed and analysed as part of this thesis (in addition to that at Galeras). Inset map displays the location of Colombia and its active volcanoes (black triangles).*

1.3.3 Santorini, South Aegean Volcanic Arc

The majority of my research has focussed on Santorini volcano, Greece. This study area was chosen to determine whether a multi-data stream approach - similar to that employed in Colombia, but this time combining InSAR, GPS, seismicity and gas measurements - would provide insight into various volcanic processes occurring during periods of quiescence and unrest and the implications for other caldera-forming systems.

Santorini is a young, active caldera system in the southern Aegean Volcanic Arc (Druitt et al., 1999; Vougioukalakis and Fytikas, 2005), close to an active normal fault system, the Santorini–Amorgos ridge. Regional active volcanic centres include the submarine Kolombos bank volcano and the Kameni Islands (Figure 1.6) which have been the site of the most recent eruptions. The post-Minoan shield building phase commenced in 199-197 B.C. and has included ten effusive eruptions (Pyle and Elliot, 2006), the most recent of which occurred at Nea Kameni in 1950, producing blocky dacite lava flows. The major fault system known as the Kameni line intersects the Kameni islands and has been a controlling factor in the location of historical eruption sites, with a clear progression of new vent locations, from SW to NE along the line (Fytikas et al., 1990; Vougioukalakis and Fytikas, 2005; Pyle and Elliot, 2006).

Santorini has been dormant since 1950, with no significant seismicity or deformation recorded since regular observations began in the 1980s (Fytikas et al., 1990; Bohnhoff et al., 2006; Dimitriadis et al., 2009). However, measurements of surface deformation, between 1992-2010, have detected a slow subsidence signal in the south-west corner of Nea Kameni (Lagios et al., 2005; Papageorgiou et al., 2010; Papageorgiou et al., 2012; Foumelis et al., 2013; Lagios et al., 2013 and Chapter 4) and in January 2011 the volcano entered a renewed period of unrest, characterised by the onset of detectable seismicity and caldera-wide uplift. The latter activity enabled real-time deformation monitoring via a network of continuous GPS sites installed across the Santorini archipelago, as well as the comparison of GPS and InSAR derived displacements with changes in gas emissions and micro-seismic activity. My results have not only revealed comparative trends exist between deformation, degassing and seismicity measurements, but they also provide insight into the cause of the slow subsidence signal identified prior to 2011; confirmation that the unrest observed between 2011-2012 was the result of a new magmatic intrusion and they have enabled estimates of the rate of melt supply to the shallow chamber during this period. Each of these observations may aid the interpretation of deformation signals identified at other caldera-forming systems.

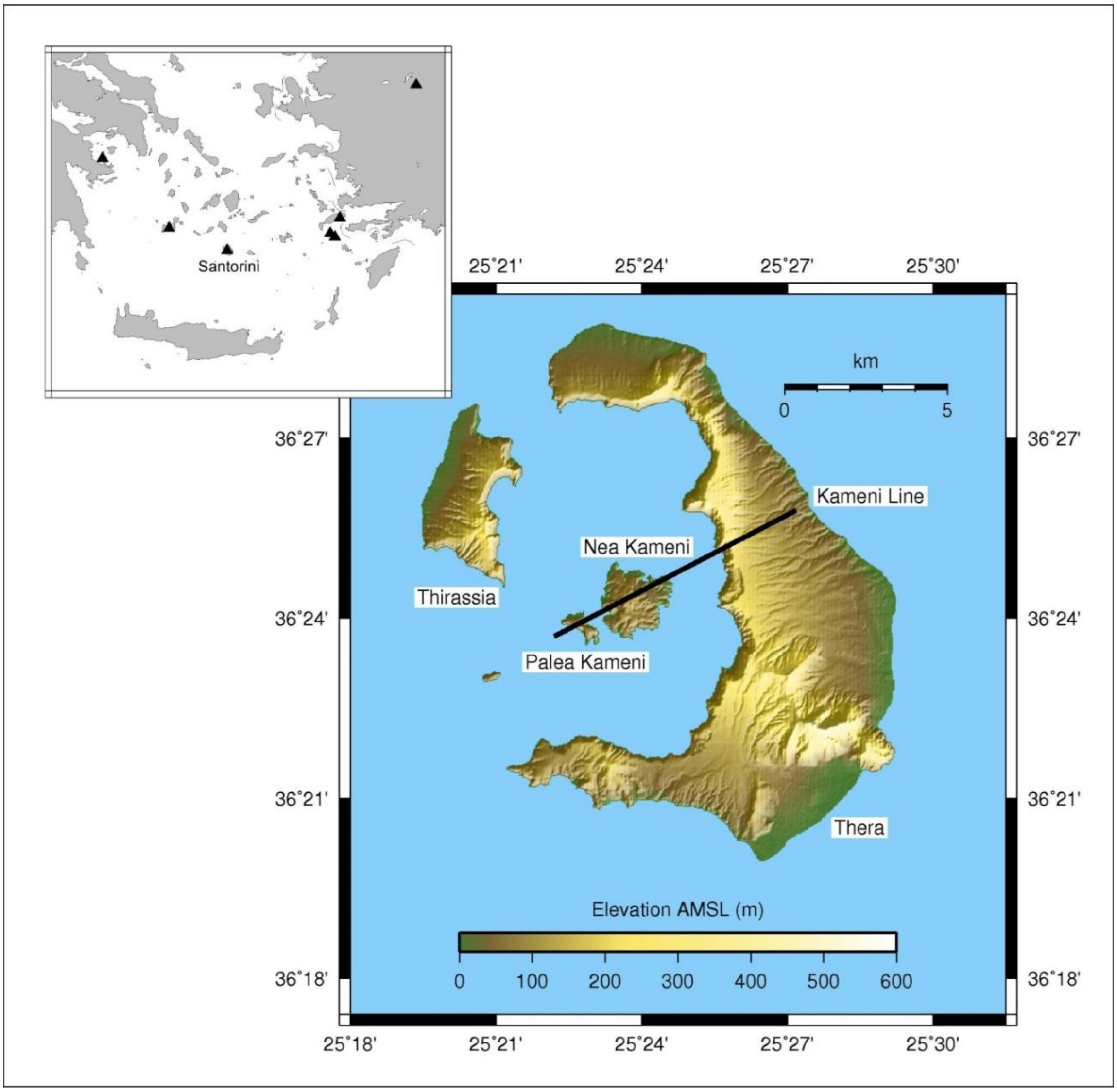

***Figure 1.6:** Digital elevation model of the Santorini archipelago and the volcano-tectonic Kameni line (black line). Inset map displays the location of Santorini with respect to the other volcanoes within the South Aegean Volcanic Arc (black triangles).*

1.4 Overview of Thesis

This thesis is concerned with the application of InSAR to monitor ground deformation at active volcanoes and highlights the advantages of combining InSAR measurements with complementary field datasets.

Chapter 2 summarises the results of an InSAR survey of 15 active volcanoes situated in the Colombian segment of the Northern Volcanic Zone. The main focus of this chapter is the interpretation of a subsidence signal identified at Galeras volcano. The origin, size and location of the source of the subsidence are determined by combining InSAR, ground-based field measurements and source modelling. This work commenced as part of an MSc thesis at the University College of London, however the results presented in this chapter represent additional analysis completed during my D.Phil. This work was published as: Parks et al., 2011. Co-eruptive subsidence at Galeras identified during an InSAR survey of Colombian volcanoes (2006-2009). *Journal of Volcanology and Geothermal Research*, 202, 228-240, 2011 (doi:10.1016/j.jvolgeores.2011.02.007).

Chapter 3 outlines the results of the initial InSAR and GPS analysis undertaken at Santorini volcano during the 2011-2012 period of unrest. InSAR analysis was employed to determine the volume of melt intruded beneath the volcano since the start of unrest in January 2011. Reoccupation of triangulation pillars using GPS was used to determine whether or not any other volumetrically significant intrusions occurred beneath the Kameni islands since 1955. This work was a collaborative effort between several institutions and a version of this chapter has been published as: Parks et al., 2012. Evolution of Santorini Volcano dominated by episodic rapid flux of melt from depth. *Nature Geoscience*, 5, 749–754, 2012 (doi:10.1038/ngeo1562). The individual author contributions to this article are listed at the beginning of Chapter 3.

Chapter 4 provides a more detailed analysis of deformation at Santorini volcano from 1993 to 2012. It includes the analysis of a slow subsidence signal identified at Nea Kameni between 1993-2010 along with joint inversion of cGPS and persistent scatter InSAR (PS-InSAR) measurements during the recent 2011-2012 period of unrest, to illustrate the temporal evolution of source parameters. This chapter represents a version of an article currently under preparation for submission to a journal. The individual author contributions to this article are listed at the beginning of Chapter 4.

Chapter 5 outlines the joint analysis of high-resolution LiDAR data and multibeam bathymetry data acquired in the vicinity of the central volcanic islands of Nea Kameni and Palea Kameni. The merged LiDAR/bathymetry grid enabled detailed mapping of the onshore and offshore extents of historic lava flows emplaced in the centre of the Santorini caldera since 47 AD, revised volumetric estimates for each of the lava flows and the derivation of rheological properties.

Chapter 6 summarises the results of 9 CO_2 soil gas-measurement campaigns undertaken on the central volcanic island of Nea Kameni bewteen 1994 and 2012, a radon survey undertaken in September 2011 and $\delta^{13}C$ isotopic analysis of CO_2 samples collected in April and September 2011. This chapter reveals the temporal variation in gas emissions at Nea Kameni before and during the recent phase of unrest and presents a new approach using ^{222}Rn-$\delta^{13}C$ systematics to identify and quantify the source of diffuse degassing throughout this period. This chapter has recently been published as: Parks et al. (2013). Distinguishing contributions to diffuse CO_2 emissions in volcanic areas from magmatic degassing and thermal decarbonation using soil gas ^{222}Rn-$\delta^{13}C$ systematics: application to Santorini volcano, Greece. *Earth and Planetary Science Letters*, doi:10.1016/j.epsl.2013.06.046). The individual author contributions to this article are listed at the beginning of Chapter 6.

Chapter 7 provides an overall summary of the results. It comprises a discussion on the suitability of InSAR to monitoring active volcanoes; where it is applicable and its usefulness with regards to determining the characteristic behaviour of volcanoes and detecting changes in volcanic activity as well as an assessment of the additional information that combining InSAR with ground-based data streams can yield.

Chapter 2

Co-eruptive subsidence at Galeras identified during an InSAR survey of Colombian volcanoes (2006-2009)

A version of this chapter has been published as: Parks et al., 2011. Co-eruptive subsidence at Galeras identified during an InSAR survey of Colombian volcanoes (2006-2009). *Journal of Volcanology and Geothermal Research*, 202, 228-240 (doi:10.1016/j.jvolgeores.2011.02.007).[1]

http://www.sciencedirect.com/science/article/pii/S0377027311000540

2.1 Introduction

Colombia's active volcanoes pose a significant hazard and challenge for monitoring, with notable recent events including the 1985 eruption at Nevado del Ruiz and the 1993 eruption at Galeras. Due to the inaccessibility of some sites for field-based monitoring and the probable exposure to hazards, Interferometric Synthetic Aperture Radar (InSAR) is ideally suited to make a significant impact on the monitoring and understanding of volcanic activity in Colombia.

InSAR is an established technique that is routinely used to measure changes in surface elevation between repeat passes of a satellite. InSAR has been successfully employed to determine rates of volcanic deformation associated with structural, hydrothermal and magmatic processes. Examples include the co-eruptive subsidence of Okmok volcano, Alaska (Lu and Dzurisin, 2010) and the uplift resulting from a sill intrusion at Eyjafjallajökull volcano, Iceland (Pedersen and Sigmundsson, 2006; Sigmundsson et al., 2010). Volcanic deformation is a complex phenomenon that can occur to various extents and over varying time scales. Deformation may not necessarily be indicative of a pending eruption – for example, the Three Sisters volcanic centre (central Oregon, Cascade Range) displayed ~ 14 cm of uplift between 1995-2001 without subsequent eruption (Dzurisin et al., 2006) and eruptions may also occur without any displacement being detected, e.g. Shishaldin volcano, Alaska (Moran et al., 2006).

In this study we assess the potential of InSAR in terms of measuring displacement rates at Colombian volcanoes. A 550 km long segment of the Colombian Northern Volcanic Zone (NVZ) was surveyed, using L-band SAR data acquired between December 2006 and September 2009, by the Japanese Advanced Land Observing Satellite (ALOS) (JAXA, 2009). Results were classified into four categories: volcanoes exhibiting deformation, atmospheric signal, incoherence and no deformation. Where deformation was observed, we employ modelling techniques to determine the most likely source parameters and interpret complementary field data to verify our observations. We also discuss the advantages of L-band interferometry and the effects of atmospheric delay.

---

[1] This work commenced as part of my MSc thesis at the University College of London. However, the work presented in this chapter is the result of significant additional analysis completed during my DPhil.

2.1.1 Introduction to Colombian Volcanism

South America is one of the most active volcanic regions on Earth, with four distinct volcanically-active segments extending along the Andes, from Colombia in the north to Chile in the south, known as the Northern, Central, Southern and Austral Volcanic Zones. The Northern Volcanic Zone (NVZ) extends for 900 km through Ecuador and Colombia, and is associated with the subduction of the Nazca plate beneath South America at a rate of 58 mm/yr (Trenkamp et al., 2002).

A previous C-band survey was undertaken at Galeras volcano (Zebker et al., 2000), but only one interferogram could be generated because of a lack of available data. Furthermore, the data quality was too poor to be able to make any interpretation. A recent large-scale survey has also been undertaken covering the whole of Latin America. The results of this study showed no deformation at any of the Colombian volcanoes (Fournier et al., 2010). However, this survey was aimed at identifying larger deformation rates, over longer time periods and on a regional scale.

The Smithsonian Institution (GVPa, 1994-) catalogues 15 active volcanoes in Colombia, which are concentrated on the Cordillera Central, the Cordillera Occidental and the Cauca-Patia depression (Stern, 2004). Colombia is dominated by large andesitic-dacitic stratovolcanoes. These account for 13 of the 15 active volcanoes (Table 2.1). This study focuses on Galeras volcano in particular and so this system is introduced in more detail in the following section.

Table 2.1: *Summary of Colombian volcanoes.*[2]

Name	Elevation (m)	Last Eruption	Volcanic Explosivity Index (VEI)	Morphology	Eruptive characteristics
Romeral	3858	5950 BC +/- 500 years	4?	Complex volcano.	Plinian eruptions.
Cerro Bravo	4000	1720 +/- 150 years	4	Dacitic lava dome complex.	Dome extrusion and pyroclastic flows.
Nevado del Ruiz[a,b]	5321	Apr 1994 - uncertain	Unknown	Summit comprises a series of lava domes and two parasitic cones.	Phreatic eruptions, pyroclastic flows, surges and lahars.
		Sep 1985 - Jul 1991	3		
Santa Isabel[c]	4965	2800 BC +/- 100 years	Unknown	Elongated summit consists of a series of arc shaped domes.	Lava flows and pyroclastic flows.
Nevado del Tolima[c]	5220	Mar 1943	2	Consists of a series of lava domes and a funnel-shaped crater.	Dacitic lava flows, pyroclastic flows and lahars.
Nevado del Huila[c,d]	5364	Feb 2007 - 2010 (continuing)	3?	Elongated NS trending glacial-capped volcanic chain. Hot springs and fumaroles.	Phreatic eruptions, radial fissure eruptions, dome extrusion, ash falls and lahars.
Cerro Machín[e,f]	2750	820 +/- 100 years	3	2.4 km wide tuff ring crater comprising three lava domes.	Pyroclastic flows and lahars.
Puracé	4650	Mar 1977	2	Truncated cone comprising of an inner 500m wide crater containing fumaroles. Overlies dacitic shield volcano.	Pyroclastic flows, lahars and lava flows.
Sotará	4580	Unknown	Unknown	Site of active fumaroles and hot springs.	No historical eruptions known.
Volcán Petacas	4054	Unknown	Unknown	Lava dome.	No historical eruptions known.
Doña Juana	4160	Nov 1897 - Aug 1936	4	Consists of two calderas and a series of lava domes.	Dome extrusion, lava flows, pyroclastic flows and lahars.
Galeras[g,h]	4276	Oct 2008 - 2010 (continuing)	1?	Consists of a cone within an older volcano – open to the west.	Pyroclastic flows, lahars, dome extrusion.
Azufral[i]	4070	930 BC?	4?	Crescent shaped acid lake, fumaroles and dacitic lava dome complex.	Lava flows, dome extrusion and pyroclastic flows.
Cumbal[j]	4764	Dec 1926	2	Lava dome within a 250 m wide crater. Hot springs and fumaroles.	Lava flows, pyroclastic flows and lahars.
Cerro Negro de Mayasquer	4470	Jul 1936?	2	Small crater lake within a caldera.	Lava flows.

---

[2] Information was primarily compiled from the Smithsonian Institution, Global Volcanism Program (GVPa, 1994-) and Instituto Colombiano de Geologia y Mineria (INGEOMINAS, 2010a) websites. Additional references: [a]Williams, 1990a and 1990b, [b]Banks et al., 1990, [c]Huggel et al., 2007, [d]Pulgarín et al., 2001, [e]Thouret et al., 1995, [f]Murcia et al., 2010, [g]Calvache et al., 1997, [h]Cortés and Raigosa, 1997, [i]Bechon and Monsalve, 1991, [j]Lewicki et al., 2000.

2.1.2 Geology of Galeras Volcano

Galeras volcanic complex lies approximately 10 km west of the city of Pasto (population approx. 330 000) (Figure 2.1). Galeras consists of a cone within a crescent shaped rim of a paleo-volcano (formed during a summit collapse event occurring between 12 and 5 ka ago (Calvache et al., 1997)). Eruptions have occurred at the summit crater, as well as at a series of vents distributed around the rim. It is one of the most active Colombian volcanoes – 6 major eruptions have occurred in the last 4500 years, producing pyroclastic flows and extensive tephra deposits. The volcano's most recent phase of activity commenced in 1988, following 40 years of quiescence (Williams et al., 1990). The renewed activity comprised the emplacement of a lava dome in late 1991, followed by a series of vulcanian eruptions from the summit crater between 1992 and 1993 (Stix et al., 1997). On 14 January 1993, an unexpected eruption at Galeras killed 6 volcanologists and 3 tourists during a field trip organised as part of the UN's Decade for Natural Disaster Reduction Workshop in Pasto (Baxter and Gresham, 1997). After 7 years of relative quiet, activity resumed in March 2000, culminating in 2 explosive eruptions from the El Pinta vent (east of the main crater) in 2002 and 2004, and additional eruptions from the summit crater in 2005, 2007, 2008, 2009 and 2010 (GVPb, 1994-). This study examines data covering the period of unrest between October 2007-January 2008 (including a VEI 1 eruption on 17 January 2008), dome growth during October 2008-February 2009 and a series of explosions occurring between February-June 2009. The volcano continues to display signs of activity at the time of writing. A comprehensive monitoring network has been established at Galeras, including broadband seismometers, gas and infrasound sensors, electronic tiltmeters and a weather station (Seidl et al., 2003).

2.2 Methods and Data Quality

2.2.1 InSAR

Active satellites, such as ALOS, illuminate a swath of the earth's surface with electromagnetic radiation and record the backscattered waves. If the volcano deforms during the repeat period of the satellite (for ALOS this is 46 days), the displacement can be measured by observing the difference between the two radar returns when the satellite is in approximately the same position overhead. This path difference results in a phase shift, which can be detected by computing an interferogram (Massonnet and Feigl, 1998). The phase change observed in a single interferogram is the result of a combination of differences in orbital position, topography, atmospheric delay and ground deformation. To separate out the phase change resulting from deformation only, the other components must first be removed. Throughout this study, processing was undertaken using the Repeat Orbit Interferometry Package (ROI_PAC) (Rosen et al., 2004), the topographic correction was applied using the Shuttle Radar Topography Mission (SRTM) 90 m resolution digital elevation model (DEM) (Gesch et. al, 2006) and interferograms were unwrapped using the branch cut algorithm (Goldstein et. al, 1988).

InSAR has the ability to measure deformation over large areas (60×60 km) at high resolution (~ 90 m) with accuracies better than 1 cm. However, measurements of displacement rates at stratovolcanoes are notoriously difficult (Zebker et al., 2000; Pritchard and Simons, 2004). In order to successfully measure ground displacement, the ground surface needs to remain relatively unchanged between acquisitions, which is why the steep slopes and often snow covered peaks of stratovolcanoes produce areas of decorrelation. Highly vegetated areas, which are common in the tropics, can also be problematic. The coherence of ALOS L-band (λ=23.6 cm) interferograms is typically higher than that obtained using C-band data (λ=5.65 cm) from other satellites (e.g. RADARSAT or ENVISAT). This has now allowed measurements at volcanoes in tropical vegetated regions such as Arenal (Ebmeier et al., 2010) and Tungurahua (Biggs et al., 2010a).

2.2.2 Atmospheric Contributions

Changes in apparent path length can be caused by variations in temperature, pressure and water vapour in the troposphere, although path delays resulting from variations in water vapour are typically more common. Two types of tropospheric delay are prevalent in InSAR results. This first is caused by turbulent mixing in the atmosphere, which affects all landscapes (both rugged and flat terrain). The second type is caused by stratification and affects mountainous regions. Atmospheric delay from stratification is caused by variations in vertical refractivity profiles in either of the two SAR acquisitions (Hanssen, 2001). This type is of most concern with regards to the interpretation of volcanic deformation. Phase delays can be up to 11 cm (Heleno et al., 2010), which is well within the range of expected uplift or subsidence during volcanic unrest. The effects are generally observed over the highest peaks, which often correspond to volcanic edifices. Fortunately these effects have a strong correlation with topography, aiding their identification.

2.2.3 Data Integrity

We employed stacking throughout the study in order to reduce random atmospheric noise. This technique consists of averaging a number of interferograms to enhance the signal to noise ratio. Interferograms displaying noise in the vicinity of the anomaly were not incorporated in the stack, to avoid bias in the averaged interferogram. Direct comparisons were then made between the DEM and the stacked interferogram, to assess the likely occurrence of phase variations related to stratified water vapour. The majority of interferograms used in the analysis have small perpendicular baselines (B⊥), (Appendix A) which ensures that the altitude of ambiguity (difference in elevation responsible for producing a full fringe (12 cm) of deformation) is significantly larger than the error in the SRTM data. Comparisons were also made between B⊥ and phase to identify any trends that may be indicative of an error in the DEM (e.g., Hooper et al., 2004).

Where appropriate, source modelling was undertaken using the University of Miami's GeodMod software (MIMIC, 2008) to establish the most likely source parameters to explain the observed deformation. Some of the methodology of GeodMod is described by Amelung and Bell, 2003. We used a simulated annealing inversion technique to determine the optimal source geometry and a linear inversion to compute the source strengths and simultaneously solve for a linear ramp to compensate for long-wavelength artefacts in the interferograms. Atmospheric noise is considered to be the largest contributor to error in the analysis. The magnitude of the water vapour contribution was estimated by fitting a 1D covariance function to each of the interferograms (Wright et al., 2003). Confidence intervals were estimated using a Monte Carlo type algorithm. We simulated 100 sets of atmospheric noise with the same magnitude and spatial correlation as the original interferograms. These were added to each of the input interferograms and the inversion was re-run to determine the range and trade-offs between each of the parameters (Wright et al., 1999; Biggs et al., 2009).

2.3 Results and Discussion

One hundred interferograms (Appendix A) were analysed as part of this study to determine whether any of the Colombian volcanoes were exhibiting signs of deformation. Figure 2.1 summarises the results of the analysis. Of the 15 volcanoes studied, 1 is believed to have undergone deformation during the observation period (Galeras), 6 are affected by atmospheric delay (Nevado del Ruiz, Nevado del Tolima, Nevado del Huila, Doña Juana, Azufral and Cumbal), 3 are incoherent (Romeral, Cerro Bravo and Cerro Machín) and the remaining 5 show no signs of deformation (Santa Isabel, Puracé, Sotará, Volcán Petacas and Cerro Negro de Mayasquer). Each of these categories will be discussed in more detail in the following section; however the main focus of the discussion is Galeras.

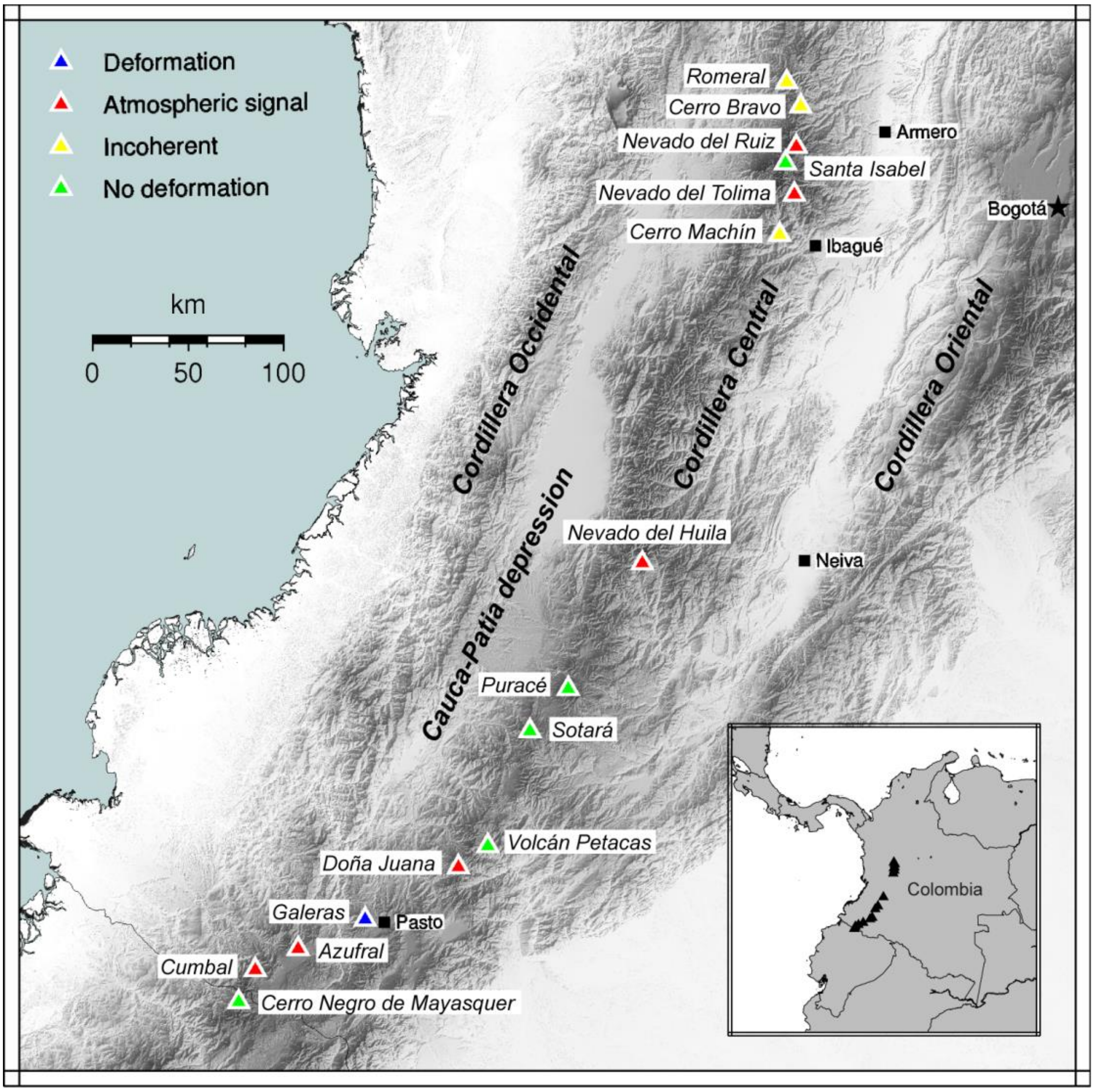

Figure 2.1: *Digital elevation model showing the location of Colombia's 15 active volcanoes (Table 2.1) and results of the InSAR study. The location of Bogotá is displayed as a black star and other major settlements as black squares. Inset shows location of the Colombian volcanic chain.*

2.3.1 Galeras Volcanic Complex

Numerous studies have been undertaken at this volcano, with correlations made between variations in SO_2 emissions, tilt, the duration and amplitude of LP events and the onset of eruptions (e.g., Fischer et al., 1994, Ordóñez and Rey, 1997 and Narváez et al., 1997). Volume changes associated with inflation or deflation of the magma chamber have also been derived by modelling variations in tilt (Ordóñez and Rey, 1997 and Narváez Medina, unpub. data). InSAR is a complementary technique which provides insight into patterns of magma movement and storage and may be used to optimise the placement of ground monitoring equipment.

2.3.1.1 InSAR

Eight interferograms generated between June 2007 and September 2008, from ALOS tracks 152 and 153, display an anomaly on the northeast-east flank of Galeras volcano that is equivalent to approximately 3 cm of vertical subsidence. Three interferograms are independent – that is, they do not share a common master or slave date (Figure 2.2). This confirms that the anomaly cannot be the result of noise or atmospheric conditions on one particular date, and the interferograms span sufficiently different time periods for phase changes resulting from seasonal variations to be limited. The location of the peak deformation varies slightly in each of these interferograms due to differences in atmospheric conditions, variations in the viewing geometry of the satellite on different acquisition dates and the varying degrees of temporal coverage of each of the interferograms. Phase variations observed between interferograms covering different time periods may reflect subsurface processes such as post-eruptive relaxation of the magma chamber, magma recharge and degassing or surface processes related to ground instability or changes in atmospheric conditions.

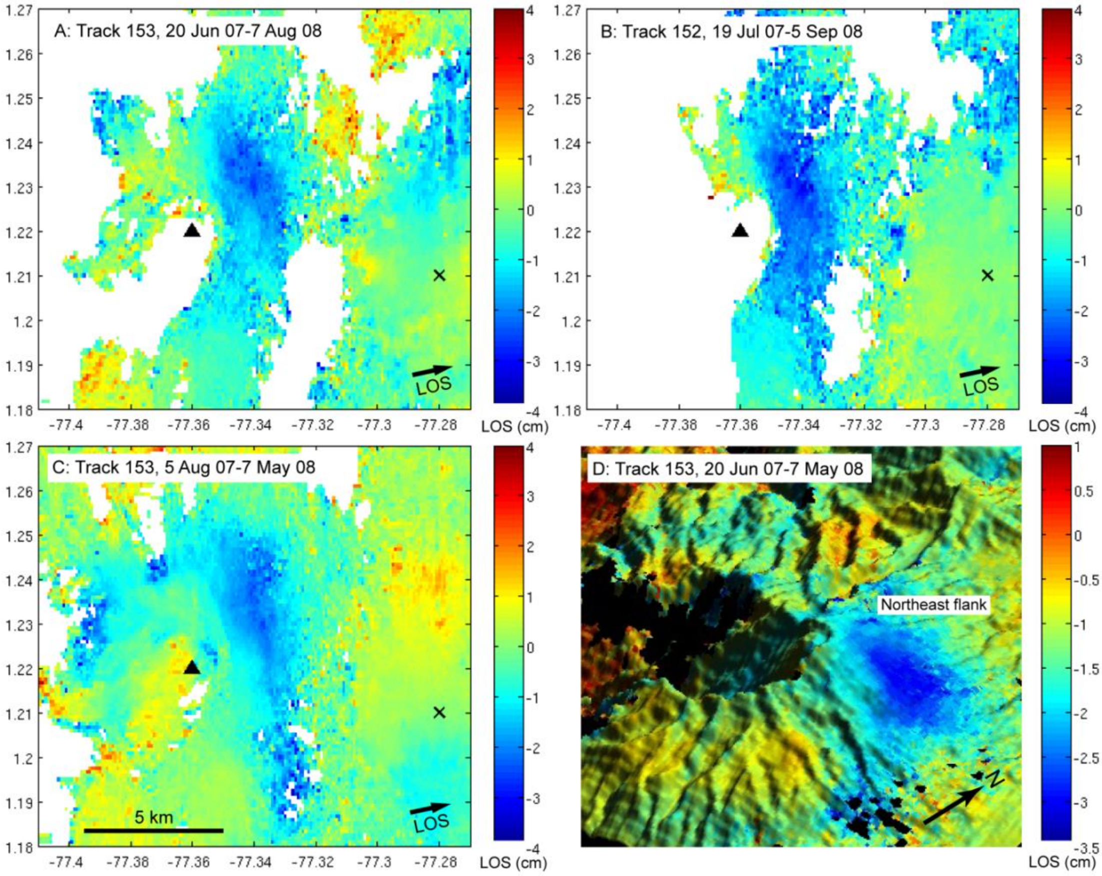

Figure 2.2: *L-band interferograms generated over Galeras for the period June 2007-September 2008.* ***(a)*** *20 Jun 07-07 Aug 08.* ***(b)*** *05 Aug 07-07 May 08.* ***(c)*** *19 Jul 07-05 Sep 08.* ***(d)*** *Perspective view of interferogram 20 Jun 07-7 May 08 superimposed on a shaded relief DEM. The subsidence signal is displayed on the NE flank of the volcano, corresponding to ~ -3 cm. The amplitudes of the independent interferograms (a-c) are given relative to a common reference point, displayed as a cross. The triangle marks the location of the summit at Galeras volcano.*

A stack of seven interferograms from tracks 152 and 153 (Figure 2.3a) clearly shows subsidence on the NE flank of the volcano. The maximum average displacement is -2.8 cm in the satellite's line of sight (LOS), which assuming purely vertical deformation corresponds to 3.4 cm of subsidence. Although one additional interferogram also displayed subsidence, this was affected by noise in the vicinity of the summit (Appendix A) and was not included in the stack. As the stack was generated by averaging interferograms from multiple tracks, it should be noted that the satellite's line of sight changes across the swath by ~ 10%, leading to an inherent error in the extracted deformation measurements (of order 10%). Comparing profiles of displacement with that of topography (Figure 2.3b), we find that the phase increase is offset from the peak elevation, making it unlikely that the phase change is caused by stratified water vapour.

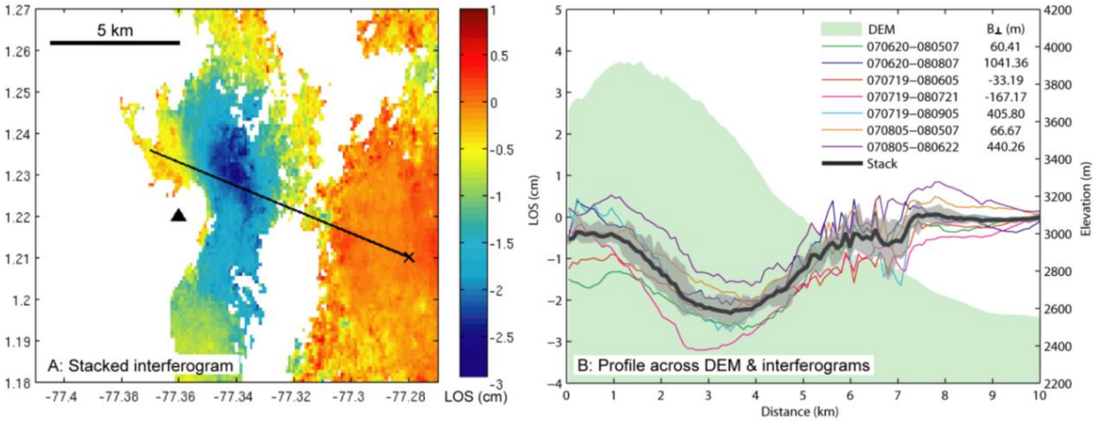

Figure 2.3: ***(a)*** *Galeras stacked interferogram, derived by averaging 7 L-band interferograms from tracks 152 and 153 over the period 20 June 2007-5 September 2008. The reference point used to scale amplitudes is displayed as a cross and the traverse used for extracting phase and elevation data is shown as the NW-SE trending line. The triangle marks the location of the summit at Galeras volcano.* ***(b)*** *Profiles extracted from interferograms and DEM across Galeras. Profiles across individual interferograms are displayed as thin coloured lines. The profile across the DEM is displayed as the green shaded area. The profile across the stacked interferogram is displayed as the black line and the difference between minimum and maximum values as the grey filled area. Interferogram master and slave dates are in the format yymmdd.*

A subsidence signal may be caused by many processes, including co-eruptive deflation of a crustal magma reservoir, post-eruptive viscoelastic relaxation, edifice collapse, lava subsidence, degassing or depressurisation of a hydrothermal reservoir (e.g., Hurwitz et al., 2007). Only by refining the period of observed deformation, undertaking source modelling and comparing InSAR results with field observations, is it possible to differentiate between these various physical processes. Analysis of the interferogram time coverage plot (Figure 2.4), suggests that the bulk of the deformation occurred during the 6 weeks between 4 December 2007 and 19 January 2008. This coincides with an explosive eruption at Galeras on 17 January 2008 (INGEOMINAS, 2008), during which incandescent blocks and bombs were ejected from the main crater and ash was dispersed up to 70 km to the west of the volcano. Preliminary analysis by INGEOMINAS scientists suggested that ~ 80% of the material ejected during the eruption was juvenile magma (INGEOMINAS, 2008).

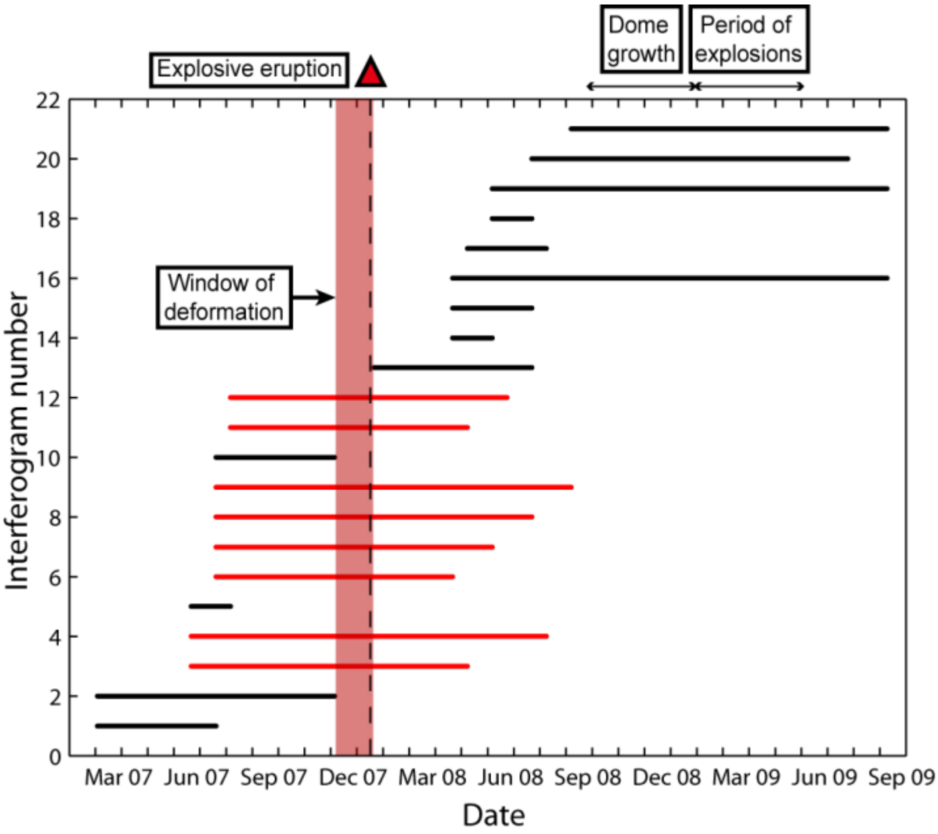

Figure 2.4: *ALOS interferograms used in the analysis at Galeras (from 3 March 2007-8 September 2009). Interferograms displaying subsidence at the volcano are displayed in red. Red shaded area represents time window during which the subsidence can have occurred. The red triangle and dashed line mark the explosive eruption at Galeras on 17 January 2008. Periods including dome growth and additional explosions are also annotated (cf. 2.3.1.3). Interferograms displaying significant atmospheric phase contributions are not included.*

2.3.1.2 Modelling

We tested both a point source (Mogi, 1958) and an Okada dislocation model (sill) (Okada, 1985) to determine the approximate location, depth and injection volume for the source of deflation at Galeras. These are flat earth models that assume a pressure source in a homogeneous, isotropic, elastic half-space.

The best fitting model is the deflation of a rectangular dislocation, which can be thought of as a sill, situated at a depth of ~ 2 km and corresponding to a volume change of approximately -6.5×10^5 m^3 (Table 2.2; Figures 2.5d and 2.5f). The sill is near-horizontal with an approximate length and width of 8 km and 3 km respectively. The dimensions, depth and dip of the sill considered suggest that the displacement resulted from the deflation of a thin magma lens, beneath the NE flank of the volcano. Although the RMS misfit is comparable for both the Mogi point source and Okada sill, the Okada sill provides the best fit to the data, producing an elongated ellipsoidal pattern similar to the observed displacement (Figures 2.5a and 2.5d).

Table 2.2: *Source model parameters.*

Source	**RMS misfit (mm)**	**Depth (km)**	**Length (km)**	**Width (km)**	**Volume change (m^3)**
Point source (Mogi)	3.06	2.8 ± 0.3	–	–	$-7.4\times10^5 \pm 1.9\times10^5$
Sill (Okada dislocation)	2.73	1.8 ± 0.2	7.9 ± 0.2	2.9 ± 0.2	$-6.5\times10^5 \pm 8.7\times10^4$

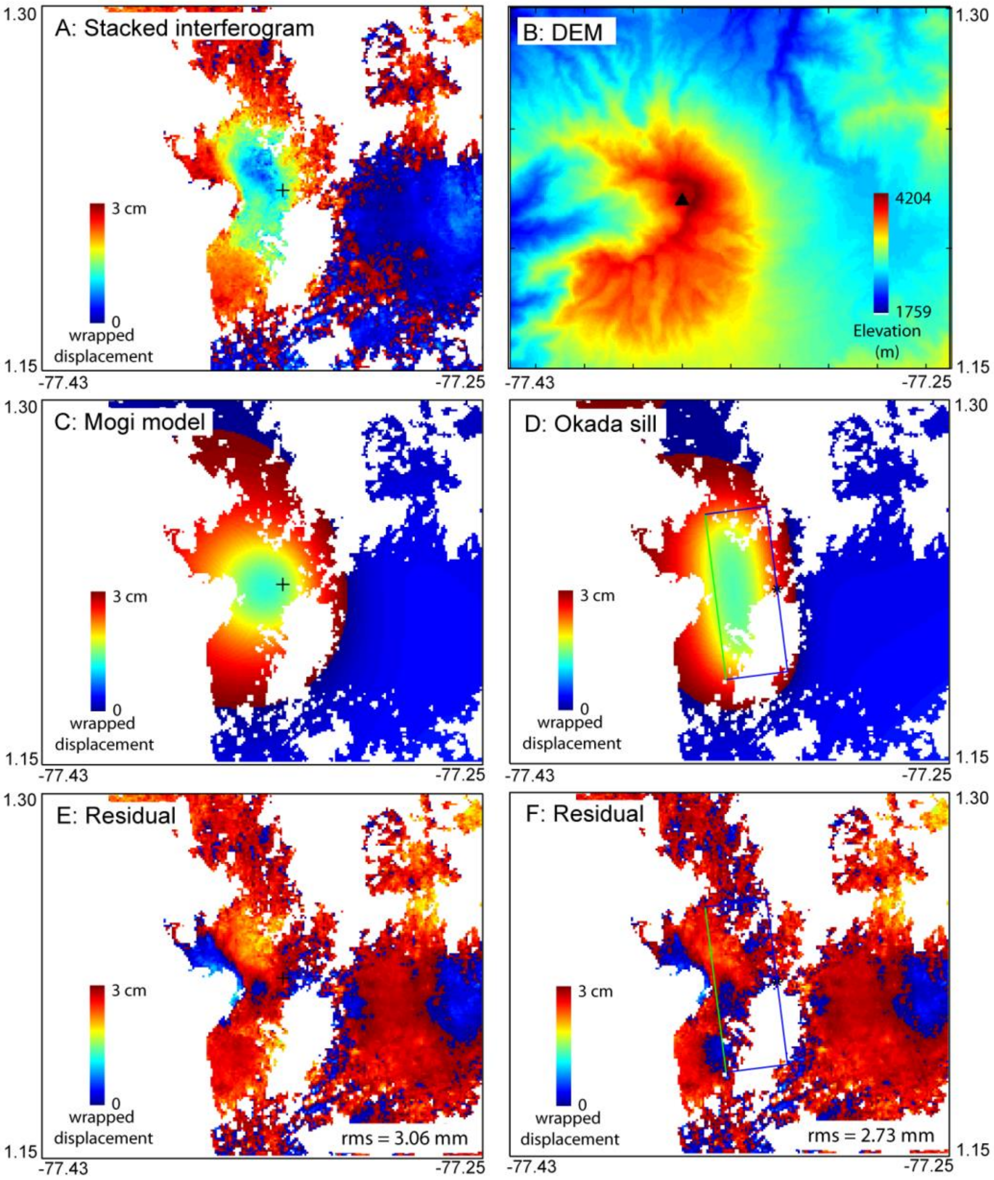

Figure 2.5: *Galeras 2D source modelling.* ***(a)*** *Stacked interferogram.* ***(b)*** *DEM.* ***(c)*** *Modelled interferogram using Mogi point source.* ***(d)*** *Best-fit model (Okada sill).* ***(e)*** *Difference between stack and modelled interferogram in Figure c.* ***(f)*** *Difference between stack and modelled interferogram in Figure d. The location of the Mogi point source is displayed as the cross in Figures a & c. The outline of the Okada sill is displayed as the rectangle in Figures d & f.*

The magnitude of the water vapour contribution was estimated by fitting a 1D covariance function to each of the interferograms (Wright et al., 2003). For a single interferogram the amplitude was ~ 6 mm. If the errors were uncorrelated, a stack of N observations with error (σ) will have an error of $\sigma/\sqrt{N}$. Thus we expect the error on the averaged interferogram to be of the order 2 mm. This is in agreement with the observed RMS misfits between the forward models and the averaged interferogram (Table 2.2). We estimated the confidence intervals using a Monte Carlo type algorithm (Table 2.2). We simulated 100 sets of atmospheric noise which were added to each of the input interferograms and the inversion was re-run to determine the range and trade-offs between each of the parameters (Wright et al., 1999; Biggs et al., 2009). The primary trade-offs observed were between depth and the amount of opening, and depth and volume change (an increase in ΔV requires an increased depth to source to produce the same amount of displacement).

Although the point source (Mogi, 1958) and Okada dislocation (Okada, 1985) models do not take into account variations in topography, we tested a 1D model incorporating topographic corrections (Williams and Wadge, 1998) (Appendix B, Supplementary Figure 1) for the profile displayed in Figure 2.3b. Our results suggest only a minimal change would be observed, with a lateral displacement of the maximum amplitude to the east by approximately 500 m. Of course, a number of the assumptions made during modelling are unlikely to hold true. For example, the crust is unlikely to be homogeneous or isotropic in the vicinity of an active volcano and an intrusion of magma will heat the surrounding crust, producing weak thermally altered zones. By assuming a purely elastic, homogeneous half-space we possibly overestimate the depressurisation and underestimate the depth to the magma chamber (Masterlark et al., 2010). We also assume that the magma is incompressible; however it is likely to be a mixture of crystals, liquid and gas, and the behaviour of 3 phase fluids is poorly understood.

The derived volume change of -6.5×10^5 m^3 is close to the estimated erupted volume of 8.7×10^5 m^3, reported by INGEOMINAS (2008) for the 17 January eruption, which lends credibility to our interpretation of the deformation as resulting from deflation of the magma chamber during this small event. Although the modelling has inherent limitations, the modelled depth range, dimensions and location of the source are considered reasonable and are in broad agreement with contemporaneous tiltmeter data (INGEOMINAS, 2008 and Narváez Medina, unpub. data) discussed in section 2.3.1.3, historic gravity anomalies (Jentzsch et al. 2004), a zone of low p-wave velocity (Londoño and Ospina, 2008), seismic attenuation anomalies (Carcolé et al., 2006; Lacruz et al., 2009) and cluster locations of historic seismic crises (Cortés and Raigosa, 1997) discussed further in section 2.3.1.4. Previous petrological studies support magma storage at shallow levels beneath Galeras, with the majority of samples analysed from earlier eruptive phases showing evidence for amphibole instability (reaction rims replaced by oxides, pyroxene and plagioclaise). This suggests some magma residence at pressures of less than 2 kbar, assuming a temperature of 900°C (Calvache and Williams, 1997).

The high spatial density of InSAR measurements has allowed us to identify a deformation source on the NE flank of Galeras. In light of this discovery, we review observations from sparser datasets (tilts and gravity) to see whether they are consistent with our InSAR measurements.

2.3.1.3 Observations from tiltmeters

We start by discussing other data, spanning the period of the 2008 activity covered by the InSAR signals. Two tiltmeters situated on the NE flank of the volcano registered displacement during the eruption on the 17 January 2008 - ‘Crater’, situated 0.8 km ENE, and ‘Peladitos’, located 1.4 km SE of the crater (Figure 2.6a). Crater displayed variations in tangential and radial components of 24 and 26 microradians (μrads) respectively, while variations observed at Peladitos were 5 and 20 μrads (INGEOMINAS, 2008). Mogi modelling of the tilt data acquired between 17 and 19 January 2008 predicts a volume change of -7×10^5 m^3 with a deflation source located at a depth of 1.4 km (Narváez Medina, unpub. data). Both the volume and source depth computed from the tilt data correspond well with our InSAR modelling estimates of -6.5×10^5 m^3 and 1.8 km. Additional data are desirable to make a fully quantitative comparison of measurements. However, we can have confidence that the tilts are in agreement with the InSAR observations in that they also display subsidence, are in close proximity to the InSAR anomaly and are during the same window of deformation.

The detection of co-eruptive subsidence by two tiltmeters on 17 January 2008 and the fact that seismicity measurements recorded during January 2008 display a clear increase in LP events on 17 and 18 January (INGEOMINAS, 2008), lead us to believe that the displacement observed on the interferograms occurred on 17 January 2008. The occurrence of a VEI 1 eruption during the window of deformation suggests that the January 2008 subsidence signal was associated with co-eruptive processes within the magmatic and hydrothermal systems. Furthermore, the reasonable agreement between our model derived volumes and the estimated erupted volume suggests the subsidence may be the result of magma withdrawal.

The January 2008 period was not the only occasion on which the tiltmeters have measured deformation at Galeras. Deformation believed to be associated with magma movement has been detected at both Peladitos and Crater on four other occasions:

August-November 1991 (Ordoñez and Rey, 1997), August-October 2005, June-December 2008 and January-April 2009 (Narváez Medina, unpub. data). The first three periods were related to magma ascent and the extrusion of lava domes, whereas the decline observed during January-April 2009 is believed to be associated with a series of explosions occurring between 14 February and 29 April 2009 (Narváez Medina, unpub. data). The majority of interferograms spanning the periods June-December 2008 and January-April 2009, were either affected by stratified water vapour or showed long wavelength diagonal striping (caused by the dispersion of the radar wave by interactions with free electrons in the ionosphere (Gray et al., 2000; Hanssen, 2001)). After filtering attempts to reduce the atmospheric phase contribution, several interferograms displayed signs of possible deformation in accordance with the tilt measurements, but because remnant atmospheric phase variations still remained we did not undertake source modelling. Four interferograms covering both episodes (dome growth and explosions) display no deformation (Figure 2.4). It is considered unlikely that dome growth alone would be detected via InSAR, as the length-scale is too short and interferograms span both of these periods, so this lack of observed deformation may be the result of any pre-eruptive deformation being cancelled by co-eruptive or post-eruptive deformation.

2.3.1.4 Evidence for a recurrent magma chamber

Our results are consistent with previous studies on Galeras since 1989. Although these earlier studies support the possibility of a recurrent chamber, InSAR provides the first piece of evidence linked to an eruption. Carcolé et al. (2006) suggested the presence of a shallow magma chamber beneath the NE flank of the volcano based on higher scattering coefficients of shallow earthquakes recorded between 1989-2002, and Lacruz et al. (2009), utilising 435 VT events recorded during the same period, detected strong seismic attenuation anomalies to the NE of the crater (between latitudes 1.22N to 1.28N and longitudes -77.35 to -77.30W) at depths between 2.5 to 5 km.

The position of our anomaly also corresponds with hypocentral cluster locations from 3 seismic crises in April 1993, November-December 1993 and March 1995 (Cortés and Raigosa, 1997). These events were located beneath the NE flank of the volcano at depths between 2-8 km below the surface. Stix et al. (1997) and Zapata et al. (1997) suggested that these events could be related to magma intrusion, whereas Jiménez et al. (2009) argued that these events may have resulted from the activation of local faults. In either case, it is feasible that previous tectonic earthquakes beneath the NE flank have resulted in zones of weakness providing preferential pathways for the migration of fluids. Furthermore, a tomographic inversion study undertaken by Londoño and Ospina (2008) identified a corresponding zone of reduced P-wave velocity. Their anomaly was located east of the crater at a depth of ~ 1-3 km beneath the summit, between longitudes -77.35W to -77.32W. The location is in good agreement with the position of our source of deflation derived from modelling. This low-velocity zone was interpreted by the authors as corresponding to a more fluid resident magma chamber.

Gravity campaigns undertaken by Jentzsch et al. (2004), between September 1998 and March 2000 detected an anomaly close to our observed subsidence signal (Figure 2.6a shows the location of their gravity stations). The peak increases in gravity of 81 and 87 μGals (in the second and third campaigns respectively) were recorded approximately 3.5 km to the NE of the crater (Figure 2.6b) (250 m from our modelled Mogi point source). The data indicates that the gravity increase occurred between acquisition of the first and second gravity surveys (over the 6-month period from September 1998 - March 1999). The anomaly was observed in the same location one year later, when the third survey was undertaken.

Gravity measurements can be used to calculate changes in mass distribution, while deformation measurements are sensitive to volume change. Where both are available simultaneously, it is possible to calculate the density of the intrusion directly (Battaglia et al., 1999). In this case only gravity measurements from 1998-2000 were available, but by assuming that the location and depth to the source are the same as for our 2008 InSAR measurements (section 2.3.1.2), the corresponding changes in mass during the period 1998-2000 may be estimated. If we are able to fit the 1998-2000 gravity data using our 2008 source location, this also suggests some decadal-scale stability in terms of the shallow internal structures within the volcano.

A spherical body was chosen for the modelling because of its straightforward comparison with Mogi point source models. The gravity anomaly produced by a buried sphere is a combination of two phenomena – a change in mass distribution at depth, plus a change in height as a result of the pressure change (Segall, 2010). We refer to these separate contributions as '$g$mass' (the gravity anomaly resulting from the redistribution of mass) and '$g$def' (that resulting from the induced deformation). The gravity change resulting from the combination of these (δgz(t)) is equal to:

$$\delta g\mathrm{z(t)} = \delta g\mathrm{mass} + \delta g\mathrm{def} \tag{2.1}$$

and

$$\delta g\text{mass} = \frac{G\Delta M d}{(x^2 + d^2)^{3/2}}$$

(2.2)

where ΔM is the change in mass, d is the depth from the centre of the chamber to the measurement point on the surface, x is the horizontal distance from the centre of the chamber to the reference point and G is the gravitational constant (6.67×10^{-11} m^3 kg^{-1} s^{-2}).

Since no deformation was observed at tiltmeter Peladitos (or indeed at Crater), but a gravity anomaly of 30 μGals was observed at gravity station Pela (2.7 km from Mogi source) (Figure 2.6b) between September 1998 and March 2000, we assume that the majority of the anomaly is the result of changes in mass. Large variations in gravity have been observed at other volcanoes with little or no corresponding elevation changes, including Etna (Rymer et al., 1995), Merapi (Jentzsch et al., 2004) and Kilauea (Johnson et al., 2010). Furthermore, while no eruption was reported during the time span between the first and second gravity surveys, tornillos and harmonic tremor were recorded during October 1998-January 1999 (GVPc, 1994-). Tornillos are low frequency quasi-monochromatic seismic signals (Chouet, 1992) which have previously been associated with the resonance of fluids or gas moving along migration pathways. Harmonic tremor is often detected during periods of degassing (Cruz and Chouet, 1997). Both processes suggest mass transfer within the system. There were also reports from INGEOMINAS scientists of cracks appearing at the summit and numerous fissures emitting gas (GVPc, 1994-).

We model the effects of mass redistribution by employing a linear inversion technique to minimise the misfit between the calculated and observed gravity measurements at each of the 7 stations. The distance to each station was computed radially from our Mogi point source location (used rather than the Okada sill for simplicity). The optimal ΔM was determined to be 9.7×10^{10} kg, which will be discussed in greater detail later in this section. The model (Figure 2.6b) provides a good match to the measured data, with the exception of the observed value at station Tel1. The half-width of the observed gravity anomaly and the subsidence anomaly from the stacked interferogram were also computed, to compare the wavelength of the gravity and InSAR measurements. The derived values are in good agreement (~ 2 km – Figures 2.6b and 2.3b), which supports our modelled source location and depth (2.8 km) being characteristic of the system 10 years prior.

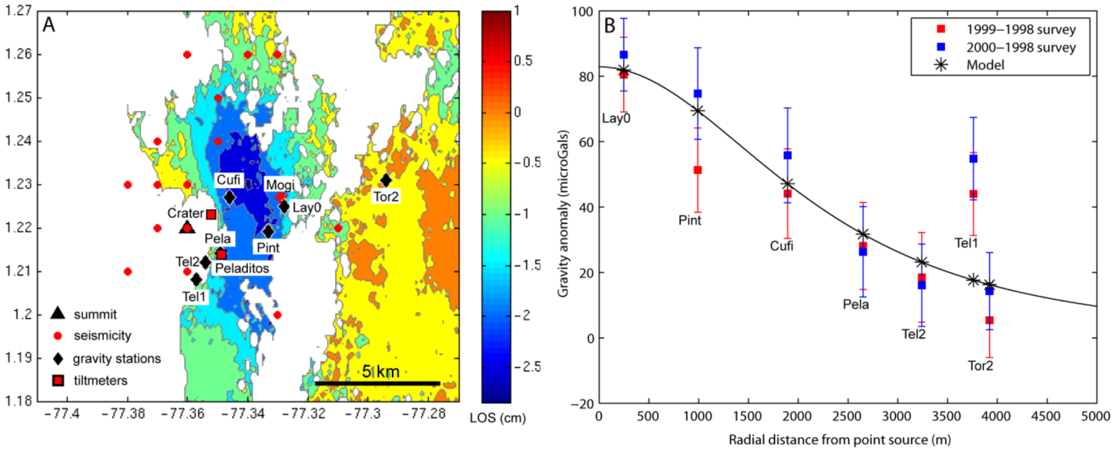

Figure 2.6: *Comparison of InSAR and field data at Galeras volcano.* ***(a)*** *Stacked interferogram showing locations of seismic events recorded in Jan 2008, gravity stations and tiltmeters at Galeras volcano.* ***(b)*** *Comparison of modelled gravity anomaly, gz(t) (assuming that the location and depth to the source are the same as for our 2008 InSAR measurements) and measured gravity data recorded at Galeras (after Jentzsch et.al, 2004).*

Two small eruptions occurred on 21 March and 5 April 2000, after the gravity surveys were acquired. The description of grey/white emissions (GVPc, 1994-) suggests that these events had a phreatic component. Acid gas variations at active fumaroles and thermal springs provide evidence of an active but immature hydrothermal system at Galeras (Alfaro and Zapata, 1997), and pre-eruptive decreases in HCl/CO_2 ratios also suggest selective absorption of volatiles by a shallow hydrothermal reservoir (Fischer et al., 1996). In light of these observations, we consider two possible scenarios that could be responsible for the increase in gravity by causing a sub-surface variation in mass with little or no resultant deformation: 1) magma intrusion, devesiculation and degassing (e.g., Eggers, 1983; Rymer, 1994 and Crider et al., 2008) and 2) groundwater recharge/migration (e.g., Jachens and Roberts, 1985). A similar effect could also be produced by magma intrusion into pre-existing open fractures (e.g., Johnson et al., 2010).

Applying the source location parameters calculated from InSAR has allowed us to estimate the mass increase associated with the gravity increase observed between 1998 and 2000 as 9.7×10^{10} kg. Therefore by assuming typical density changes associated with scenarios 1 and 2 we can assess the volume of new material introduced to the system (Table 2.3) using the relationship $V=\Delta M/\Delta\rho$. It is assumed that this volume change is accommodated within the edifice without causing deformation, either by migration through open pores and fractures or in the magmatic scenario, as a result of degassing. For example, the magma intrusion and degassing scenario requires that the loss of volatiles from a vesiculated magma (via fumarolic degassing over a 6 month period) is balanced by the influx of melt (Table 2.3) such that the pressure remains approximately constant.

Table 2.3: *Parameters used to model 2 possible scenarios that may be responsible for the observed increase in gravity at Galeras.*[3]

Model	**$\rho 2$ (kg m^{-3})**	**$\rho 1$ (kg m^{-3})**	**$\Delta\rho$ (kg m^{-3})**	**V (m^3)**	**Minimum inferred rate of fluid movement[a] (m^3 s^{-1})**
Magma intrusion, devesiculation & degassing[b]	2600	1600	1000	9.7×10^7	6
Groundwater recharge/migration[c]	1000	0	180	5.4×10^8	35

A gravity increase related to groundwater replenishment might be accomplished by either meteoric recharge, or the migration of groundwater to this area, as a result of induced pore-pressure gradients. Groundwater flow along open faults and fractures (Jónsson et al., 2003) might also explain the decline detected on two portable tiltmeters (Chorrillo and Huairatola) to the north of the volcano (between late September 1998 to the end of January 1999, the instruments showed a cumulative decline in the radial component, of ~ 35 and ~ 600 µrads at Chorrillo and Huairatola respectively (GVPc, 1994-).

---

[3] [a]Computed by assuming fluid movement was evenly distributed over the 6-month period between the 1998 and 1999 gravity campaigns. Magma densities were computed using KWare Magma (KWare, 1999) assuming an andesitic magma, at a temperature of 900°C and pressure of 900 bars (corresponding to ~ 3 km depth). $\rho 1$ is the density of the material in place, $\rho 2$ is the density of the intruding material, $\Delta\rho$ is the overall change in density and V is the volume of new material introduced to the system, associated with the change in mass (it is assumed that this volume change is accommodated within the edifice without causing deformation, either as a result of degassing or intrusion into open pores and fractures).

[b]Modelled by replacing a vesiculated magma (1600 kg m^{-3}) with an unvesiculated magma.

[c]Assuming an average porosity of 18% and meteoric water with a density of 1000 kg m^{-3} is filling empty voids resulting in an overall increase in density of 180 kg m^{-3}.

The meteoric recharge model requires a volume change of 5.4×10^8 m^3 (Table 2.3). Loboguerrero and Gilboa (1987) estimated the volume of the average groundwater recharge in the Cauca valley (within which Galeras is located) to be ~ 1.6×10^5 m^3 per year, per km^2. If we assume the recharge zone at Galeras comprises the region east of the amphitheatre margin, incorporating the active cone and fumaroles, this equates to an area ~ 0.8 km^2. Over the 6-month period (in which the gravity increase was observed) this would correspond to a volume of water accumulation of 6.3×10^4 m^3, which is too low to account for the gravity anomaly. Groundwater migration meanwhile would require a lateral fluid flux of 35 m^3 s^{-1} (Table 2.3) to produce the detected increase in gravity. This is significantly higher than that which has been reported in this area (~ 0.001 to ~ 0.3 m^3 s^{-1}, Loboguerrero and Gilboa, 1987; Fischer et al., 1997). Therefore meteoric recharge or lateral fluid flow alone, do not seem sufficient to account for the observed anomaly.

Our preferred interpretation is that magmatic processes are a more probable explanation of the gravity anomaly. The model yields injection rates (~ 6 m^3 s^{-1}) comparable to those seen at other andesitic volcanoes such as Soufrière Hills, Montserrat (Elsworth et al., 2008; Melnik and Sparks, 2005). Although the gravity anomaly cannot be explained solely by groundwater recharge/migration, we do not discount the interaction between magma intrusion and degassing, and the selective absorption of soluble volatiles into shallow ground waters, during sealing of migration pathways, which may have led to the repeated episodes of pressure build-up and eruption (e.g., Fischer et al., 1996; Boichu et al., 2008).

In summary, from a combination of independent observations (InSAR and tilts), source modelling and the episodic nature of the observed displacement, we infer that the 2008 subsidence measured at Galeras is likely to have resulted from processes related to the explosive eruption occurring in January 2008. It is proposed that during this event the expulsion of gas and ash caused a reduction in pressure of a magma chamber, situated ~ 2–3 km NE of the summit at a depth of ~ 2 km. This new understanding of the nature of the shallow volcanic system at Galeras in 2008 has allowed us to re-examine the nature of the activity and the gravity anomaly observed between 1998-2000. We are able to model this data successfully using the same source parameters as for 2008, suggesting some stability in the subsurface structure on a decadal timescale. Based on volumetric calculations and visual observations it would seem that the small eruptions in 2000 were most likely a combination of both hydrothermal and magmatic processes.

2.3.2 InSAR survey of Colombian volcanoes

Although the volcanoes discussed in this section are not thought to be deforming, we have included a brief review of our results. Many of these volcanoes are of great interest to the scientific community and to others concerned with hazard management.

2.3.2.1 Atmospheric signals

Interferograms covering Nevado del Ruiz, Nevado del Tolima, Nevado del Huila, Doña Juana, Azufral and Cumbal appear to be affected by tropospheric delay. These displayed significant phase changes during the observation period, but in each case displacement could either be correlated with topography or was reversible with seasons. At Nevado del Tolima, a possible subsidence signal (increase in range) was observed on multiple interferograms from separate tracks (Figures 2.7a and 2.7b). However each of these spanned the latter half of the calendar year and a decrease in range was detected on an interferogram covering the 12 August 2007-29 June 2008. The apparent reversal in polarity and comparison of displacement and DEM (Figure 2.7b) suggests this is likely the result of seasonal variations in water vapour.

Doña Juana is potentially one of the most hazardous volcanoes in Colombia, due to its history of large eruptions (>VEI 4) and capacity for generating major pyroclastic flows. At Doña Juana several interferograms exhibit phase changes of up to 4 cm of displacement in the satellite’s LOS. However, a NE-SW traverse across the anomaly from the interferogram 19 July 2007 - 3 September 2007 shows that the extracted phase is highly correlated with topography (Figure 2.7d). Doña Juana and Cerro Animas (peak to the NE) have roughly the same relief (~ 4150 metres) and similar phase change. This would seem to be a clear example of the effect of stratified water vapour. There is some recent evidence for new activity in the region of Doña Juana and Cerro Animas. VT earthquakes were recorded on 20 and 21 May 2009, (INGEOMINAS, 2009) and a cluster of earthquakes were detected in June 2010, in close proximity to Cerro Animas (Monsalve, unpub. data). The 2 interferograms covering the first period of seismic activity (May 2009) are affected by tropospheric delay so additional scenes will be required to determine whether this volcano is deforming.

After 450 years of quiescence, activity resumed at Nevado del Huila in February 2007, with a VEI 3 explosive eruption that produced damaging mudflows. Successive eruptions followed in November 2008 and October 2009 (GVPd, 1994-). Nevado del Huila displayed possible uplift on one interferogram covering the period 17 March 2008 – 18 December 2008 (Appendix B, Supplementary Figure 2). Although the observed anomaly coincides with the most recent periods of activity (2 January 2008 - April 2008 and 26 October 2008 - 2010 (GVPe, 1994-), the phase signature over the summit appears correlated with topography. This suggests phase variations are the result of stratified water vapour. There is however an anomaly on the western flank (~ 3.5 cm) that is offset from the DEM (Appendix B, Supplementary Figure 2), but this was only visible on one interferogram and so cannot be viewed as conclusive.

Nevado del Ruiz has a propensity for creating large destructive lahars. The November 1985 eruption produced small pyroclastic flows and surges that melted part of the ice-cap. This generated lahars that crashed through the towns of Armero and Chinchina (Naranjo et al., 1986). Nevado del Ruiz displays a decrease in range (~ 2.5 cm LOS) on one interferogram. This was not observed at any of the 3 other volcanoes, which were also covered by the image 11 December 2007-13 December 2008 (Appendix B, Supplementary Figure 3). Using additional interferograms which show no deformation, we narrow down the time window to between 27 April 2008 and 28 July 2008. We attribute this anomaly to atmospheric contributions because no volcanic activity was reported for this time interval, the signal has a high correlation with topography and it was only observed for this one time period with no other supporting observations.

A number of interferograms from multiple tracks displayed long wavelength diagonal striping, possibly the result of ionospheric interactions (Gray et al., 2000; Hanssen, 2001). Although this kind of delay is unlikely to be misinterpreted as volcanic deformation, it may mask small displacement signals.

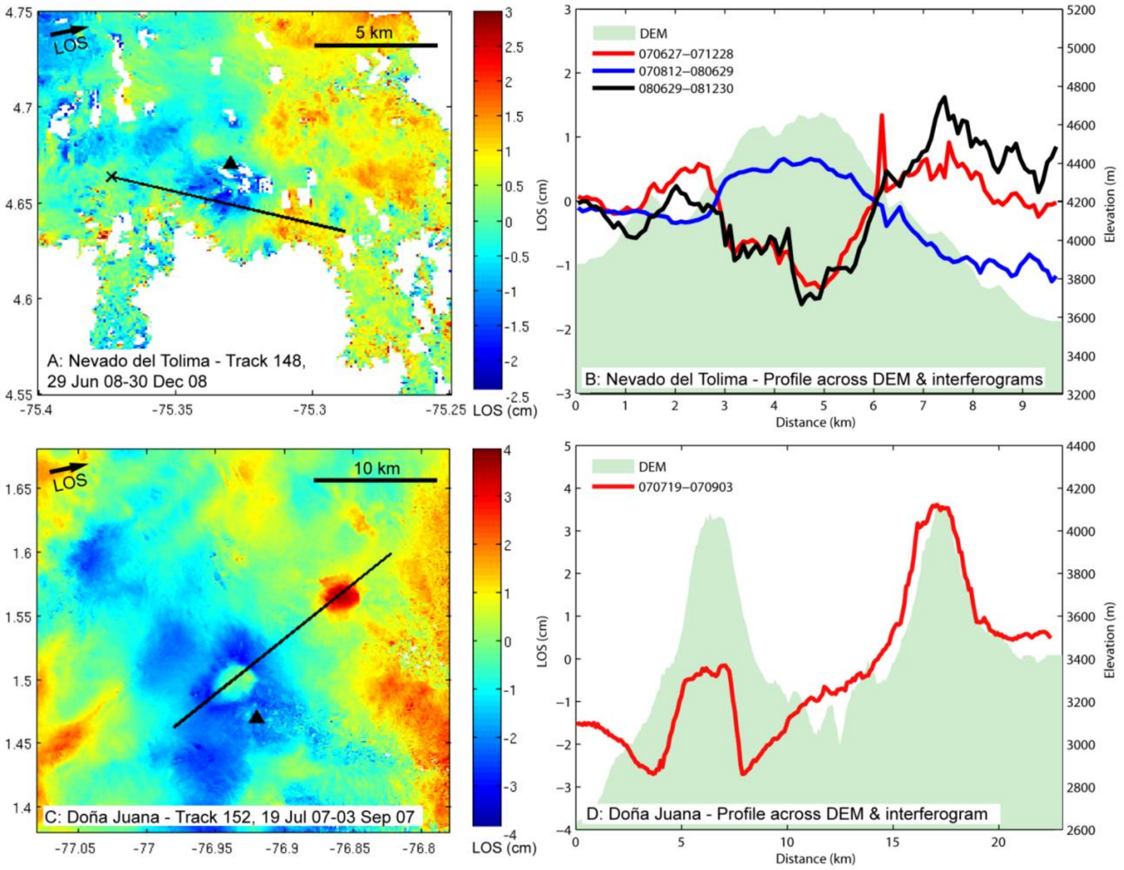

Figure 2.7: ***(a)*** *Interferogram generated over Nevado del Tolima for the period 29 Jun 08-30 Dec 08.* ***(b)*** *Profile extracted across DEM and interferograms for Nevado del Tolima.* ***(c)*** *Interferogram generated over Doña Juana for the period 19 Jul 07-03 Sep 07.* ***(d)*** *Profile extracted across DEM and interferogram for Doña Juana (SW) and Cerro Animas (NE). Interferogram master and slave dates in Figures b & d are in the format yymmdd.*

2.3.2.2 Volcanoes not displaying signs of deformation

No deformation was observed at Romeral, Cerro Bravo, Santa Isabel, Cerro Machín, Puracé, Sotará, Volcán Petacas and Cerro Negro de Mayasquer. It should however be noted that for several of these, InSAR coverage is limited by poor coherence (Romeral, Cerro Bravo and Cerro Machín). Cerro Machín (currently limited by coherence) is important to target because after four years of relative quiet, anomalous seismic activity was detected in the vicinity of the main dome in January 2008. This was followed by a seismic crisis on 9 November 2008 and swarms of shallow earthquakes on 18

December 2008 and 6 June 2009 (INGEOMINAS, 2010b). Unfortunately no interferograms covering these periods maintain coherence in the vicinity of the volcano. At the time of writing, the frequency of swarms at Cerro Machín appears to be increasing, with additional events occurring in December 2009, March 2010, July 2010 and September 2010.

2.4 Conclusions

Following the analysis of 100 interferograms, covering a 550 km segment of the Colombian NVZ between 2006 and 2009, we conclude that the majority of volcanoes are not exhibiting deformation. Of the 15 volcanoes surveyed, atmospheric signals have been observed at 6 (Nevado del Ruiz, Nevado del Tolima, Nevado del Huila, Doña Juana, Azufral and Cumbal), 5 displayed no sign of deformation (Santa Isabel, Puracé, Sotará, Volcán Petacas and Cerro Negro de Mayasquer), 3 were incoherent (Romeral, Cerro Bravo and Cerro Machín) and a subsidence signal was detected at 1 (Galeras).

Three independent interferograms over Galeras from two ALOS tracks display similar displacements, coinciding with the October 2007 - January 2008 unrest and eruption. The maximum observed change corresponds to approximately -3 cm vertical displacement. We propose that this signal was caused by deflation of the magma chamber during an explosive event on 17 January 2008. Source models provide a good fit to the data and insight into the injection volume, depth to source, and the dimensions of the chamber. The observed displacement is consistent with deflation of a magma lens under the NE flank of the volcano, caused by a volume change of -6.5×10^5 m^3 from a deformation source situated at a depth of ~ 2 km below the surface. This information may be useful in characterising part of the magma plumbing system. Prior studies, including gravity measurements (Jentzsch et al., 2004), deformation measurements (Narváez Medina, unpub. data), seismic attenuation studies (Carcolé et al. 2006; Lacruz et al. 2009) and a tomographic inversion (Londoño and Ospina 2008) all support the existence of a resident/recurring chamber at this location over a decadal timescale. This suggests that future field monitoring efforts could benefit by increasing deployment of equipment in this region.

Nevado del Huila also entered an eruptive phase during the observation period. However we were not able to confirm any deformation at this volcano. More frequent SAR acquisitions are required to better determine the deformation characteristics of this volcano. Atmospheric delay is the primary contributor to noise in interferograms. Atmospheric signals were identified at 6 volcanoes with Doña Juana and Nevado del Tolima providing good examples of phase variations resulting from a stratified troposphere. Santa Isabel, Puracé, Volcán Sotara, Volcán Petacas and Cerro Negro de Mayasque showed no signs of deformation, and no activity was reported at these volcanoes during the observation period. Coherence was limited at Cerro Machín, Cerro Bravo and Romeral. Cerro Machín has showed recent signs of seismic unrest and would benefit from additional observation.

This study highlights the potential use of InSAR for measuring displacement at active volcanoes, and demonstrates how combining the results with modelling and complementary field data (e.g. gravity and tilts) can provide further confidence concerning the likely origin and dimensions of the source of deformation. We demonstrate that L-band interferometery provides improved coherence over C-band data at Galeras, but coverage is still limited by incoherence as well as by atmospheric delay at several volcanoes. Lack of observed deformation may be a result of limited

SAR acquisitions or internal processes which offset surface displacements. This question may only be answered with increased coverage.

With the launch of new satellites such as Sentinel-1 and DESDynI (Deformation, Ecosystem Structure and Dynamics of Ice - a dedicated InSAR and LIDAR mission) acquisition parameters will be improved and satellite repeat times reduced (e.g. from 46 to ~ 12 days). More frequent observations would facilitate detection of renewed activity, while weekly/daily measurements during volcanic crises would provide a better understanding of both the magmatic processes involved and the potential hazard.

Chapter 3

Evolution of Santorini volcano dominated by episodic and rapid fluxes of melt from depth

A version of this chapter has been published as: Parks et al., 2012. Evolution of Santorini Volcano dominated by episodic rapid flux of melt from depth. *Nature Geoscience*, 5, 749–754 (doi:10.1038/ngeo1562).[4]

http://www.nature.com/ngeo/journal/v5/n10/full/ngeo1562.html

3.1 Introduction

The Kameni Islands (Figure 3.1) are the surface expression of a dacitic volcanic dome complex that has grown during the past 3,600 yr in the caldera of the Minoan eruption (Fouqué, 1879; Barton & Huijsmans, 1986; Druitt et al., 1999) of about 1600 BC (Friedrich et al., 2006). Mineral thermobarometry and experimental petrological studies show that the lavas of the Kameni dome completed their pre-eruptive storage in a shallow reservoir at pressures of about 100 MPa (3–4 km in depth) (Barton & Huijsmans, 1986; Nicholls, 1971a; Martin et al., 2006). The lavas from each eruption

---

[4] Co-author contributions: The source modelling was undertaken by P. England, J. Biggs and I. The re-occupation of old triangulation sites was carried out by D. Paradissis, C. Raptakis, V. Zacharis, P. England, P. Nomikou and I. Processing and interpretation of Greek triangulation network data were undertaken by D. Paradissis, C. Raptakis, X. Papanikolaou and P. England. The GPS sites used in this

include a minor component of more mafic magma that forms enclaves that are significantly more crystalline and vesicular than the bulk lavas (Nicholls, 1971a). Disequilibrium chemical gradients within olivine crystals in dacites of the AD 1925 eruption suggest that these melts arrived within a pre-existing magma chamber a month or less before the eruption (Martin et al., 2008), and feldspar crystals from the host lavas contain diffusive compositional gradients consistent with residence for less than 100-500 years in a shallow reservoir (Zellmer et al., 1999). Textural observations of crystal-size distribution are also interpreted in terms of a persistent shallow reservoir topped up, in the decades before eruption, by magmas with varying phenocryst contents (Higgins, 1996). These observations have led to a model in which, during its dome-forming phase, Santorini is underlain at shallow depth (~ 4 km) by a persistent dacitic magma chamber, which is charged by frequent batches of mafic melt that are small compared with the volume of the chamber (Barton & Huijsmans 1986; Martin et al., 2006; Martin et al., 2008; Mann, 1983). The disequilibrium and vesicularity in the mafic enclaves are taken to suggest that the latest batch of melt triggered eruption by releasing volatiles that caused buoyant overturning of the magma chamber (Martin et al., 2006; Martin et al., 2008; Sparks & Sigurdsson, 1977).

This model has recently been challenged in Druitt et al., (2012), in which it is argued that, in the preparation phase for the Minoan eruption, the shallow magma chamber was charged by an event that contributed at least 15% of the erupted volume, in a time (about 100 years) that was very short in comparison with the interval since the previous major explosive eruption (18,000 years; Druitt et al., 1999). Here we present evidence that, during its present dome-forming phase, the volcano is also charged by

---

study were installed by C. Raptakis, K. Palamartchouk and B. Parsons, and K. Palamartchouk assisted in processing their data.

short-lived events, each of which contributes a significant fraction of the eventual erupted volume.

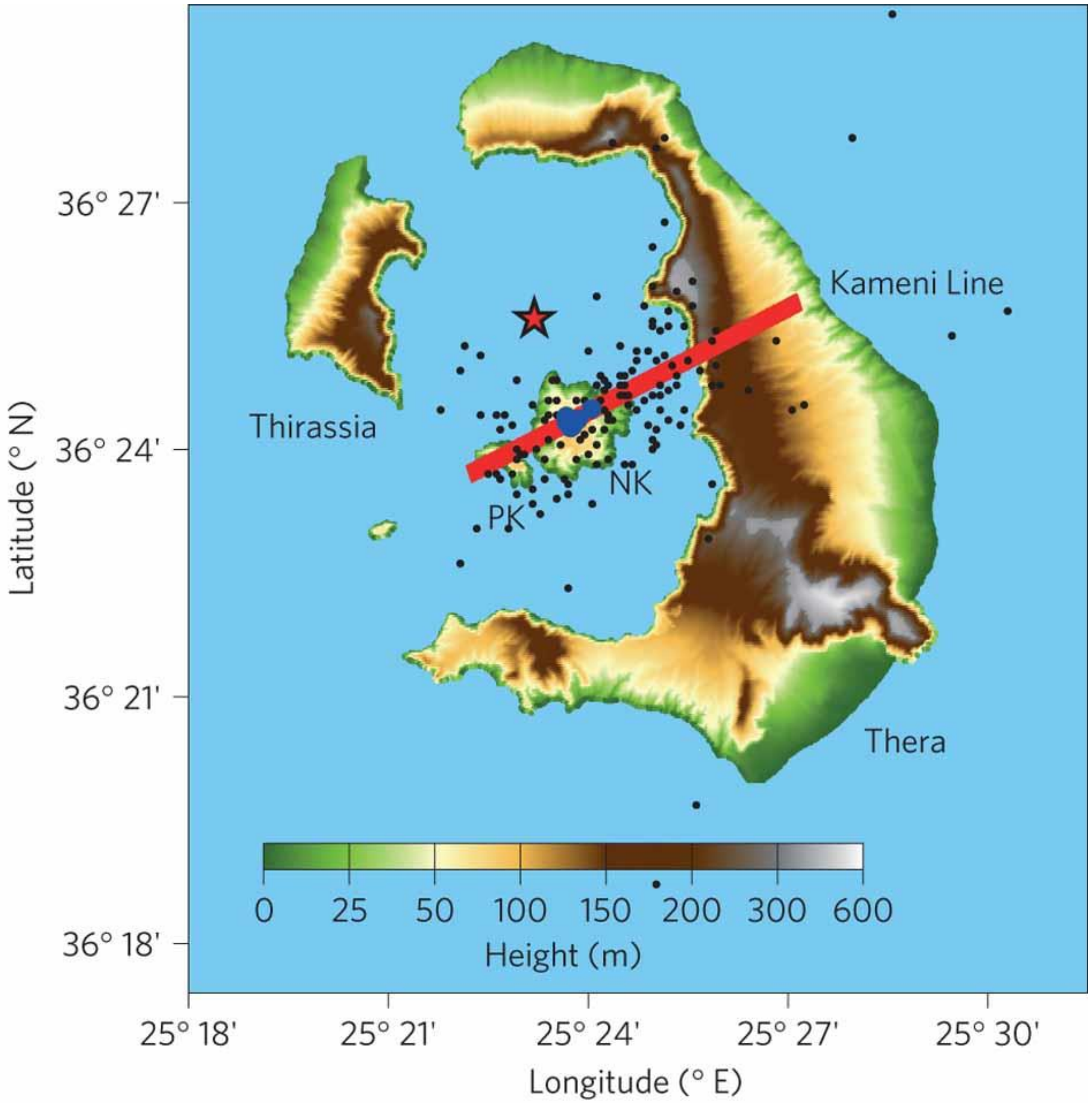

Figure 3.1: *The islands of the Santorini volcanic centre, and the location of the centre of recent volcanic and seismic activity. PK and NK denote the islands of Palaea and Nea Kameni, respectively; the Kameni Line (Druitt et al., 1999), shown in red, passes through the locations of the vents of all the post-1570 eruptions (blue dots), and is probably an active normal fault that dips north-northwest. The red star shows the location of the centre of inflation deduced from the InSAR data reported here (Figure 3.2). The black dots show epicentres of earthquakes of magnitude greater than two located by the Aristotle University of Thessaloniki (http://geophysics.geo.auth.gr/) between January 2011 and April 2012. The present episode of volcanic unrest seems to have begun with three earthquakes of magnitude 1 on the 9 January 2011.*

3.2 Historical eruptions and inflation of Santorini since 2011

Most of the post-Minoan edifice in the caldera of Santorini is submarine, but since AD 1570 five subaerial eruptions have formed the island of Nea Kameni (Table 3.1). The volumes of those eruptions (each a few times 10^7 to 10^8 m^3) are proportional to the repose period between them, as are the durations (1–4 years) of the eruptions themselves (Pyle & Elliott, 2006). Both the volume of the dome built since the Minoan eruption (about 2.5 km^3 in 3,600 years) and the volume erupted since AD 1570 ($1.5–4 \times 10^8$ m^3) are equivalent to a time-averaged flux of between 0.5 and 1×10^6 m^3 yr^{-1} (Druitt et al., 1999; Martin et al., 2006; Druitt et al., 2012; Pyle & Elliott 2006). The most recent sizeable eruption on Santorini took place in 1939–1941 (Table 3.1); multiplication of the time interval since 1941 by the average magma flux yields an expected volume for the next eruption, if it were to occur in the next few years, of between 3 and 7×10^7 m^3. Our measurements indicate that a volume of magma towards the lower end of that range has arrived beneath the caldera of Santorini since a period of volcanic unrest began in January 2011.

Table 3.1: *Timing and volumes of dome-forming eruptions on Nea Kameni since 1570, modified from Pyle & Elliott (2006).*[5]

Eruption start date	**Duration**	**Minimum volume (m^3)**	**GVP volume (m^3)**
1570 or 1573	?	2.9×10^6	1.2×10^6
1707	$4\frac{1}{3}$ yr	1.1×10^7	8.1×10^7
1866	$4\frac{3}{4}$ yr	6.7×10^7	1.4×10^8
1925	9 months	2.5×10^7	10^8
1939	2 yr	4.3×10^7	6×10^7
(1950	23 d	6×10^5	7×10^4)
Total		1.5×10^8	3.8×10^8

The onset of the unrest was marked by an increase in the rate of micro-seismic activity beginning in January 2011; at the same time, the coordinates of continuous GPS stations operating on Santorini began to deviate from their longer-term average velocities (Newman et al., 2012). We have used interferometric synthetic-aperture radar (InSAR) to measure ground deformation since March 2011 (Figure 3.2 and section 3.5). We convert this signal into sub-surface volume increase by treating the displacements as arising from a pressure increase at a point within an elastic crust. Although the surface deformations at volcanoes may well result from complex distributions of sources at depth, such complexity is masked by the elasticity of the crust, which smooths disturbances over a horizontal scale comparable with their depth.

---

[5] Minimum volumes are estimated from the subaerial volumes of the flows, measured from a high resolution digital elevation model (Pyle & Elliott, 2006). GVP volumes are those quoted by the Global Volcanism Program of the Smithsonian Institution (Siebert & Simkin, 2002). The eruption of 1950 is regarded as an appendix to the 1939-1941 eruption (Pyle & Elliott, 2006).

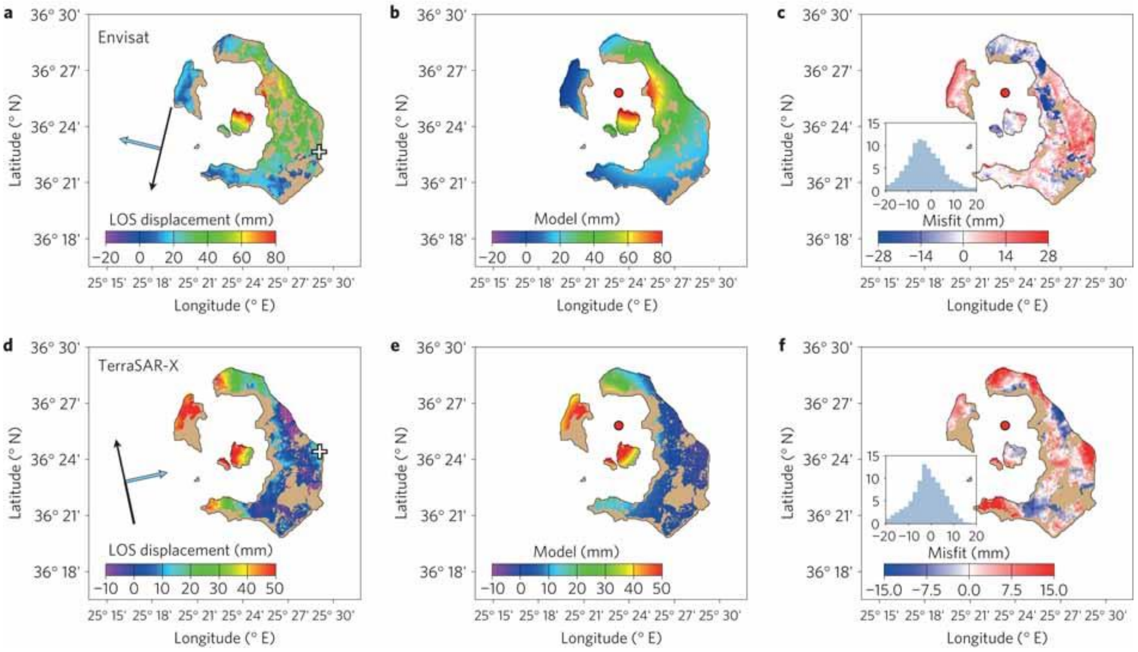

Figure 3.2: *InSAR measurements, and fits to them of the best-fitting spherical inflationary source, whose parameters are given in Table 3.2.* ***(a)*** *Chain-stacked Envisat interferogram from 3 March to 28 December 2011; brown shading shows areas of land that were de-correlated. Thin arrow indicates orientation of satellite orbit, and thick arrow indicates the look direction of the satellite. Colours show ground displacement in the direction from the ground to the satellite.* ***(b)*** *Calculated line-of-sight displacements for best-fitting spherical point source (Mogi, 1958), which is at a depth of 4.4 km below the red dot (see Table 3.2).* ***(c)*** *Misfits between best-fitting model (b) and the Envisat interferogram (a); inset histograms shows the distribution of misfits.* ***d,e,f,*** *As a,b,c, for chain-stacked TerraSAR-X interferograms from 25 July 2011 to 14 April 2012.*

The simplest model, often referred to as a Mogi source, represents the magma chamber as a sphere whose radius is small compared with its depth (Mogi 1958; McTigue 1987). We also investigated other simple sources: an ellipsoidal source (Davis, 1986; Yang et al., 1988; Newman et al., 2006) and a horizontal penny-shaped crack, representing a sill (Sun, 1969). The ellipsoidal model produced fits that were indistinguishable from the spherical source. We found, as was found previously (Newman et al., 2012) for GPS data, that sill-shaped sources produce significantly poorer fits, and that it was not possible to resolve any finite-sized source. The quantity of importance to our argument is the volume of intruded magma, and the dominant uncertainties in that quantity are associated with compressibility of the magma, and the depth of the source, not with its shape. We therefore restrict discussion to the spherical source.

The best-fitting spherical source has an effective volume in the range 1–2×10^7 m^3, and is centred slightly to the north of Nea Kameni at a depth of $4.4 \pm \frac{1.1}{1.0}$ km (Figure 3.2 and Table 3.2). These estimates are similar to those obtained from GPS data up to December 2011 (Newman et al., 2012) except that the geometry of the InSAR observations allows us to place a tighter upper bound on the effective volume of the source than can be obtained from the GPS data (Figure 3.3, Figure 3c of Newman et al., (2012)).

Table 3.2: *Best-fitting Mogi sources to interferogram stacks (Figure 3.2).*[6]

	TerraSAR-X	**Envisat**	**Estimate**	**Total**
Time interval	25 July 2011-14 April 2012	3 March 2011-28 December 2011	9 January 2011-3 March 2011	9 January 2011-14 April 2012
Heading/incidence	-12.2°/39.5°	-166.4°/39.2°		
Wavelength (mm)	31	56		
Volume ($\times 10^6$ m^3)	8.8	9.5	1.6	$14.9 \pm \frac{7}{3}$
Rate ($\times 10^3$ m^3 d^{-1})	33	32	(32)	32
r.m.s. misfit (mm)	7.3	6.2	–	6.8
	Location	25.389° E	36.430° N	Depth $4.4 \pm \frac{1.1}{1.0}$ (km)

---

[6] The bounds on depth and volume are derived from the trade-off between depth and volume of the source (Figure 3.3). The inflation between January and March 2011 is calculated from the daily rate given by the Envisat stack which is shown in parentheses.

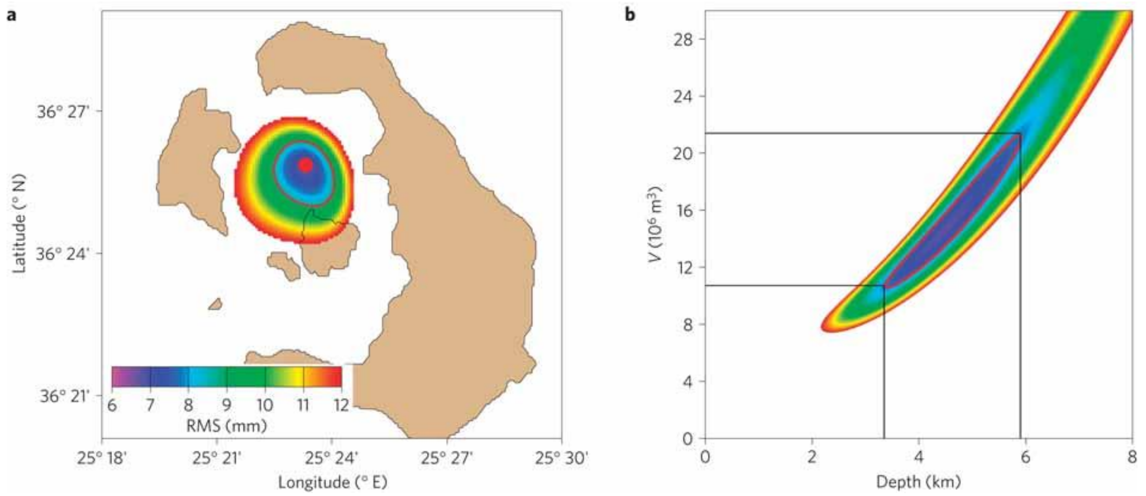

Figure 3.3: *Bounds on the location and volume of the magma body intruded beneath Santorini since January 2011.* ***(a)*** *The colours show the minimum r.m.s. misfit between modelled and observed interferograms for spherical sources (Mogi, 1958) beneath each location; where no colour is shown the r.m.s. misfit exceeds 12 mm.* ***(b)*** *Trade-off between the depth of the spherical source and its effective volume. The colours (same scale as in a) show the r.m.s. misfit between observed and modelled interferograms with the depth and effective volume fixed at their respective values. The black lines correspond to the limits on source depth and effective volume given in Table 3.2. Effective volumes are calculated as described in section 3.5; actual volumes could be considerably larger if the magma is entering an existing magma chamber (see text). Bounds on source location, depth and strength are shown by the red contours; solutions outside those contours show systematic misfits to the data.*

This effective volume represents a lower limit on the actual volume of magma intruded between January 2011 and April 2012. If the magma is entering an existing magma chamber then some of the intruded volume will be accommodated by compression of the surrounding magma, with a corresponding reduction in surface deformation (see Segall (2010), p. 210). Under those circumstances, the effective volume calculated from displacements of the land surface ought to be multiplied by a factor of at least two and, if the magma contains volatiles in the gas phase, the multiplicative factor could be 5 or greater (Segall 2010; Rivalta & Segall 2008; Martin et al., 2008) . Nevertheless, in the following discussion, we use a figure of 1–2 × 10^7 m^3 for the intruded volume of magma, which is the range shown in Figure 3.3; this would be an underestimate if the magma is entering a chamber that contains a significant volume of compressible magma.

3.3 Episodic rapid charging of the shallow magma chamber

We can place constraints on pre-2011 inflation of the volcano using earlier geodetic data. Electronic distance measurements taken between 1994 and 2000 suggest an inflationary episode of a few times 10^5 m^3 during that interval (Stiros et al., 2010; Saltogianni & Stiros 2012) which is negligible in comparison with the volume intruded in the present episode of inflation. A stronger constraint is provided by a triangulation survey of Santorini carried out in 1955. We re-occupied monuments of that survey in September 2011 using GPS. Displacements of the monuments between 1955 and September 2011 (Figure 3.4a) are consistent with the ground deformation measured between January and September 2011; residuals (Figure 3.4b) are a few centimetres in magnitude, consistent with uncertainties in the original triangulation, and show no systematic pattern. These observations imply either that there was no significant inflation of Santorini between 1955 and the beginning of 2011, or that any ground deformation that did take place was subsequently reversed to within a window of a couple of centimetres.

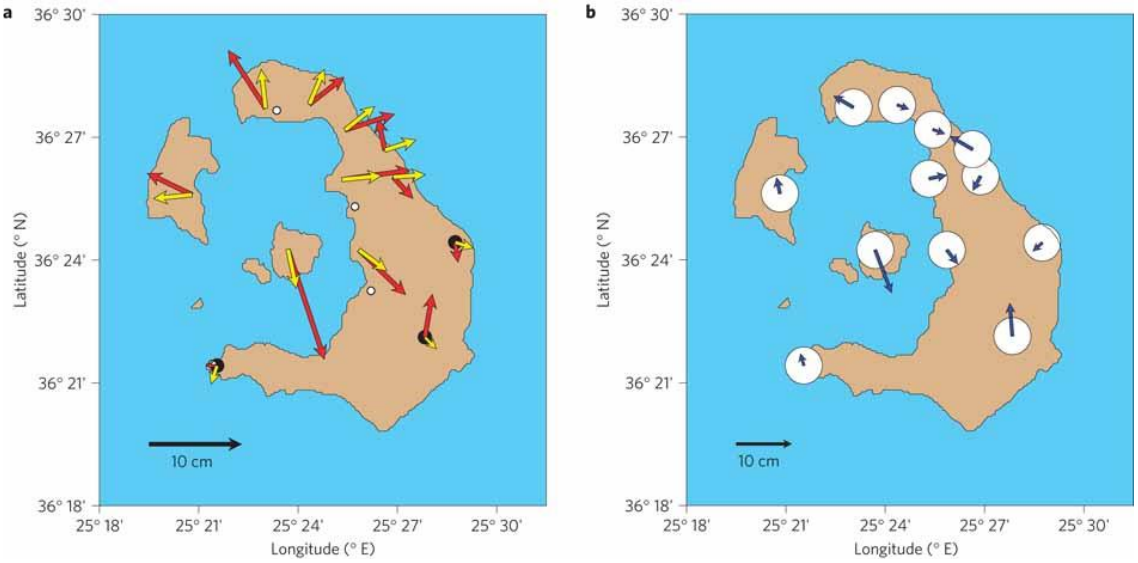

Figure 3.4: *Horizontal surface displacements of Santorini between 1955 and 2011 from triangulation and GPS data.* ***(a)*** *The yellow vectors show the expected displacements if the only deformation in that time interval is that due to the inflation detected since the beginning of 2011 (Table 3.2). The red vectors show displacements of monuments between 1955 and 2011, calculated from measurements of angle made in 1955 and coordinates determined in 2011 using GPS. The white circles show the locations of continuous GPS sites used in GPS processing. The scale of the network in 1955 is determined using the points indicated by black circles (section 3.5).* ***(b)*** *The blue vectors show the differences between the model (yellow in a) and observed (red) displacements; these represent displacements of the monuments between 1955 and the beginning of the volcanic unrest in January 2011. Uncertainties in triangulation measurements are discussed in the section 3.5, and are equivalent to 20 mm in each horizontal coordinate, as shown by the white circles.*

Since 1570, the interval between significant eruptions of Santorini has ranged from 14 to 160 years. It has been 70 years since the last significant eruption, and it is therefore prudent to consider whether the present unrest might presage the next eruption. The history of the volcano suggests that, if the present rate of inflation were to continue for a small number of years, the intruded volume would be equivalent to the volumes of previous eruptions (Table 3.1). The significant eruptions of last century had volumes of $4–6 \times 10^7$ m^3 (1939-1941) and $2.5–10 \times 10^7$ m^3 (1925-1926); if an eruption were to occur in the next few years, its expected volume, on the basis of long-term rates of eruption (Pyle & Elliott, 2006), would be between 3 and 7 × 10^7 m^3.[7] Our range of estimates of the volume intruded since the beginning of 2011 is equivalent to 15–60% of that volume. It is known that many episodes of inflation at caldera-forming volcanoes do not end in eruption (for example, Chang et al., 2010; Fournier et al., 2010; Liu et al., 2011); on the other hand, dome-forming eruptions at Montserrat are preceded by 10–20 cm of uplift (Mattioli et al., 2010) similar to the uplift on Santorini since January 2011. We therefore consider that it would be unwise to assume that the present state of unrest will not end in an eruption, although, at the time of writing, there is no indication that an eruption is imminent.

Our geodetic observations, which span 56 of the 70 years since the last sizeable eruption of Santorini, provide an unusual and perhaps unique example of long-term measurement of the surface deformation of a large silicic caldera that also has a centuries-long historical record of eruption. They strongly suggest that the present episode of volcanic inflation is the only significant one since the eruption of 1939-1941, or shortly thereafter. The volume intruded since the beginning of 2011 is of the same order of magnitude as the volumes of historical dome-forming eruptions. We therefore suggest that, during the dome-forming phase of its evolution, the shallow magma chamber beneath Santorini is charged by infrequent short-lived intrusive events, each of which delivers a significant fraction of the eventual erupted volume.

---

[7] This value is slightly modified in Chapter 5, following revised volumetric estimtaes for each of the historic lava flows (cf. section 5.3.3).

3.4 Magmatic evolution controlled by deeper reservoirs

Existing models envisage that the shallow magma chamber beneath Santorini is recharged by many small batches of andesitic melt, which fractionate within this reservoir to yield the more silicic magmas that finally erupt (for example, Barton & Huijsmans, 1986; Martin et al., 2008). Recently, it was argued (Druitt et al., 2012) that the magma charging the shallow reservoir immediately before the Minoan eruption was predominantly silicic: a dacite-to-rhyolite magma formed by fractional crystallization at greater depths. We suggest that this also holds true for the present magmatic system. The erupted products of the Kameni domes consist almost entirely of homogeneous dacites (Barton & Huijsmans, 1986; Nicholls 1971a); the mafic (basaltic-andesitic) enclaves form less than 1% of the volume (Martin et al., 2006). Although the model of a persistent shallow magma chamber recharged by many small batches of mafic melt is consistent with these observations, it is not demanded by them. Our data contradict the temporal aspect of that model, by showing that the shallow chamber is charged by infrequent large batches of magma; indeed, it is possible that the shallow magma chamber exists only in the relatively short interval (a year to a few years) immediately before dome-forming eruptions occur. The episodic nature of the recharging also casts doubt on the compositional aspect of the present model, because it is difficult to explain the observed petrological relationships if these infrequent charges of melt are mafic. If that were the case, the composition of the magma chamber would evolve episodically, as each large batch of melt arrived and fractionated, with the last batch needing to fractionate almost completely (leaving a very small fraction of mafic enclaves) in the short time before eruption (Martin et al., 2008). A simpler alternative is that the batches of melt reaching the shallow magma chamber are already dacitic in composition.

The major explosive eruptions of Santorini produce volumes of ejecta that range from ~10^9 to ~5×10^{10} m^3 (Druitt et al., 1999), whereas the dome-forming eruptions are in the range 10^7 to 10^8 m^3. Despite the great disparity between these scales, there are fundamental similarities in the behaviour of the volcanic system in these two phases of eruptive activity. In each case, the high-flux events charging the shallow magma chamber are dacitic in composition, they contribute a significant fraction (some tens of per cent) of the final erupted volume, and the durations of those events are short in comparison with the intervals of repose that separate them. Our observations, combined with those of Druitt et al., (2012), strongly suggest that these similarities arise because, during either phase of its eruptive activity, the evolution of the shallow magma chamber beneath Santorini is regulated by the release of magma from a deeper reservoir, or reservoirs. Petrological evidence from the products of a number of eruptions on Santorini shows that such a reservoir exists at a depth of 10-14 km (Cottrell et al., 1999; Gertisser et al., 2009; Andújar et al., 2010).

These observations also suggest that the dynamics of the deep reservoirs are more intimately linked to eruption processes than has hitherto been recognized. The relations between the mafic enclaves and the host dacite have been taken to imply that small volumes of gas-rich mafic melt can trigger eruption from a shallow magma chamber (Martin et al., 2006; Martin et al., 2008; Sparks & Sigurdsson, 1977); this argument is still feasible, but it may apply to a deeper reservoir, rather than to the shallow chamber. Furthermore, the short timescales recorded by the disequilibrium chemical gradients in the lavas, previously thought to represent residence in the shallow magma chamber (Martin et al., 2008; Zellmer et al., 1999; Higgins, 1996), probably represent the time taken for the large batches of dacitic magma to travel from a deep reservoir to the surface, including storage in the shallow chamber before eruption.

Although the historical record suggests that dome-forming eruptions last for only a few years (Table 3.1), the deep magmatic system is capable of delivering pulses that can last for the order of a century (Druitt et al., 2012). We are not aware of a mechanism that would restrict the deeper chamber to delivering a bimodal distribution of pulse durations (years or centuries); pulses of decadal duration may therefore also be expected, so future eruptions of Santorini will not necessarily be restricted to the range seen in the 500–year historical record. The need to acquire a better understanding of these processes is reinforced by the fact that the present episode of magma supply to the shallow chamber has a duration comparable to that of historical eruptions.

3.5 Methods

3.5.1 InSAR measurements

We measured the surface deformation on Santorini using InSAR analysis on data from the Envisat and TerraSAR-X satellites (Table 3.2), and a 15-m digital elevation model provided by P. Moore of IntegralGIS. We chain-stacked (Biggs et al., 2007) the interferograms so that atmospheric noise on individual dates cancels out. Having obtained an approximate location for the source, we reduced the number of observations by forming averages that were equally spaced in distance (100 m) and azimuth ($\pi/50$ rad) from the source location. Rectangular grids with spacing between 200 and 500 m yielded results indistinguishable from those shown in Figure 3.2.

As the area of interest consists of four islands, there is a potential ambiguity of an integer number of half-wavelengths in the displacements of the three smaller islands relative to Thera. However, the ground displacements between successive interferograms were small compared with half a wavelength, and the GPS data show no abrupt changes in deformation (Newman et al., 2012) so we were able to resolve the ambiguities by assuming monotonic, minimal, displacement of each island. This assumption was checked *a posteriori* by inspecting the residuals of each island to the best-fitting models; no island in either interferogram exhibited a misfit compatible with even a single half-wavelength offset (28 mm for Envisat or 16 mm for TerraSAR-X: each large in comparison with the root mean squared (r.m.s.) misfit of about 7 mm).

We calculated the location and volume of the intrusion from the interferograms using a spherical source (Mogi, 1958; McTigue, 1987). We searched a rectangular mesh of spacing 100 m in all three dimensions, covering the plausible range of source locations. At each point, we solved for the best-fitting source strengths for the 300-day Envisat stack and for the 264-day TerraSAR-X stack, and for the offset of the reference points on Thera (Figure 3.2). This procedure yielded an estimate for the volumes intruded during the (overlapping) time intervals covered by each interferogram stack; the rates of volume increase agreed between the two time intervals to within a few per cent (Table 3.2). We estimated the inflation between 25 July 2011 and 28 December 2011 (the period of overlap of the two interferogram stacks) by using the average of the rates of volume increase; outside that interval, we used the individual rates. We estimated the volume increase between the beginning of January 2011 and the first radar image on 03 March 2011 using the rate obtained for the Envisat stack. The results of this analysis are shown in Table 3.2.

3.5.2 Triangulation and GPS measurements

Triangulation observations were carried out on Santorini by the Hellenic Military Geographic Service in 1955. Each angle was the subject of a minimum of 12 independent measurements. In 1955 these observations were combined with assumptions of scale and orientation, by standard methods that have not changed (Bomford, 1980), to yield a solution for coordinates (latitude, longitude and orthometric height); for comparison with GPS data, we subtracted the geoidal height (Pavlis et al., 2008) from the orthometric height.

Twelve of the original monuments on Santorini survive in usable condition, and we occupied these with GPS between 23 and 26 September 2011 (Figure 3.4). The data from these sites, and from four continuous GPS sites on Santorini (whose locations are shown on Figure 3.4), were analysed using Bernese v5.0 GPS software (Dach et al., 2007). Coordinates were estimated in an ambiguity-fixed solution, using absolute antenna calibration corrections and International GNSS Service (IGS) final products (Dow et al., 2009). The datum was realized by means of minimum constraints, imposed on IGS stations BOR1, BUCU, GLSV, ISTA, MATE, NICO, NOT1, PENC and WTZR. The processing was compliant with present Center for Orbit Determination in Europe (CODE) standards (http://igscb.jpl.nasa.gov/igscb/center/analysis/code.acn).

Owing to the imprecision of distance measurements of the time, the 1955 network contains an undetermined scale error, which we solved for as follows. We took the three points most distant from the centre of inflation (identified on Figure 3.4) and subtracted from their 2011 coordinates the displacements calculated from our model for the inflation (spherical solution, Table 3.2, scaled for January-September, 2011). This adjustment is small in comparison with the motions of points nearer the source, because displacements decay as the square of distance from the source. We then found the isotropic horizontal dilatation to the 1955 coordinates that provided the best fit, in the least-squares sense, to the lengths of the baselines between these points in the adjusted

2011 coordinates. Finally, we oriented the 1955 network by finding the rigid-body rotation that produced the best fit to the calculated displacement vectors.

Although the original angular measurements were made using Wild T2 theodolites, which can measure to half a second of arc, which is equivalent to 10 mm over a typical side length of 5 km in the triangulation, we adopt a conservative estimate of 20 mm for the uncertainty in positions of the original coordinates. My Greek collegues (D. Paradissis, C. Raptakis and X. Papinakolaou) have compared many triangulation surveys with GPS observations in the past 15 years, and have found that relative coordinates based on terrestrial measurements are generally accurate to the order of 10–20 mm.

Chapter 4

From quiescence to unrest – 20 years of geodetic measurements at Santorini volcano, Greece

This chapter represents a version of an article (Parks et al., in prep.) that is in preparation for submission to a journal.[8]

4.1 Introduction

Santorini archipelago, situated in the south Aegean, consists of five islands, which together comprise a volcanic caldera (Figure 4.1). For the past 360,000 years, the volcano has experienced major explosive eruptions every 10,000 to 30,000 years. These major eruptions are separated by periods during which andesite shields and dacite lava domes are built by multiple smaller effusive eruptions (Druitt et al., 1989, 1999). The present day outer islands - Thera, Therassia and Aspronisi - are the remnants of the explosive caldera-forming events, the last of which occurred in approximately 1620 BC (the Minoan eruption). Since this time Santorini has been in a dome-forming phase, responsible for the growth of the two intra-caldera islands (Nea Kameni and Palea

---

[8] I undertook the InSAR processing and analysis under the supervision of J. Biggs. GPS processing was undertaken by X. Papanikolaou. J. Moore and I produced the lava contraction model presented in section 4.5.1.2. J. Moore derived the visco-elastic solutions for the models presented in sections 4.5.1.2 and 4.6.2.

Kameni). The last eruptions on the Kameni islands took place from 1939-1941, with a minor phase of extrusion in 1950.

Between 1950 and 2010 the volcano remained quiet, with no documented reports of seismic activity, and inconclusive reports of minor inflation (Stiros et al., 2010; Saltogianni and Stiros, 2012). However, multiple measurements of surface deformation between 1992 and 2010 have confirmed a slow subsidence signal in the southwest region of Nea Kameni. The location and velocity of this signal remained relatively stable throughout this period, with an observed subsidence rate in the order of 5 to 6 mm/yr (Lagios et al., 2005; Papageorgiou et al., 2010; Papageorgiou et al., 2012; Foumelis et al., 2013 and Lagios et al., 2013).

In January 2011, the volcano entered a period of unrest. This was characterised by the onset of detectable seismicity and caldera-wide uplift (Newman et al., 2012; Parks et al., 2012; Chapter 3). Figure 4.1 shows the location of volcano-tectonic (VT) earthquakes > local magnitude (ML) 2.0, which have occurred within the caldera between October 2010 and September 2012. The earthquakes are clustered close to the Kameni line – a NE-SW trending normal fault/fracture zone, which is believed to control vent locations for historic dome-forming eruptions on Nea Kameni (Pyle & Elliott, 2006).

In this study we analyse deformation measurements derived from C-band (5.65 cm wavelength) and X-Band (3.11 cm wavelength) satellite SAR data acquired between 1993 and 2012 and continuous GPS (cGPS) data from 2010 to 2012, collected from a network of receivers installed on the caldera complex. We employ a joint inversion technique to interpret both Interferometric Synthetic Aperture Radar (InSAR) and GPS measurements as a time series of sub-surface volume change, which we use to infer the evolution of various volcanic processes occurring at Santorini over this extended period.

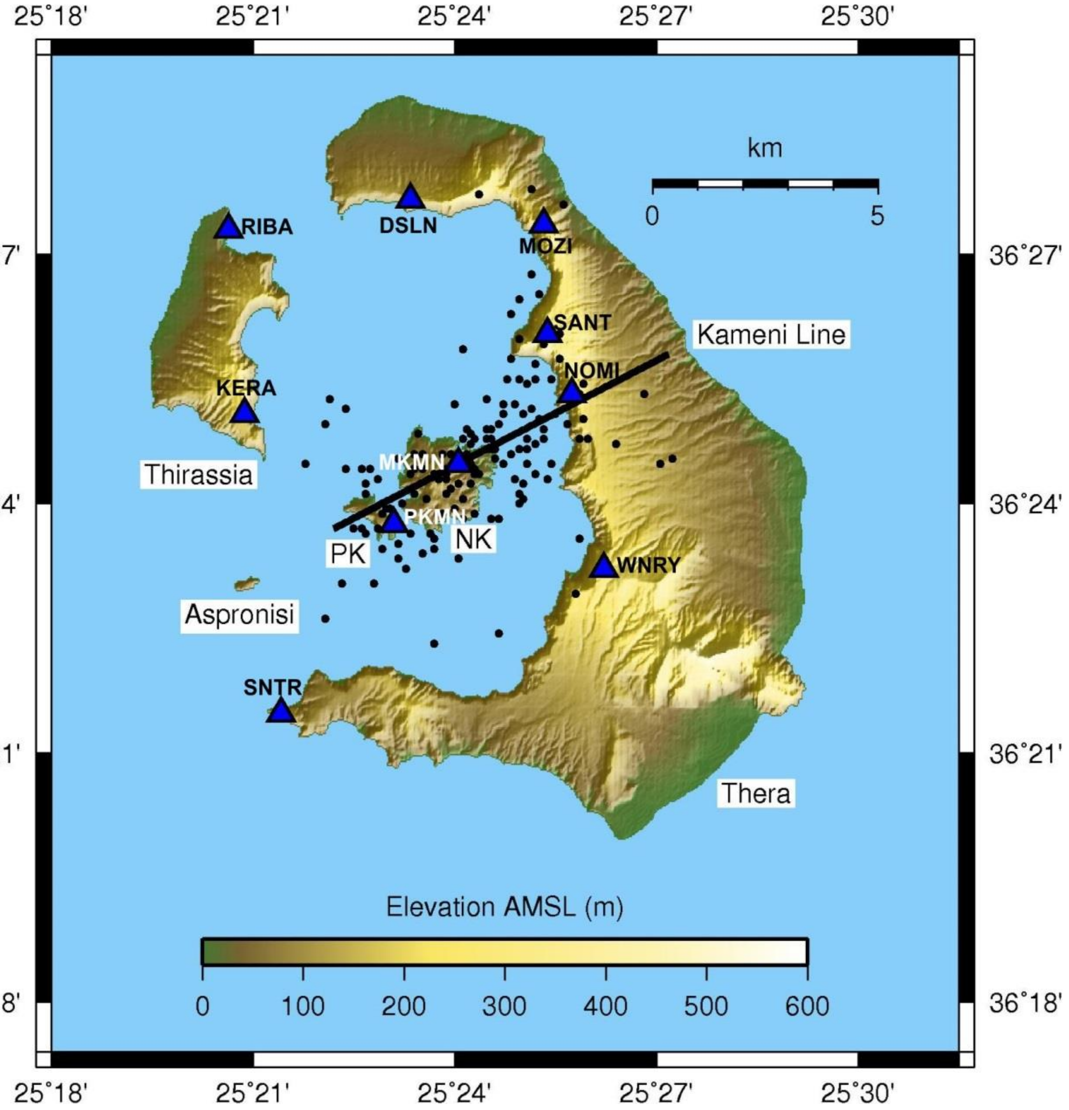

Figure 4.1. *Map of Santorini, showing the location of recent seismic activity and continuous GPS sites. The black dots show epicentres of earthquakes greater than ML 2.0 occurring from October 2010 to September 2012. Earthquakes were located by the Aristotle University of Thessaloniki (Aristotle University of Thessaloniki, 2005-). NK and PK label Nea Kameni and Palea Kameni respectively. cGPS sites are presented by the blue triangles. SNTR, WNRY, MKMN and DSLN were established and are operated by the University of Oxford and National Technical University of Athens. Sites KERA, RIBA, NOMI, PKMN and MOZI were established and are maintained by the Georgia Institute of Technology. SANT is operated by the National and Kapodistrian University of Athens.*

4.2 Geodetic Methods

4.2.1 Interferometric Synthetic Aperture Radar (InSAR) Processing

Synthetic aperture radar interferometry (InSAR) is an established technique, routinely employed to measure centimetre-scale ground movements at volcanoes between repeat passes of a satellite (e.g. Massonnet and Sigmundsson, 2000; Pritchard and Simons, 2004; Hooper et al., 2012).

Throughout this study, we utilised SAR data from ERS, ENVISAT and Terra-SAR-X satellites acquired between 1993 and 2012. Interferogram processing was undertaken using the Stanford Method for Persistent Scatterers software (StaMPS) (Hooper et al., 2007; Hooper, 2008). This method was chosen to provide improved coherence on the island of Thera and minimise small unwrapping errors observed in the previous two-pass processing (see Figure 3.2 in Chapter 3). The initial InSAR processing comprises a series of steps including SLC generation, orbit extraction, coregistration of the various images, the generation of simulated DEM interferograms, SLC resampling (so that the slave images cover the same area as the master) followed by the formation of the master-slave interferograms. ROI_PAC software (ROI_PAC, 2013) was used to focus the raw ERS and ENVISAT data, with interferogram formation undertaken using DORIS software (TUDelft, 2013). We used a 15 m digital elevation model (DEM) (Figure 4.1), provided by P. Moore of IntegralGIS, to remove topographic fringes and precise orbits to correct for orbital effects. The phase component of an interferogram is not a continuous signal, being modulo 2π - thus interferograms must be “unwrapped” before observations may be converted into line-of-sight (LOS) displacements. The StaMPS software incorporates a 3D statistical cost flow algorithm for unwrapping, which may be applied to either single or multiple master time series (e.g. both Persistent Scatterer (PS) and small baseline (SB) interferograms) (Hooper, 2010).

StaMPS incorporates both the PS and SB techniques to map the temporal evolution of deformation, whilst improving coherence and reducing residual orbital and DEM errors. We tested both the PS and SB techniques available in StaMPS, concluding that in general the SB interferograms exhibited a higher signal to noise ratio and an increased number of stable pixels. Consequently, for this particular study, we have used only SB interferograms in our analysis (Appendix C and Table 4.1). An overview of both the PS and SB processing workflows is presented in Appendix D.

Several of the interferograms were significantly affected by atmospheric delay on the eastern coast of Thera. To reduce this problem, we created plots of phase against elevation for consecutive interferograms, over a region deemed unlikely to be affected by volcanic deformation. This enabled us to identify individual scenes with topographically correlated phase (Appendix E), which were then excluded from the analysis.

Table 4.1: *Parameters for the satellite observations used in this study. A complete list of interferograms is provided in Appendix C.*

Satellite	**Wavelength (cm)**	**Track**	**Orbit**	**LOS Vector [East North Up]**			**Number of interferograms**	**Period of coverage**
TerraSAR-X	3.1	85	Ascending	[-0.6199	-0.1337	0.7732]	69	14-Jul-11 to 26-Sep-12
TerraSAR-X	3.1	138	Descending	[0.4632	-0.1001	0.8806]	72	07-Apr-12 to 19-Sep-12
ENVISAT	5.6	93	Descending	[0.6142	-0.1493	0.7749]	58	03-Mar-11 to 26-Feb-12
ENVISAT	5.6	329	Ascending	[-0.3692	-0.0872	0.9252]	15	14-Jul-04 to 23-Jun-10
ENVISAT	5.6	422	Descending	[0.3477	-0.0839	0.9339]	27	25-Aug-04 to 06-Jan-10
ERS 1&2	5.7	422	Descending	[0.3477	-0.0839	0.9339]	6	20-Jun-93 to 16-Aug-00

4.2.2 Continuous Global Positioning Satellite (cGPS) processing

Prior to the recent phase of unrest, four permanent continuous global positioning satellite (cGPS) stations were operating on Santorini (SNTR, NOMI, KERA and PKMN). Since July 2011, a further six cGPS sites have been installed across the Santorini archipelago (MOZI, SANT, MKMN, DSLN, WNRY and RIBA). Data from each of these ten cGPS sites were processed with Bernese GPS Software V5.0 (Dach et al., 2007), using the double differenced carrier-phase observables approach and final IGS products (Dow et al., 2009). We solved for daily site coordinates and hourly tropospheric parameters using Niell mapping functions (Niell, 1996), with the wet part of the tropospheric delay estimated as a piecewise linear function every two hours. Horizontal tropospheric gradient parameters were estimated for each station in 24 hour intervals, using the "tilting" model (Meindl et al., 2004).

We initially processed data from a larger network, covering all of Greece (~55 stations) and including the SNTR station situated on the south-west tip of Thera (Figure 4.1). This network is aligned to IGS08 reference frame via the minimum constraint method, using three no-net-translation conditions imposed on a set of fiducial sites, enforcing their barycentre after the solution to coincide with the one computed using the *a-priori* coordinate set. This is currently the recommended option for the realisation of a reference frame of this size (Dach et al., 2007). We then processed the Santorini network, including a series of neighbouring sites from the Greek network serving as "tie" stations. The datum in this case was realised with exactly the same method as before, but instead of the European fiducial stations, we used a set of neighbouring Greek sites. In this way, the Santorini coordinates were translated to the IGS08 reference frame. This two-tier approach was used to reduce the baseline length between local and reference sites, whilst minimising the spatial and geometric inhomogeneity associated with referencing the dense network at Santorini with a comparatively sparse network in Northern Greece. This approach also has the benefit of making the ambiguity resolution step more efficient.

The time series data for each of the cGPS sites were not detrended prior to incorporation into the volumetric inversion (sections 4.2.3 and 4.6.1). The majority of the sites were only operating since July 2011 (or later) and it is considered ambiguous to estimate annual and semi-annual signals over such short time periods. Instead, we accounted for these residual trends in the volumetric inversion by solving for several nuisance parameters, including a constant offset and velocity for the North, East and Up (NEU) components at each cGPS site.

4.2.3 Joint Inversion of Geodetic Observations (JIGO) for determining the temporal evolution of source parameters

We employed a joint inversion technique outlined by Biggs et al. (2010b) and adapted from Berardino et al. (2002), to convert cGPS and InSAR observations into sub-surface volume change, by treating the displacements as arising from a pressure variation at depth within an elastic crust. Unlike standard joint inversion techniques, this method provides a time series of the change in source volume through time, which is more useful for interpreting changes in the behaviour of a volcano over a selected time period. The joint inversion method used to determine the temporal variation in source parameters is bound by the same assumptions constraining the Mogi model (i.e., it assumes an elastic homogenous half-space).

We defined a series of linear equations in the form **Ax = b** where **A** is the temporal design matrix, **x** is the model vector for the incremental displacements, and **b** is a vector containing the measured displacements (Biggs et al., 2010b). For a series of satellite images acquired at different times (e.g. C, D, E and F) we solve for displacements in a series of small steps, whereby the matrix equation can be represented by:

$$\begin{pmatrix} 1 & 0 & 0 \\ 0 & 1 & 0 \\ 0 & 1 & 1 \\ 1 & 1 & 0 \end{pmatrix} \begin{pmatrix} \mathbf{x}_{CD} \\ \mathbf{x}_{DE} \\ \mathbf{x}_{EF} \end{pmatrix} = \begin{pmatrix} \mathbf{b}_{CD} \\ \mathbf{b}_{DE} \\ \mathbf{b}_{DF} \\ \mathbf{b}_{CE} \end{pmatrix} \tag{4.1}$$

For a series of cGPS displacements we solved for the vector of incremental displacements using the cumulative displacement since the first observation and a lower triangular matrix as the design matrix. The matrix equation can be represented by:

$$\begin{pmatrix} 1 & 0 & 0 \\ 1 & 1 & 0 \\ 1 & 1 & 1 \end{pmatrix} \begin{pmatrix} \mathbf{x}_{12} \\ \mathbf{x}_{23} \\ \mathbf{x}_{34} \end{pmatrix} = \begin{pmatrix} \mathbf{b}_2\text{-}\mathbf{b}_1 \\ \mathbf{b}_3\text{-}\mathbf{b}_1 \\ \mathbf{b}_4\text{-}\mathbf{b}_1 \end{pmatrix}$$

(4.2)

where displacements are measured in a series of time steps, t = 1, 2, 3, 4 … (Biggs et al., 2010b).

We employed a simple Mogi source (Mogi, 1958), to convert our displacement time series to volume change. We estimate the incremental volume change of the Mogi source V, using equations 4.3 & 4.4 (Biggs et al., 2010b). The primary strength of this method is that it enables us to jointly invert InSAR measurements from multiple tracks with different look angles and 3 component GPS measurements from multiple sites.

$$\begin{pmatrix} m_x \\ m_y \\ m_z \end{pmatrix} = (1 - \nu) \frac{\Delta V}{\pi} \begin{pmatrix} \frac{x}{R^3} \\ \frac{y}{R^3} \\ \frac{z}{R^3} \end{pmatrix}$$

(4.3)

$$\begin{matrix} (\mathbf{l}_\mathrm{n} . \mathbf{M}_\mathrm{n}) \mathbf{A}_\mathrm{n} \\ (\mathbf{l}_\mathrm{p} . \mathbf{M}_\mathrm{p}) \mathbf{A}_\mathrm{p} \\ \vdots \end{matrix} \begin{pmatrix} V_{12} \\ V_{23} \\ V_{34} \\ \vdots \end{pmatrix} = \begin{pmatrix} \mathbf{b}_\mathrm{n} \\ \mathbf{b}_\mathrm{p} \\ \vdots \end{pmatrix}$$

(4.4)

where ν is Poisson's ratio, R is the distance from the source to the observation, subscripts n, p … represent the observation group (e.g. $\mathbf{b}_\mathrm{n}$ may represent the measured LOS displacements from a series of interferograms from the same satellite track and $\mathbf{b}_\mathrm{p}$ all the observations for one component at a single GPS site), then $\mathbf{l}_\mathrm{n}$ is the LOS unit vector for the InSAR observations and $\mathbf{l}_\mathrm{p}$ is the 3 component unit direction vector for

GPS; $\mathbf{M_n}$ and $\mathbf{M_p}$ are the 3 component displacement vectors (m_x, m_y, m_z) predicted by the Mogi model and $\mathbf{A_n}$ and $\mathbf{A_p}$ are the temporal design matrices illustrated in equations 4.1 & 4.2 respectively. The incremental volumes are then integrated to provide a time series of volume change (Biggs et al., 2010b). We solved for several different sources of noise or nuisance parameters: those which were temporally and spatially correlated and those which were uncorrelated. The correlated nuisance parameters included a constant offset and velocity for the NEU components at each cGPS site and a constant phase shift in the interferograms. The random noise component was estimated using the relative errors on each observation and a diagonal variance-covariance matrix to weight the inversion (Menke, 1989; Sudhaus & Jónsson 2009). The cGPS uncertainties were estimated during the initial Bernese processing and the error on each interferogram was estimated by calculating the standard deviation beyond a radius of 4 km from the source location. More detailed information regarding both the inversion technique and error estimation may be found in Biggs et al. (2010b).

Prior to running the inversion, the SB interferograms were resampled to a grid with a spacing of 200 m up to an inner radius of 4 km from the source, followed by a coarser spacing of 400 m outside this area. This increased the number of sample points close to the source and reduced those more likely to be affected by atmospheric delay on the eastern edge of Thera. For each dataset we searched a three-dimensional grid of 200 m spacing in x,y,z to determine the optimal source location that minimised the misfit between the data and the model. For the InSAR-only inversions, the bounds on the geographic location of the source were computed using a cut-off contour equal to the average misfit between the interferograms and the model outside a radius of 4 km. For the GPS-only and joint inversion results, the cut-off contour was equal to the minimum root mean square (rms) error plus 10%. In each case, the error on the total volume estimate is the cumulative sum of the weighted root mean square (wrms) residual for individual observations (computed during the inversion). The optimum depth was located using the minimum wrms derived during the inversion. The bounds on the depth estimate were derived using the volume change error estimates and the trade-off plot between depth and volume.

4.3 Previous Studies

The period of slow subsidence occurring at Nea Kameni prior to 2011 was originally reported by Lagios et al. (2005) and Papageorgiou et al. (2007), although no detailed interpretation of the signal was provided by the authors at this time. The recent period of unrest (commencing in January 2011), marked the first significant activity detected at Santorini since the end of the last eruption in 1950. The results of several geodetic studies covering both periods have already been published (Tables 4.2 & 4.3). These studies have used both GPS and InSAR measurements to model the location for the source of the inflation observed at Santorini between January 2011 and April 2012, however only one of these studies (Foumelis et al., 2013) attempted to model the earlier subsidence signal observed at Nea Kameni, assuming a deflating spherical source. Although the authors do not cite the exact geographic location in the text, the inferred location of the deflating point pressure source (Mogi, 1958) is at a depth of 800 ± 200 m beneath the south-west corner of Nea Kameni. The average rate of deflation determined during this study was $(-14 \pm 3) \times 10^3$ m^3 yr^{-1} (Foumelis et al., 2013 and Table 4.2).

In general, the source locations derived from the studies covering the period of unrest are in good agreement. With the exception of Papoutsis et al. (2013), they typically agree within ~ 500 m (Table 4.3). The offset identified in the Papoutsis et al. (2013) InSAR source location is likely derived from the use of data from only one satellite track (descending ENVISAT track 93). The median longitude, latitude and depth to source calculated from these studies are 25.389° E, 36.426° N and 4.2 km respectively. The median rate of inflation during the unrest was 10.4×10^6 m^3 yr^{-1}. These studies have all attempted to determine the source location, total volume change and associated errors. However none of these prior studies has examined in any detail the evolution of either the position of the source or the volume change in the shallow chamber throughout the period of unrest.

Table 4.2: *Best-fitting spherical source parameters used to model ground displacements derived from InSAR measurements during the period of slow subsidence on Nea Kameni (1992-2010).*

Study	**Longitude °E**	**Latitude °N**	**Depth (km)**	**Average Rate of Volume Change ($\times 10^4$ m^3/yr)**	**Total Volume ($\times 10^6$ m^3) 18/06/93-12/08/09**
InSAR [Foumelis et al., 2013]	-	-	0.8 ± 0.2	-1.4 ± 0.3	-
InSAR [this study]	$25.392 \pm^{0.02}_{0.01}$	$36.401 \pm^{0.01}_{0.02}$	$1.6 \pm^{0.3}_{0.4}$	-7.31 ± 0.91	-1.19 ± 0.15

Table 4.3: *Best-fitting spherical source parameters used to model ground displacements derived from InSAR and GPS measurements during the period of unrest (2011-2012).*[9]

Study	**Longitude °E**	**Latitude °N**	**Depth (km)**	**Average Rate of Volume Change (× 10^6 m^3/yr)**
GPS [Newman et al., 2012]	25.389 - 25.390	36.423 - 36.430	3.9 - 4.0	9.5 - 17.4
InSAR [Parks et al., 2012]	25.389	36.430	4.4	11.8
GPS [Papoutsis et al., 2013]	25.384	36.429	3.5	12.4
InSAR [Papoutsis et al., 2013]	25.403	36.426	6.3	24.2
InSAR [Foumelis et al., 2013]	25.389	36.429	4.3	9.4
GPS [Foumelis et al., 2013]	25.389	36.424	4.0	10.3
Joint InSAR-GPS [Foumelis et al., 2013]	25.389	36.425	3.8	9.2
InSAR [Lagios et al., 2013]	25.395	36.426	4.5	9.2
GPS [Lagios et al., 2013]	25.389	36.426	4.9	~ 10.4
Median	**25.389**	**36.426**	**4.2**	**10.4**
Interquartile range	**0.001**	**0.004**	**0.6**	**2.8**
InSAR [this study]	$25.390 \pm^{0.01}_{0.01}$	$36.428 \pm^{0.01}_{0.01}$	$4.2 \pm^{1.3}_{1.4}$	[a](11.2 ± 0.6)
GPS [this study]	$25.388 \pm^{0.01}_{0.01}$	$36.428 \pm^{0.01}_{0.01}$	$4.4 \pm^{0.5}_{0.6}$	[a]15.3 ± 3.0
Joint InSAR-GPS [this study]	$25.388 \pm^{0.01}_{0.01}$	$36.428 \pm^{0.01}_{0.01}$	$4.4 \pm^{0.5}_{0.6}$	[a]15.3 ± 3.0

---

[9] [a]The average rate is computed using measurements up until 29 April 2012.

4.4 Geodetic Results

4.4.1 Period of subsidence (1993-2010)

Mean LOS velocity maps from 1993-2010 (generated using ERS and ENVISAT SB interferograms) display a slow subsidence signal on the central volcanic island of Nea Kameni (the blue colours on Nea Kameni in Figures 4.2a-c). The observed signal displays an average rate of approximately -6 mm/yr and extends across the entire southern half of the island. Comparison of the time series from the ERS and ENVISAT interferograms suggests that the rate of subsidence remained fairly constant between 1993 and 2010 (Figures 4.2d-f). This signal was identified in previous geodetic studies undertaken by Lagios et al., 2005; Papageorgiou et al., 2012; Foumelis et al., 2013 and Lagios et al., 2013. Foumelis et al. (2013) modelled the observed subsidence using a deflating Mogi source. However no detailed explanations for the source of deflation or alternate processes which may also be responsible for the observed subsidence were provided in any of these studies.

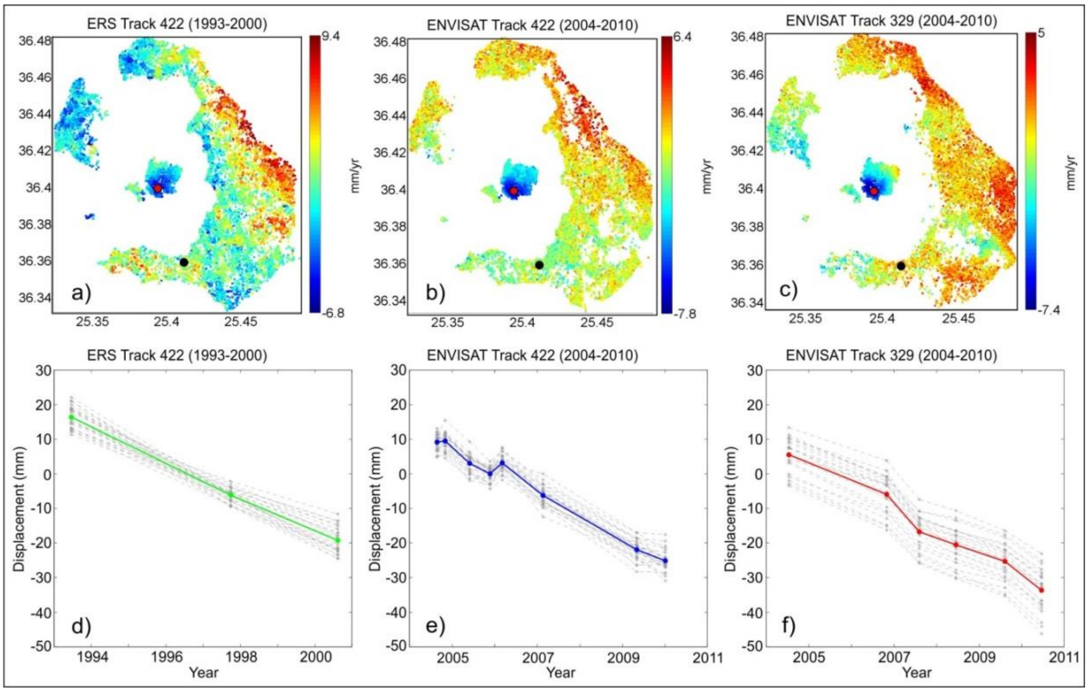

Figure 4.2. *Mean line-of-sight LOS velocities on Santorini from June 1993 to June 2010, derived using the StaMPS SB method.* ***(a)*** *Descending orbit data from ERS track 422 between June 1993 and August 2000.* ***(b)*** *Descending orbit data from ENVISAT track 422 between August 2004 and January 2010.* ***(c)*** *Ascending orbit data from ENVISAT track 329 between July 2004 and June 2010.* ***(d-f)*** *Time series of displacements generated using SB interferograms. The data point used to generate the time series is displayed as the red filled circle in figures (a-c). Displacements are displayed relative to the reference point (black filled circle) on Thera (see figures (a-c)). The solid coloured lines in figures (d-f) display the average displacements. The grey lines on the time series plots (d-f) represent the range of displacements within 100 m of the red filled circle. The ERS and Envisat data were processed at 4 looks and a 15 m DEM (resampled to 30 m) was used to remove topographic fringes.*

4.4.2 Period of uplift (2011-2012)

Mean LOS velocities derived from descending Envisat orbit data (track 93) throughout the period March 2011-February 2012 and from ascending TSX orbit data (track 85) from October 2011-August 2012 are displayed in Figures 4.3 & 4.4. The pattern of deformation is consistent with that reported in earlier interferometric studies at Santorini covering a similar time period (e.g. Parks et al. 2012; Foumelis et al., 2013 and Lagios et al., 2013; Papoutsis et al., 2013). Since displacements are measured in the satellite’s LOS, the difference in the apparent location of the uplift (red colours) between Figures 4.3 & 4.4 results primarily from differences in the satellite azimuths and incidence angles of the radar pulse. Both figures display a dominant uplift signal in the caldera from March 2011-February 2012 for the ENVISAT interferograms (Figure 4.3) and from October 2011-May 2012 for the TSX interferograms (Figure 4.4). However, the time series of LOS displacements for descending TSX track 138 (Figure 4.5), covering the period April 2012 to September 2012, shows a noticeable reduction in the rate of inflation after April 2012 (Figure 4.5b). The waning of this signal continues into September 2012 (Figures 4.5c-e).

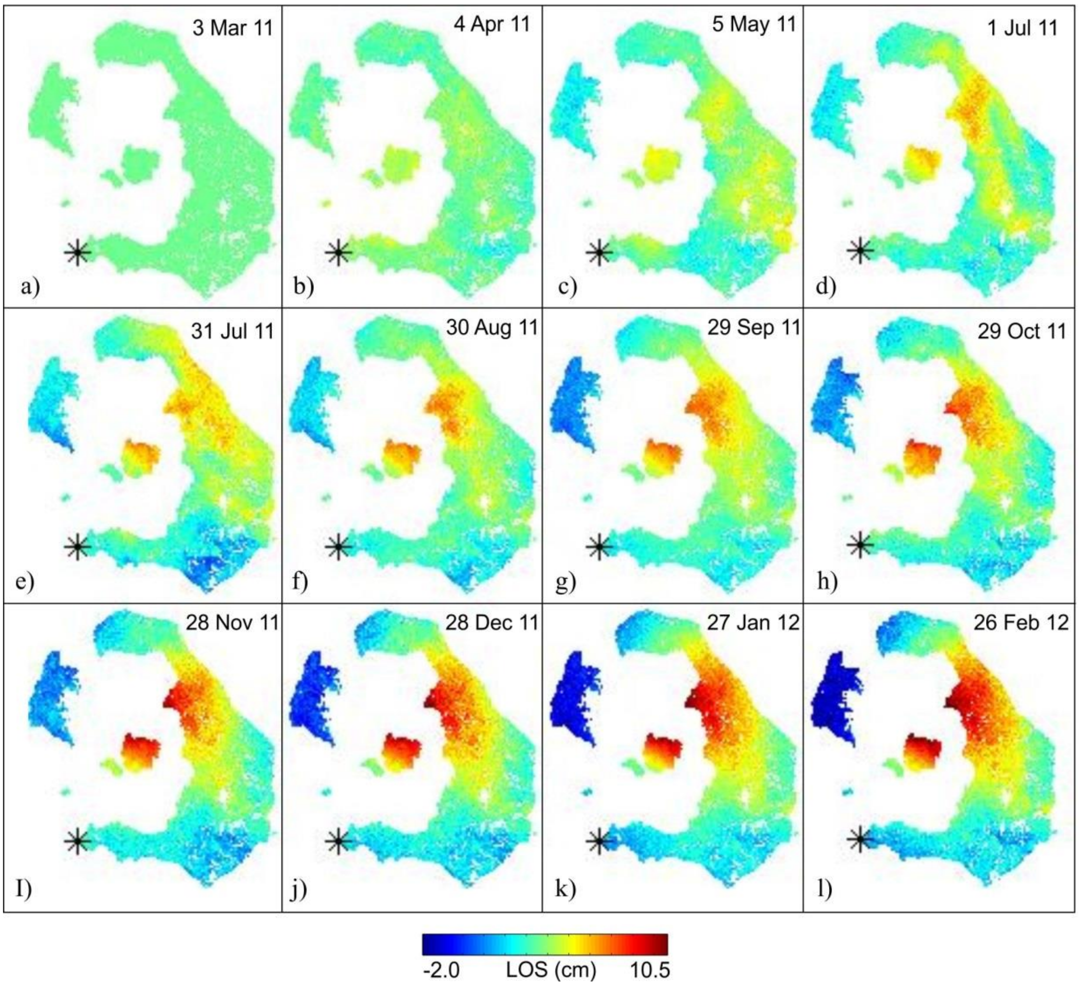

Figure 4.3. *Time series of line-of-sight (LOS) displacements for Santorini using StaMPS SB interferograms from descending ENVISAT track 93. Each image represents cumulative displacement since the first image in the time series (3 March 2011). LOS displacements are given relative to the estimated LOS displacements at cGPS station SNTR, marked by an asterisk. The Envisat data were processed at 1 look and we used a 15 m DEM (resampled to 30 m) to remove topographic fringes.*

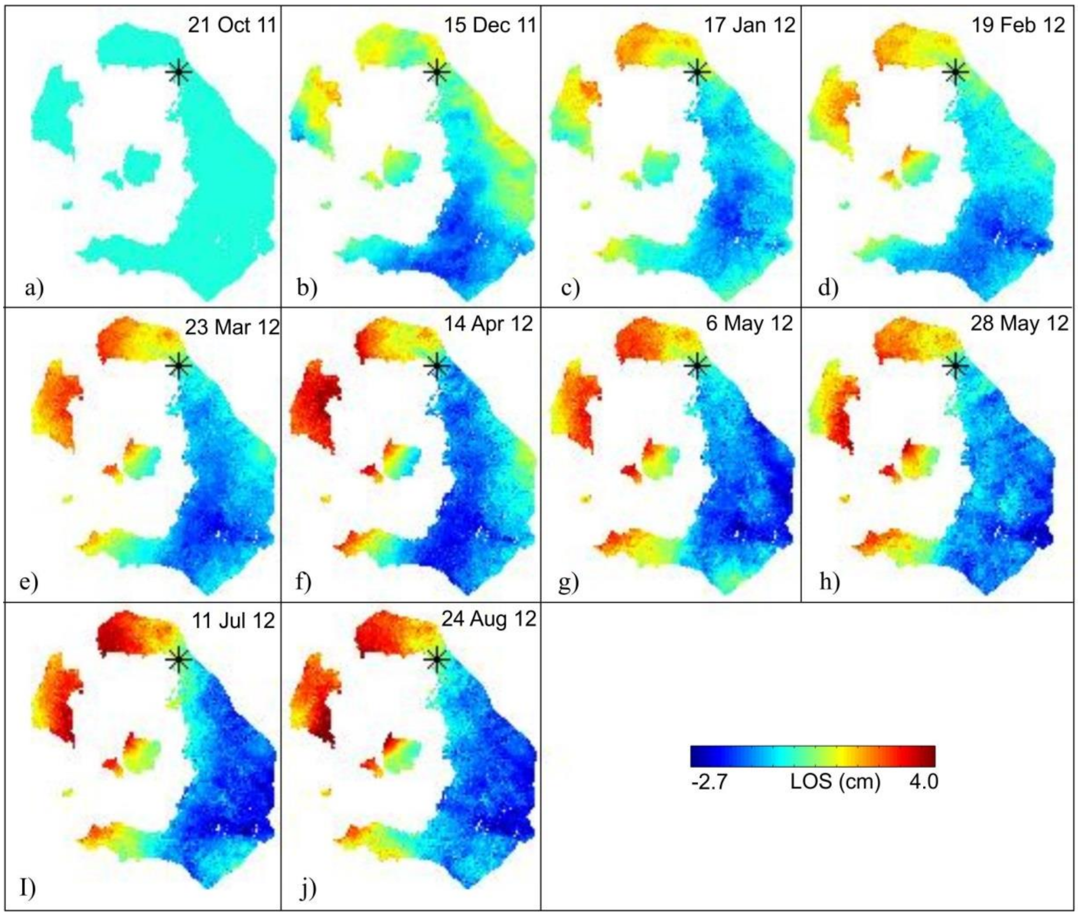

Figure 4.4. *Time series of line-of-sight (LOS) displacements for Santorini using StaMPS SB interferograms from ascending TerraSAR-X track 85. Each image represents cumulative displacement since the first image in the time series (21 October 2011). LOS displacements are given relative to the estimated LOS displacements at cGPS station MOZI, marked by an asterisk. The TSX data were processed at 10 looks and we used a 15 m DEM (resampled to 30 m) to remove topographic fringes.*

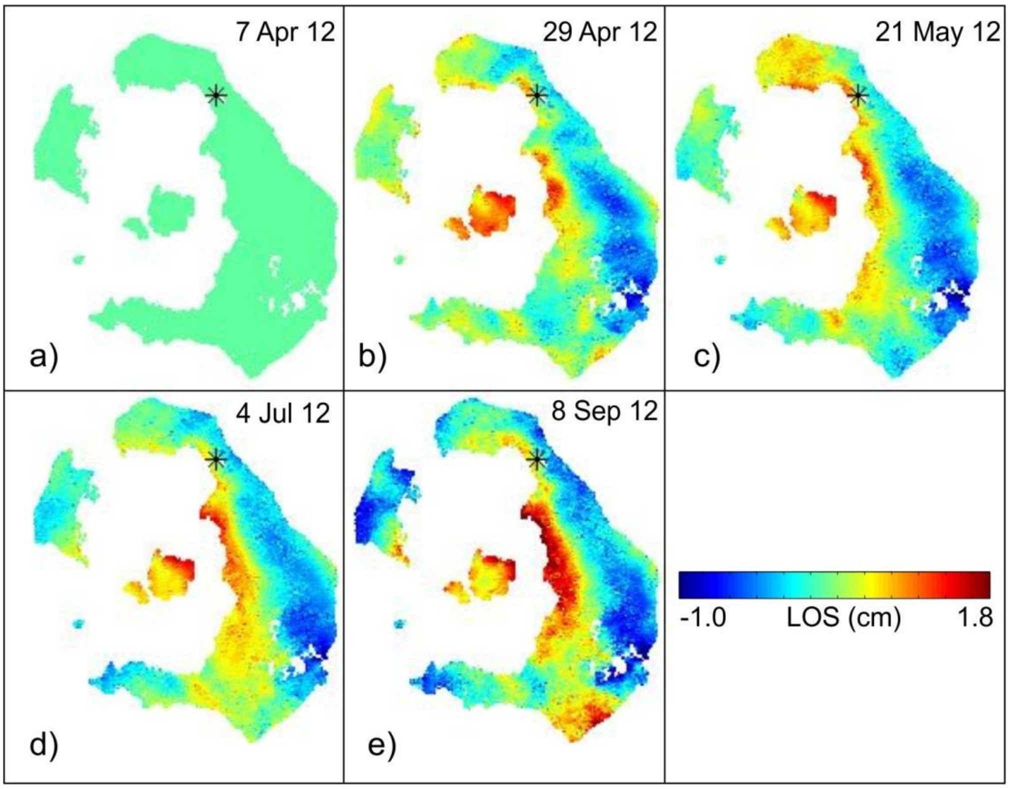

Figure 4.5. *Time series of line-of-sight (LOS) displacements for Santorini using StaMPS SB interferograms from ascending TerraSAR-X track 138. Each image represents cumulative displacement since the first image in the time series (7 April 2012). LOS displacements are given relative to the estimated LOS displacements at cGPS station MOZI, marked by an asterisk. The TSX data were processed at 10 looks and we used a 15 m DEM (resampled to 30 m) to remove topographic fringes.*

4.4.3 High resolution interferograms (Nea Kameni: 2011-2012)

To determine whether any localised deformation was occurring on Nea Kameni, we reprocessed the PS interferograms for TerraSAR-X track 85, using a 2-m DEM derived from LiDAR point cloud data acquired over the Kameni islands in May 2012, by the NERC Airborne Research Survey Facility. The TerraSAR-X data were processed at 2 looks providing a final resolution of approximately 4-m. These high resolution interferograms show no evidence for local deformation related to the Nea Kameni vent system or the underlying Kameni line, but they do confirm that deformation on Nea

Kameni continued into April 2012 (Figure 4.6), some 3 months after the cessation of detectable earthquake activity beneath the caldera.

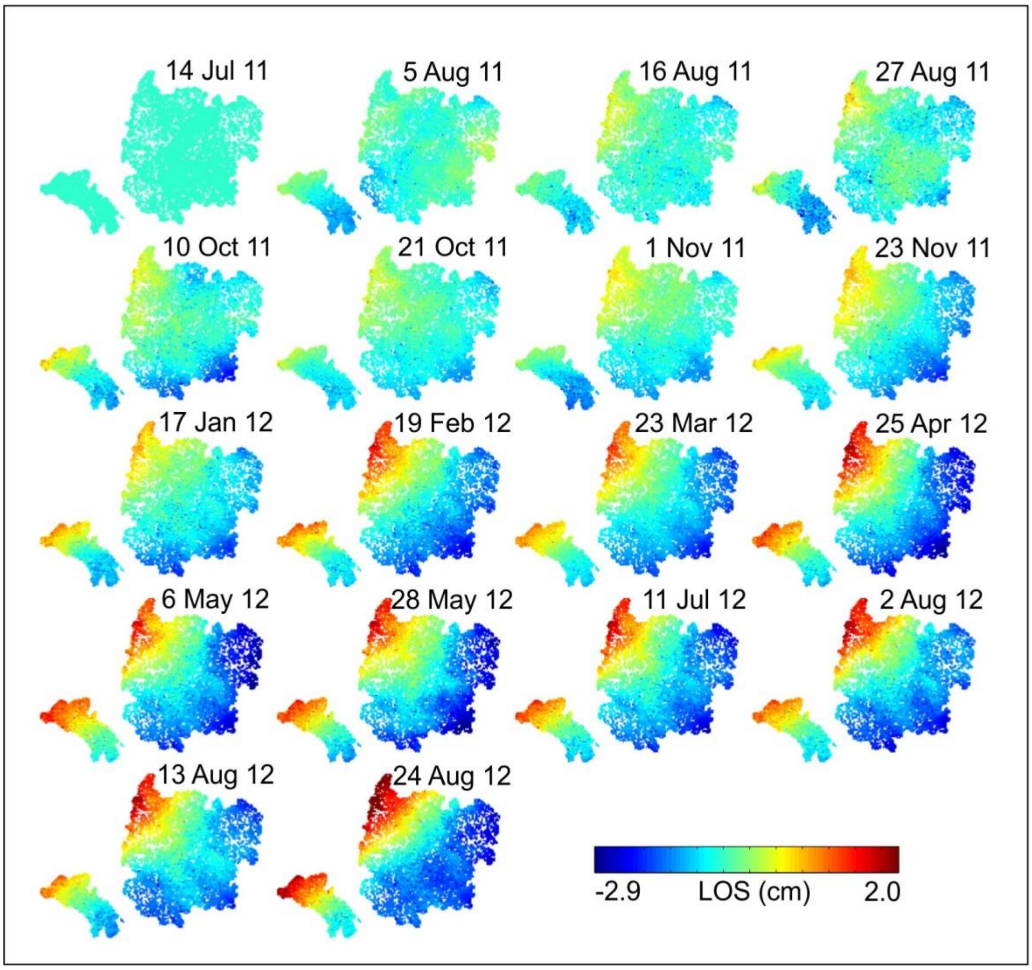

Figure 4.6. *Time series of line-of-sight (LOS) displacement for Santorini using PS interferograms for ascending TerraSAR-X track 85. Each image represents cumulative displacement since the first image in the time series (14 July 2011). A 2 m LiDAR derived DEM was used to remove topographic fringes and the interferograms were processed at 2 looks.*

4.5 Modelling and Interpretation

4.5.1 Slow subsidence (Nea Kameni)

We investigated several possible scenarios that might explain the steady slow subsidence identified on Nea Kameni over the 17-year period from 1993-2010. These include the cooling and contraction of a historic magma body, and thermal contraction and loading by historic lava flows.

4.5.1.1 Cooling and contraction of a historic subsurface magma body

To investigate whether the observed signal may be related to cooling and contraction of a historic subsurface magma body, we used the simple Mogi model and the volumetric time series technique as outlined in section 2 of Biggs et al. (2010b), to determine the temporal evolution of the best-fit parameters for the deflating source. The variation in cumulative volume change over the period 1993-2009 is shown in Figure 4.7a, however only SB interferograms between 2004 and 2009 were used to model the source location (Figures 4.7b & c), as these comprised data from both ascending and descending tracks. Prior to this, the only data available to us had been from the descending ERS track 422, which would likely bias the source location. There was also a gap in available satellite data between ERS and ENVISAT acquisitions from 2001 to 2004 (Figure 4.7a).

The Mogi model provides a good-fit for the observed subsidence on the south of Nea Kameni, but requires a very shallow source (1.6 km) situated in the SW of the volcano (Figures 4.7b & c). The rate of volume change determined from the inversion for the period June 1993-August 2000 (ERS observations) is $(-6.25 \pm 0.77) \times 10^4$ m^3/yr and for July 2004-August 2009 (ENVISAT observations) is $(-8.36 \pm 1.06) \times 10^4$ m^3/yr. We estimated the volume change between August 2000 and July 2004 (data gap between ERS and ENVISAT acquisitions) using an average of the two rates. The total volume change calculated for this 16-year period is (-11.6 ± 1.5) × 10^5 m^3. This average rate of deflation is greater than that reported by Foumelis et al. (2013), (Table 4.2). This arises from the difference between the source depths determined in both studies (Table 4.2) (1.6 km in this study compared to 0.8 km in Foumelis et al. (2013)), and the trade-off between volume change and depth. The InSAR residuals for selected interferograms are displayed in Figure 4.8.

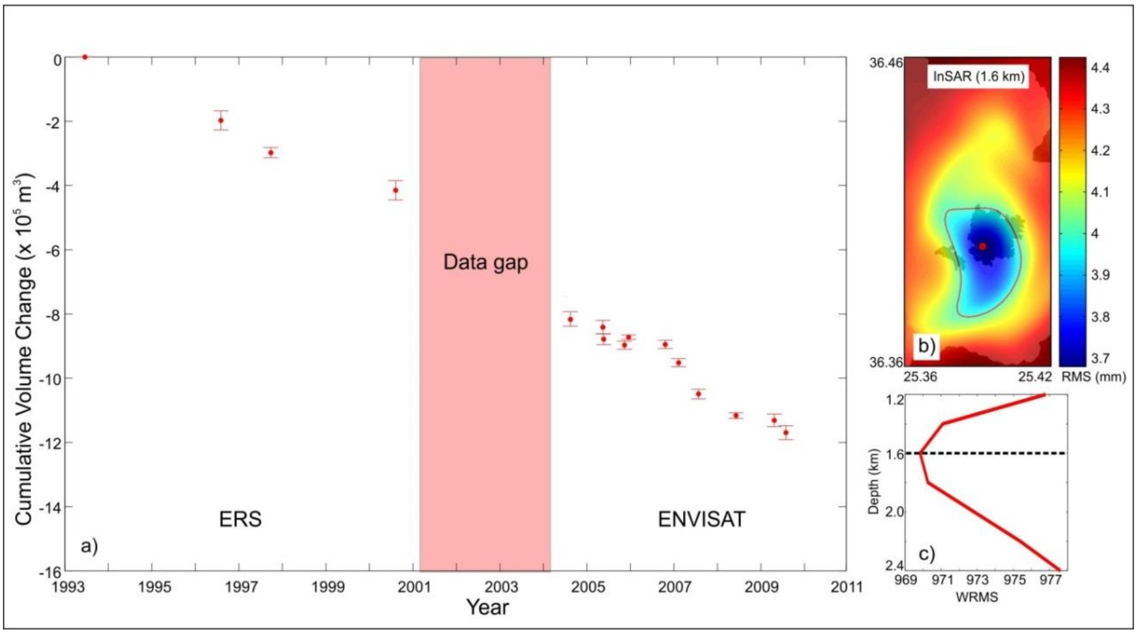

Figure 4.7. *Volumetric time series and source location plots derived from the InSAR-only inversion of SB interferograms from the descending ERS and ENVISAT tracks 422 and ascending ENVISAT track 329.* ***(a)*** *Temporal evolution of volume change. A shift has been applied to ENVISAT time series (2004-2009) based on the total volume calculation for the period 1993-2009 (Table 4.2).* ***(b & c)*** *Best-fit source location derived from the InSAR-only volumetric inversion. The red filled circle in figure c represents the best-fit geographic location determined in this study, with the red contour outlining the error bounds.*

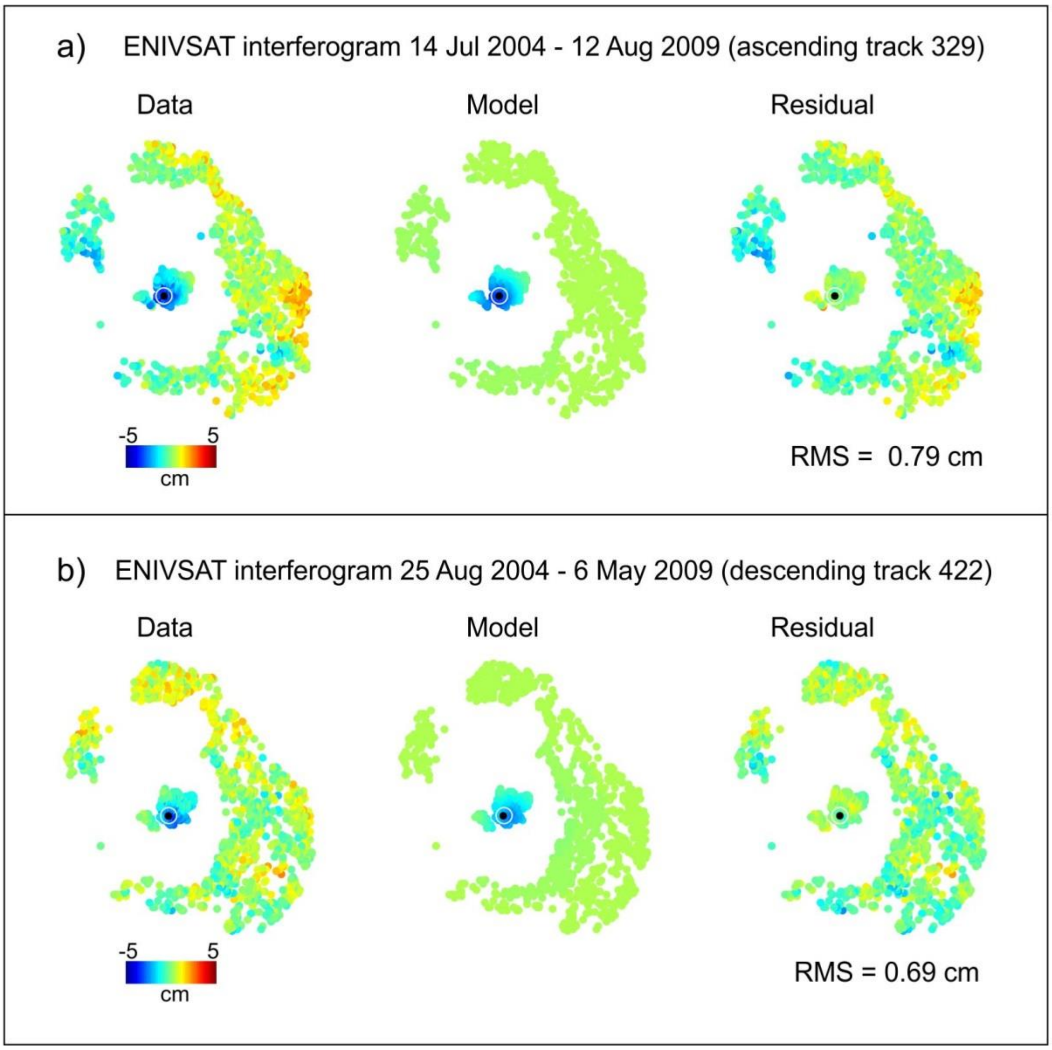

Figure 4.8. *InSAR residuals. Example interferograms showing observations (left), model (middle) and residuals (right).* ***(a)*** *14 July 2004 to 12 August 2009 and* ***(b)*** *24 August 2004 to 6 May 2009. The black filled circle represents the best-fit source location.*

4.5.1.2 Thermal contraction and loading of historic lava flows

The emplacement of lava flows may result in observable surface deformation via three primary processes: (1) Repacking of clasts and compression of voids within underlying flows or strata; (2) Thermal contraction of lava flows; (3) Loading from historic lava flows and viscoelastic relaxation of the substrate. It is likely that compaction and loss of residual void space in underlying lava flows occurs fairly rapidly following emplacement (Stevens et al., 2001) so we do not consider (1) a likely on-going phenomenon for flows emplaced over 65 years prior and as such only address (2) and (3) in the following section.

The slow subsidence signal observed at Nea Kameni appears to correspond spatially to the locations of the 1866-1870 and 1939-1940 dacite lava flows (Figure 4.9a). We first explore whether the observed subsidence on Nea Kameni between 1993 and 2010 may be related to the cooling and contraction of this lava pile by modelling each flow as a slab of thickness *d*, with temperature *T* (relative to ambient) and coefficient of thermal expansion α. If the individual flows are emplaced at time *t* before present, on a semi-infinite medium of thermal diffusivity κ (Carslaw and Jaeger, 1959), then the rate of contraction ω, is

$$\omega = \frac{\alpha\kappa T\left(e^{-d^2/4\kappa t} - 1\right)}{\sqrt{\pi}\sqrt{\kappa t}}$$

(4.5)

We computed the expected contraction rate as a function of flow thickness (Figure 4.9b) for the 1866-1870, 1925-1928 and 1939-1940 lava flows, using the input variables: $\alpha = 3 \times 10^{-5}\ \mathrm{K^{-1}}$, $\kappa = 10^{-6}\ \mathrm{m^2\ s^{-1}}$ and $T = 1223$ K. The time since emplacement (t) is ~ 140 years for the 1866-1870 flow, ~ 80 years for the 1925-1928 flow and ~ 65 years for the 1939-1940 flow. The difference between the three curves (displayed in Figure 4.9b) results from the different emplacement times. The average thickness of the 1886-1870 flow is approximately 90 m, which corresponds to ~ 3 mm/yr of subsidence. The average thickness of the 1939-1941 flow is ~ 20 m, which corresponds to less than 1 mm/yr and the 40 m thick 1925-1928 flow would produce < 2 mm/yr (Figure 4.9b). This plot shows that despite having the longest period since emplacement, the 1866-1870 flow has the largest continuing contraction rate based on its substantial thickness and that this could account for ~ 50% of the observed subsidence for the period 1993-2010. Although the combined rates from the 3 lava flows would add up to the -6 mm/yr of observed subsidence, the -2 mm/yr from the 1925-1928 flow cannot contribute the total subsidence observed in the vicinity the 1866-18070 lava flows as the 1925-1928 flow was only extruded in the northwest part of the island (Figure 4.9a).

Comparison between our model and a recent compilation of InSAR measurements of lava subsidence made to date (Ebmeier et al., 2012) suggests that processes other than lava contraction may contribute significantly to rates of lava subsidence. The time between emplacement of the Paricutin lava flow (Table 1 of Ebmeier et al., 2012) and that of the InSAR measurements (54-65 years) is not too dissimilar to that for the Nea Kameni 1939-1941 flow, although the Paricutin flow is considerably thicker. Our lava contraction model would predict ~ 5 mm/yr contraction for this flow assuming an average thickness of ~ 70 m. This is approximately one tenth of the subsidence rate observed at Paricutin by Fournier et al. (2010).

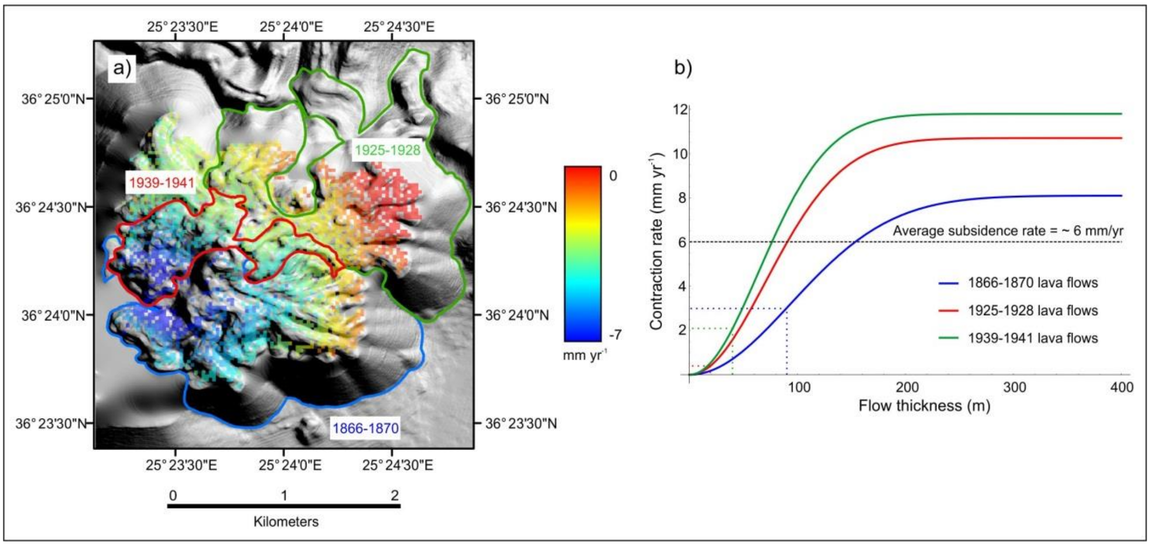

***Figure 4.9. (a)** Merged bathymetry and LiDAR grid from Nomikou et al. (in prep.), overlain with mean LOS displacements (mm/yr) computed using descending ENVISAT interferograms from track 422. The blue polygon represents the outline of the 1866-1870 lava flow. The green polygon represents the outline of the 1925-1928 lava flow and the red polygon represents the outline of the 1939-1941 lava flow. **(b)** Thermal contraction rate of historic lava flows (mm/yr), plotted as a function of lava flow thickness.*

The 1866-1870 lava flow was the most voluminous and spatially extensive historical flow extruded on Nea Kameni (Pyle and Elliott, 2006). To test whether the observed subsidence may relate to viscoelastic relaxation of the caldera floor or substrate in response to loading from the 1866-1870 flow, we modelled a cylindrical load placed on an elastic lid of thickness H, on a viscoelastic half space (Nakiboglu and Lambeck, 1982; England et al., 2013). The load has a radius of 1 km, height of 100 m and density of 2500 kg/m^3. The elastic lid has a shear modulus of 3.75 GPa, a density of 1800 kg/m^3 and Poisson's ratio of 0.2. The thickness and shear modulus of the viscoelastic layer are 80 km and 33 GPa respectively. It is assumed that loading commenced in 1866. Our model suggests that the observed rate of subsidence at Nea Kameni may be induced by the loading of a 100 m thick lava flow, however both a high viscosity (5.6×10^{18} Pa s) and a small elastic lid thickness are required (500m). The contoured quantity in Figure 4.10a is the rms misfit (in mm/yr) between the model and mean LOS displacements, computed using descending ENVISAT interferograms from track 422. The minimum rms misfit associated with this model (Figure 4.10a) is 0.6 mm/yr - equivalent to 3.2 mm for the ~ 5 yr period covered by the input interferograms. This is slightly less than the minimum misfit observed in section 4.5.1.1 and Figure 4.7 (3.7 mm) for the model representing the cooling and contraction of a historic magma body. However, despite the reasonable fit to the InSAR observations (Figure 4.10b), the loading model might not be considered physically realistic, as it requires a thin elastic lid. This suggests that the viscoelastic medium extends from 500 m beneath the surface – a zone which has hosted the majority of the volcano-tectonic earthquakes since the onset of unrest, indicating elastic rather than viscoelastic behaviour. However, it has been observed (Smith et al., 2009) that volcano-tectonic earthquakes can occur at temperatures and depths where the material would otherwise behave in a ductile fashion, indicating brittle failure when local stresses exceed a threshold value.

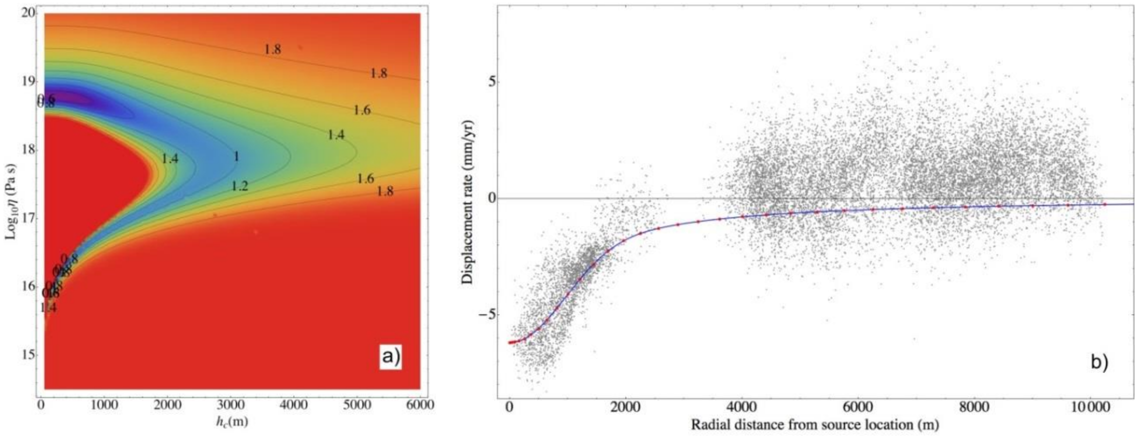

Figure 4.10. (a) *Viscoelastic model for a 100 m thick lava flow emplaced in 1866. The contoured quantity is the residual between the model and the mean LOS displacements computed using descending ENVISAT interferograms from track 422, for data points < 4 km from the centre of the load. The unit of the rms contours is mm/yr. A viscosity of* 5.6×10^{18} *Pa s and an elastic lid thickness of 500 m provides the best-fit to the data.* ***(b)*** *A comparison between the best-fitting model (blue-red) and the mean LOS displacements computed using descending ENVISAT interferograms from track 422. The source location (load) is situated in the centre of the deflation signal (see Figure 4.8).*

The two models discussed here: i) cooling and contraction and ii) loading, are not mutually exclusive, so the observed subsidence signal between 1993 and 2010 may in fact result from a combination of both processes. Given that the location of the signal agrees closely with the extent of the 1866-1870 lava flow, we suggest that a combination of thermal contraction and loading from this historic lava flow can account for the observed subsidence, rather than hypothesising a shallow subsurface deformation source for which we have no additional evidence.

4.6 Caldera wide uplift

4.6.1 Joint inversion

We have also used the volumetric time series technique to convert deformation measurements derived from ten cGPS sites (Figure 4.1), and 199 SB interferograms (Appendix C) covering the period of unrest, into sub-surface volume change. The time series of cumulative volume change for each of these datasets is shown in Figure 4.11 and the best-fit source locations in Figure 4.12.

The combined InSAR, GPS and joint inversion results (Figure 4.11 and Table 4.3) suggest that the best fitting spherical source has an effective volume of ~ 14–23 × 10^6 m^3, centred slightly to the north of Nea Kameni at a depth of ~ 4 km (Table 4.3, Figures 4.11 & 4.12). The depth to the source is in good agreement with those reported in previous studies (Table 4.3), as is the geographic location (longitude: 25.388–25.390 latitude: 36.428) and rate of volume change within the shallow chamber ~ 11–18 × 10^6 m^3/yr. The estimated total volume change from the InSAR-only inversion (from January 2011-April 2012) is ~ (15 ± 1) × 10^6 m^3. The volume change between January and March 2011 (data gap in InSAR measurements) is estimated using the average rate displayed in parentheses in Table 4.3. The total volumes computed from the GPS-only and joint inversion are slightly higher (~ 19 ± 4) × 10^6 m^3. These differences may result from the varying sensitivity of InSAR and GPS measurements to vertical and horizontal movements or may be suggestive of a higher horizontal to vertical expansion of the source; although a previous study by Newman et al. (2012) suggests this was not the case. The misfit between the input observations and model is displayed in Figures 4.13 & 4.14.

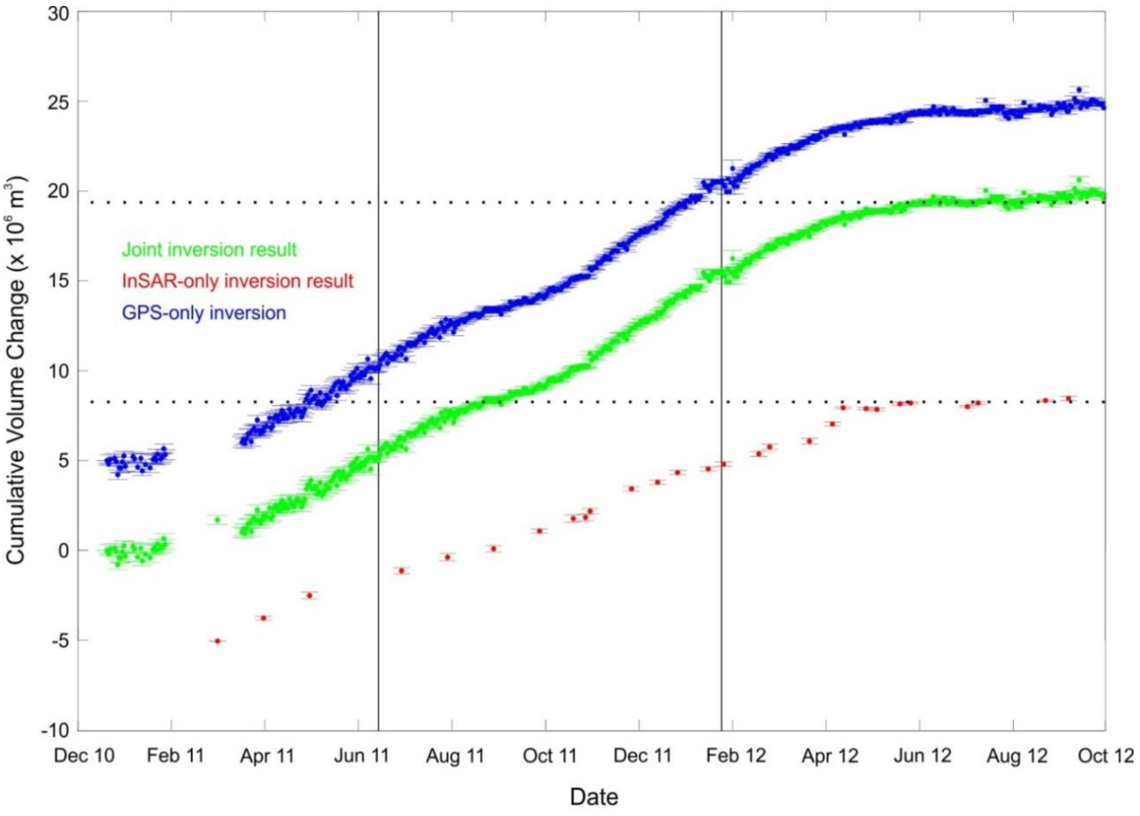

*Note - A vertical offset has been applied to the InSAR-only and GPS-only inversion results for display purposes.

Figure 4.11. *Temporal evolution of volume change derived from the inversion of cGPS measurements for 10 sites, from December 2010 – October 2012 (blue), of PS InSAR measurements from March 2011 – September 2012 (red) and Joint inversion result covering the period December 2010 – October 2012 (green). A vertical offset of* ± *5 ×* 10^6 m^3 *has been applied to the GPS-only and InSAR-only inversion results respectively for display purposes.*

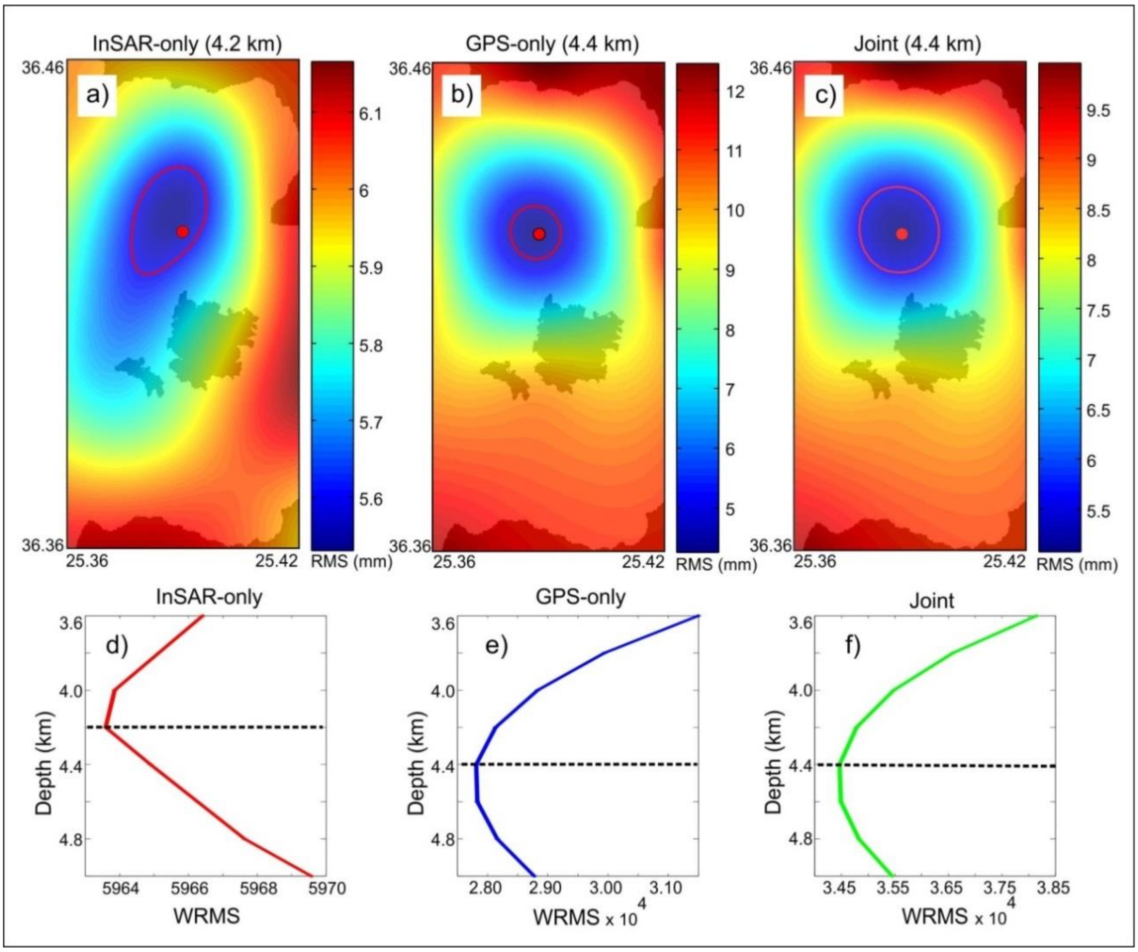

Figure 4.12. *Source location plots.* ***(a & d)*** *Best-fit source location derived from the InSAR-only volumetric inversion.* ***(b & e)*** *Best-fit source location derived from the GPS-only volumetric inversion.* ***(c & f)*** *Best-fit source location derived from the Joint volumetric inversion. The red filled circle in each figure represents the best-fit geographic location of the source of the deformation determined in this study. The red contours outline the error bounds.*

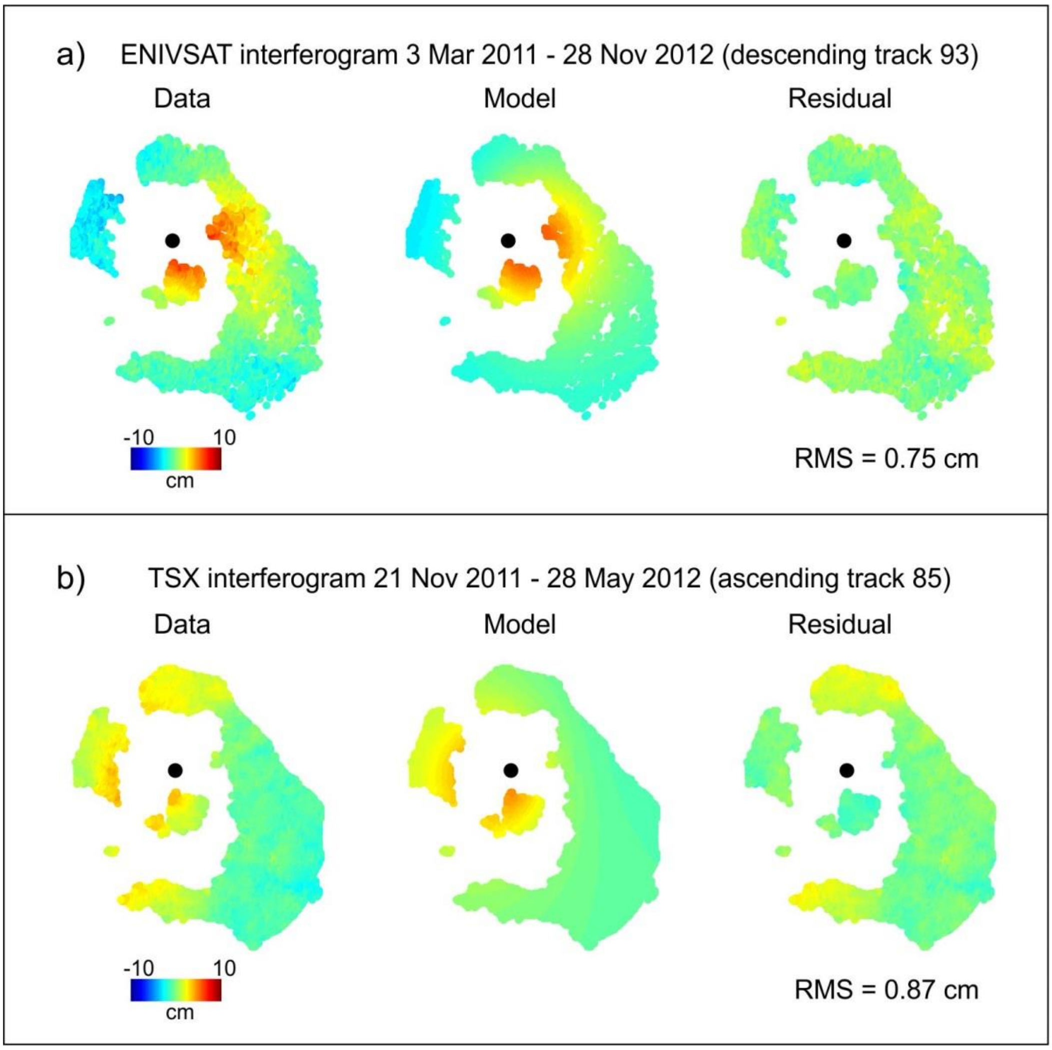

Figure 4.13. *InSAR residuals. Example interferograms showing observations (left), model (middle) and residuals (right). The interferograms were chosen to represent different periods during the phase of unrest at Santorini volcano.* ***(a)*** *3 March 2011 to 28 November 2011,* ***(b)*** *21 November 2011 to 28 May 2012. The black filled circle represents the source location.*

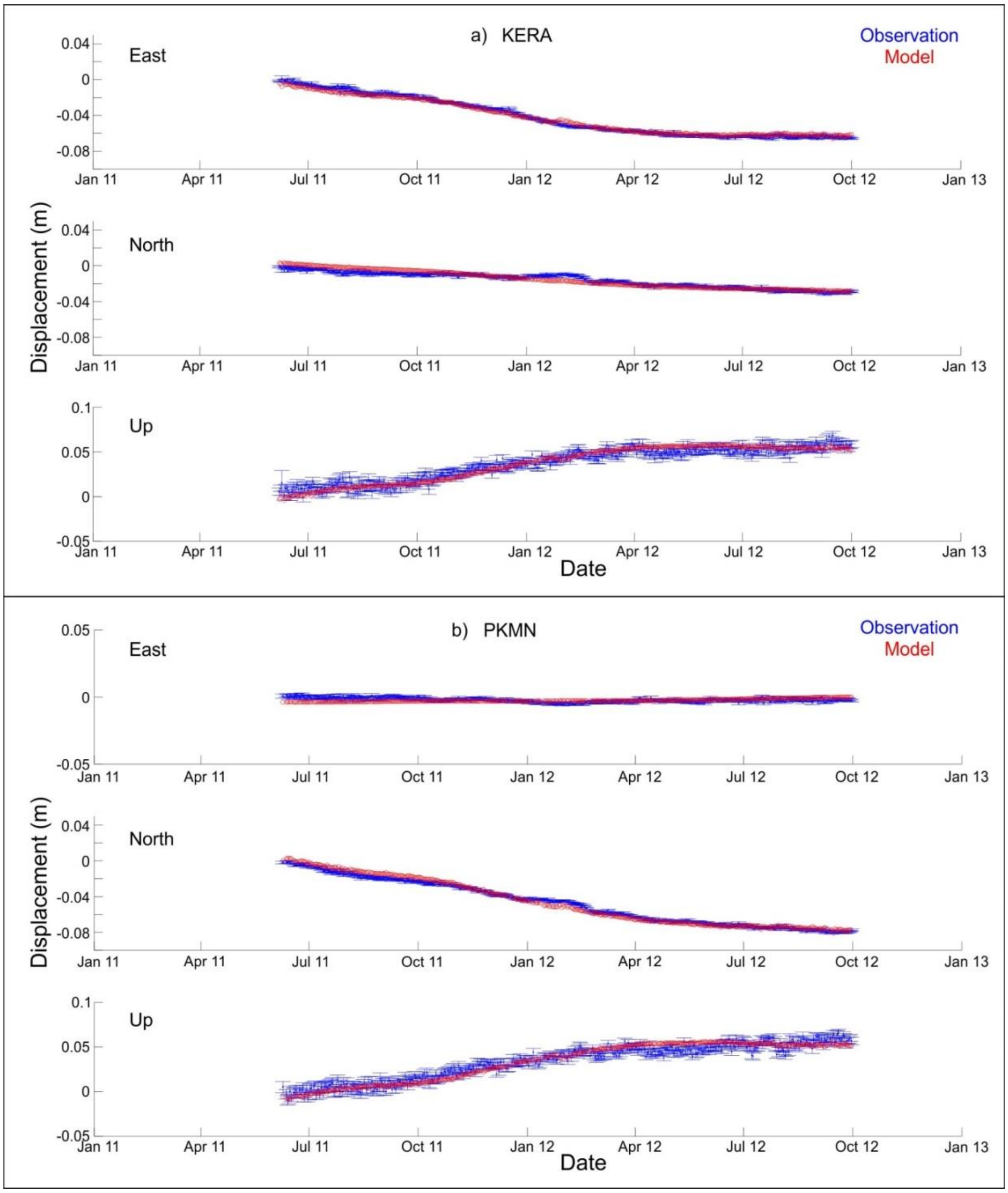

Figure 4.14. *GPS measurements and models.* ***(a)*** *GPS measurements from cGPS site KERA and corresponding models derived for east, north and up components. (b) As a, for cGPS site PKMN.*

The time series plot (Figure 4.15) provides some evidence that two pressure pulses were supplied to the shallow chamber between January 2011 and April 2012. A steady volume increase was observed between January-August 2011 (first pulse), coinciding with an increase in VT earthquake activity. We interpret this first pulse as an initial increase in pressure within the shallow magma chamber (associated with the magmatic intrusion in January 2011) which resulted in a volume change of approximately 8 × 10^6 m^3. This was followed by a short decrease in the rate of volume change from August-October 2011, followed by an increased rate from October 2011 to the end of April 2012. The second pressure pulse (August 2011-April 2012) corresponds to a volume change of 11 × 10^6 m^3 (Figure 4.15). There appears to be a lag between the reduction in earthquake seismicity (in both June 2011 and February 2012) and the decline in the volumetric growth rate (in August 2011 and April 2012). The latter lull in activity (April 2012-October 2012) continues at the time of writing (July 2013).

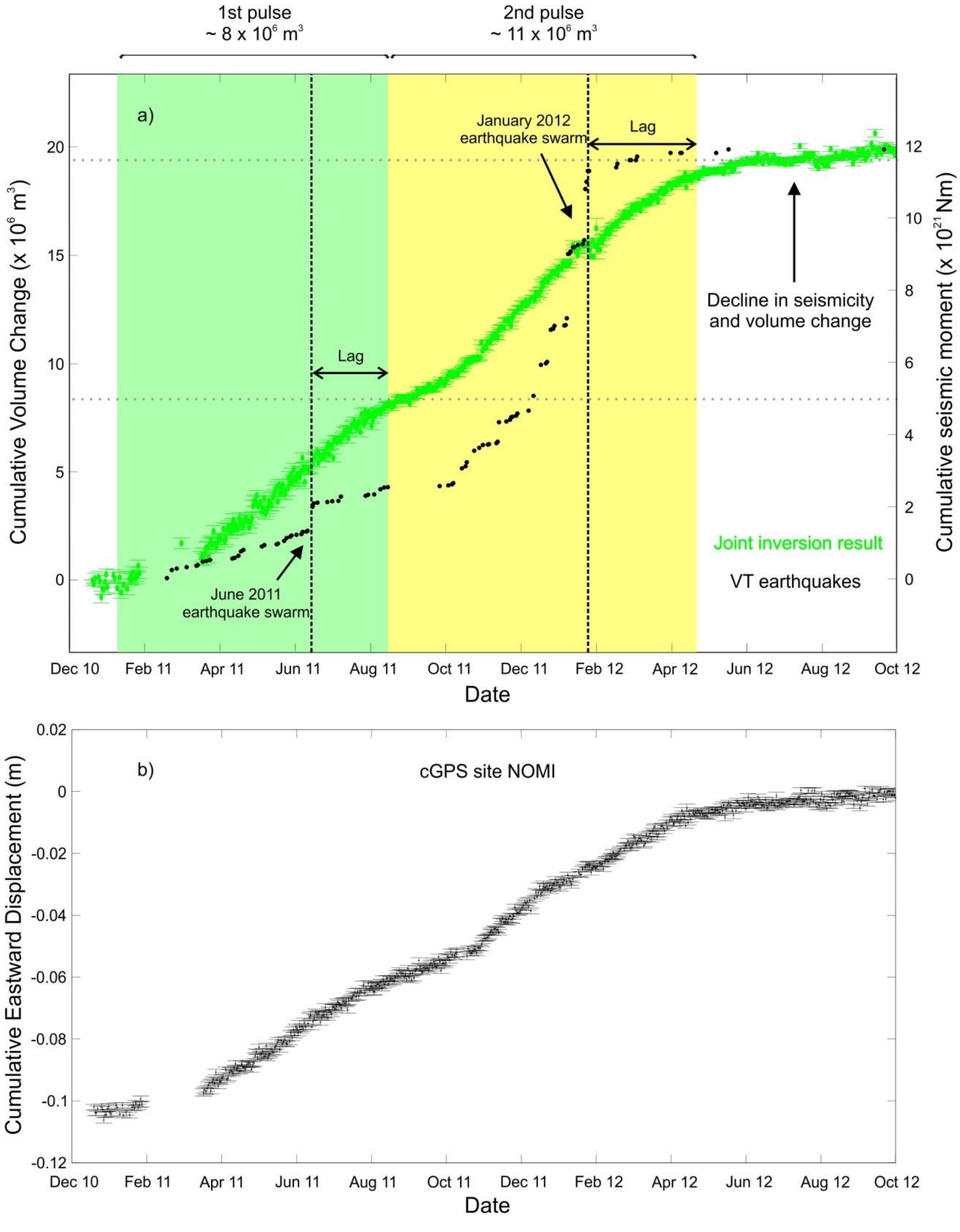

Figure 4.15. *Comparison of joint inversion result with cumulative seismicity and cGPS data. (a) Cumulative variation in volume change derived from the joint inversion of cGPS measurements and PS InSAR measurements covering the combined period of December 2010 – October 2012 (green). Cumulative energy release from earthquakes (> ML 2.0) occurring within the caldera during the same period is also shown (black filled circles). The first pressure (January-August 2011) is shaded in green and the second pressure pulse (August 2011-April 2012) in yellow. (b) Cumulative eastward displacement from cGPS site NOMI, covering the same time period as shown in (a).*

4.6.2 Viscoelastic modelling

Field evidence and thermal models demonstrate that thermal aureoles may develop in the host rock surrounding magma intrusions (Hodge, 1974; Gasparini et al., 1981). There is strong evidence for the existence of a thermal or metamorphic aureole beneath the Kameni islands, both from basement rock inclusions in Kameni lavas, and also from the carbon-isotopic compositions of Kameni CO_2 emissions (e.g. Parks et al., 2013; Chapter 6). Temperatures in the thermal aureole and outer margin of the magma chamber will exceed the brittle-ductile transition, sufficient to allow ductile flow and stress relaxation in the vicinity of the magma chamber. Thus, we assume a viscoelastic rather than purely elastic model to model any observed deformation.

We investigate whether a viscoelastic rheology may be invoked to explain the pattern of increase and subsequent decay in cumulative volume change observed during and after the second pressure pulse (from August 2011 to October 2013). The first pulse was not modelled because the relaxation response associated with this is partially masked by the initiation of the second pulse. We modelled the observed temporal variation in volume change (derived from the joint inversion) associated with the second pulse, in terms of the ductile deformation of a concentric viscoelastic shell of radius R_2-R_1, surrounding a shallow magma chamber of radius R_1, driven by an initial increase in pressure. Several other studies at active volcanoes have used viscoelastic modelling to better constrain source parameters responsible for observed deformation (e.g. Dragoni and Magnanensi, 1989; Newman et al., 2001; Hickey et al., 2013) but to our knowledge, this is the first attempt to use a viscoelastic analytical half-space solution to understand the temporal evolution of a deformation signal.

The original analytical solution by Dragoni and Magnanensi (1989) assumes a magma chamber surrounded by a viscoelastic shell embedded in an infinite medium (full-space). Although this solution is useful in determining the variation in the shape of the deformation pattern over time, the output may not be directly compared with GPS or InSAR measurements due to the exclusion of the free-surface. Full-space models typically underestimate the observed deformation by a factor of ~ 3 (Newman et al., 2001). For this reason more recent studies (Newman et al., 2001; Masterlark et al., 2010; Hickey et al., 2013) have used a finite element approach to model viscoelastic deformation within an elastic half-space. Segall (2010) presented two analytical solutions to model vertical displacements due to a pressurised sphere in an elastic half-space, based on a modification of Dragoni and Magnanensi's (1989) original full-space solution. The first of Segall's solutions models the pressure change within the magma chamber as an instantaneous step increase (Heavyside function) whereas the second models the pressure change as a gradual increase followed by an exponential decay (Segall, 2010). Although we applied both solutions in an attempt to model the variation in volume change/deformation observed at Santorini between August 2011 and October 2012, the solutions did not provide a good fit to the observations. This suggests that the pressure increase within the shallow magma chamber at Santorini was not instantaneous nor did it gradually decay with time. Here we present a new analytical solution to model the variation in volume change within a shallow magma chamber surrounded by a viscoelastic shell, considering an alternate pressure history.

We suggest that the observed decline in seismicity at the end of January 2012, with the coincident decline in the rate of volume change, resulted from the cessation of melt supply to the shallow chamber. To test this idea, we followed the full-space solution of Dragoni and Magnanensi (1989) and used the method of McTigue (1987) to derive a half-space solution for a generic pressure function, representing a linear increase in pressure (ramp) between t = 0 and t = t_1, after which time the pressure within the shallow chamber remains constant.

We modelled the observed deformation response for the second pressure pulse (commencing in August 2011) in terms of the ductile deformation of a viscoelastic shell with a rigidity (μ), surrounding a shallow magma chamber, located at a depth of (d) beneath the surface (Figure 4.16 & Table 4.4). We then compared our viscoelastic relaxation model with a time dependant Mogi model to express the time dependent volume change in terms of the parameters in our model.

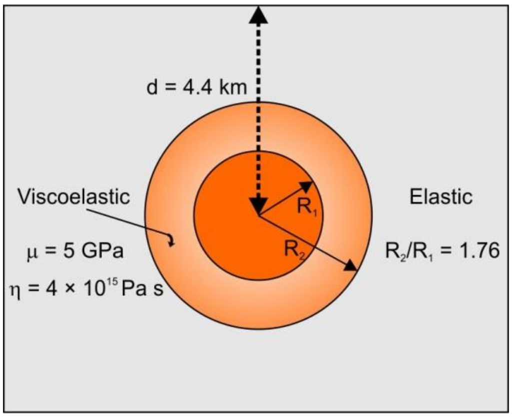

Figure 4.16. *Schematic diagram of a concentric viscoelastic shell with viscosity η and rigidity μ, surrounding a spherical magma chamber of radius R_1. R_2 is the distance from the centre of the magma chamber to the outer boundary of the viscoelastic shell (after Segall, 2010).*

Table 4.4: *Parameters for viscoelastic shell model.*

Variable	**Definition**
P_0	Maximum pressure
R_1	Radius of magma chamber
R_2	Radius of magma chamber plus viscoelastic shell
μ	Elastic shear modulus
ν	Poisson's ratio
η	Viscosity
t_1	Shut off time for pressure change

We modelled an injection of melt into the shallow chamber by an initial increase in pressure as a ramp function with a cut-off (Figure 4.17a). This corresponds to a constant supply of melt (and a linearly increasing pressure) to the shallow chamber between t = 0 and t = t_1, and then a fixed pressure for t > t_1. The increase in pressure within the shallow magma chamber may be represented in terms of volume change (McTigue 1987). The time-dependent volume change is given by equation (4.6) (derived by J. Moore):

$$\begin{aligned}\Delta V(t) = \frac{\pi p_0 (R_2)^3}{\mu^2(\nu+1)t_1(R_1)^3}&[(R_1)^3 f(t, t_\mathrm{R}, \eta, \nu) + (R_1)^3\mu(1+\nu)t \\ &- (R_2)^3 f(t, t_\mathrm{R}, \eta, \nu) \ldots + (R_2)^3 f(t - t_1, t_\mathrm{R}, \eta, \nu) \\ &- (R_1)^3 f(t - t_1, t_\mathrm{R}, \eta, \nu) - (R_1)^3 (t - t_1)\mu(1+\nu))H(t - t1)]\end{aligned} \tag{4.6}$$

where

$$f(t, t_R, \eta, \nu) = 3\eta(1-\nu)(1-e^{-t/t_R})$$

(4.7)

and

$$t_R = \frac{3\eta(1-\nu)\,(R_2)^3}{\mu(1+\nu)(R_1)^3}$$

(4.8)

The pressure function is given by equation (4.9) (derived by J. Moore):

$$p(t) = \frac{p_0}{t_1}(t + (t_1 - t)H(t - t_1))$$

(4.9)

The predicted volume change is fitted to the data, weighted by the errors between consecutive observations, using a least squares minimisation routine in Mathematica (http://www.wolfram.com/mathematica/). We solve for the ratio of the outer to inner radius (R_2/R_1), the characteristic relaxation time (t_R), the shut-off time (t_1) and a scaling coefficient which is a combination of the pressure increase within the magma chamber and the chamber radius (R_1) (see Figure 4.16). The pressure and radius terms in the Mogi approximation are coupled (Mogi, 1958) and it is not possible to individually determine either parameter. However, a trade-off curve between pressure change and radius may be used to determine a range of physically viable parameters. The computed trade-off curve is displayed in Figure 4.17b (for example: if the pressure in the shallow chamber was increased to 20 MPa this would dictate a chamber radius

(R_1) of 560 m and an outer radius (R_2) of 990 m). To derive the viscosity of the shell surrounding the magma chamber we specify μ (5 GPa) and ν (0.25). The best-fit parameters minimising the misfit between the volume change derived from the joint inversion and the viscoelastic model are displayed in Table 4.5.

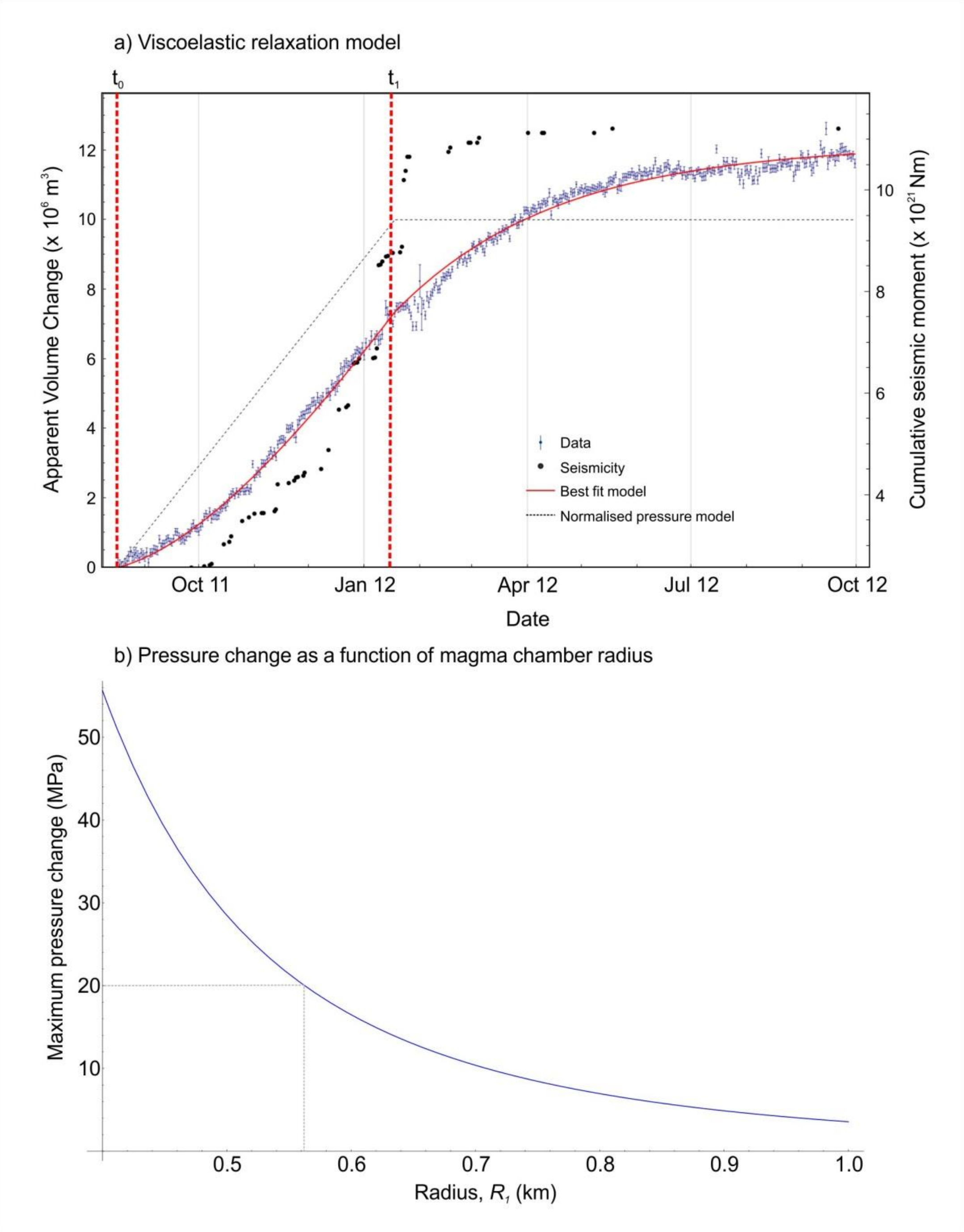

Figure 4.17. ***(a)*** *Comparison between the viscoelastic relaxation model (red), joint inversion result (blue) and the cumulative seismic moment released during VT earthquakes > M2.0 occurring within the caldera (black dots). The dashed line represents the normalised pressure model, displaying a linearly increasing pressure between* t_0 *and* t_1 *(red dashed lines), after which time the pressure within the shallow magma chamber is held constant.* ***(b)*** *Trade-off curve between pressure change and radius. The dashed line indicates the relationship between pressure change and radius as referred to in the text. e.g., if the pressure in the shallow chamber was increased to 20 MPa this would dictate a chamber radius (*R_1*) of 560 m.*

Table 4.5: *Best-fit parameters derived from the viscoelastic model. η is the viscosity of the viscoelastic shell surrounding the magma chamber. R_2/R_1 is the ratio of the outer-inner radius. The increase in pressure commences at t_0 and is shut off at t_1, after which time the pressure is held constant. t_R is the relaxation timescale.*

η (Pa s)	**(R_2/R_1)**	**t_0**	**t_1**	**t_R (days)**
4×10^{15}	1.76	20th Aug 2011	20th Jan 2012	90

The best-fit model provides a good match to the joint inversion result and the derived shell viscosity (4×10^{15} Pa s) and R_2/R_1 ratio (1.76) are within the expected range, considering values reported from other studies (e.g., Newman et al., 2001 and references therein). The derived shut-off time for the pressure function also provides a good fit to the observed cumulative seismicity (Figure 4.17). This derived pressure history corresponds to a constant supply of melt to the shallow chamber between late August 2011 and late January 2012. At the end of January 2012, melt supply to the shallow chamber ceases, but the displacements and cumulative volume change continue to increase at an exponentially decaying rate. This mechanism explains the lag between the cessation in earthquake activity and the flattening of the cumulative volume change curve shown in Figures 4.15 & 4.17. The timing of the pressure shut off corresponds to an earthquake swarm at the end of January 2012, which was followed by an almost complete cessation in micro-seismic activity in the centre of the caldera.

4.7 Discussion

The joint InSAR-GPS approach provides an improved estimate of the depth and volume change associated with the recent intrusion beneath Santorini volcano, as well as additional insight into the temporal evolution of melt supply to the shallow reservoir.

Between the start of January 2011 and August 2011, the joint inversion curve displays an increasing linear trend, suggesting a steady rate of injection to the shallow chamber. After August 2011 there is a slight reduction in the cumulative volume change, which lags behind a short-lived hiatus in earthquake activity, followed by an additional increase in volume change from October 2011 to the end of April 2012. The earthquake swarm at the end of January 2012 corresponds to a change in CO_2 emissions on the summit of Nea Kameni (Parks et al., 2013; Chapter 6), perhaps resulting from the coalescence of fractures providing new gas migration pathways to the surface (Kilburn, 2003; Wright et al., 2009). After this swarm ceased, the rate of volume change begins to decline and the volcano enters an extended aseismic period.

Caldera-forming volcanoes such as Campi Flegrei, Yellowstone, and Long Valley have all experienced well-documented episodic phases of non-eruptive unrest (e.g. Del Gaudio et al., 2010; Wicks et al., 2006; Hill & Prejean, 2005; summarised in Table 4.6). In particular, there are several similarities that can be drawn between the recent unrest at Santorini and the episodes of minor uplift and seismicity that occurred at Campi Flegrei between 1989 and 2012 (Chiodini et al., 2012 & Table 4.6). These include: (i) the inferred existence of multiple reservoirs (shallow and deep) in both settings (Cottrell et al., 1999; Gottsmann et al., 2006), (ii) the observation that seismicity and deformation are not spatially coincident (D’Auria et al., 2011; Konstantinou et al., 2013) and (iii) the observed delay between the onset of unrest and an increase in gas emissions (Chiodini et al., 2012; Parks et al., 2013; Chapter 6). Several authors (e.g. D’Auria et al., 2011; Chiodini et al., 2012) have suggested that the recent phases of minor uplift and seismicity at Campi Flegrei are related to the repeated transfer of magmatic fluids to a shallow hydrothermal reservoir. A similar cause of unrest has been inferred for the pulses of uplift, accompanied by earthquake swarms and increased CO_2 emissions that occurred at Long Valley between 1978 and 1998 (Table 4.6). The role of (hydrous) fluid migration in the recent unrest at Santorini remains unknown. Although both geodetic and gas-chemical datasets can be interpreted in terms of a pulse of magma arriving in a shallow reservoir beneath Santorini (Parks et al., 2012, 2013; Tassi et al., 2013), and this model is consistent with viscoelastic modelling (section 4.6.2), a detailed gravity survey would still be required to constrain the mass changes associated with this phase of unrest.

Table 4.6: *Examples of geodetic and seismic unrest at several caldera systems.*

Caldera volcano	**Period of unrest**	**Vertical deformation (cm)**	**Comments**	**References**
Santorini	Jan 2011 – April 2012	~ 20 cm of uplift between Jan 2011 and Jan 2012	Accompanied by earthquakes, although VT events were not collocated with the source of inflation. Source of deformation ~ 4 km beneath the surface.	Newmann et al., 2012; Parks et al., 2012; this study.
Campi Flegrei	1982-1984	1.79 m	Rapid uplift followed by intense seismicity. At the end of 1984 the ground began to subside and seismicity declined.	Orsi et al., 1999; Troise et al., 2007; Del Gaudio et al., 2010; D'Auria et al., 2011; Chiodini et al., 2012.
	1989-2010	Each episode was accompanied by between ~ 1-10 cm of uplift.	5 episodes of minor uplift and seismicity in 1989, 1994, 2000, 2006 and 2010. These events are thought to have been triggered by the repeated injection of magmatic fluids into a geothermal reservoir at a depth of ~ 2.5 km.	
Long Valley	1978-1983	25 cm of uplift between 1979 and 1980 7 cm uplift in Jan 1983	Accompanied by intense earthquake swarms, with several earthquakes ~ M6.0. Source of deformation ~ 4 km beneath the surface.	Savage & Clark, 1982; Savage & Cockerham, 1984; Sorey et al. 1993; McGee et al. 2000; Hill, 2006.
	1984-1988	<1 cm/yr of uplift followed by slight subsidence	Following an earthquake swarm in July 1984 both deformation and seismicity declined.	
	1989	1-2 cm of uplift	Minor uplift accompanied by a low energy, 11 month long earthquake swarm. The swarm was associated with the onset of deep LP earthquakes, diffuse CO_2 emissions and an increase in $^3He/^4He$ ratios; thought to have resulted from the release of CO_2 rich fluids from a series of dykes and sills intruded ~ 10-25 km.	
	1990-1995	Initially 7 cm/yr, slowing to 2-3 cm/yr	Accompanied by more energetic earthquake swarms that gradually declined from early 1994 onwards.	
	1996	< 1 cm/yr of uplift	More than1600 earthquakes (M>0.5) occurred during March-April 1996, with a cumulative seismic moment release of ~ 5×10^{15} N m. The swarm occurred whist uplift was declining.	
	1997-1998	~ 10 cm of uplift	Unrest resumed in mid-1997 with extension across the dome and earthquake swarms. More than 12 000 M>1.2 over 7 months and a cumulative seismic moment of 3.3×10^{17} N-m. Increased CO_2 emissions accompanied earthquake swarm.	
	Mid 1998	-	Negligible deformation and seismicity within the caldera.	
Yellowstone	1995-1997	Caldera-wide uplift. ~ 3 cm between 1996-1997	Both the uplift and subsidence is believed to be related to deep magmatic processes; primarily variations in the rate of basaltic magma flux and the migration of melt beneath the caldera. Changes from subsidence to uplift and vice-versa are either accompanied or preceded by earthquake swarms.	Wicks et al., 1998; Ingebritsen et al., 2001; Waite & Smith, 2002; Hill & Prejean, 2005; Wicks et al., 2006.
	1997-2002	Continued uplift beneath the north caldera rim – area of isolated deformation		
	1997-2002	More than 3 cm caldera-floor subsidence between 1997-2000		

There are several possible scenarios that may be responsible for the reduction in both the rate of cumulative volume change and seismicity from January 2012 to October 2012, however based on the prolonged absence of detectable seismicity, it is likely that the supply of either magmatic fluids/melt to the shallow chamber has ceased. This would explain both the extended period of aseismicity and decline in deformation. If the magma residing in the shallow chamber has a high volatile content, uplift may continue at a reduced rate following the cessation of melt supply (due to volatile saturation and vesiculation), or the system may be undergoing slow deformation associated with continued relaxation of the viscoelastic shell surrounding the magma chamber. The latter scenario was modelled in section 4.6.2 and provides a good fit to the temporal variation in volume change observed between August 2011 and October 2012. It is possible that the pressure pulses identified in Figure 4.15 represent either batches of melt supply to the shallow chamber, or episodes of vesiculation. The observation that VT swarms occur immediately before the decline in the rate of volume change suggest that volatile exsolution and vesiculation may be the driving force behind both the observed pressure pulses and the earthquake swarms. In this scenario, fracture propagation may be triggered by a combination of processes including increasing pore pressure (e.g., Martens & White, 2013) and stress corrosion (Kilburn et al., 1998 and references therein).

Obviously there are several scenarios that may be responsible for the observed decline in both the seismicity and uplift, but the conceptual model proposed here is considered a viable option as it also accounts for the temporal variation and relationship between the micro-seismicity, deformation and gas emissions.

4.8 Conclusions

Prior to the start of 2011, a slow subsidence signal persisted at Nea Kameni with no evidence from InSAR of any uplift. Our modelling suggests that this subsidence could be accounted for by the cooling and contraction of a shallow (1.6 km) historic subsurface magma body or the combination of thermal contraction and viscoelastic relaxation of the substrate associated with recent lava flows. We prefer this latter explanation due to the correspondence between the signal and the outline of the 1866-1870 lava flow, the most voluminous and spatially extensive historical flow. A new phase of unrest commenced at Santorini volcano in January 2011, characterised by the onset of micro-seismic activity focussed along the Kameni line, as well as caldera wide uplift. We have used a joint inversion of InSAR and GPS data to determine the temporal evolution of source parameters by converting both InSAR and GPS observations into a time series of sub-surface volume change. The best fitting parameters derived from the combined InSAR-GPS inversions are in good agreement with most other studies and suggest that the spherical source has an effective volume in the order of ~ 14–23 × 10^6 m^3, and is centred slightly to the north of Nea Kameni at a depth of ~ 4 km beneath the surface. The time series of sub-surface volume change has identified two separate pressure pulses between January 2011 and April 2012. A lag response is also identified between the cessation in micro-seismicity activity within the caldera (in late January 2012) and a significant decline in the rate of sub-surface volume change (several months later). We propose that these pulses represent episodes of vesiculation and that the resulting increase in pressure within the shallow chamber is responsible for the VT earthquake swarms. Since late January 2012, geodetic measurements have displayed an exponentially decaying rate of inflation, coinciding with a cessation in earthquake activity within the caldera (in February 2012). It is likely that this lull in activity results from an interruption in melt supply from a deeper reservoir and we have used modelling to show how the lag with the seismicity and shape of the deformation time series can be accounted for by considering the magma chamber as a sphere inside a viscoelastic shell (representing a ductile aureole around the magma chamber). It is currently not possible to determine when or if a new pulse of magma will be supplied to the existing shallow chamber, or indeed if the next pulse will bypass this chamber completely and be intruded at an alternate location. However, this information does provide insight into historic reservoir locations and melt supply during periods of unrest. Not only is the melt delivered to the shallow chamber in rapid batches, but it also seems that a series of batches may be required before the volcano is primed for eruption. The next phase of unrest will provide important constraints on the time period between these rapid pulses. Continuous deformation, seismicity and gas monitoring are essential to identify the onset of renewed unrest.

Chapter 5

Improved volumetric estimates and new rheological properties derived from detailed mapping of historic lava flows in the vicinity of the Kameni islands, Santorini

This chapter represents a significant contribution to an article (Nomikou et al., in prep.) that is in preparation for submission to a journal.[10]

5.1 Introduction

Analysis of lava flow morphologies can improve our understanding of historical effusive eruptions by providing insight into the evolution of flow fields, lava effusion rates and bulk rheological properties (e.g., Pyle and Elliott, 2006; James and Varley, 2012; Deardorff and Cashman, 2012). Lava flows are considered non-Newtonian and are often modelled as Bingham fluids, which require a critical shear stress (yield strength) to be exceeded to initiate viscous flow (Robson, 1967, McBirney and Murase, 1984). Determination of non-Newtonian properties (such as yield strength) provides insight into eruptive behaviour and the origin of flow morphologies (e.g., Hulme 1974;

---

[10] The bathymetry grid was provided by P. Nomikou (University of Athens). I generated the LiDAR grid, using point cloud data provided by the UK's Airborne Research and Survey Facility. The two grids were merged by Isidoros Livanos. The volumetric estimates displayed in Table 5.3 were computed by L. Kalnins and E. Simou.

Sparks et al., 1976; Moore et al., 1978; Peterson & Tilling, 1980; Cigolini et a1., 1983). Morphological studies undertaken on terrestrial volcanoes and Olympus Mons (Mars) reveal a strong linearly increasing relationship between silica content and lava lobe width which has enabled the estimation of lava compositions on Mars (Wadge & Lopes, 1991 and references therein). In addition, it has been demonstrated that detailed mapping and accurate volumetric estimates of historic extrusions may be used to forecast the evolution of future lava flows (Pyle & Elliott, 2006).

This study follows on from that undertaken by Pyle & Elliott (2006), in which the authors derived bulk rheological properties of historic dacite lava flows at Santorini, based on the analysis of a high resolution LiDAR dataset, acquired over the Kameni islands in April 2004. They demonstrated the time-predictable nature of historic eruptions on Nea Kameni and that it was possible to forecast both the size and duration of future dome-forming eruptions, based on the relationship between eruption length and the time interval between consecutive eruptions (pre-eruption interval).

The LiDAR dataset acquired in 2004 was typically of high quality, comprising 4.52 million LiDAR measurements acquired over an area of ~ 8 km^2 (Pyle & Elliott, 2006). Unfortunately a section of data was missing from the central part of Nea Kameni, due to absorption from low lying cloud. The LiDAR survey was repeated in May 2012, shortly after a period of volcanic unrest from January 2011 to April 2012 characterised by caldera-wide inflation and increased seismicity (Newman et al., 2012; Parks et al., 2012; Foumelis et al., 2013, Chapters 3-4). This time weather conditions were more favourable and full LiDAR coverage was achieved.

This current study expands on this previous work by combining the new 2012 LiDAR dataset with a high-resolution multi-beam bathymetry grid. This merged dataset provides complete coverage of the historic lava flows, enabling mapping of both the onshore and offshore extents extruded in the vicinity of the Kameni islands since 46 AD (Table 5.1). The updated lava flow outlines are used to generate revised estimates of the lava volumes for each of the historic flows, including previously unidentified submarine flows and cones. This allows a new analysis regarding the relationship between eruption volume and pre-eruption interval that may be used to forecast the size and duration of future dome-forming events at Santorini.

Table 5.1: *Characteristics and historical accounts of dome-forming eruptions in the vicinity of the Kameni islands (after Nomikou et al., in prep).*[11]

Eruption	Location	*Eruptive characteristics and historical accounts
AD 1950	Nea Kameni	Extrusion of small lava dome (Liatsikas) preceded by phreatic explosions. The eruption lasted for less than one month.
AD 1939-1941	Nea Kameni	Extrusion of lava domes (Triton, Ktenas, Fouqué, Smith-Reck and Niki) and flows, summit crater explosions and ash plumes. Phreatic explosions typically preceded episodes of lava extrusion. A rise in sea temperature in the bay of Agios Georgios, was observed ~ 3 months prior to the eruption.
AD 1925-1928	Nea Kameni	Extrusion of lava domes (Daphne and Nautilus) and flows, summit crater explosions, and ash plumes. Growth of Nea Kameni to the north and east of the island filling the bay between Mikri Kameni and Nea Kameni. The start of the eruption (Aug 1925) was marked by vapour fountaining and a rise in sea temperature in the red bay (Kokkina Nera) on the eastern shore of Nea Kameni, combined with subsidence along the eastern coast and the extrusion of the Daphne lava dome. Explosive activity culminated in a phreatomagmatic column up to 3.3 km high. A pause in activity between May 1926 and Jan 1928 was followed by a series of phreatic explosions and the formation of the Nautilus lava dome.
AD 1866-1870	Nea Kameni	The largest historical eruption of the Kameni islands. The eruption commenced in late Jan/early Feb 1866. Fytikas et al., (1990) report that there were 'increases in seawater temperature, and some subsidence of the shores in Vulkano bay. The first lavas were slowly extruded, and the first explosions followed two days later.' At the beginning Feb 1866 steam columns were observed and dark lava blocks rose to the surface of Vulkano bay. This site was named "Georgios". A second eruptive centre, called "Aphroessa" also formed to the south of Nea Kameni and in May 1866, 2 small islands appeared in the canal between Nea Kameni and Palea Kameni ("Maionisi", the May islands) but disappeared shortly thereafter.
AD 1707-1711	Nea Kameni (new burnt)	The first well-documented historical eruption of the Kameni islands. The eruption began in May 1707 with 'subterraneous fires, several violent earthquakes, a roaring noise, sulphurous exhalations and a black smoke' (Goree, 1707). Other reports include the formation of a white island to the west of Mikri Kameni which grew to ~ 70-80 m high and ~ 500-600 wide. Shortly after, a black island began to emerge and grow to the north of the white island. The black island and the white eventually merged in September 1707.
AD 1570 or 1573	Mikra Kameni (small burnt)	Extrusion of a small lava dome - Mikri Kameni.
AD 726	Palea Kameni	Explosive and effusive activity. The latter is responsible for lobe of blocky lava near Agios Nikolaos on the north-eastern side of Palea Kameni.
AD 46-47	Palea Kameni (old burnt)	Appearance of a new island south-west of Hiera (at the location of the present day Palea Kameni), with a circumference of approx. 5600 m.
199-197 BC	Hiera/Lera (the holy one)	The first documented appearance of a new island inside the caldera. Possibly Bankos reef (a small island ~ 2 km north-east Palea Kameni which was covered with lava during the 1925–1926 eruption).

---

[11] References: Goree, 1710; Tarillon, 1715a; Tarillon, 1715b; da Corogna, 1867; von Fritsch et al., 1867; Reiss & Stubel, 1868; Fouqué, 1879; Ktenas, 1926; Washington, 1926; Ktenas, 1927; Reck, 1936a; Reck, 1936b; Reck, 1936c; Georgalas, 1953; Fytikas et al., 1990; Pyle & Elliott, 2006.

5.2 Methods

Onshore LiDAR data was acquired over the central volcanic islands of Nea Kameni and Palea Kameni on the 16th May 2012 by the UK's Airborne Research and Survey Facility's (ARSF) Dornier 228 aircraft. The aircraft was equipped with a Leica ALS50 Airborne Laser Scanner, AISA Eagle and Hawk hyperspectral instruments, a Daedalus 1268 Airborne Thematic Mapper (ATM) and a Leica RCD105 39 megapixel digital camera. Two stand-alone georeferencing systems (the Applanix PosAV system and the Leica IPAS20 Navigation system) recorded position measurements at both the sensor and the aircraft frame. The measurements were combined with ground control measurements from two local continuous GPS stations (MKMN and DSLN) to obtain accurate aircraft position measurements.

The survey comprised 12 north-south flightlines acquired in Single Pulse in the Air (SPiA) mode, at an altitude of ~ 1100 m and average speed of 135 knots. An additional SW-NE flightline was acquired at an altitude of ~ 2000 m and speed of 143 knots, using high resolution Multiple Pulse in the Air (MPiA) (e.g. Roth and Thompson, 2008) LiDAR (Figure 5.1). The SPiA LiDAR was acquired using a pulse repetition frequency (PRF) of 94.7 KHz and scan frequency of 58.2 Hz. The MPiA flightline was acquired using a PRF of 119 KHz and scan frequency of 55.7 Hz. The final dataset comprised > 40 million point measurements and provided an average point density of ~ 5 points per m^2.

Following the application of a point cloud filter to remove noisy data points, we generated a new digital elevation model (DEM) from the 2012 LiDAR dataset using gridding functionality available in Generic Mapping Tools (GMT) software. To minimise the roll-boresight error (e.g., Toth, 2002; Glennie, 2007) and the potential for acquisition artefacts in overlapping regions between adjacent flightlines, the point cloud data was resampled and filtered prior to gridding. The data points were then interpolated to a 2-m grid using a continuous curvature surface gridding algorithm.

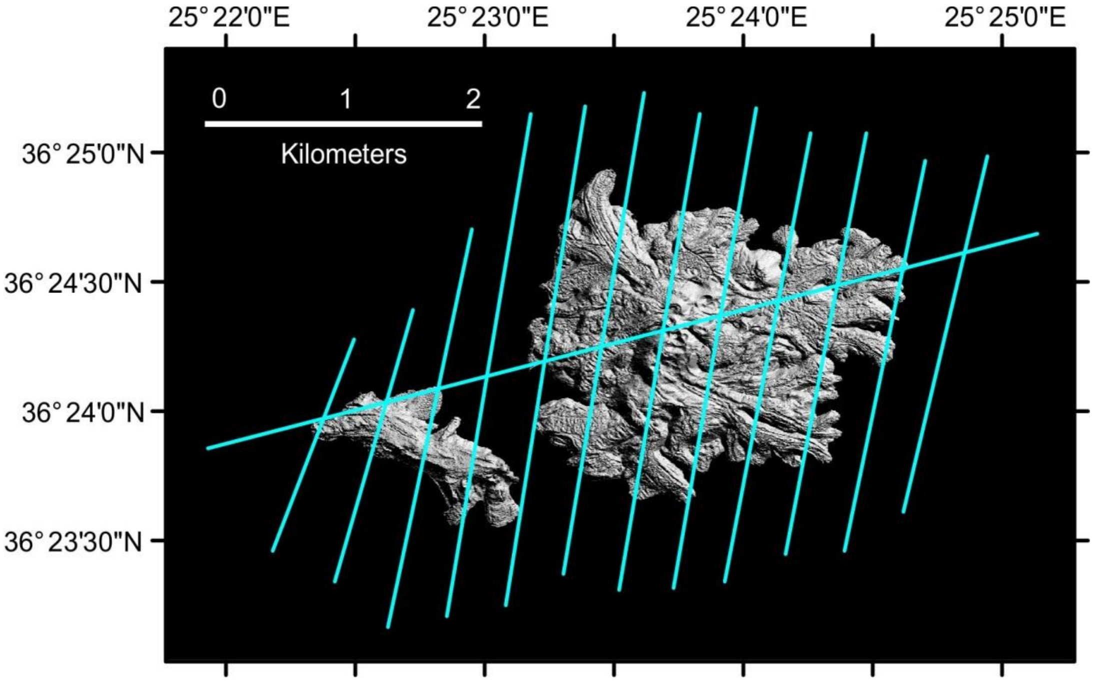

Figure. 5.1. *Hillshade attribute map generated from the 2 m resolution 2012 LiDAR digital elevation model displaying morphological features of historic lava flows and domes on the Kameni islands. The flightlines are displayed as blue lines.*

Multibeam bathymetric surveys were carried out by the Hellenic Centre for Marine Research (HCMR), during two successive cruises (on R/V AEGAEO) conducted in 2001 and 2006. The surveys utilised SEABEAM 2120 (http://www.hcmr.gr/gr/listview3.php?id=454); a 20 kHz, hull-mounted swath system, suitable for operation in water depths not exceeding 6000 m. The SEABEAM 2120 system provides an angular coverage of 150° with 149 beams, covering a swath width from 7.5 to 11.5 times the water depth for depths between 20 m to 5 km. The maximum swath coverage can reach 9 km at maximum depth and produces satisfactory data quality at speeds up to 11 knots. GPS navigation (Trimble 4000) provides the average position of the ship to within ±10 m. The multibeam data processing was undertaken by staff at the University of Athens. This included georeferencing using navigation data, removal of erroneous beams, noise filtering and interpolation of missing data (e.g., Caress et al. 2008).

The 5-m resolution multibeam dataset was merged with the new digital elevation model (DEM) to provide a detailed onshore-offshore grid, enabling the first joint mapping of both subaerial and submarine historic lava flows emplaced in the centre of the Santorini caldera since 46 AD. High-resolution merged LiDAR-Bathymetry grids have been utilised at other volcanoes for improved geomorphological analysis of volcanic deposits and to facilitate hazard mapping (Massimo et al., 2010; Riguzzi et al., 2008). In the current study, a series of attribute maps were used to aid the delineation of the extent of flows (both onshore and offshore). These included hillshade, curvature, relief and slope attributes generated using ArcMAP software. The revised lava flow outlines were then used to compute accurate volumetric estimates for each of the historic flows.

Volumes were estimated using two approaches. Firstly, volumetric calculations were carried out using Surfer software to determine the residual volume between consecutive grid files, representing the post-eruption and the pre-eruption surfaces. This is done sequentially in the reverse chronological order to which the flows were originally emplaced. For example the first post-eruption surface is defined by the present day grid of the Kameni islands. The first pre-eruption surface is the simulated topography prior to the most recent eruption in 1950. This is generated by stripping off the region within the outline of the 1950 lava flow and creating a new surface by interpolating the data gap using a Natural Neighbour Gridding Method. This method produces a smooth surface, simulating the relief prior to emplacement of the lava flow and is repeated for each of the historic flows so that the simulated pre-eruption grid becomes the post-eruption grid for the earlier lava flow. The volumes for the individual flows were generated by subtracting the hypothesised pre-eruption surfaces from the post-eruption surfaces. A similar DEM subtraction technique was employed by Coltelli et al. (2007) and Neri et al. (2008) to determine lava flow volumes for historic eruptions at Mt Etna.

To gain a better understanding of the errors associated with the volume estimates, a second method was employed using GMT software. In this instance polygons outlining the flows from each historic eruption were again used to mask out the target flow from the DEM. This time the gap in the data was interpolated using a continuous curvature surface with variable tension producing a near-flat pre-eruption surface across the masked region. In general we found that a tension of 0.9 was optimal with the exception of the 1950 flow where a tension of 0.2 was used. The DEM subtraction technique was used to compute the residual volume between the new pre- and post-eruption surfaces, providing a second set of volumetric estimates for each of the historic lava flows.

Graphs of pre-eruption interval against volume of extruded lava and eruption duration were created to determine the relationship between these eruptive properties. Finally a series of profiles were extracted from the DEM to determine flow levée width, flow height and flow width for the offshore segment of the 1570 lava flow and estimates of yield strength were derived, assuming a Bingham rheology and using the flow width method (Hulme 1974; Hulme and Fielder, 1977).

5.3 Results and Discussion

5.3.1 Mapping of historic lava flows

Figures 5.2 and 5.3 display a series of attribute maps generated from the merged grid, which assisted in mapping the extent of the submarine and subaerial historic lava flows extruded in the centre of the caldera. These flow outlines were used to calculate revised volumetric estimates for each of the flows and generate graphs of pre-eruption interval against the volume of extruded lava and eruption duration.

Minimum and maximum polygons were constructed for several of the flows (46-47, 726, 1707-1711 and 1866-1870), for which there was some uncertainty in the actual extent. For the 46-47, 726, 1707-1711 and 1866-1870 flows the solid line in Figure 5.3 represents the minimum extent and the dashed line the maximum extent. These multiple flow outlines were used in the volumetric calculations to provide a range of estimates.

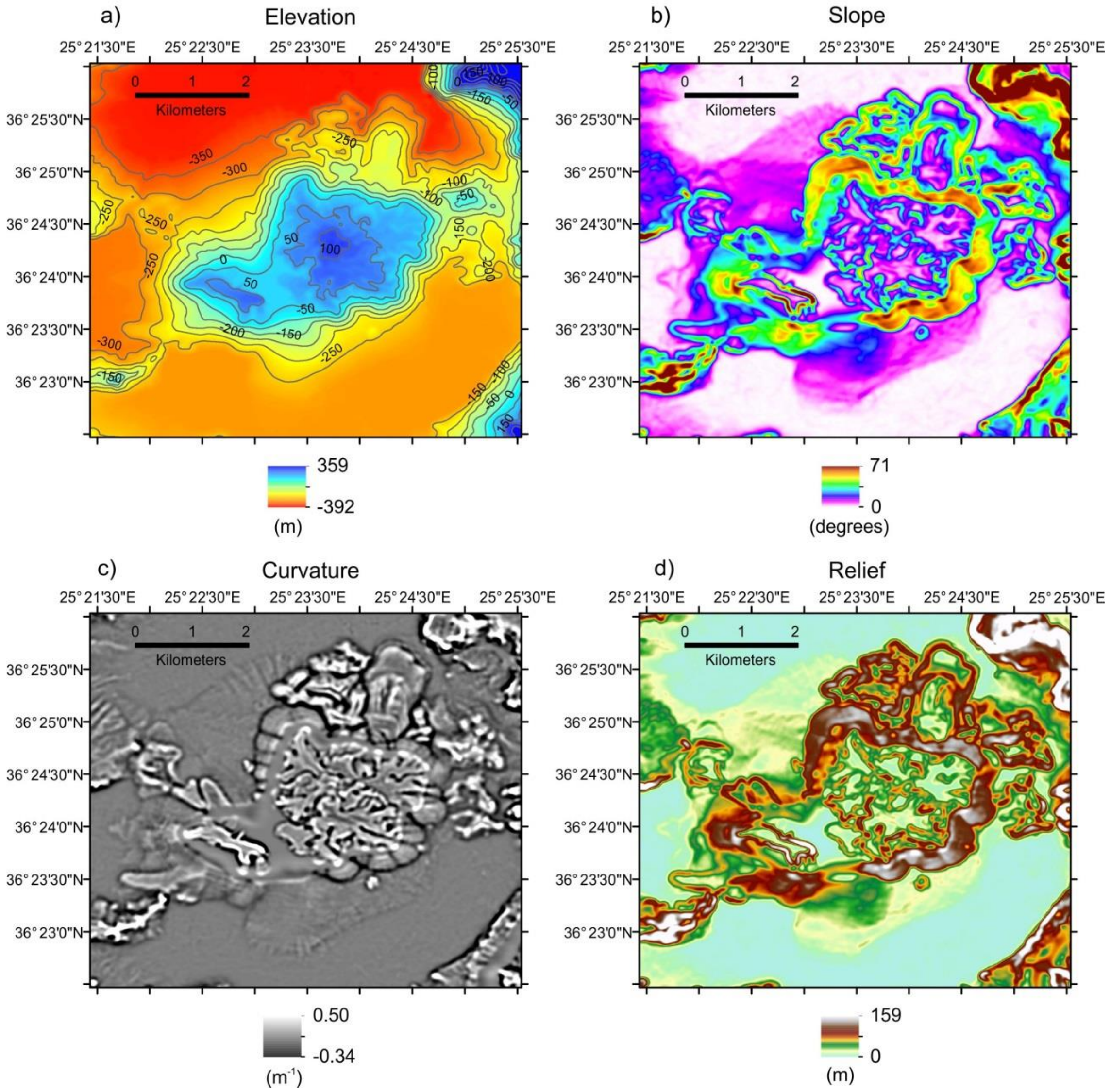

Figure. 5.2. *Elevation and attribute maps.* ***(a)*** *5 m resolution merged onshore/offshore digital elevation model with 50 m contours.* ***(b)*** *Slope attribute, generated using the 5 m merged DEM as the input and calculating the maximum rate of change between adjacent cells.* ***(c)*** *Curvature attribute, generated by calculating the second derivative of the 5 m DEM* ***(d)*** *Relief attribute, also generated using the 5 m DEM as the input and calculating the range of the cells within a given neighbourhood.*

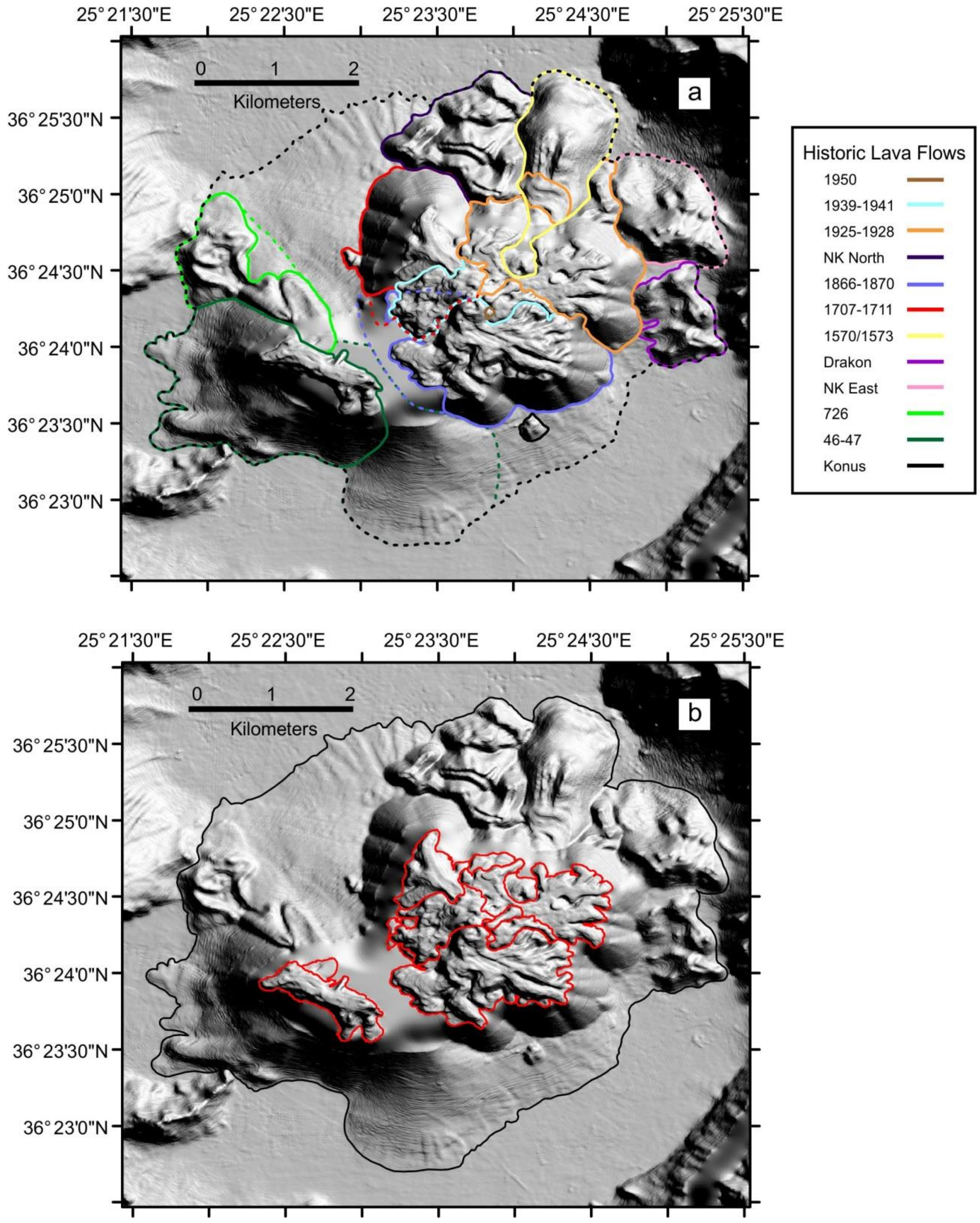

Figure. 5.3. *Lava flow outlines for historic lava flows in the vicinity of the Kameni islands.* ***(a)*** *New onshore/offshore lava flow outlines, mapped as part of this study. For the 46-47, 726, 1707-1711 and 1866-1870 flows the solid lines represents the minimum extent of the flows and the dashed line the possible maximum extent. The maximum extent of submarine talus deposits is shown by the black dashed line.* ***(b)*** *Onshore lava flows mapped by Pyle & Elliott (2006) (red contours). The black contour represents the maximum extent of submarine talus deposits mapped during the current study.*

5.3.2 Flow identification, morphologies and yield strength

The new dataset provides a wealth of information, including previously unidentified submarine lava flows and cones, as well as some interesting submarine morphologies. The historic flows emplaced on Nea Kameni since 1570/1573 are classified as blocky lava flows. These flows are characterised by a broken fractured crust, comprising smooth angular blocks of dm- to m-scale. The flows are typically tens of metres thick and several kilometres long. Blocky lava flows tend to advance as single units, forming channels and occasional lava tubes (Kilburn and Lopes, 1991). These in turn feed the advancing lava front, which crumbles to produce a snout and may trigger small pyroclastic flows. The advance of the flow does not stop until the eruption ends. Overflow or intrusive levées may develop along the edges of channels as the crust along the channel margin begins to cool and solidify. An example of this may be seen in the medial section of the 1570/1573 submarine flow and also in a flow situated offshore, north of Nea Kameni (NK North) (Figures 5.3). An archetypal example of a single feeder channel is visible in the centre of the 1707-1711 lava flow, on the north-west edge of Nea Kameni (see Figures 5.3 & 5.5 (a)). Flow breaching is less common in blocky lava flows. However, examples are clearly visible within both the offshore NK north lava flows and the onshore 1707-1711 lava flow (Figure 5.3).

Figure 5.4 displays a series of elevation profiles across each of the historic lava flows. Of particular interest is the submarine extension of the 1570/1573 flow, the NK East and Drakon flows to the east of Nea Kameni and a newly identified submarine flow NK North. The new flow was initially interpreted as an extension of the onshore 1925-1928 lavas. However, following the analysis of elevation, slope and hillshade attributes (Figures 5.2 and 5.3) along with volumetric calculations and historic reports, we suggest that this flow was extruded during an unreported submarine eruption.

Analysis of flow morphologies suggests this extrusion occurred sometime after the 1707-1711 eruptions, but prior to the 1925-1928 eruption. The internal structure of the NK North flow indicates flow paths were determined by the pre-existing 1707-1711 and an obvious break in slope is visible on both the hillshade attribute and the north-south oriented traverses that transect both the NK North and 1925-1928 flows (Figures 5.6 (a) and 5.6 (e)). This break in slope appears at the edge of submarine talus deposits eroded off the 1925-1928 flows, which were identified during a research cruise in September 2011 (Nomikou et al., 2012a). In addition the general morphology of the flow also changes significantly after this break in slope and is more similar to that observed at the Drakon lava flows, exhibiting submarine twin cone structures and intervening ridges. This morphology appears to be characteristic of submarine extrusions/eruptions; being identified on bathymetry grids at El Hierro, Canary islands (Rivera et al., 2013) and in the Marianas Arc (Bloomer et al., 1989).

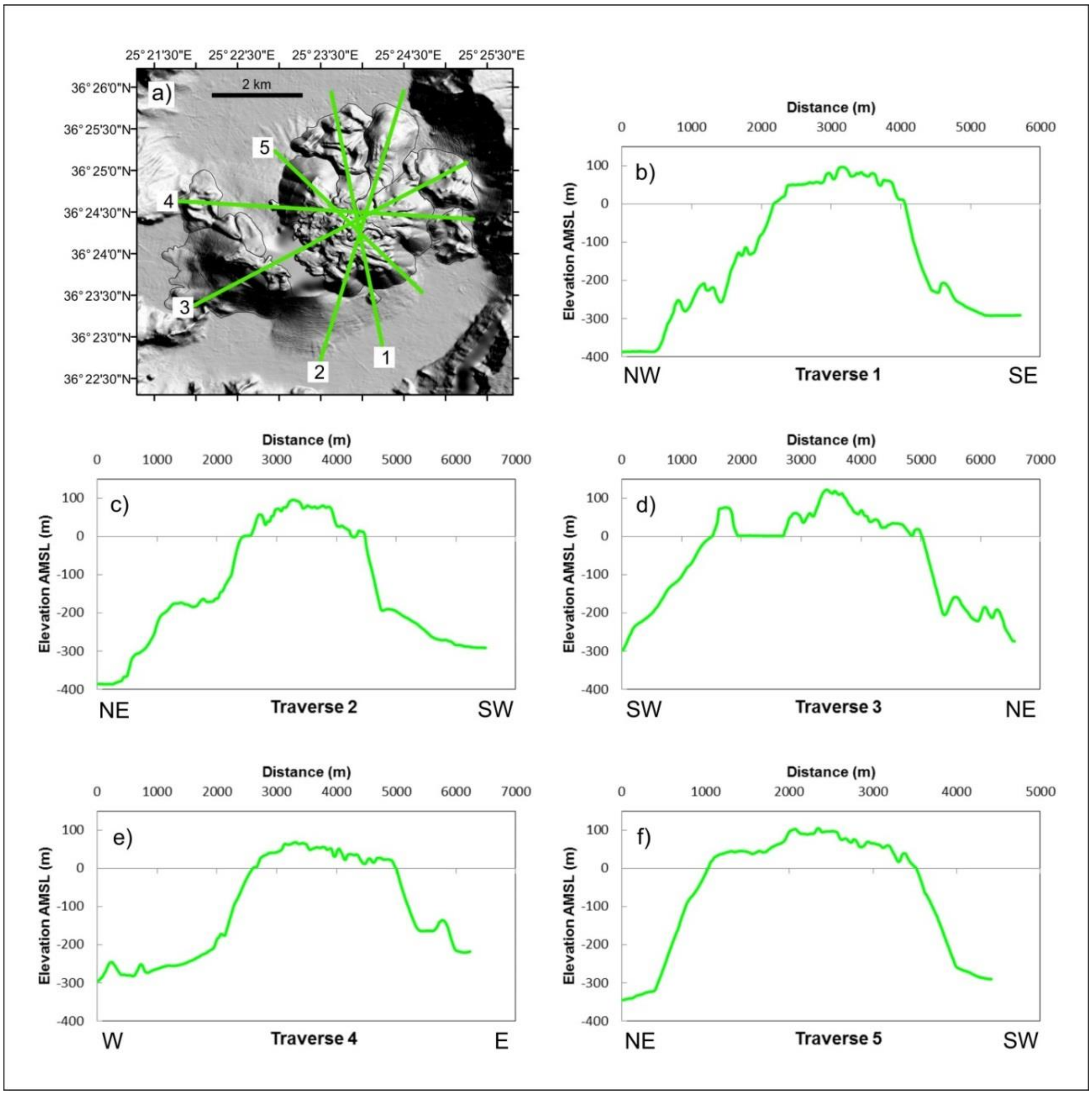

Figure 5.4. *Elevation profiles across historic lava flows extruded since 46 AD.* ***(a)*** *5 m resolution merged onshore/offshore digital elevation model.* ***(b-f)*** *Traverses across the historic submarine and subaerial lava flows extruded in the vicinity of the Kameni islands since 46 AD.*

To enable comparison of yield strength estimates for onshore lava flows (computed by Pyle & Elliott, 2006) with those of offshore lava flows, yield strengths were calculated for the submarine 1570/1573 lava lobe using flow widths and heights extracted from a series of transverse profiles displayed in Figure 5.5. The 1570/1573 was determined to be the most suitable submarine flow for this calculation due to its characteristic lava lobe morphology.

The flow width method (Hulme 1974; Hulme and Fielder, 1977) was used for this analysis, as it is considered more reliable than the levée width or levée height methods (Sparks et al., 1976; Pyle & Elliott, 2006), based on the larger uncertainties associated with the latter techniques in estimating the flow slope (at the time of emplacement) and the levée width. For a lava flow of width W, the yield strength Y, may be calculated using equation 5.1:

$$Y = \frac{\rho g h^2}{W} \tag{5.1}$$

where ρ is the bulk density of the lava flow (taken as 2700 kg m^{-3} for dacite, for direct comparison with yield strengths from Pyle & Elliott, 2006), h is the height of the lava flow and g is the gravitational acceleration.

The yield strength estimates are displayed in Table 5.2. The submarine lava flow displays an average width of 719 m, height of 74 m and yield strength of $(208 \pm 103) \times 10^3$ Pa. This is approximately 3-4 times greater than estimates reported by Pyle & Elliott (2006) (Table 3, Pyle & Elliott, 2006) for onshore lava flows on Nea Kameni using the same technique, but still within the range of yield strength estimates derived from dacitic lava flows at other volcanoes (10^4-10^6 Pa) (Wadge & Lopes, 1991). To our knowledge this is the first documented yield strength estimate for submarine lava flows. The increase in yield strength may reflect the transition from subaerial to submarine emplacement and is likely associated with increased cooling and crystallisation of the outer margins of the flow (Hulme, 1974; Marsh, 1981; Murase et al, 1985).

Table 5.2: *Yield strength estimates for the 1570/1573 submarine dacite lava flow.*

	Flow height (m)	**Flow width (m)**	**Aspect ratio (flow height/flow width)**	**Yield strength ($\times 10^3$ Pa) (Flow width method)**
Traverse 1	82	795	0.103	224
Traverse 2	106	821	0.129	362
Traverse 3	71	670	0.106	199
Traverse 4	67	671	0.100	177
Traverse 5	43	640	0.067	77
Average	**74**	**719**	**0.101**	**208**

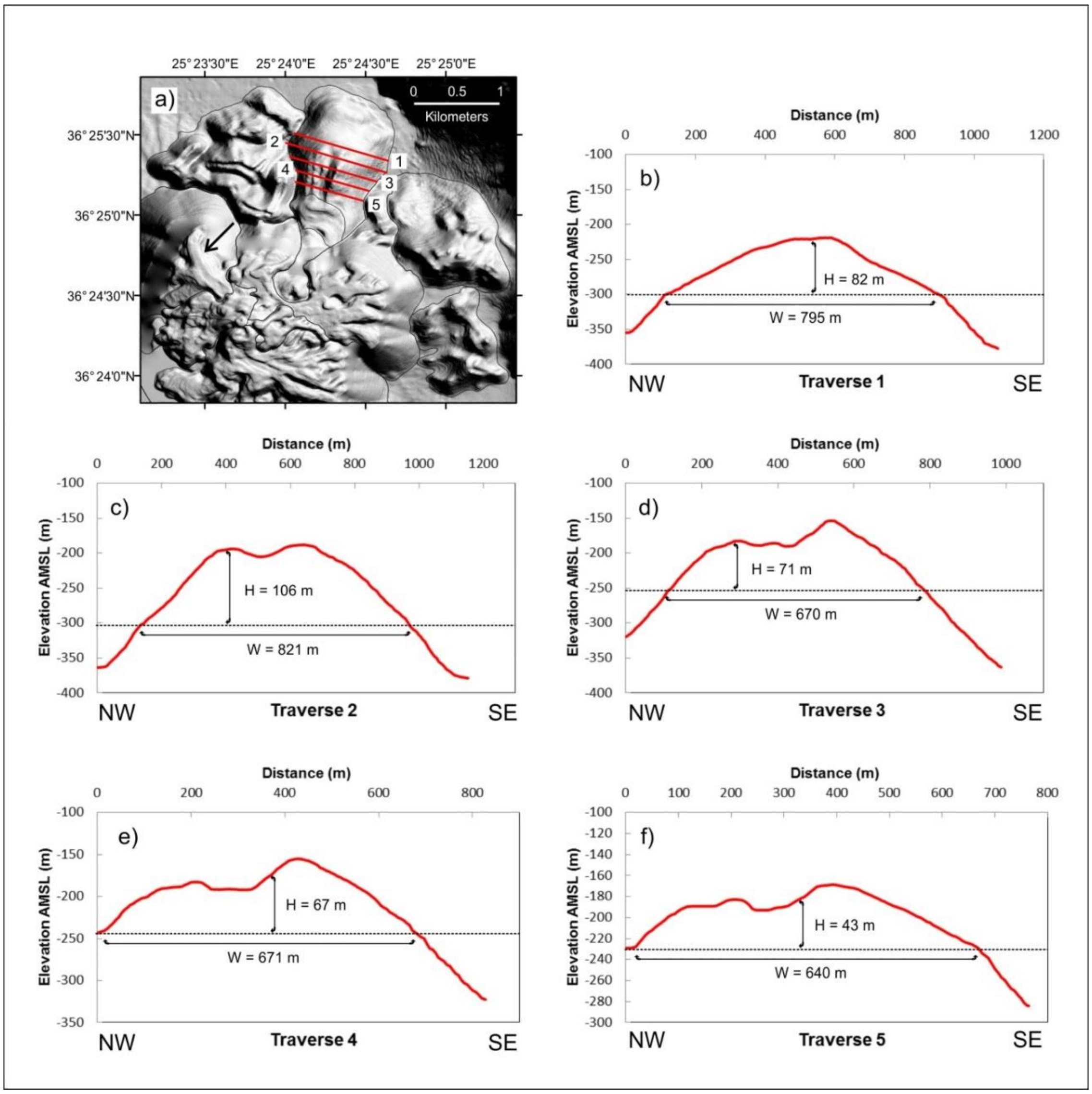

Figure 5.5. *Elevation profiles across the submarine 1570/1573 lava lobe.* ***(a)*** *5 m resolution merged onshore/offshore digital elevation model. The arrow displays the location of the 1707-1711 feeder channel referred to in in text.* ***(b-f)*** *Traverses across the historic submarine and subaerial lava flows extruded in the vicinity of the Kameni islands since 46 AD.*

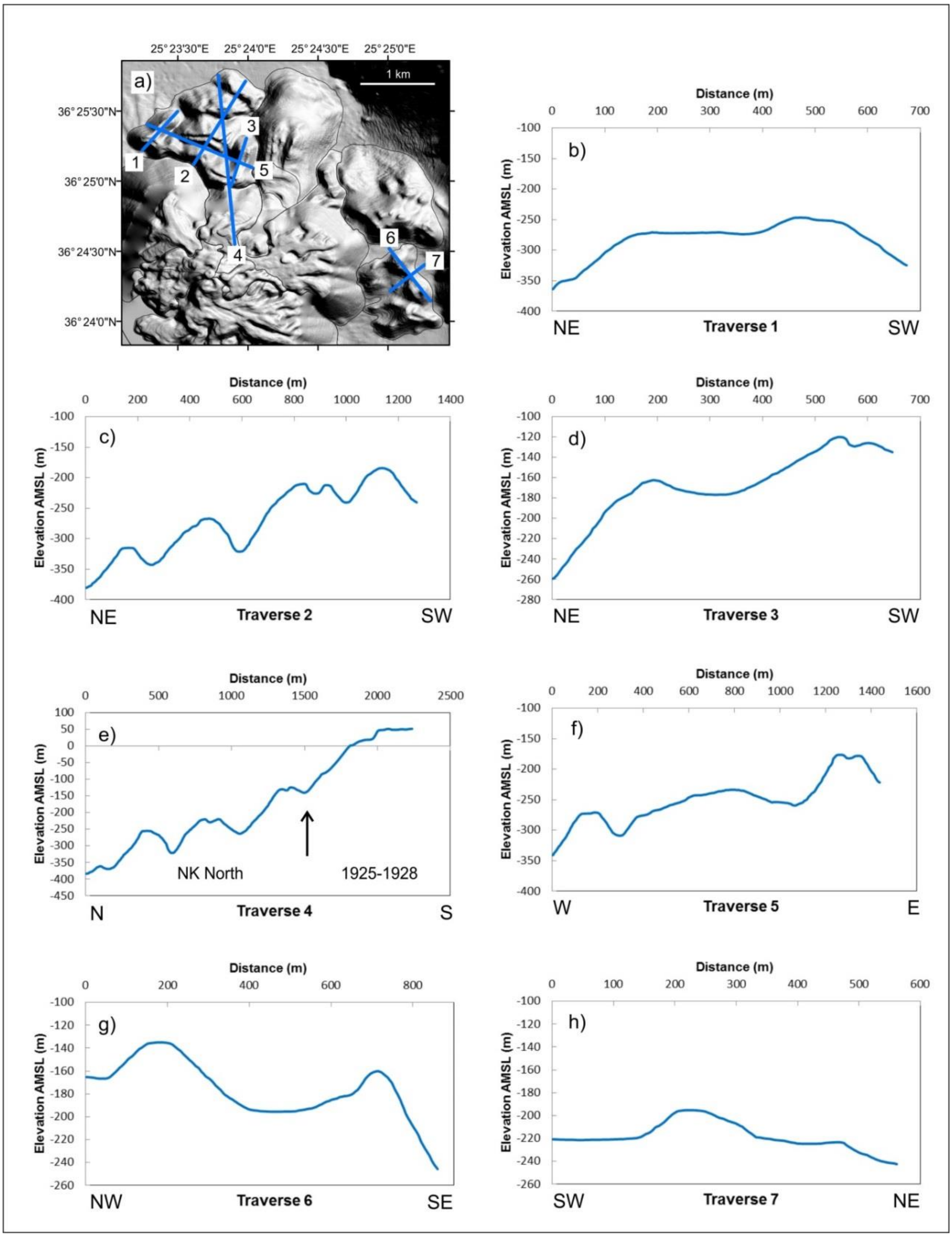

__Figure 5.6.__ Elevation profiles across the NK North, 1707-1711 and Drakon lava flows. __(a)__ 5 m resolution merged onshore/offshore digital elevation model. __(b-f)__ Traverses across the NK North (north of Nea Kameni) and 1707-1711 lava flows. The arrow in (e) marks the boundary between the NK North and 1925-1928 lava flows. __(g-h)__ Traverses across the Drakon (east of Nea Kameni) submarine lava flow.

5.3.3 Volumetric estimates and rates of lava effusion

Table 5.3 summarises the revised volumetric estimates for each of the historic lava flows (onshore and offshore) in the vicinity of the Kameni islands. This includes estimates for two separate offshore flows east of Nea Kameni (NK East and Drakon), one north of Nea Kameni (NK North) and a small cone identified offshore, south of the 1866-1870 flow (Konus). Table 5.4 displays revised lava effusion rate estimates for four historic eruptions on Nea Kameni. This analysis suggests an average effusion rate during 4 historic dome-forming eruptions on Nea Kameni (1939-1941, 1925-1928, 1866-1870 and 1707-1711) of ~ 2 m^3s^{-1}. This is almost twice the average rate derived from the onshore data alone (Pyle & Elliot, 2006).

Figure. 5.7 reveals a linear relationship between pre-eruption interval (the intervening period between eruptions) and the volume of lava extruded in historic dome-forming eruptions. This correlation allows estimation of the size of future eruptions on Nea Kameni – for example, if an eruption were to occur in the next few years the pre-eruption interval period would be ~ 75 years (time since the last significant eruption on Nea Kameni from 1939 to 1941). The volume of extruded lava would be in the order of 8×10^7 m^3 and the eruption would continue for approximately 3 years. Geodetic studies suggest that a melt volume of 10–20 × 10^6 m^3 has already been supplied to the shallow magma chamber during the recent (2011-2012) period of unrest (Newman et al., 2012; Parks et al., 2012; Chapter 4).

Table 5.3: *Volume estimates of historic lava flows extruded in the vicinity of the Kameni islands since 46 AD.*[12]

Eruption	**[a]Pre-eruption interval (yr)**	**Eruption length (days)**	**GMT minimum volume (km^3)**	**GMT maximum volume (km^3)**	**Surfer minimum volume (km^3)**	**Surfer maximum volume (km^3)**	**Average Volume (km^3)**
Konus	-	-	0.000667	0.000667	0.000633	0.000633	0.000650
1950	9	23	0.000014	0.000014	0.000004	0.000004	0.000009
1939-1941	11	682	0.010948	0.010948	0.010147	0.010147	0.010547
1925-1928	[b]55	949	0.092023	0.092023	0.072095	0.072095	0.082059
NK North	-	-	0.052522	0.052522	0.057313	0.057313	0.054917
1866-1870	155	1723	0.170032	0.244097	0.124684	0.139351	0.169541
1707-1711	137	1575	0.094230	0.149662	0.081138	0.113004	0.109508
1570	844	-	0.066521	0.067975	0.069479	0.069479	0.068364
Drakon	-	-	0.016029	0.016029	0.016853	0.016853	0.016441
NK East	-	-	0.047582	0.047582	0.041253	0.041253	0.044417
726	679	-	0.019135	0.021998	0.017175	0.023445	0.020438
46-47	-	-	0.134211	0.178033	0.100327	0.142690	0.138815
		Total	0.703915	0.881551	0.591098	0.686265	0.715707

---

[12] [a]The pre-eruption interval is the time between consecutive eruptions.

[b]This represents the interval between 1870 and 1925. It is possible the NK North lava flow was extruded during this time period, however the date of this extrusion is currently unknown.

Note: GMT volumes were computed by L. Kalnins (University of Oxford) and Surfer volumes by E. Simou (University of Athens). For comparison with earlier estimates by Pyle & Elliott (2006) derived from the subaerial flows, the reader is referred to Chapter 3, Table 3.1.

Table 5.4: *Effusion rate estimates.*[13]

Eruption	**Approximate flow duration (d)**	**Volume (km^3)**	**Minimum effusion rate ($m^3 s^{-1}$)**	**Maximum effusion rate ($m^3 s^{-1}$)**	**Averaged effusion rate ($m^3 s^{-1}$)**
1939-1941	147-282	0.010547	0.43	0.83	0.43
1925-1928	230-263	0.082059	3.61	4.13	3.61
1866-1870	690-1090	0.169541	1.80	2.84	1.80
1707-1711	300-600	0.109508	2.11	4.22	2.11
				Average	**1.99**

---

[13] Note: The anomalous 1950 eruption is interpreted as a minor extrusion of remnant magma, following the 1939–1942 activity (Pyle & Elliott, 2006), and has not been included in this calculation.

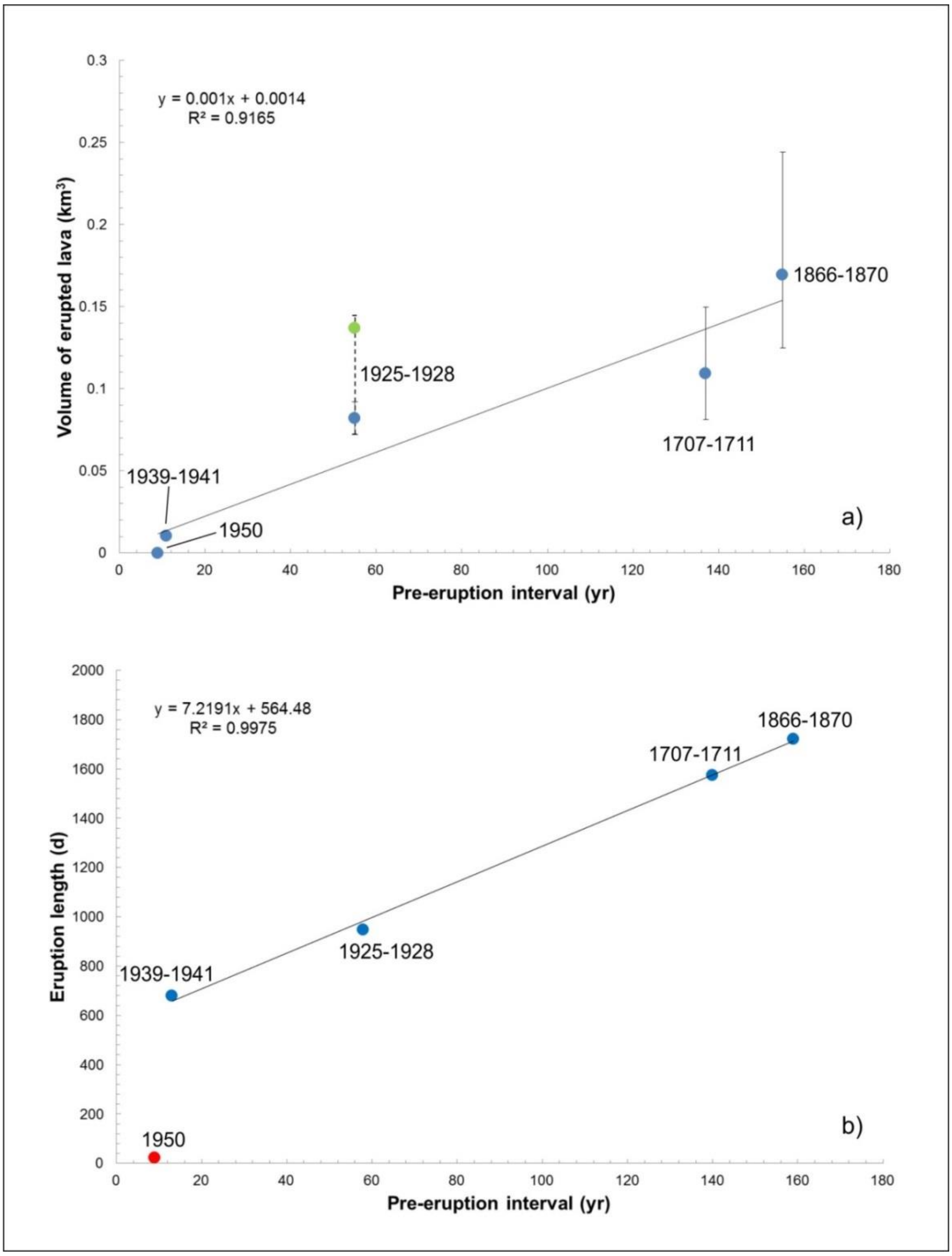

Figure 5.7. *Graphs of pre-eruption interval against volume of erupted lava and eruption length.* ***(a)*** *Relationship between volume of erupted lava and pre-eruption interval for the historic dome-forming eruptions on Nea Kameni. The green filled circle indicates the combined volume of the NK North and 1925-1928 lava flows (assuming both flows were extruded during 1925-1928). This data point was not incorporated in the linear regression. The associated blue point represents the volume of the 1925-1928 lava flow (as indicated in Figure 5.3), which was incorporated in the linear regression.* ***(b)*** *Relationship between eruption length and pre-eruption interval (after Pyle & Elliott, 2006). The red filled circle represents the 1950 eruption. As this eruption was anomalous and lasted less than one month this data point was not included in the linear regression.*

5.4 Conclusions

This study highlights the benefits of combining high-resolution LiDAR and multibeam bathymetry data to accurately map the subaerial and submarine extensions of lava flows at partially submerged island volcanoes. The new dataset reveals a wealth of information regarding the emplacement of historic lava flows and insight into bulk rheological properties of the magma. Several previously undetected submarine flows have been identified off the northern and eastern coasts of Nea Kameni. The ages of the NK East and Drakon flows are currently unknown, however the NK North flow appears to have been emplaced prior to the 1925-1928 lava flows but subsequent to the 1707-1711 lava flows. Yield strength estimates from the submarine 1570/1573 flow suggest at least a three-fold increase in lava strength upon entering the ocean.

Accurate volumetric estimates derived from the merged LiDAR-Bathymetry grid suggest an average lava extrusion rate ~ 2 m^3s^{-1} during historic eruptions on Nea Kameni, this is approximately two times faster than the initial estimate by Pyle & Elliott (2006) which was based solely on onshore data. The new volumetric estimates have allowed me to expand on the original work of Pyle and Elliott (2006), in terms of forecasting the characteristics of future eruptions at the Kameni Islands. I present a new relationship between the volume of erupted lava and the intervening period between eruptions. This will enable forecasting of the magnitude of new lava extrusions on the Kameni Islands at the onset of future dome-forming eruptions.

Chapter 6

Distinguishing contributions to diffuse CO_2 emissions in volcanic areas from magmatic degassing and thermal decarbonation using soil gas ^{222}Rn-δ^{13}C systematics: application to Santorini volcano, Greece

A version of this chapter has been published as: Parks et al. (2013). Distinguishing contributions to diffuse CO_2 emissions in volcanic areas from magmatic degassing and thermal decarbonation using soil gas ^{222}Rn-δ^{13}C systematics: application to Santorini volcano, Greece. *Earth and Planetary Science Letters*, 377-378, 180-190 (doi:10.1016/j.epsl.2013.06.046).[14]

http://www.sciencedirect.com/science/article/pii/S0012821X13003695

6.1 Introduction

Santorini is an active caldera system in the southern Aegean Volcanic Arc (Druitt et al., 1999; Vougioukalakis and Fytikas, 2005). The caldera lies close to an active normal fault system associated with the Santorini–Amorgos ridge. Historic volcanic centres in the region include the submarine Kolumbo volcano, 7 km north-east of Santorini

---

[14] Co-author contributions: I undertook all field measurements and data reduction, other than where indicated. S. Caliro determined the δ^{13}C values of the gas samples I collected, using a mass spectrometer

(Nomikou et al., 2012b; Nomikou et al., 2013), and the intra-caldera Kameni Islands (Figure 6.1) which have been the site of the most recent eruptions in the region. The Kameni islands are formed of dacite lavas and domes, and probably began forming as a submarine shield shortly after the Minoan eruption ~ 3600 years ago. The first reported eruption associated with the Kameni islands was in 199-197 BC; and there have been 10 effusive eruptions reported during the historical period (Pyle and Elliott, 2006), the most recent of which occurred at Nea Kameni in 1950. A major volcano-tectonic fault system, the Kameni line, intersects the Kameni islands. This has been a controlling factor in the location of historical eruption sites, with a progression of vent locations from SW to NE along the line (Fytikas et al., 1990; Druitt et al., 1999; Vougioukalakis and Fytikas, 2005; Pyle and Elliott, 2006).

---

at the Vesuvius Observatory. G. Chiodini and I undertook the graphical statistical analysis and sequential Gaussian simulation of the CO_2 soil gas measurements.

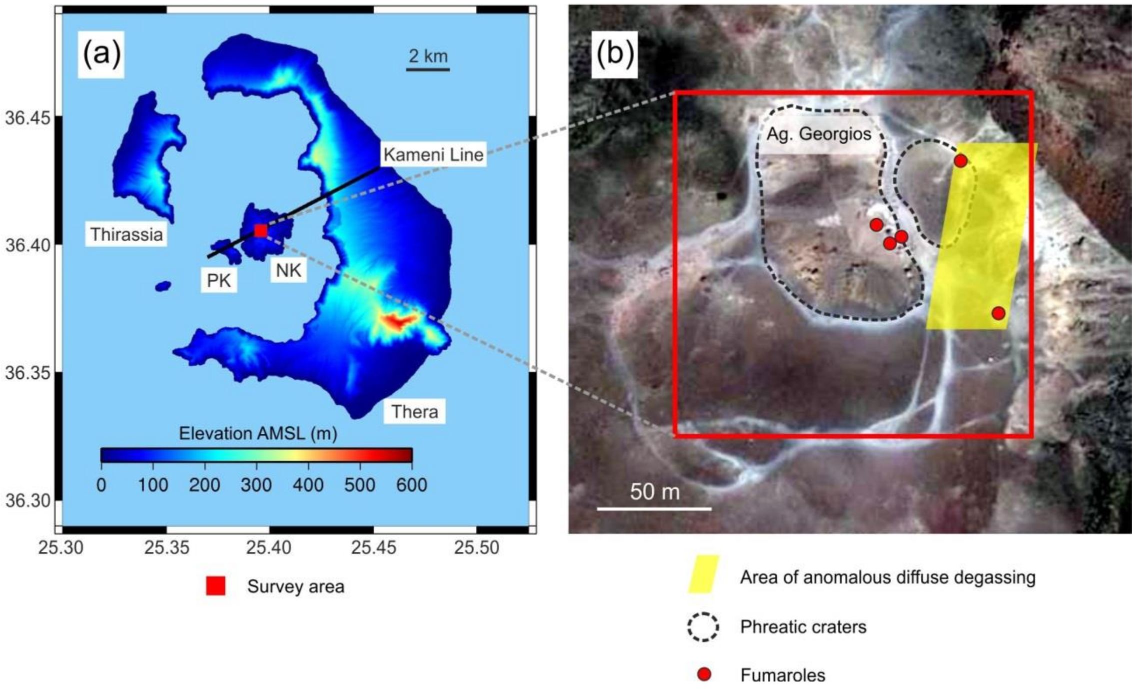

Figure 6.1. ***(a)*** *Elevation map of the islands of the Santorini volcanic centre (PK and NK denote Palaea and Nea Kameni). The Kameni line (solid black line) is an active volcano-tectonic fault/fracture zone, believed to influence vent locations of historic dome-building eruptions on Nea Kameni. The coordinates displayed on the axes are latitude and longitude, reported in decimal degrees.* ***(b)*** *Satellite image of the summit of Nea Kameni. The gas survey area on the summit of Nea Kameni is defined by the red box. Craters are displayed by black dashed circles and the area of elevated diffuse degassing (observed by Chiodini et al. (1998) and in this study) is displayed by the yellow box. Fumaroles NK1, 3, 4, 5 and 10 from Tassi et al. (2013) are marked as red dots.*

Surveys of the diffuse CO_2 flux from the ground have been made at numerous volcanoes to monitor flank emissions and to detect buried faults and fracture zones (Farrar et al., 1995; Chiodini et al., 1998, 2001; Hernandez et al., 2001; Rogie et al., 2001; Caliro et al., 2005; Giammanco et al., 2010). At Usu volcano, Japan, an increase in diffuse soil CO_2 flux from 120 to 340 t d^{-1} was detected on the summit caldera six months before the March 2000 eruption (Hernandez et al., 2001), and continuous soil-flux measurements on Stromboli (Italy) show promise as eruption precursors

(Inguaggiato et al., 2011). On Etna (Sicily), at Solfatara (Campi Flegrei, Italy) and at Lakki plain (Nisyros, Greece) buried faults have been mapped on the basis of detailed CO_2 flux surveys (e.g., Chiodini et al., 2001; Caliro et al., 2005; Bonforte et al., 2013).

In June 1994, Chiodini et al. (1998) carried out a CO_2 flux measurement campaign on Nea Kameni, using an accumulation chamber method. They discovered an anomalous zone of diffuse degassing on the summit of the volcano, in the vicinity of the craters (Figure 6.1b) and measured CO_2 effluxes as high as 6.6 kg m^{-2} d^{-1} with an estimated total CO_2 output of 15 t d^{-1} (over an area of 2.8 ha). Three further accumulation chamber surveys were performed by the same team at Nea Kameni in April, June and September 1995, and we use these previously unpublished data in the current study.

The aim of this study was initially to repeat these earlier surveys, to establish whether or not there were any significant temporal variations in CO_2 flux during a quiescent phase at Santorini volcano, and to use isotopic analysis of carbon to place constraints on the source of the outgassing CO_2. However in early 2011, geodetic monitoring at Santorini revealed an early stage of caldera-wide uplift (Newman et al., 2012; Parks et al., 2012), accompanied by an ongoing swarm of shallow earthquakes. Modelling of GPS and InSAR displacements from March 2011 - April 2012 suggests that the observed uplift corresponds to a volume change of ~ $1–2 \times 10^7$ m^3 due to a magmatic intrusion located slightly north of Nea Kameni, at a depth of ~ 4 km below the sea surface (Newman et al., 2012; Parks et al., 2012). The onset of a new phase of unrest, considered to be the first since the last eruptive activity in 1950 (Parks et al., 2012), offered an opportunity to observe how the soil-gas flux would respond. We completed further gas-measurement campaigns during 2011 and 2012, including a radon survey in September 2011, to help determine the origin of the outgassing. In a complementary study, Tassi et al. (2013) examined the response of fumarole compositions to this unrest.

Radon is a naturally occurring noble gas, produced in the decay chains of uranium and thorium. The isotope ^{222}Rn is commonly used in geochemical surveys – it is produced by the decay of ^{226}Ra and has a half-life of 3.8 days. Radon is volatile, and will readily partition into the gas phase during degassing. It is also soluble, and will dissolve in aqueous fluids. The volatile and short-lived nature of ^{222}Rn means that variations in ^{222}Rn activity can be used to map fluid flow along active faults and fractures in volcanic areas (e.g., Burton et al., 2004; Neri et al., 2011; Bonforte et al., 2013) and to detect changes in volcanic activity (e.g., Giammanco et al., 2007; Laiolo et al., 2012).

Here we present the results of 5 soil CO_2 surveys undertaken on Nea Kameni between September 2010 and January 2012, along with $\delta^{13}C$ isotopic analysis of CO_2 samples collected in April and September 2011, and ^{222}Rn measurements acquired during September 2011. We also include the previously unpublished results of 3 surveys performed by the Italian team at Nea Kameni in April, June and September 1995, and the results from a survey in June 1994 previously published by Chiodini et al. (1998) for comparison.

6.2 Materials and methods

We used the accumulation chamber technique (Chiodini et al., 1998) to measure CO_2 effluxes across the summit of Nea Kameni in 5 repeat surveys undertaken in September 2010, April 2011, July 2011, September 2011 and January 2012. The surveys were carried out using a portable CO_2 analyser (LI-COR LI-8100 automated soil CO_2 flux system), which consists of an inverted 10 cm accumulation chamber attached to an infrared gas analyser (IRGA). Gas diffuses from the soil into the base of the chamber, is pumped into the IRGA and circulated back into the chamber. The same equipment was used for each survey to ensure consistency between repeat measurements. To minimise lateral diffusion, soil collars were positioned in the ground prior to each measurement, and the accumulation chamber was placed on the soil collar for the duration of each measurement. Multiple measurements (typically 2 - 3) were made at approximately 100 site locations during each field campaign and the average flux at each site was used for geostatistical analysis. Difficulties were encountered in laying a regular grid due to logistical problems (e.g., terrain, soil properties and tourist trails). Nevertheless we endeavoured to perform CO_2 measurements at similar locations during each campaign and to cover approximately the same area. Similar surveys were performed by the Italian team at Nea Kameni in June 1994, April, June and September 1995 using a Draeger CO_2 IR sensor (Chiodini et al., 1998).

To constrain the origin of the CO_2, gas samples were collected during the April and September 2011 surveys for carbon isotopic analysis, using methods described in detail in Chiodini et al. (2008). A T-connector with a pierceable septum was inserted in the flowline between the IRGA and the accumulation chamber and 12 ml of gas was extracted using a syringe with a shut-off valve. The sample was injected into a 12 ml evacuated vial through a pierceable butyl rubber septum. The rate of carbon dioxide loss and associated carbon isotope fractionation is very low through the pierced rubber septum (Tu et al., 2001), and the collected samples were analyzed for carbon isotopic composition within a few days of sampling. The analysis was performed using a continuous flow isotope ratio mass spectrometer (Thermofinnigan Delta XP) interfaced with a Gasbench II device equipped with autosampler (GC-MS system), at the Geochemistry Laboratory of INGV-Osservatorio Vesuviano (Naples). The results are expressed in delta notation as per mil values (δ‰) relative to PDB (Pee Dee Belemnite) using an internal standard and are characterised by a $\delta^{13}C$ standard error ± 0.1‰. Isotopic data were compared with CO_2 concentrations measured in the field, within the accumulation chamber by means of the LI-COR detector at the moment of the sampling. The CO_2 concentrations in samples were also determined from the mass spectrometry data based on the peak areas of the mass 44-ion trace. Six standards with CO_2 concentrations ranging from 400 to 12,000 ppmv were injected in the GC-MS in the same manner as the samples. Plotting peak area of mass 44-ion versus concentration of CO_2 in these standards gives a good linear correlation ($r^2=0.999$, n=18), indicating that CO_2 concentrations of the samples could be quantified using this method. The relative standard uncertainty of the CO_2 concentration measurement in this study was better than ± 2%. In total, 192 and 164 samples were collected and analysed in April 2011 and September 2011 respectively.

The Graphical Statistical Analysis method (GSA) of Sinclair (1974) was used as described by Chiodini et al. (1998) to determine temporal variations in low and high-flux populations and investigate background and hydrothermal-volcanic sources of CO_2 active in the surveyed areas. This technique involves plotting log [CO_2 flux] against cumulative probability, and identifying inflection points within each dataset. These break points signify partitions between different statistical log-normal populations that may represent discrete sources of soil-CO_2. The mean and the standard deviation of each population were computed following the method of Chiodini et al. (1998).

Ninety TASTRAK radon detectors (TASL, 2011) were deployed during the September 2011 campaign to measure the distribution of ^{222}Rn activity at site locations corresponding to the soil CO_2 measurements. The radon detectors are cylindrical plastic containers (diameter ~ 5 cm) that encase a piece of alpha-particle sensitive plastic, TASTRAK PADC (TASL, 2011; Stejny and Portwood, 1986). The detectors were buried to a depth of ~ 10 cm, with the top of the detector facing upwards enabling the radon to diffuse from the soil into the container through a small gap in the base. ^{222}Rn decays by alpha decay, which produces a track on the internal plastic (referred to as latent tracks). The track analysis was undertaken by Radosure (TASL, 2011). This involved immersing the detectors in a sodium hydroxide solution to develop the tracks, which were then analysed with a microscope and image analysis system, which takes into account track shape and the depth of penetration (e.g., Fews and Henshaw, 1982; Yamauchi, 2003). Corrections were applied for the degradation of the plastic in the wet and warm (<100°C) conditions of the volcanic soil, and for track producing-short-lived daughter isotopes of ^{222}Rn (Radetco, 2005). The track detectors were deployed for between 4 to 8 days. The track density accumulated over this period was converted to a dose and divided by the length of deployment to arrive at a spatial distribution of ^{222}Rn soil activity. The reported detection limits of this system are between 5 Bq/m^3 and 15 MBq/m^3 with an accuracy of 3-6% over the studied range (http://www.tasl.co.uk/radon.php). Four detectors were kept in the original Rn-proof bag, but exposed to air when the bag was opened in order to take the other detectors out. These detectors provide a median background level of 44 Bq m^{-3}, with a lower quartile of 14 and an upper quartile of 78 Bq m^{-3}. The precision based upon the median relative standard deviation of the observed doses is 23 % (+13, -7).

Following the approach of Deutsch and Journel (1998), we used Sequential Gaussian Simulation (sGs) to map the CO_2 and ^{222}Rn flux distributions, and to determine the total CO_2 output over a common area for each soil gas survey (Cardellini et al., 2003). This allows us to compare datasets containing differing numbers of sample points (Table 6.1). The sGs method is a probabilistic approach to mapping the spatial variation of an attribute, which generates a series of equi-probabilistic realisations with similar statistical and spatial properties. The method, which is described in detail in Deutsch and Journel (1998) and Cardellini et al. (2003), allows one to (i) map the spatial distribution of CO_2 flux, (ii) compute the total output from the surveyed area and (iii) estimate the uncertainty on the total output. We performed 200 equi-probabilistic realisations for each data set. The total CO_2 output flux is computed for each realization by summing the product of the simulated value of each grid cell and the cell surface over all grid cells within a box representing a target area common to all surveys. The mean and the standard deviation of the 200 simulated values of total CO_2 output, computed for the 200 realisations, are assumed to be the characteristic values of the CO_2 release and of its uncertainty for each area, with uncertainties being in part dependent on the number of sample points (Cardellini et al., 2003). Although fluxes were only calculated based on the points inside a target area common between surveys, we visually present the mean values for grid cells over the full area sampled in each campaign in order to show the spatial patterns of the degassing as well as raw flux numbers. A comparison among different methods concluded that the sGs approach yields the most realistic representation of the spatial distribution of CO_2 flux (Lewicki et al., 2005).

6.3 Results and discussion

6.3.1 Analysis of bimodal CO_2 flux distributions

The nine soil gas surveys performed in the area of the craters covered zones of different dimensions. In order to compare their results, each data set has been restricted to the points that lie within the 1.96 ha area covered by all the surveys. Probability plots of log CO_2 flux for each data set display bimodal distributions given by the partial overlapping of a high flux population (A) and a low flux population (B) (Figure 6.2). The mean, the 90% confidence interval and the fraction of the two populations in each survey have been estimated by applying the GSA method as described by Chiodini et al. (1998) and are reported in Table 6.1. Figure 6.3 displays the temporal variation of the mean soil CO_2 fluxes for populations A and B between 1994 and 2012.

Table 6.1: *Estimated parameters of partitioned* CO_2 *flux populations in the 9 surveys (flux values in g* m^{-2} d^{-1}*; f = fraction of population; n.s.= number of samples; c.i. = confidence interval).*[15]

Date[a]	**n.s.**	***f* A**	***f* B**	**Mean flux of population A (90% c.i.)**[b]	**Mean flux of population B (90% c.i.)**[b]
June 1994	36	0.20	0.80	5000 (1600-11100)	32 (17-57)
April 1995	39	0.25	0.75	490 (290-770)	18 (10-33)
June 1995	27	0.40	0.60	800 (530-1160)	42 (13-100)
Sept. 1995	34	0.40	0.60	5100 (1900-10600)	28 (9-64)
Sept. 2010	31	0.50	0.50	5000 (1800-10800)	32 (10-75)
April 2011	86	0.45	0.55	4800 (3300-6800)	170 (72-360)
July 2011	78	0.52	0.48	3400 (2500-4500)	86 (41-165)
Sept. 2011	68	0.48	0.52	4700 (3200-6800)	210 (71-500)
Jan. 2012	71	0.46	0.54	6000 (3800-9100)	340 (150-690)

---

[15] [a]Soil CO_2 flux measurements made in June 1994 are presented in Chiodini et al. (1998); those from 1995 are unpublished results from INGV; the 5 campaigns carried out between September 2010 and January 2012 were undertaken by M. Parks and co-workers. Data from each of the surveys were reanalysed as part of this study and treated using the same GSA geostatistical approach.

[b]High and low flux populations (A and B respectively) were derived using the GSA geostatistical approach.

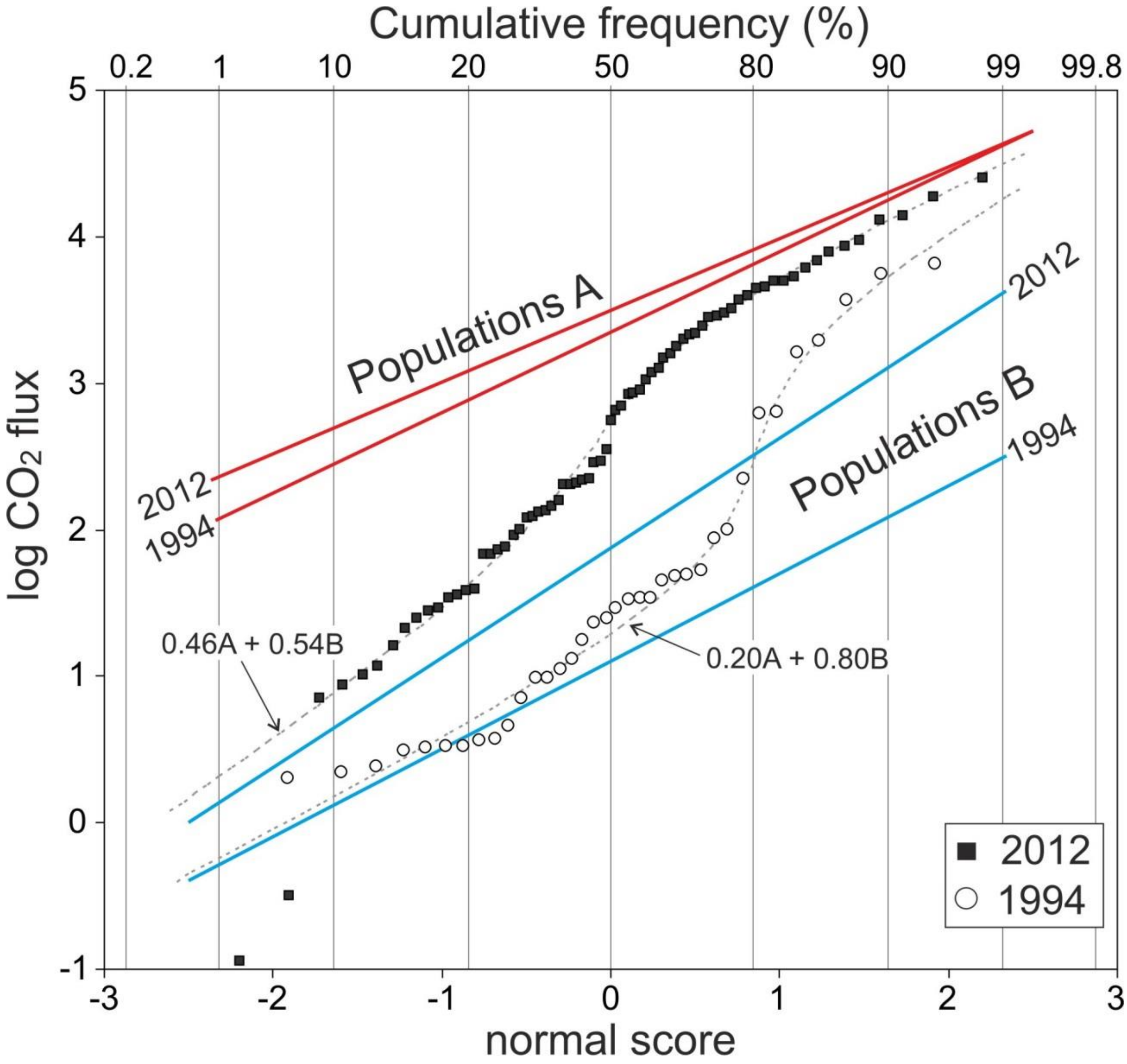

Figure 6.2. *Log probability plot of soil CO_2 fluxes. Open circles represent data from the Chiodini et al. (1998) June 1994 survey and black squares are data from the January 2012 survey. Solid lines represent flux distributions of populations A and B, derived using the GSA geostatistical approach. High flux populations (A) are displayed as red lines and low flux populations (B) as blue lines. The lowest values from 1994 should be treated with caution as they were close to the detection limit of the Draeger CO_2 IR sensor used. It is not possible to define the detection limit precisely, as it varies with factors including wind speed and soil type, but it is likely that some of the lowest flux measurements over estimate the actual values. Hence we do not interpret these lowest flux measurements in 1994 as a separate population.*

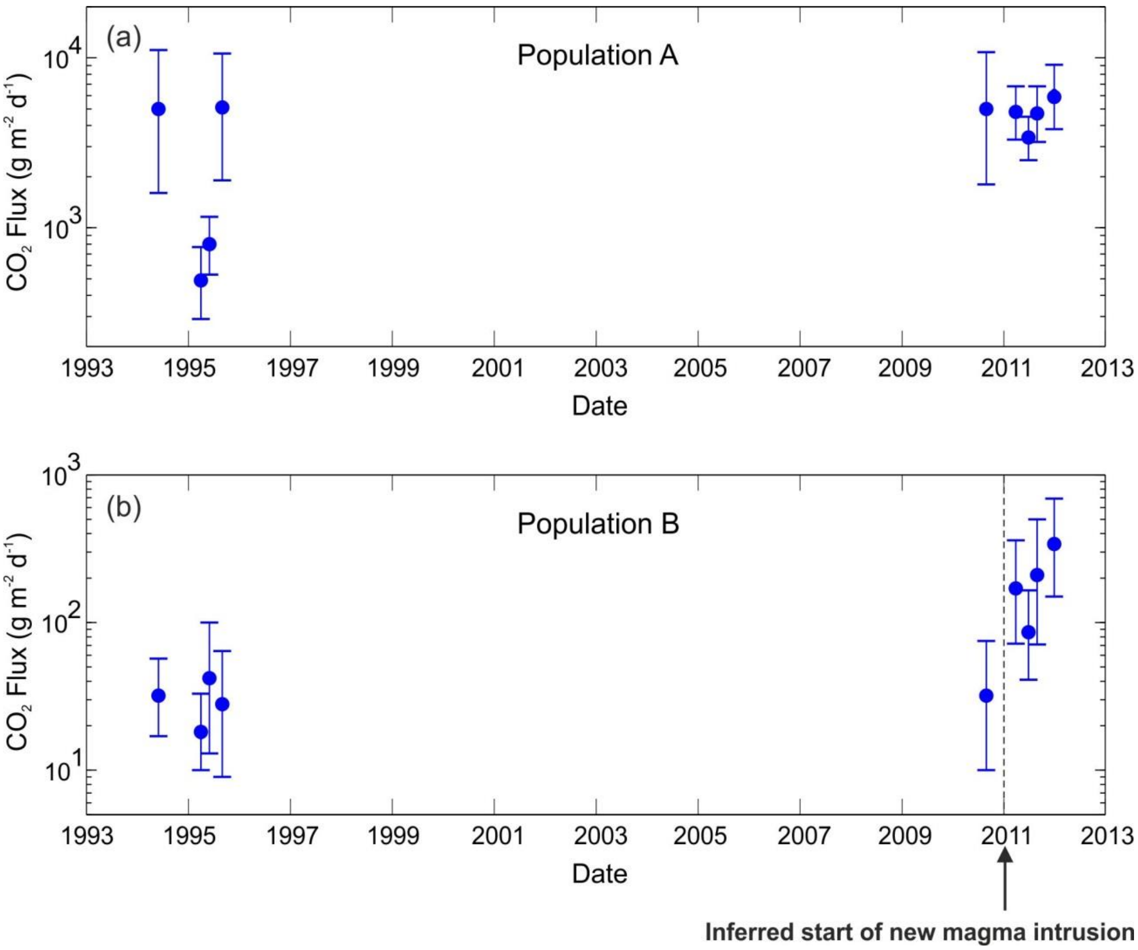

Figure 6.3. *The temporal variation of soil CO_2 fluxes for the high (A) and low (B) flux populations identified using the GSA geostatistical approach.* ***(a)*** *Mean and 90% confidence interval of the high flux populations for each of the nine surveys.* ***(b)*** *Mean and 90% confidence interval of the low flux populations for each of the nine surveys.*

As Table 6.1 shows, the fraction of the high CO_2 flux population A (*f*A) for the post-2010 surveys is systematically higher (0.45-0.52) than that of the 1994 to 1995 campaigns (0.20-0.40). Furthermore, a marked increase of up to an order of magnitude in the mean flux of the background population B is observed after the September 2010 survey (from 18-42 g m^{-2} d^{-1} during 1994-2010 to 86-340 g m^{-2} d^{-1} during the period 2011-2012). A bimodal distribution of CO_2 fluxes is typical for volcanic or hydrothermal areas, and explained by the presence of a deep source of gas (e.g., a volcanic-hydrothermal source sustaining high CO_2 flux at the surface), with a background source responsible for low CO_2-fluxes (e.g., biological activity in the soil; Chiodini et al., 1998; Chiodini et al., 2008; Giammanco et al., 2010). In this light, the increased fraction of fA could represent an increase in the degassing rate of the deep source during 2011-2012 compared to 1994-1995. This result must be treated with some caution as logistical constraints meant that sample grids were not exactly replicated between campaigns and, due to the seismic and geodetic unrest that started in January 2011, denser sampling was undertaken during the subsequent field campaigns. However, the increase of the mean background values (population B) observed in the 2011-2012 field campaigns is also consistent with an increase of the flux from the deep source after January 2011, infiltrating areas previously unaffected by deep gases, although not sufficiently to shift all sample points to population A. Tassi et al. (2013) identified significant changes in the H_2 content of fumarole emissions in the period from May 2011 to February 2012, which they interpreted as the consequence of a convective heat pulse from depth associated with a magma intrusion, or increased permeability of the volcanic plumbing system.

Comparing the GSA plots from 1994 and 2012 (Figure 6.2) suggests that variations in sampling density have not affected the definition of population B using this method. Further, Table 6.1 shows that the mean flux for population B observed for post-January 2011 surveys are up to an order of magnitude higher than those from pre-January 2011 surveys. Typical biogenic CO_2 fluxes from soils normally range from 0.2 to 20 g m^{-2} d^{-1}, and only rarely reach fluxes of 40–50 g m^{-2} d^{-1} in environments such as agricultural fields or grasslands (Chiodini et al., 2008 and references therein). The study area is largely unvegetated, with what vegetation there is mostly consisting of small shrubs such as curry plant (*Helichrysum italicum*) and tall grasses (*Hyparrhenia hirta*) (Raus, 1988). It is therefore unlikely that the higher flux values within population B, recorded in 2011-2012 (86-340 g m^{-2} d^{-1}) originate from increased biological activity, as they are much higher than reasonable maximum values from biological soil CO_2.

In summary, the degassing observed in 2011-2012 is distinct from that of 1994-1995 for two reasons: the higher fractions of the high flux population A, and the significantly larger mean values for the low flux population B. These differences are evident when comparing the probability plot of the first campaign (June 1994) with that of the last campaign (January 2012) (Figure 6.2).

6.3.2 Changes in the pattern of degassing

The post-2010 surveys were analysed with the sGs method to derive maps of CO_2 diffuse degassing (Figs. 4a-e) and to estimate the CO_2 output from the target area (with associated uncertainties). The earlier surveys (1994-1995) were not incorporated in this analysis as they covered a smaller area and may not be representative of the broader variation. Figure 6.4 shows that in January 2012 the area was affected by a change in the degassing pattern, with the data suggesting an increase in total CO_2 emissions, although this is difficult to resolve with the associated errors. Prior to January 2012, the total CO_2 output from the target area varied from 21 ± 4 to 29 ± 5 t d^{-1}, exhibiting a spatially-similar pattern of anomalous degassing in the region east of the Agios Georgios crater (Figure 6.1b and Figs. 6.4a-d). In contrast, the average flux map for the January 2012 survey displays anomalously high emissions over a much broader area (Figure 6.4e) extending to the north, south and west of the target region with a concomitant increase in the total CO_2 output to 38 ± 6 t d^{-1} (within the target area). Observed changes in the CO_2 degassing at the summit may be related to a swarm of earthquakes beneath the Kameni islands that occurred between the 23-25 January 2012, a few days before our sampling campaign. The estimated magnitudes of these volcano-tectonic (VT) events were between ML1 – ML3 with hypocenters located at depths between 3 and 12 km (NOA, 2001). It is therefore possible that the change in degassing could be the result of increased fracturing, providing new migration pathways for gas to reach the surface.

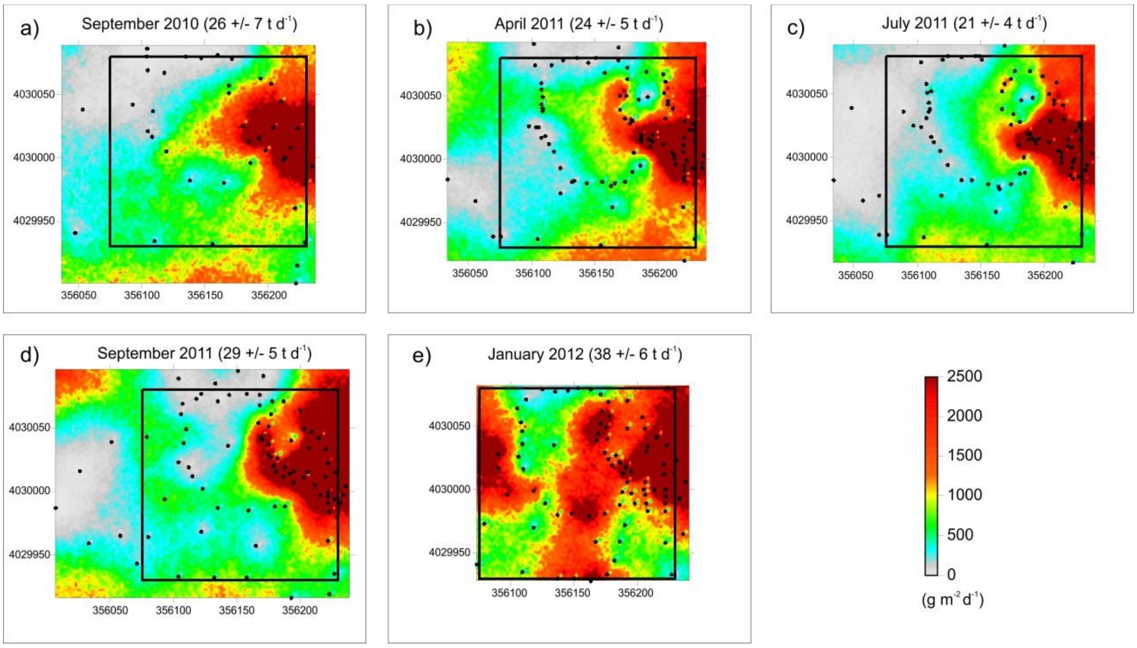

Figure 6.4. *Maps of the CO_2 flux distribution over the target area (see Figure 6.1b) on the summit of Nea Kameni, derived using the sGs approach. The five surveys were performed over areas of slightly different dimensions. To compare results, the total CO_2 output was computed within the bounding box (black box) common to all surveys. The total CO_2 output for each survey is reported above the individual figures (a-e) in tonnes day^{-1}. The coordinates displayed on the axes in figures a-e are UTM coordinates - zone 35N.*

6.3.3 The origin of the CO_2

Carbon isotope data from the April and September 2011 campaigns are presented in Figure 6.5. The measured soil gas $\delta^{13}C$ (CO_2) values span a large range, (-17‰ to 0‰), but there is a positive correlation between $\delta^{13}C$ and CO_2 concentration in the gas samples analysed (Figure 6.5). Data from the two campaigns both define a triangular field, which can be interpreted in terms of mixing between soil CO_2 (a mixture of biogenic and air-derived CO_2) and deep CO_2. This trend is characterised by a light endmember ($\delta^{13}C$ from -11‰ to -16‰) at low CO_2 concentrations (generally from 400 to 700 ppmv) and a heavier endmember ($\delta^{13}C$ close to 0‰) at high CO_2 concentrations (up to ~12,000 ppmv). The light endmember ($\delta^{13}C$ from -11‰ to -16‰) is a soil gas mixture of air contaminated by biogenic CO_2 (soil CO_2, Figure 6.5) (Tan, 1998; Chiodini et al., 2008). The heavy endmember, with $\delta^{13}C$ -0.2 ± 2.7‰, is approximately the same carbon isotopic composition as that measured in the fumaroles of Nea Kameni by Dotsika et al. (2009) and Tassi et al., (2013), representing a deeper source of CO_2 (deep CO_2, Figure 6.5). There are three possible scenarios for the origin of this deeper, higher concentration CO_2:

(a) Degassing of magma, including new magma intruded beneath the volcano since January 2011.

(b) Release of CO_2 via decarbonation of basement limestone, induced either by heating by, or reaction with, intruding magma.

(c) A combination of both of these processes.

In general, $\delta^{13}C$ values close to 0‰ are not typical for magmatic $CO_{2,}$ which is usually lighter (-4 to -8‰; Macpherson and Mattey, 1994 and references therein). Local variations in $\delta^{13}C$ values may be largely explained by variable degrees of degassing and crustal contamination during magma ascent and storage (Bottinga and Javoy, 1989; Javoy and Pineau, 1991; Macpherson and Mattey, 1994; Macpherson et al., 2010), however deviations from the ‘typical mantle’ values of -4 ‰ to -8 ‰ may also result from source heterogeneity, for example reflecting a slab contribution from subducted carbonate (Macpherson et al., 1999).

Volcanic CO_2 in the Mediterranean region tends to be characterised by relatively elevated $\delta^{13}C$ compositions (see Chiodini et al., 2011, Tassi et al., 2013, and Table 6.2). The similarities in $\delta^{13}C$ compositions from various Mediterranean volcanoes suggest that this is a regional rather than a local effect. Carbonate basement is found beneath each of the volcanoes listed in Table 6.2, so it is possible that their unusual CO_2 - $\delta^{13}C$ isotopic compositions result from a mixed magmatic-crustal limestone source (e.g., Tassi et al., 2013 and references therein) although contamination of the mantle at depth has also been suggested (e.g., Grassa et al., 2006 and references therein).

Table 6.2: *$\delta^{13}C$ isotopic signature of CO_2 samples collected from volcanoes in the Mediterranean region.*[16]

Volcano	**References**	**$\delta^{13}C_{CO_2}$ (‰)**	**Suggested origin**
Santorini (Nea Kameni)	Dotsika et al. (2009)	-0.68 to 0.14 (fumarolic gases)	Possible high magmatic contribution
Santorini (Nea and Palea Kameni)	Tassi et al. (2013)	-0.90 to 0.03 (fumaroles and submarine gases)	Mixed thermo-metamorphic and magmatic source
Nisyros	Brombach at al. (2003)	-4.1 to -0.4 (fumarolic gases)	Partial magmatic contribution
	Fiebig et al. (2004)	-1.6 to -0.9 (fumarolic gases)	Mixture of magmatic CO_2 and that derived from the thermal breakdown of carbonates or metasomatised mantle
Vesuvius	Fiebig et al. (2004)	-0.3 (fumarolic gases)	As above
Methana	D'Alessandro et al. (2008)	[a]-3.5 to 0.5 (soil gas)	Limestone decomposition
Milos	Botz et al. (1996)	-1 to 1.1 (hydrothermal and fumarolic gases)	Dissociation of marine carbonates
Etna	Chiodini et al. (2011)	-1.5 to -0.33 (volcanic plume samples)	Magma carbonate assimilation/carbon isotopic fractionation due to degassing/change of magma source
	Martelli et al. (2008)	-2.2 to -1. 3 (fumarolic gases)	Magmatic degassing
Vulcano	Capasso et al. (1997)	-3.4 to 0.7 (fumarolic and soil gases)	Crustal contamination of ascending magmas
	Chiodini et al. (2011)	-1.94 to -1.18 (volcanic plume samples)	Reflects a regional scale process – metasomatism or crustal contamination
Solfatara	Chiodini et al. (2011)	-2.34 to -1.68 (volcanic plume samples)	Reflects a regional scale process – metasomatism or crustal contamination

---

[16] [a]$\delta^{13}C$ values for samples with CO_2 concentrations > 500 ppm.

By itself, the $\delta^{13}C$ of the emitted CO_2 provides no constraint on the depth of origin of the isotopically heavier C. Nonetheless, petrological evidence from Santorini and other volcanoes in the region provides ample evidence for CO_2 release from shallow crustal sources, and we suggest that this is a sufficient explanation for the isotopic composition of volcanic CO_2 in the region, without the need to appeal to the signature of a deeper slab-component within the mantle. Metamorphosed fragments of basement carbonates are found as inclusions in the Kameni island lavas of Santorini (Nicholls, 1971b), with high-temperature clinopyroxene and wollastonite-rich assemblages; and clinopyroxenite xenoliths, also formed by magmatic assimilation of carbonate, are found at Nisyros volcano (eastern Aegean; Spandler et al., 2012). This suggests that at least a proportion of the CO_2 emissions at both volcanoes are derived from breakdown of basement carbonates, either during heating by, or direct reaction with, magma (cf. Deegan et al., 2010; Di Rocco et al., 2012). At both Santorini and Nisyros, the measured CO_2 - $\delta^{13}C$ values are consistent with a gas phase that is a mixture of magmatic CO_2 with CO_2 released from shallow crustal carbonates, rather than CO_2 derived solely by decarbonation. Aegean limestones have $\delta^{13}C$ ranging from -0.5 to 2.5‰ (Dotsika et al., 2009; Gärtner et al., 2011), so given a CO_2-calcite fractionation factor of 2.7 to 3.5‰ (at ~ 800-950°C; Rosenbaum, 1994; Scheele and Hoefs, 1992; Chacko et al., 1991) we would expect CO_2 - $\delta^{13}C$ from limestone decarbonation of ~ 2.2‰ to 6‰ (i.e., too heavy to be solely responsible for the observed values).

Further supporting evidence for this shallow mixing includes: (1) at Nisyros, fumarole $CO_2/^3He$ ratios and CO_2-$\delta^{13}C$ data plot on a mixing line between ‘typical’ MORB-source mantle and limestone-derived CO_2 (Brombach et al., 2003). (2) During the main period of recent unrest at Santorini (May 2011 – March 2012), the fumarole

δ^{13}C values (~ -0.3‰ to -0.8‰) were lighter than those in July 2010 (~ -0.2‰ to -0.3‰) or July 2012 (-0.1‰) (Tassi et al., 2013). Tassi et al. (2013) interpret this signature as an increased contribution of 'mantle' CO_2 during the 2011-2012 unrest, compared to emissions during quiescent periods when CO_2 is predominantly sourced from thermometamorphic reactions involving crustal limestone. If there was no CO_2 release from crustal limestone at Santorini, but instead the heavier δ^{13}C values (~ 0 ‰) reflected a mantle source modified by a subducted carbonate component, we would not expect to see the observed temporal variation in δ^{13}C associated with a new pulse of magma into the shallow system. In summary, we suggest that the measurements from Santorini (and Nisyros) are more consistent with a model of CO_2 release from a shallow crustal limestone source mixing with magmatic emissions, rather than simply from a mantle source modified by a subducted carbonate component.

6.3.4 The proportion of magmatic gas in the CO_2 flux

In order to understand the contribution of volcanoes to the geological carbon cycle it is important to quantify magmatic versus shallow 'crustal' contributions (e.g., thermal or metamorphic decarbonation of limestone) to CO_2 emissions. Changes in the balance between these different fluxes may also have important volcanological implications (e.g. Troll et al., 2012). Due to the low solubility of carbon in magmas, CO_2 is often released deep within the magmatic system. This can result in a significant diffuse flux of magmatic gases through the volcanic edifice and surrounding area, which then contribute to soil gas emanations. While noble gases such as He can be used as sensitive tracers of this magmatic gas component, this approach has not yet been widely used in the study of diffuse emanations, although recent work shows promise in this area (e.g. Padron et al., 2013).

The CO_2-$\delta^{13}C$ measurements do not provide quantitative constraints on the proportions of gas from each source, due to uncertainties in the $\delta^{13}C$ compositions of the magmatic and crustal CO_2 (see section 3.3). To constrain the proportion of the ‘deeper’ CO_2 flux that is sourced from magma, we need to use an additional tracer that is a more sensitive discriminant of ‘limestone’ and ‘magma’ than $\delta^{13}C$ alone. We use ^{222}Rn for this purpose since it is short-lived (half life of 3.8 days), partitions strongly into the gas phase and it is also possible to measure it in diffuse soil gas emissions (see section 6.2).

Studies in a number of locations suggest that ^{222}Rn is a good proxy for magmatic activity (e.g., Yang et al., 2011, Tatun Volcanic Group, Taiwan). At Mt Etna, ^{222}Rn–CO_2 systematics clearly distinguish a shallow soil-gas component from a deeper, high-CO_2 flux and high ^{222}Rn magmatic component (Giammanco et al., 2007; 2010). In a volcanic edifice that contains a hydrothermal system, matters may be complicated by ^{222}Rn production by alpha-recoil from rock surfaces within the hydrothermal system (e.g. Dymond et al., 1983; Kadko and Moore, 1988; Clark and Turekian, 1990), but there have been few radiochemical studies of actively degassing volcanoes from which we may draw more detailed inferences.

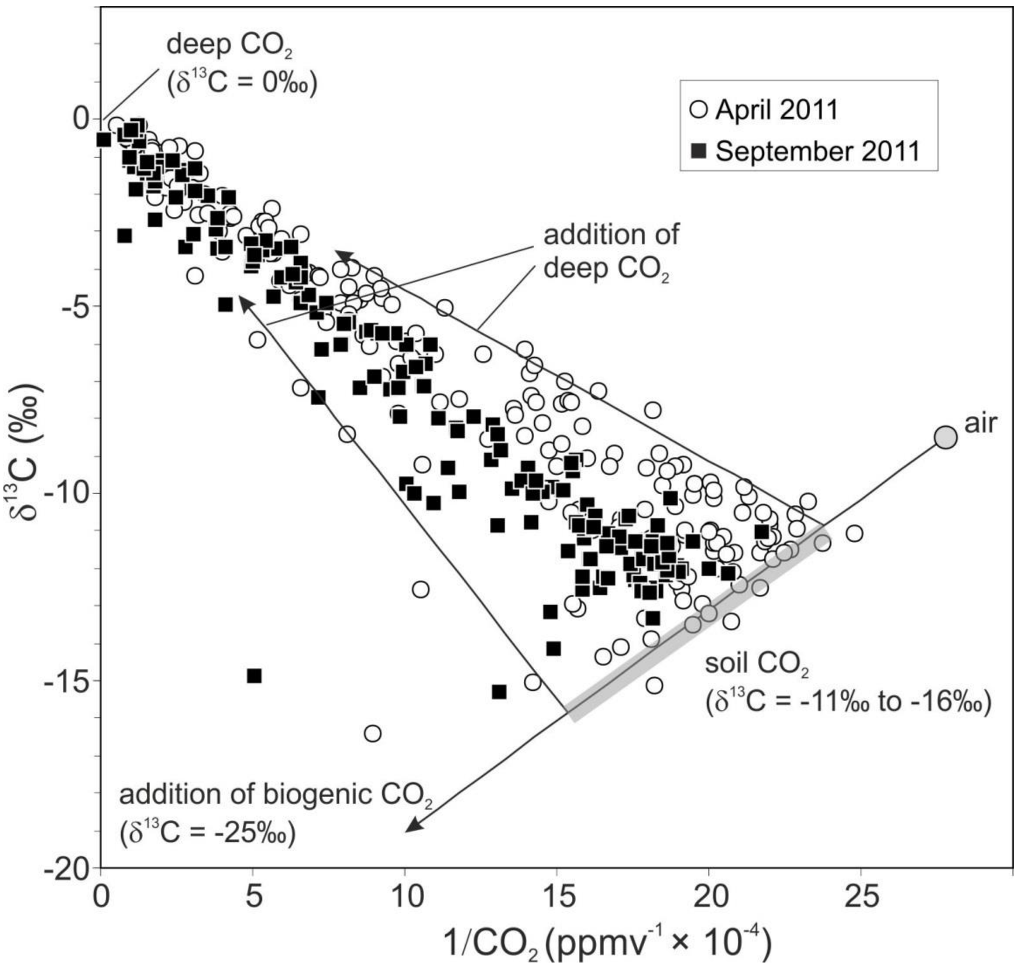

Figure 6.5. *Graph of carbon isotopic composition ($\delta^{13}C$) of soil CO_2 efflux vs. the reciprocal of CO_2 concentration in the gas samples acquired during the April and September 2011 campaigns. A minimum of 2 samples were collected at each site and each sample is plotted separately. CO_2 mixing lines are displayed. The "addition of biogenic CO_2" line represents a mixing between air and an endmember characterised by high CO_2 concentrations and light $\delta^{13}C$ values approaching -25‰ (biogenic CO_2). The grey bar represents the soil CO_2 endmember characterised by relatively low CO_2 concentrations and light $\delta^{13}C$ values ~ -11‰ to -16‰ (soil CO_2). The region between the "addition of deep CO_2 lines" trends towards an endmember characterised by high CO_2 concentrations and heavier $\delta^{13}C$ values approaching 0‰ (CO_2 derived from a deeper source).*

At Santorini, the highest measured $^{222}Rn/CO_2$ values (>3 MBq kg^{-1}) have $\delta^{13}C$ values of ~ -1 ‰. This value corresponds closely with the high-flux deep CO_2 end member in Figure 6.5, and is consistent with our hypothesis of a magmatic source of ^{222}Rn. At the present time, there is insufficient evidence to allow us to determine the role that the shallow hydrothermal system at the Kameni islands may play as a source of radon. Compositions of fluids and hydrothermal sediments suggest that the hydrothermal system is a region of mixed seawater and meteoric water (e.g., Varnavas and Cronan, 2005), modified by the arrival of heat and fluids from below. Apart from U however, there are no radiochemical data from these fluids (Boström et al., 1990), and there is no evidence from the sampled fluids, or from shallow drilling, for strong wall-rock alteration (e.g. Papavassiliou et al., 1990; Paritsis et al., 1990). This is clearly an area for future work. Leaving the role of the hydrothermal system to one side, we explore below the hypothesis that ^{222}Rn – CO_2 systematics can distinguish between the products of decarbonation of limestone (with a low ^{222}Rn/CO_2) and gas, recently degassed from magma (with a high ^{222}Rn/CO_2).

The results from the radon activity survey in September 2011 are shown in Figure 6.6. ^{222}Rn activities measured during this survey ranged from 31 to 10,469 Bq m^{-3}, with a mean activity of ~ 2,200 Bq m^{-3}. Appendix F provides a comparison of ^{222}Rn measurements obtained from soil gas studies at other volcanoes. The spatial variation of ^{222}Rn (Fig 6a) is very similar to that of CO_2 measurements acquired during the same period (Figure 6.4d). The clear spatial (Figure 6.6a) and quantitative (Figure 6.6b) correlation between the ^{222}Rn activity and CO_2 flux suggests a mutual source (see also discussion above). Either the volatiles are being released from a magma body within the volcano, or the magma is heating or reacting with the surrounding host rock, which is in turn releasing radon and CO_2.

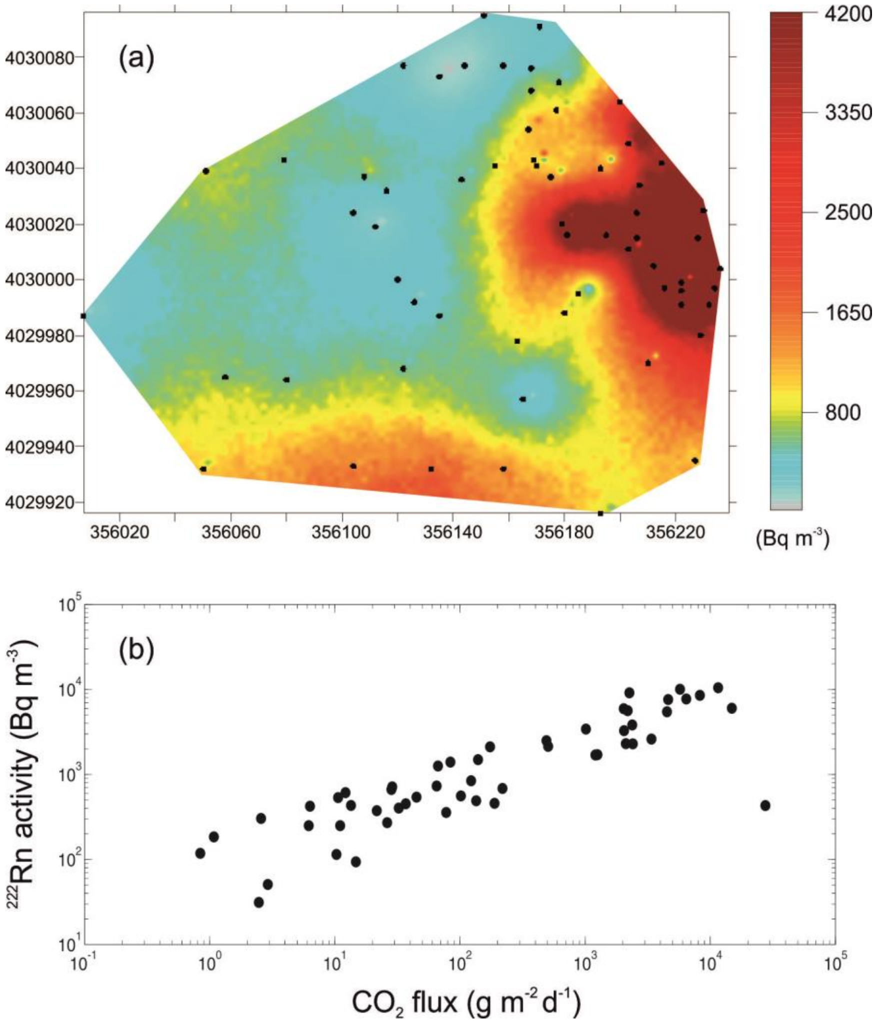

Figure 6.6. (a) *Map of the ^{222}Rn activity over the target area on the summit of Nea Kameni in September 2011, derived using the sGs approach.* ***(b)*** *A plot of ^{222}Rn activity against CO_2 flux.*

To quantify the origin of the ^{222}Rn and CO_2 emissions from the summit of Nea Kameni we adopt a simple mixing model with three potential gas sources: 1) shallow soil, 2) magma and 3) limestone (Table 6.3; Figure 6.7). The endmember compositions assumed for each reservoir are summarised in Table 6.3. For the magma reservoir we assume that CO_2 is released in a single batch as the magma reaches shallow levels and that the magma fully degasses ^{222}Rn at the same time as the CO_2 is released. Nea Kameni dacites contain approximately 4 ppm U (e.g., Druitt et al., 1999; Zellmer et al., 2000), corresponding to an activity of 50 Bq (^{222}Rn) per kg of degassing magma, assuming secular equilibrium. For the limestone reservoir we assume that the limestone contains 1 - 10 ppm U, in secular equilibrium, and that all of the radon produced during decarbonation ends up in the gas phase. So decarbonation of 1 kg of $CaCO_3$ releases 0.44 kg CO_2 and ~ 12 - 120 Bq kg^{-1} of ^{222}Rn. Using these ranges, we can explore the systematics of mixing between different reservoirs, allowing additionally for the decay of ^{222}Rn over the days/weeks of transfer to the surface. The mixing equations are provided in Appendix G. Figure 6.7 displays the measured field data and an example mixing model.

Table 6.3: *End member compositions used in simple model for ^{222}Rn-CO_2 mixing.*[17]

Reservoir	**CO_2 concentration in final gas (%)**	**$\delta^{13}C$ (‰)**	**U content (ppm)**	**[a](^{222}Rn)/CO_2 (initial) (Bq kg^{-1})**
[b]Soil gas	0.04	-15	n/a	3×10^4
[c]Magma	5	-1 to -5	4	3.7×10^6 to 6.2×10^6
[d]Limestone	100	5	1 to 10	30 to 300

---

[17] [a] The soil gas (^{222}Rn)/CO_2 ratio was converted to Bq kg^{-1} assuming a constant temperature of 40°C.
[b] The soil gas endmember was estimated from our own data ($\delta^{13}C$ ~ -15‰; CO_2 concentration of 0.04% from the soil gas data in Figure 6.5, and (^{222}Rn)/CO_2 = 3×10^4 from the minimum measured value in Figure 6.7).
[c] We derive a possible range of ^{222}Rn activities from Druitt et al. (1999) and Zellmer et al. (2000), for magma with a U content of 4 ppm (corresponding to a radon activity of ~ 50 Bq kg^{-1} assuming secular equilibrium). We then estimate the magma endmember 'maxima' and 'minima' from the observed data. These range from $\delta^{13}C$ of -1‰ and (^{222}Rn)/CO_2 ratio of ~ 3.7×10^6 Bq kg^{-1}, (Figure 6.5) to $\delta^{13}C$ of -5‰ with a corresponding (^{222}Rn)/CO_2 ratio of ~ 6.2×10^6 Bq kg^{-1}. This implies a CO_2 release of ~ 8 – 14 ppm in the final gas mix. We assume that CO_2 accounts for ~ 5% of the total magmatic gas phase.
[d] Limestone endmember ranges were derived from Fiebig et al. (2004), Dotsika et al. (2009), and Gärtner et al. (2011) assuming a U content of 1 - 10 ppm, and CO_2 - $\delta^{13}C$ of 5‰, given the assumptions about isotopic fractionation between the limestone and the gas released described in section 6.3.3 of the text.

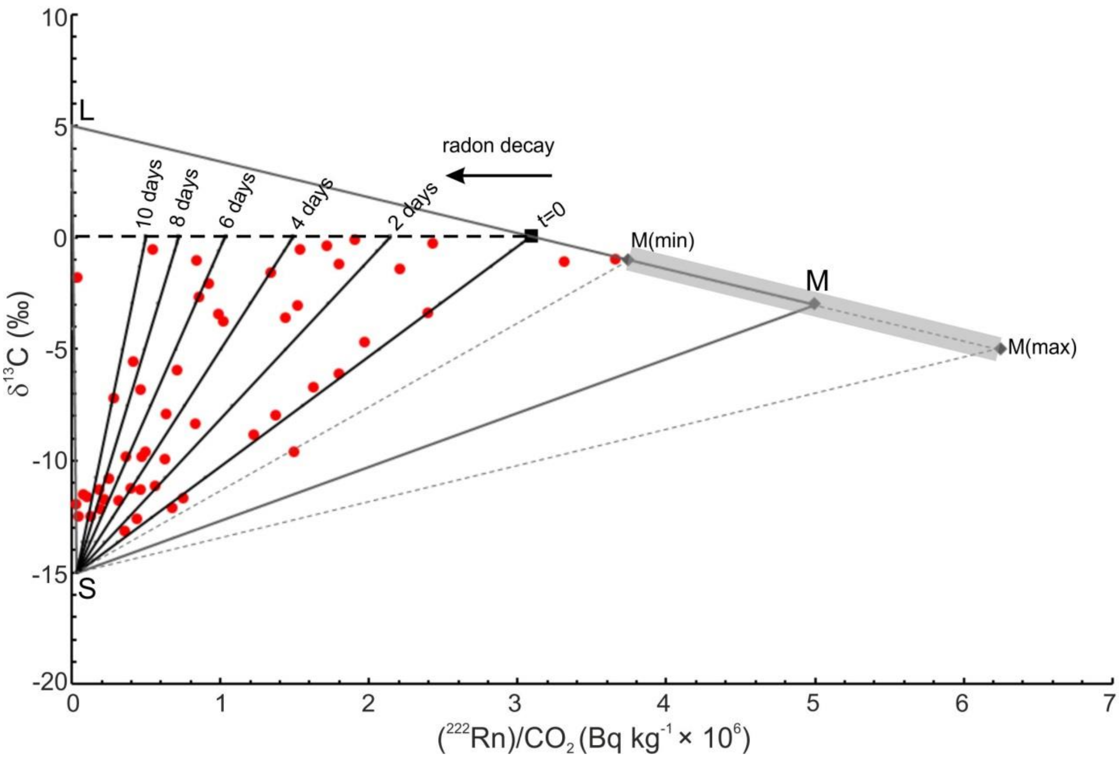

Figure 6.7. *Three component mixing model illustrating the relationship between (^{222}Rn)/CO$_2$ and δ^{13}C values for three different endmembers: magma (M), limestone (L) and soil (S) (Table 6.3). The magma endmember used in this model has δ^{13}C ~ -3‰ and (^{222}Rn)/CO$_2$ ratio of 5×10^6Bq kg^{-1}, and lies mid-way between the estimated minimum and maximum magma endmembers (M(min) and M(max) respectively). The range of possible magma endmembers is displayed as a grey bar. The red circles show the measured data. The black square represents a gas mix with δ^{13}C ~ 0‰, corresponding to the deep CO$_2$ source in Figure 6.5. The solid black lines are mixing trends for a deep gas mixture (assuming the starting CO$_2$ concentration and ^{222}Rn activity of the mixed magma-limestone source shown by the black square) within which the ^{222}Rn has decayed for the time period labelling each line.*

Figure 6.7 shows that (as concluded in section 3.2) a magmatic component is essential to explain the mixing trends towards a component with a δ^{13}C value of ~ 0‰, and the elevated (^{222}Rn)/CO$_2$ ratios measured for most samples. The simplest model to explain the distribution of the data is that the gas sampled at the surface comprises a mixture of CO$_2$ released from magma and limestone decarbonation (with combined δ^{13}C ~ 0‰), that then takes a range of timescales (hours to weeks) to reach the surface and mix with soil gas. Assuming that the CO$_2$ produced by thermal or metamorphic breakdown of limestone has a $\delta^{13}C$ of ~ 5‰ and (^{222}Rn)/CO_2 ratio of 300 Bq kg^{-1}, and a magmatic endmember of $\delta^{13}C$ of ~ -3‰ and (^{222}Rn)/CO_2 ratio of 5×10^6 Bq kg^{-1}, then about 60% of the carbon in the high flux deep CO_2 endmember must be of magmatic origin in order for the measured gas samples to have a $\delta^{13}C$ of ~ 0‰. Although simple, this model is sufficient to explain all of the observed data, and does not require any additional sources of either radon, or CO_2.

This simple model is consistent with the model developed by Tassi et al., (2013), based on their analysis of changes in the point-source fumarole discharges at the Kameni islands from July 2010 – July 2012. They saw changes in fumarole composition, notably a strong increase in H_2 concentration, from May 2011 to February 2012, and detected an increase in light hydrocarbons, including CH_4, from March to July 2012. On this basis, they proposed that hot, deep gases from both magmatic and thermo-metamorphic sources intersect a shallow hydrothermal reservoir, where high-temperature reactions produce H_2 and light hydrocarbons (e.g., Giggenbach, 1987; Chiodini and Marini, 1998). Boiling of this reservoir yields the fluid rich in CO_2, into which Rn, H_2 and other species will partition, which ultimately feeds fumaroles and the high-temperature component of the soil-gas. Our model shows that the gas escaping from the Kameni islands is dominated by a magmatic component (with a high (^{222}Rn)/CO_2 ratio) that has been mixed with a component from decarbonation of limestone. An important constraint on the nature of the magmatic component arises from the observation that this endmember must have (^{222}Rn)/CO_2 > 4×10^6 Bq kg^{-1} to account for the full range of gas compositions measured. Assuming the magma has a ^{222}Rn activity of 50 Bq kg^{-1}, and a very simple 'batch' degassing process, the CO_2 release from the melt during degassing is likely to be of the order of 8 - 14 ppm. This is consistent with the observation that Santorini melt inclusions are CO_2-poor (T. Druitt

2012, pers. comm.) and is also consistent with the inference that the intruding melt is more likely to be an evolved dacite, rather than a primitive (CO_2-rich) basalt (Druitt et al., 2012; Parks et al., 2012).

6.4 Conclusions

Analysis of 9 soil CO_2 surveys undertaken on Nea Kameni between June 1994 and January 2012 reveal temporal changes in the pattern of CO_2 degassing from the summit of Nea Kameni, and are suggestive of an increase in soil CO_2 emissions between September 2010 and January 2012. The results of the $\delta^{13}C$ isotopic analysis and ^{222}Rn measurements indicate the high-flux CO_2 and ^{222}Rn emissions are derived from a common deep source, which has a significant magmatic component.

Temporal variations in CO_2 flux distributions are in accordance with the concurrent deformation and seismicity. The onset of the seismic and geodetic unrest in January 2011 hinted at renewed magmatic activity beneath Santorini. Subtle yet important temporal changes in degassing, combined with $(^{222}Rn)/CO_2$ systematics (from the September 2011 campaign), provides new evidence that the recent period of unrest is the result of the injection of a new pulse of magma.

Continued study of the hydrothermal, fumarolic and soil-gas emissions at Santorini will improve our understanding of the behaviour of caldera forming systems during transitional periods. Future monitoring would benefit from the installation of additional sites for continuous CO_2-^{222}Rn monitoring (e.g., Zimmer & Erzinger, 2003), augmented by soil-gas CO_2 $\delta^{13}C$ sampling, combined with the regular acquisition of denser soil-gas sampling surveys (> 300 sites) covering a wider area on Nea Kameni.

The combination of $\delta^{13}C$ and (^{222}Rn) measurements to investigate and quantify the source of diffuse CO_2 emissions that we demonstrate here will have application in other volcanic areas, under the right circumstances, especially those where thermal or metamorphic decarbonation of crustal limestone is likely to contribute significantly to the CO_2 flux.

Chapter 7

Conclusions

The new results presented in this dissertation highlight the potential of InSAR for measuring displacement rates at active volcanoes. In particular, they demonstrate that the combination of InSAR results with complementary field data may provide additional constraints on the processes controlling the deformation signals observed, as well as the underlying causes of volcanic unrest. This section provides a summary of the main conclusions drawn from Chapters 2 to 6, followed by comparisons with other multi-data stream studies and suggestions for future work.

7.1 Summary

Chapter 2 presented the results of a regional InSAR survey, covering a 550 km segment of the Colombian Northern Volcanic Zone. This study highlighted the benefits of using L-band interferometry for improved coherence in rugged and highly vegetated regions. Interferograms covering 12 of the 15 surveyed volcanoes maintained coherence throughout the observation period. Atmospheric signals were observed at 6 volcanoes, 5 displayed no sign of deformation, and a deflation signal was detected at 1 (Galeras). This subsidence signal corresponding to approximately -3 cm displacement in the satellite's line of sight was observed on 3 independent interferograms over Galeras, coinciding with the October 2007 - January 2008 eruption. Source models provide a good fit to the data and are consistent with deflation of a magma lens at a depth of ~ 2 km, under the NE flank of the volcano. The modelled volume change (-6.5×10^5 m^3), is consistent with that derived from tilt measurements and the volume of ejected material expelled from the volcano during an explosive event on the 17 January 2008. Historical gravity measurements support the existence of a resident/recurring chamber at this location.

Chapter 3 outlines the results of the initial InSAR and GPS analysis undertaken at Santorini volcano during a period of unrest in 2011-2012. InSAR modelling revealed that the source of inflation was located slightly north of Nea Kameni at a depth of ~ 4 km beneath the surface and that between 10–20 × 10^6 m^3 of magma was intruded beneath the volcano during the period of unrest covered by this chapter (January 2011-April 2012). Reoccupation of triangulation pillars using GPS demonstrated that this was the only volumetrically significant intrusion to occur beneath the Kameni islands since shortly after the last eruption in 1950. Previous petrological studies on material erupted during prior eruptions had suggested the existence of a shallow magma reservoir filled with silicic magma beneath the volcano (e.g., Martin et al., 2006). Prior work had also suggested that many of the smaller eruptions of Santorini appear to be triggered by the influx of more mafic magma into the system shortly before eruption (e.g., Cottrell et al., 1999; Martin et al., 2006). The applicability of this interpretation to the explosive Minoan eruption, however, has recently been challenged based on the results of a very careful investigation of the glass and mineral chemistry of its products (Druitt et al., 2012). Druitt et al. (2012) proposed that prior to the Minoan eruption a significant portion (~15%) of the final volume of erupted material only arrived in the magma chamber within ~100 years of the eruption. Our results imply more similarities (in terms of melt supply) between the “Minoan type” eruptions and smaller dome-forming eruptions, whereby melt is supplied in a series of infrequent rapid pulses. The duration of these pulses is much shorter than the intervening period between eruptions.

Chapter 4 expanded on this work by analysing a slow subsidence signal observed on Nea Kameni between 1993 and 2010, and the detailed temporal evolution of volume change within the shallow chamber throughout the 2011-2012 period of unrest. Prior to 2011, InSAR analysis revealed an extended period of aseismic slow subsidence on the SW corner of Nea Kameni, corresponding to an average rate of ~ 0.6 cm/yr. Modelling results suggest the observed subsidence likely results from a combination of cooling and contraction of the 1866-1870 lava flows, with loading from these historic flows inducing viscoelastic relaxation of the substrate. The joint inversion of InSAR and continuous GPS measurements acquired throughout 2011-2012 reveals two distinct pressure pulses during the period of unrest. These pulses may be explained by batches of melt supply delivered to the shallow chamber, or they may represent episodes of vesiculation, or possibly a combination of both. The decline in activity observed from January 2012 onwards likely results from the cessation in melt supply to the shallow magma reservoir. The variation in sub-surface volume change between August 2011 and October 2012 has been successfully modelled in terms of constant melt supply/pressure increase to the shallow reservoir between August 2011 and January 2012, followed by the continued relaxation of a viscoelastic shell surrounding the magma chamber.

Chapter 5 presents revised volumetric estimates (based on a new LiDAR survey of the subaerial portion of the Kameni islands, combined with new bathymetry data acquired around them) for each of the lava flows extruded in the vicinity of the Kameni islands since 47 AD, (including previously unidentified submarine flows and cones). The revised volumes enabled the derivation of a new relationship between eruption volume and pre-eruption interval for historic effusive eruptions. This may be used to estimate the size and duration of future dome-forming events at Santorini. If an eruption were to occur in the next few years the pre-eruption interval period would be ~ 75 years. Therefore the expected volume of extruded lava would be of the order of 8×10^7 m^3 and the eruption would continue for approximately 3 years. The new volume estimates indicate an average lava extrusion rate of ~ 2 m^3s^{-1} during four historic eruptions on Nea Kameni. Morphological analysis of the 1570/1573 submarine lava lobe suggests a three- to four-fold increase in lava strength upon entry into the sea.

Chapter 6 reveals the variation in gas emissions measured on the summit of Nea Kameni since 1994. Probability plots of log CO_2 flux for nine data sets display bimodal distributions representing the partial overlapping of a high flux population (A) and a low flux population (B). An increase is observed in the low flux CO_2 population between the September 2010 and April 2011 surveys, coinciding with the onset of the new unrest at Santorini. Flux maps of the CO_2 output at the summit generated using sGs analysis are suggestive of an increase in total CO_2 outgassing. They also indicate a change in the pattern of degassing following an earthquake swarm in January 2012. Both of these observations may be interpreted as the result of CO_2 infiltration into areas previously unaffected by deep gases. Isotopic analysis of the soil gas $\delta^{13}C$ (CO_2) suggests a mixture of biogenic and air-derived CO_2 (with $\delta^{13}C$ from -11‰ to -16‰) at low CO_2 concentrations (~ 400 to 700 ppmv), and deep CO_2 ($\delta^{13}C$ close to 0‰) at high CO_2 concentrations (up to ~12,000 ppmv). A strong correlation between ^{222}Rn activity and CO_2 flux measurements acquired in September 2012, combined with a three component mixing model, suggests the emissions are derived from a mutual deep source with a significant magmatic component (> 60%). This analysis confirms the recent phase of unrest at Santorini is the result of an injection of fresh magma.

7.2 Comparison with other studies

In this dissertation I have demonstrated the applicability of InSAR to the monitoring of active volcanoes. It has particular application in the identification of changes in the behaviour of volcanoes, the exploration of causative volcanic processes responsible for observed deformation, the characterisation of part of the magma plumbing system and for inferring rates of melt supply. Table 7.1 provides an overview of other studies which have employed a multi-data stream approach by combining InSAR with additional monitoring techniques to gain an improved understanding of volcanic processes. I draw on these examples from the literature to illustrate the relevance of my work and to demonstrate how these techniques are applicable at other volcanoes.

Table 7.1: *Information derived from various studies by combining InSAR with different volcano monitoring techniques.*

Technique combined with InSAR	**Applicability**	**Selected references**
Gravity	Distinguish between different processes responsible for observed ground displacements based on density estimates derived from gravity and height measurements.	Vigouroux et al. (2008); Tizzani et al. (2009); González et al. (2010); de Zeeuw-van Dalfsen et al. (2013).
GPS and tilts	Improve spatial and temporal resolution of deformation measurements.	Cervelli et al. (2002a & b); Bonaccorso et al. (2004); Dzurisin et al. (2006); Pagli et al. (2006); Palano et al. (2008); Biggs et al. (2010b).
LiDAR	Improved digital elevation model for topographic phase correction. High resolution morphological analysis. Hazard mapping.	Wadge et al. (2006); Sedze et al. (2012); Richter et al. (2013).
Gas measurements	Detection of buried faults/fractures. Differentiation between magmatic and hydrothermal processes. Insight into conduit processes.	Kwoun et al. (2006); Bonforte et al. (2013); Traglia et al. (2012).
Seismicity	Improved constraints on the source of the deformation (e.g., type, location and geometry). Insight into volcano-tectonic interactions.	Dawson et al. (1999); Chiarabba et al. (2000); Fukushima et al. (2005); d'Oreye et al. (2011); Baker and Amelung (2012); Feuillet (2013).

7.2.1 Gravity

Surface deformation is caused by subsurface volume changes, while gravity changes are caused by subsurface mass changes - together these observations tell us about the density. Combined gravity and InSAR measurements at a number of volcanoes have provided insight into the processes responsible for observed ground deformation. At Askja volcano (Iceland), de Zeeuw-van Dalfsen et al. (2013) demonstrated that a persistent slow subsidence signal observed within the caldera since 1983 was likely the result of cooling and contraction of a resident magma chamber.

They reached this conclusion by analysing gravity measurements acquired between 1998-2007 and 2009-2010 combined with InSAR displacements taken from 2000-2010. In another study, Tizzani et al. (2009) model InSAR and EDM derived displacements at Long-Valley caldera (USA) (between 1992 and 1999) to determine the optimal geometry of the source of inflation. They undertake a joint inversion of height and gravity measurements (from 1982-1999) to obtain the density of the source. Their results indicate that a magmatic intrusion beneath the caldera is responsible for both the uplift and residual increase in gravity. Extraordinary deformation and gravity changes were measured at Sierra Negra volcano (Galápagos) prior to and during the October 2005 eruption (Vigouroux et al., 2008). Uplift occurred at a rate of 1 cm/day prior to this event and a residual gravity decrease of -950 μGals was measured between 2002 and 2005. The authors employed 4D gravity modelling to determine the parameters of a magmatic intrusion which satisfy the pre-eruptive gravity anomaly. As well as determining the cause of unrest, combined gravity and deformation measurements have also been employed to identify flank instabilities at volcanoes as well as to assess the potential threat of future collapse events. InSAR derived displacements at Cumbre Vieja (Canary Islands) have been attributed to creep deformation triggered by gravitational loading, following the identification of a sub-volcanic low density gravity anomaly (González et al., 2010).

In Chapter 2, I demonstrate how the combination of gravity and InSAR measurements may also be used to infer additional information on the site of historic intrusions. I use the source parameters derived from the 2007-2008 InSAR modelling to fit a gravity anomaly observed 10 years earlier. The fact that the depth and location of the InSAR derived source provides a good match to the gravity measurements, suggests the presence of a recurrent magma chamber at this location. This result assisted scientists at INGEOMINAS in determining optimal site locations for additional field monitoring equipment.

7.2.2 Continuous geodetic measurements

InSAR has a high spatial resolution, but typical orbit repeat times of 30-45 days; in contrast cGPS and tiltmeters provide daily measurements at only a few point locations. Combining InSAR measurements with cGPS and electronic tiltmeter measurements provides a valuable means of improving both the temporal and spatial resolution of deformation measurements at volcanoes. At Okmok volcano (Alaska), Biggs et al., (2010b) employed a joint geodetic inversion technique (combining InSAR, cGPS and campaign GPS measurements) to map the temporal evolution of volume change within a shallow magma chamber. A similar technique was employed by Pagli et al. (2006) to determine the optimal source for the observed subsidence at Askja caldera. Direct comparisons between InSAR observations from 1995-2001 and tilt measurements between 1985 and 2001 enabled Dzurisin et al. (2006) to place better constraints on the timing on an intrusion beneath the Three Sisters volcanic centre (USA), whilst joint inversion of tilt, GPS and InSAR derived displacements allowed determination of the source geometry, location and volume change responsible for the observed displacements. The origin of an earthquake swarm in the Upper East Rift Zone of Kilauea Volcano (in September 1999) was determined by Cervelli et al. (2002b) using InSAR, cGPS and borehole tiltmeter mearsurements. The modelled deformation field was consistent with the intrusion of an eastward propagating dyke associated with a pressure change of 15 MPa. At Etna volcano (Italy), Bonaccorso et al. (2004) compared ground-based deformation measurements available during the first part of the 1991-1993 eruption with InSAR measurements available during the second part of the eruption, to gain insight into the subsurface plumbing system.

In Chapter 2, I show that the modelled volume change derived from tilt measurements at Galeras volcano, agrees with that derived from InSAR measurements (-6.5×10^5 m^3), and the volume of material ejected from the volcano during an explosive event on the 17 January 2008. This correlation provides additional evidence that the subsidence signal identified at Galeras is co-eruptive and directly related to the expulsion of gas and ash during this explosive event. In Chapter 3 we illustrate the benefit of reoccupying historical triangulation sites with GPS, to determine whether or not any significant displacements have occurred over an extended (~ 55 year) period. The fact that the measured displacements between 1955 and September 2011 agree with the InSAR derived displacements between January and September 2011 indicates that the inflation observed between January 2011 and April 2012 is the only volumetrically significant event to occur since shortly after the last eruption in 1950.

In Chapter 4, I demonstrate that the joint inversion of cGPS and InSAR measurements not only improves temporal and spatial resolution, but also enables the identification of underlying trends (in this case pulses of deformation) which may be representative of either batches of melt supply to the shallow chamber or episodes of magmatic vesiculation. Viscoelastic modelling is also used to show that the variation in deformation/volume change can be explained by an initial pressure increase to a shallow magma chamber surrounded by a viscoelastic shell, followed by a pressure shut-off. The shut-off time corresponds to the cessation of melt supply/pressure increase to the shallow reservoir.

7.2.3 High resolution Digital Elevation Models

DEM resolution is typically the limiting factor on several aspects of volcano monitoring: InSAR processing, volume estimates of past eruptions and flow modelling (lava, pyroclastic and lahars). The generation of high resolution interferograms is invaluable to the detection of localised deformation at volcanoes. With the increased availability of high resolution X-band satellite data (TerraSAR-X and COSMO-SkyMed), the obvious immediate benefit of obtaining airborne LiDAR data is to produce a high resolution DEM that may be utilised in the InSAR processing workflow for removal of topographic fringes, without compromising the resolution of the final interferograms. Analysis of a series of 3-m resolution TSX interferograms generated at Kilauea volcano between 2008 and 2012 reveals a variable subsidence signal in close proximity to the new vent, which opened during the March 2008 eruption (Richter et al., 2013). Sedze et al. (2012) have also used LiDAR to construct a high resolution DEM and remove the topographic phase component from L-band ALOS interferograms over the Piton de la Fournaise volcano (Reunion Island, France). It should be noted that in this instance the authors' primary motivation was the relationship between interferometric coherence and LiDAR intensity, as a means of discerning which volcanic landscapes contributed most to the loss of coherence.

In Chapter 4, I employ a high resolution (2-m) LiDAR derived DEM for the topographic correction of TSX interferograms at Nea Kameni. The results show no evidence for localised deformation related to historic vent locations, but they do confirm that inflation on Nea Kameni continued into April 2012, after the cessation of micro-seismic activity within the caldera.

7.2.4 Gas Release

Changes in temperature and pressure cause phase changes within magma – thus quantity and type of gas emitted can provide information on the conditions of magma movement and storage. Comparison of gas and deformation measurements is a useful tool for the detection of buried faults/fractures and the differentiation between magmatic and hydrothermal processes. Bonforte et al. (2013) used CO_2 and radon soil gas measurements at Etna to confirm that lineations detected on PS interferograms were in fact related to buried faults/fractures. Helium and CO_2 measurements at Aniakchak volcano (Alaska) indicate that an aseismic subsidence signal identified in interferograms acquired between 1992-2002 results from depressurisation of the hydrothermal system or cooling and degassing of a shallow magmatic intrusion (Kwoun et al., 2006). Traglia et al. (2012) demonstrate that an increase in displacement rates (measured using ground-based InSAR) is observed at Stromboli volcano prior to large explosions. The authors suggest that these rapid displacements are related to the expansion of gas within the shallow conduit system.

In Chapter 6, I demonstrate that there is an increase in the low flux CO_2 population at the inferred start of the magmatic intrusion beneath Santorini and a change in the pattern of degassing on the summit of Nea Kameni, following an earthquake swarm in January 2012. The relationship between the InSAR signal and this earthquake swarm is explored in Chapter 4. It is likely that this variation in degassing results from the propagation and coalescence of fractures within the volcanic edifice, providing new gas migration pathways to the surface.

7.2.5 Seismicity

Surface deformation and seismicity are both caused by subsurface stress changes. The onset of earthquake swarms beneath typically “quiescent” volcanoes is often the first indication of renewed activity. The location/propagation of precursory seismicity is frequently used to constrain the location and geometry of magmatic intrusions (e.g., Fukushima et al., 2005; Baker and Amelung, 2012). Coulomb stress analysis can provide insight into volcano-earthquake interactions (e.g., Hill et al., 2002; Feuillet, 2013) and comparison of the seismic moment with the geodetic moment can help determine whether ground deformation is co-seismic or related to a magmatic intrusion (e.g., d’Oreye et al., 2011 and references therein). Tomographic inversion studies have been employed at volcanoes to detect subsurface velocity anomalies related to magma emplacement (e.g., Benz et al., 1996; Dawson et al., 1999; Chiarabba et al., 2000). d’Oreye et al. (2011) undertook separate inversions of InSAR and teleseismic data to better constrain the source parameters of the 2008 Bukavu-Cyangugu earthquake in the East African Rift.

In Chapter 4, I show that a strong relationship exists between the time series of cumulative volume change (derived from geodetic data) and the cumulative variation in seismic moment (derived from intra-caldera earthquakes). An apparent lag response was observed between the reduction in earthquake seismicity (in both June 2011 and February 2012) and the decline in the volumetric growth rate (in August 2011 and April 2012). We have used a viscoelastic model with a generic pressure function to demonstrate that the cessation in earthquakes in January 2012 corresponds to a shut-off in melt supply/pressure increase to the shallow reservoir. The lag identified between the flattening of the cumulative seismicity and volumetric time series curves can be accounted for by continued relaxation of a viscoelastic shell surrounding a spherical magma chamber.

7.3 Future work

Interferometric coherence was limited at 3 Colombian volcanoes: Cerro Machín, Cerro Bravo and Romeral. Cerro Machín is a potentially hazardous volcano, with a history of explosive eruptions that have generated voluminous pyroclastic flows. The volcano has displayed signs of seismic unrest as recently as September 2012 (SGC, 2013) and would benefit from additional analysis. PS InSAR processing may be more successful in improving coherence at this volcano, enabling the determination of whether or not any deformation occurred during this period.

Continued geodetic monitoring at Santorini is essential to identify the next phase of unrest. Although the current network of cGPS installations is sufficient to detect renewed caldera wide deformation, local and potentially rapid displacements on the central volcanic island of Nea Kameni may go unnoticed, especially if this were to occur in the south of the island and was not accompanied by an increase in micro-seismic activity. At present, the differencing of point cloud data acquired throughout repeat LiDAR surveys has been limited to earthquake studies (e.g., Borsa and Minster, 2012; Nissen et al., 2012). Although I attempted LiDAR differencing of the 2012 and 2004 surveys at Santorini (unpublished), the use of different GPS base stations combined with relatively small ground displacements meant that in this instance the technique was not suitable. However, with future improvements in acquisition parameters and georeferencing, LiDAR point cloud differencing may prove beneficial for the measurement of high resolution 3-D surface displacements at volcanoes.

Additional isotopic studies at Santorini combining the analysis of $^{3}He/^{4}He$ ratios and $\delta^{13}C$ would provide further constraints on the origin of future gas emissions at Nea Kameni. Continued acquisition of denser soil-gas surveys (at regular intervals), in conjunction with the installation of additional equipment for continuous CO_2-^{222}Rn monitoring, will aid the detection of significant changes in outgassing. The mixing model I present in Chapter 6, using a combination of $\delta^{13}C$ and (^{222}Rn) measurements to quantify the source of diffuse CO_2 emissions, will have significant application at other volcanoes, especially where uncertainties exist concerning the contribution of thermal or metamorphic decarbonation of crustal limestone to the overall CO_2 flux.

At present, the use of InSAR for detecting real-time changes in volcanic activity is limited both by orbit repeat intervals (11 days for TSX) and delays incurred between the acquisition and delivery of satellite images. However, with the imminent launch of new satellites such as Sentinel-1, this is an exciting time for volcano remote sensing. Acquisition parameters will be improved and satellite repeat times reduced, facilitating more frequent observations at active volcanoes. This in turn will increase the likelihood of detection of pre-eruptive, co-eruptive and post-eruptive deformation, enabling the generation of more detailed deformation models and an improved understanding of the volcanic processes at work. Further advancements in source modelling techniques and the joint analysis of multiple data streams will provide additional insight into magma emplacement mechanisms and the potential to forecast the characteristics of future activity at well monitored volcanoes.

Appendix A: List of interferograms used in the analysis of Colombian volcanoes

Track	Frame	Interferogram	Average Bperp (m)	Volcanoes covered	Ro	CB	NdR	St I	NdT	CM	NdH	Pu	So	Pe	DJ	Gal	Az	Cu	CNM
147	80	070610-070726	52.36	Ro, CB, NdR, St I & NdT	✓	✓	✓	✓	t										
		070610-071026	-462.53				✓	✓	✓										
		070610-080427	-907.54				i	i	i										
		070726-080427	-960.16				i	i	i										
		071026-071211	321.45		✓	✓	✓	✓	t										
		071211-080728	-111.93				i	i	i										
		071211-081213	208.55		n	n	t	✓	✓										
		080728-081213	320.34		n	n	✓	✓	✓										
147	90	070610-071026	609.89	Ro, CB, NdR & St I	n	n	✓	✓											
		070610-080427	-939.55				✓	✓											
		071026-071211	316.28		✓	✓	✓	✓											
		071026-080427	-469.79				✓	✓											
148	70	061225-080629	-806.02	NdR, St I, NdT & CM					i										
		070627-071228	364.33				✓	✓	t	n									
		070812-080629	104.80				✓	✓	t	✓									
		070812-090702	-40.94				t	✓	✓										
		071228-080514	-651.47				i	i	i										
		080629-081230	98.14				n	✓	t										
		080629-090702	-60.12				✓	✓	✓	n									
149	40	070829-080415	-104.23	NdH							✓								
		070829-080531	159.90																
		070829-080716	177.70																
		070829-090116	158.63																
		080415-080531	264.16								✓								
		080415-080716	282.01																
		080415-090116	262.88								✓								
		080531-080716	7.02																
		080531-090116	-18.48																
		080716-090116	-25.45																
150	30	071216-080317	390.03	NdH & Pu							✓	✓							

Track	Frame	Interferogram	Average Bperp (m)	Volcanoes covered	Ro	CB	NdR	St I	NdT	CM	NdH	Pu	So	Pe	DJ	Gal	Az	Cu	CNM
150	30	071216-081218	347.39	NdH & Pu								✓							
		080317-081218	-42.56								u?	✓							
151	10 & 20	070702-080704	-55.62	So & Pe									✓						
		070817-080519	-101.96										✓						
		070817-090104	-92.48										✓						
		080704-090104	107.52										✓						
152	10	070303-070719	149.33	Pe, DJ & Gal										✓	✓	✓			
		070303-071204	-78.71											✓	✓	✓			
		070719-070903	85.97											✓	t	t			
		070719-071204	-227.91											✓	t	✓			
		070719-080420	147.95											✓	t	s/n			
		070719-080605	-33.19											✓	t	s			
		070719-080721	-167.17												t	s			
		070719-080905	405.80											✓	t	s			
		070719-090121	-66.31											i	i	i			
		070903-080420	62.00											✓	✓	t			
		071204-080420	375.75											✓	✓	t			
		071204-090121	-329.91											i	i	i			
		080119-080721	-229.56											✓	✓	✓			
		080119-090121	-24.57											i	i	i			
		080420-080605	-240.16											✓	✓	✓			
		080420-080721	-419.29											✓	✓	✓			
		080420-080905	-657.11											✓	✓	t			
		080420-090908	-267.06													✓			
		080605-080721	-179.21											✓	t	✓			
		080605-080905	-416.97											✓	t	t			
		080605-090908	-26.94											t	t	✓			
		080605-090121	25.86											i	i	I			
		080721-080905	-237.72											✓	✓	t			
		080721-090121	205.10											i	i	I			
		080721-090724	-95.76											✓	✓	✓			

Track	Frame	Interferogram	Average Bperp (m)	Volcanoes covered	Ro	CB	NdR	St I	NdT	CM	NdH	Pu	So	Pe	DJ	Gal	Az	Cu	CNM
152	10	080905-090121	-317.56	Pe, DJ & Gal										i	i	I			
		080905-090724	142.00											t	t	t			
		080905-090908	390.07											t	t	✓			
		090724-090908	248.10											✓	✓	u?/t?			
153	0 & 10	070620-070805	-6.24	Gal & Az												✓	✓		
		070620-071105	-67.39													i	i		
		070620-071221	338.92													i	i		
		070620-080507	60.41													s	✓		
		070620-080807	1041.36													s	✓		
		070805-071105	-61.15													i	i		
		070805-071221	345.16													i	i		
		070805-080507	66.67													s	✓		
		070805-080622	440.26													s	✓		
		071105-080507	121.69													i	i		
		071221-080507	-278.56													i	i		
		071221-080622	-445.93													i			
		071221-081223	-54.31													i			
		080507-080622	-167.31													t	t		
		080507-080807	-901.06													✓	t		
		080507-081223	224.18													i	i		
		080622-081223	398.45													i	i		
		080807-090625	1053.16													i			
		080807-090810	621.79													t?	✓		
154	0	070707-070822	-50.92	Cu & CNM														✓	✓
		070707-080107	-326.75															✓	✓
		070707-080408	-32.68															✓	✓
		070707-080524	-406.65															✓	✓
		070707-080709	-350.79															✓	✓
		070707-090109	0.51															✓	✓
		080107-080408	294.09															t	✓
		080107-080524	-79.89															t	✓

Track	Frame	Interferogram	Average Bperp (m)	Volcanoes covered	Ro	CB	NdR	St I	NdT	CM	NdH	Pu	So	Pe	DJ	Gal	Az	Cu	CNM
154	0	080107-080709	-24.08	Cu & CNM														t	✓
		080107-090109	327.19															t	✓
		080408-080524	-373.94															✓	✓
		080408-080709	-318.07															✓	✓
		080408-090109	33.19															✓	✓
		080524-080709	55.79															t	✓
		080524-090109	407.02															✓	✓
		080709-090109	351.25															✓	✓

Abbreviations	
Ro	Romeral
CB	Cerro Bravo
NdR	Nevado del Ruiz
St I	Santa Isabel
NdT	Nevado del Tolima
CM	Cerro Machin
NdH	Nevado del Huila
Pu	Purace
So	Sotara
Pe	Volcan Petacas
DJ	Dona Juana
Gal	Galeras
Az	Azufral
Cu	Cumbal
CNM	Cerro Negro de Mayasquer

Key	
✓	Coherent
n	Noisy
t	Tropospheric contamination
i	Ionospheric contamination
u	Uplift
s	Subsidence

Appendix B: Supplementary figures for Colombian volcanoes

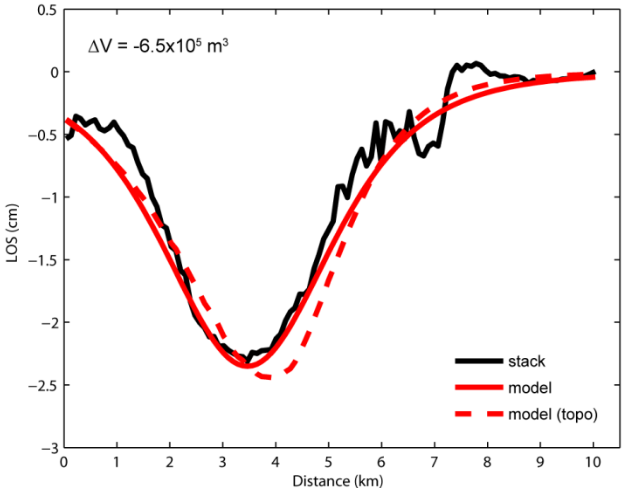

Supplementary Figure 1: 1D Rectangular sheet model (after Delaney & McTigue, 1994). Comparison between 1D rectangular sheet model and topographically corrected model shows that topographic correction has little effect on amplitude or location.

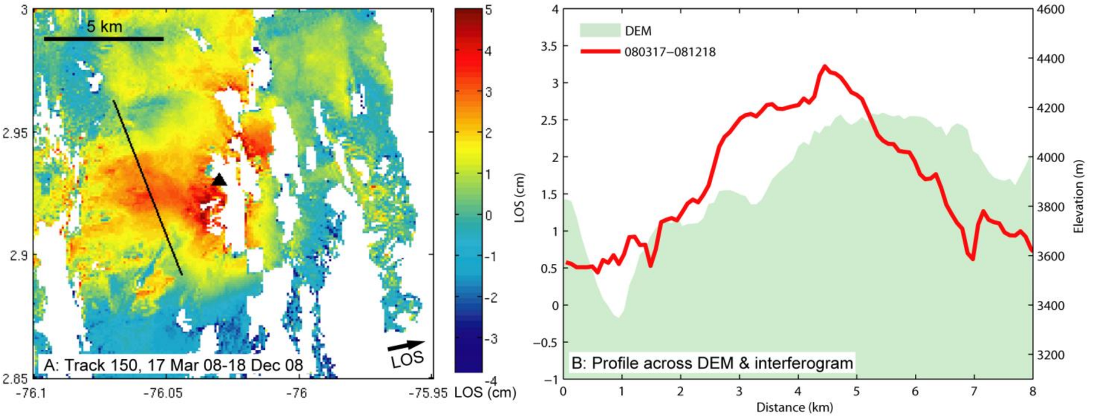

Supplementary Figure 2: Nevado del Huila. **(a)** Interferogram generated over Nevado del Huila for the period 17 Mar 08-18 Dec 08. The potential uplift signal is displayed on the western flank of the volcano, corresponding to ~ 3.5 cm LOS. The traverse used for extracting phase and elevation data is shown as the NW-SE trending line. **(b)** Profiles extracted from the interferogram & DEM. Interferogram master and slave dates in b) are in the format yymmdd.

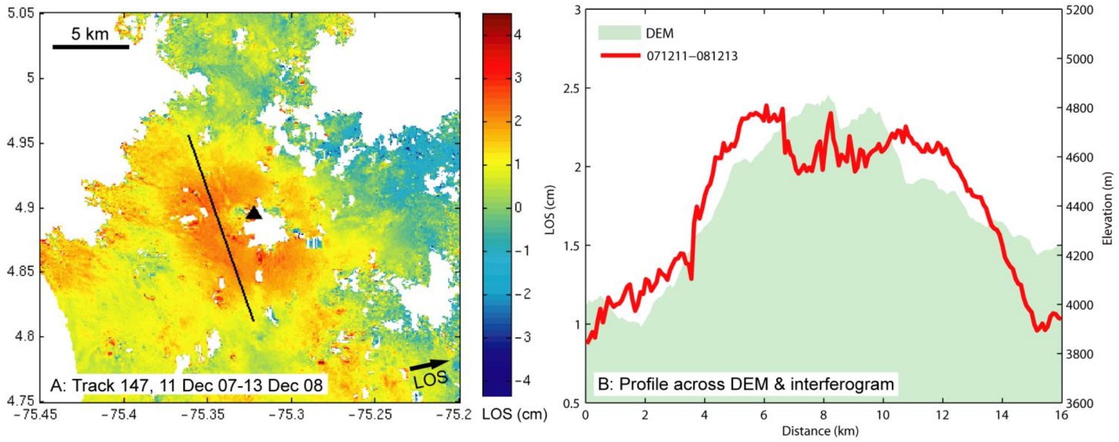

Supplementary Figure 3: Nevado del Ruiz. **(a)** Interferogram generated over Nevado del Ruiz for the period 11 Dec 07-13 Dec 08. The atmospheric signal coincides with the volcanic edifice, corresponding to ~ 2.5 cm LOS. The traverse used for extracting phase and elevation data is shown as the NW-SE trending line. **(b)** Profiles extracted from the interferogram & DEM. Interferogram master and slave dates in b) are in the format yymmdd.

Appendix C: SB interferograms used in the analysis at Santorini volcano

Date 1	Date 2	Length (days)	Bperp (m)	Track
		ERS 1/2		
20-Jun-93	07-Aug-96	1144	169	422
20-Jun-93	01-Oct-97	1564	326	422
20-Jun-93	16-Aug-00	2614	258	422
07-Aug-96	01-Oct-97	420	157	422
07-Aug-96	16-Aug-00	1470	89	422
01-Oct-97	16-Aug-00	1050	-68	422
		ENVISAT		
25-Aug-04	03-Nov-04	70	263	422
25-Aug-04	01-Jun-05	280	-163	422
25-Aug-04	23-Nov-05	455	268	422
25-Aug-04	28-Dec-05	490	121	422
25-Aug-04	08-Mar-06	560	-9	422
25-Aug-04	21-Feb-07	910	199	422
03-Nov-04	01-Jun-05	210	-426	422
03-Nov-04	23-Nov-05	385	5	422
03-Nov-04	28-Dec-05	420	-141	422
03-Nov-04	08-Mar-06	490	-271	422
03-Nov-04	21-Feb-07	840	-64	422
01-Jun-05	23-Nov-05	175	431	422
01-Jun-05	28-Dec-05	210	284	422
01-Jun-05	08-Mar-06	280	154	422
01-Jun-05	21-Feb-07	630	362	422
23-Nov-05	28-Dec-05	35	-147	422
23-Nov-05	08-Mar-06	105	-277	422
23-Nov-05	21-Feb-07	455	-69	422
23-Nov-05	06-May-09	1260	-301	422

28-Dec-05	08-Mar-06	70	-130	422
28-Dec-05	21-Feb-07	420	77	422
28-Dec-05	06-May-09	1225	-154	422
08-Mar-06	21-Feb-07	350	207	422
08-Mar-06	06-May-09	1155	-24	422
21-Feb-07	06-May-09	805	-232	422
21-Feb-07	06-Jan-10	1050	-184	422
06-May-09	06-Jan-10	245	48	422
14-Jul-04	25-May-05	315	159	329
14-Jul-04	01-Nov-06	840	302	329
14-Jul-04	18-Jun-08	1435	43	329
25-May-05	01-Nov-06	525	142	329
25-May-05	08-Aug-07	805	173	329
25-May-05	18-Jun-08	1120	-116	329
01-Nov-06	08-Aug-07	280	31	329
01-Nov-06	18-Jun-08	595	-258	329
01-Nov-06	12-Aug-09	1015	42	329
08-Aug-07	18-Jun-08	315	-289	329
08-Aug-07	12-Aug-09	735	12	329
08-Aug-07	23-Jun-10	1050	-4	329
18-Jun-08	12-Aug-09	420	301	329
18-Jun-08	23-Jun-10	735	285	329
12-Aug-09	23-Jun-10	315	-16	329
03-Mar-11	02-Apr-11	30	-170	93
03-Mar-11	02-May-11	60	-257	93
03-Mar-11	01-Jul-11	120	-226	93
03-Mar-11	31-Jul-11	150	-310	93
03-Mar-11	30-Aug-11	180	-243	93
03-Mar-11	29-Sep-11	210	-411	93
03-Mar-11	26-Feb-12	360	-93	93
02-Apr-11	02-May-11	30	-87	93
02-Apr-11	01-Jul-11	90	-56	93

02-Apr-11	31-Jul-11	120	-140	93
02-Apr-11	30-Aug-11	150	-73	93
02-Apr-11	29-Sep-11	180	-241	93
02-Apr-11	29-Oct-11	210	-413	93
02-Apr-11	28-Nov-11	240	-386	93
02-Apr-11	26-Feb-12	330	78	93
02-May-11	01-Jul-11	60	31	93
02-May-11	31-Jul-11	90	-53	93
02-May-11	30-Aug-11	120	14	93
02-May-11	29-Sep-11	150	-154	93
02-May-11	29-Oct-11	180	-327	93
02-May-11	28-Nov-11	210	-299	93
02-May-11	28-Dec-11	240	-338	93
02-May-11	27-Jan-12	270	-376	93
02-May-11	26-Feb-12	300	164	93
01-Jul-11	31-Jul-11	30	-84	93
01-Jul-11	30-Aug-11	60	-17	93
01-Jul-11	29-Sep-11	90	-184	93
01-Jul-11	29-Oct-11	120	-357	93
01-Jul-11	28-Nov-11	150	-329	93
01-Jul-11	28-Dec-11	180	-369	93
01-Jul-11	27-Jan-12	210	-406	93
01-Jul-11	26-Feb-12	240	134	93
31-Jul-11	30-Aug-11	30	67	93
31-Jul-11	29-Sep-11	60	-101	93
31-Jul-11	29-Oct-11	90	-274	93
31-Jul-11	28-Nov-11	120	-246	93
31-Jul-11	28-Dec-11	150	-285	93
31-Jul-11	27-Jan-12	180	-323	93
31-Jul-11	26-Feb-12	210	217	93
30-Aug-11	29-Sep-11	30	-168	93
30-Aug-11	29-Oct-11	60	-341	93

30-Aug-11	28-Nov-11	90	-313	93
30-Aug-11	28-Dec-11	120	-352	93
30-Aug-11	27-Jan-12	150	-390	93
30-Aug-11	26-Feb-12	180	150	93
29-Sep-11	29-Oct-11	30	-173	93
29-Sep-11	28-Nov-11	60	-145	93
29-Sep-11	28-Dec-11	90	-184	93
29-Sep-11	27-Jan-12	120	-222	93
29-Sep-11	26-Feb-12	150	318	93
29-Oct-11	28-Nov-11	30	28	93
29-Oct-11	28-Dec-11	60	-11	93
29-Oct-11	27-Jan-12	90	-49	93
28-Nov-11	28-Dec-11	30	-39	93
28-Nov-11	27-Jan-12	60	-77	93
28-Nov-11	26-Feb-12	90	463	93
28-Dec-11	27-Jan-12	30	-38	93
28-Dec-11	26-Feb-12	60	502	93
		TerraSAR-X		
14-Jul-11	25-Jul-11	11	248	85
14-Jul-11	05-Aug-11	22	94	85
14-Jul-11	16-Aug-11	33	255	85
25-Jul-11	05-Aug-11	11	-154	85
25-Jul-11	16-Aug-11	22	7	85
25-Jul-11	27-Aug-11	33	177	85
25-Jul-11	29-Sep-11	66	17	85
25-Jul-11	10-Oct-11	77	95	85
05-Aug-11	16-Aug-11	11	161	85
05-Aug-11	27-Aug-11	22	330	85
05-Aug-11	29-Sep-11	55	171	85
16-Aug-11	27-Aug-11	11	169	85
16-Aug-11	29-Sep-11	44	9	85
16-Aug-11	10-Oct-11	55	87	85

27-Aug-11	29-Sep-11	33	-160	85
27-Aug-11	10-Oct-11	44	-82	85
29-Sep-11	10-Oct-11	11	78	85
29-Sep-11	21-Oct-11	22	-314	85
29-Sep-11	23-Nov-11	55	-179	85
10-Oct-11	23-Nov-11	44	-258	85
21-Oct-11	01-Nov-11	11	-26	85
21-Oct-11	23-Nov-11	33	135	85
21-Oct-11	15-Dec-11	55	-6	85
01-Nov-11	23-Nov-11	22	161	85
01-Nov-11	15-Dec-11	44	20	85
23-Nov-11	15-Dec-11	22	-141	85
23-Nov-11	17-Jan-12	55	98	85
23-Nov-11	19-Feb-12	88	19	85
15-Dec-11	17-Jan-12	33	239	85
15-Dec-11	19-Feb-12	66	161	85
17-Jan-12	19-Feb-12	33	-78	85
17-Jan-12	23-Mar-12	66	-14	85
19-Feb-12	23-Mar-12	33	64	85
19-Feb-12	14-Apr-12	55	-28	85
19-Feb-12	17-May-12	88	17	85
23-Mar-12	14-Apr-12	22	-93	85
23-Mar-12	25-Apr-12	33	312	85
23-Mar-12	17-May-12	55	-47	85
14-Apr-12	17-May-12	33	45	85
14-Apr-12	30-Jun-12	77	-104	85
25-Apr-12	06-May-12	11	120	85
25-Apr-12	28-May-12	33	-80	85
25-Apr-12	08-Jun-12	44	69	85
06-May-12	28-May-12	22	-200	85
06-May-12	08-Jun-12	33	-51	85
06-May-12	11-Jul-12	66	-4	85

17-May-12	28-May-12	11	279	85
17-May-12	30-Jun-12	44	-149	85
28-May-12	08-Jun-12	11	149	85
28-May-12	11-Jul-12	44	196	85
28-May-12	02-Aug-12	66	84	85
28-May-12	13-Aug-12	77	-47	85
08-Jun-12	11-Jul-12	33	47	85
08-Jun-12	02-Aug-12	55	-66	85
08-Jun-12	24-Aug-12	77	-64	85
11-Jul-12	02-Aug-12	22	-113	85
11-Jul-12	13-Aug-12	33	-244	85
11-Jul-12	24-Aug-12	44	-111	85
11-Jul-12	15-Sep-12	66	-182	85
02-Aug-12	13-Aug-12	11	-131	85
02-Aug-12	24-Aug-12	22	2	85
02-Aug-12	15-Sep-12	44	-69	85
02-Aug-12	26-Sep-12	55	-34	85
13-Aug-12	24-Aug-12	11	133	85
13-Aug-12	15-Sep-12	33	62	85
13-Aug-12	26-Sep-12	44	97	85
24-Aug-12	15-Sep-12	22	-71	85
24-Aug-12	26-Sep-12	33	-35	85
15-Sep-12	26-Sep-12	11	36	85
07-Apr-12	29-Apr-12	22	-138	138
07-Apr-12	10-May-12	33	-94	138
07-Apr-12	21-May-12	44	-72	138
07-Apr-12	01-Jun-12	55	102	138
07-Apr-12	12-Jun-12	66	-111	138
07-Apr-12	04-Jul-12	88	-4	138
29-Apr-12	10-May-12	11	45	138
29-Apr-12	21-May-12	22	66	138
29-Apr-12	01-Jun-12	33	241	138

29-Apr-12	12-Jun-12	44	27	138
29-Apr-12	04-Jul-12	66	135	138
10-May-12	21-May-12	11	21	138
10-May-12	01-Jun-12	22	196	138
10-May-12	12-Jun-12	33	-17	138
10-May-12	23-Jun-12	44	235	138
10-May-12	04-Jul-12	55	90	138
10-May-12	15-Jul-12	66	141	138
10-May-12	26-Jul-12	77	64	138
10-May-12	06-Aug-12	88	-7	138
21-May-12	01-Jun-12	11	175	138
21-May-12	12-Jun-12	22	-39	138
21-May-12	23-Jun-12	33	213	138
21-May-12	04-Jul-12	44	69	138
21-May-12	15-Jul-12	55	119	138
21-May-12	26-Jul-12	66	42	138
21-May-12	06-Aug-12	77	-28	138
01-Jun-12	12-Jun-12	11	-213	138
01-Jun-12	23-Jun-12	22	38	138
01-Jun-12	04-Jul-12	33	-106	138
01-Jun-12	15-Jul-12	44	-56	138
01-Jun-12	26-Jul-12	55	-133	138
01-Jun-12	17-Aug-12	77	-74	138
12-Jun-12	23-Jun-12	11	252	138
12-Jun-12	04-Jul-12	22	107	138
12-Jun-12	15-Jul-12	33	158	138
12-Jun-12	26-Jul-12	44	81	138
12-Jun-12	06-Aug-12	55	10	138
12-Jun-12	17-Aug-12	66	139	138
12-Jun-12	28-Aug-12	77	98	138
23-Jun-12	04-Jul-12	11	-145	138
23-Jun-12	15-Jul-12	22	-94	138

23-Jun-12	26-Jul-12	33	-171	138
23-Jun-12	06-Aug-12	44	-242	138
23-Jun-12	17-Aug-12	55	-113	138
23-Jun-12	28-Aug-12	66	-154	138
23-Jun-12	08-Sep-12	77	10	138
04-Jul-12	15-Jul-12	11	50	138
04-Jul-12	26-Jul-12	22	-27	138
04-Jul-12	06-Aug-12	33	-97	138
04-Jul-12	17-Aug-12	44	32	138
04-Jul-12	28-Aug-12	55	-10	138
04-Jul-12	08-Sep-12	66	154	138
15-Jul-12	26-Jul-12	11	-77	138
15-Jul-12	06-Aug-12	22	-147	138
15-Jul-12	17-Aug-12	33	-19	138
15-Jul-12	28-Aug-12	44	-60	138
15-Jul-12	08-Sep-12	55	104	138
26-Jul-12	06-Aug-12	11	-70	138
26-Jul-12	17-Aug-12	22	58	138
26-Jul-12	28-Aug-12	33	17	138
26-Jul-12	08-Sep-12	44	181	138
26-Jul-12	19-Sep-12	55	-148	138
06-Aug-12	17-Aug-12	11	129	138
06-Aug-12	28-Aug-12	22	87	138
06-Aug-12	08-Sep-12	33	251	138
06-Aug-12	19-Sep-12	44	-78	138
17-Aug-12	28-Aug-12	11	-41	138
17-Aug-12	08-Sep-12	22	123	138
17-Aug-12	19-Sep-12	33	-207	138
28-Aug-12	08-Sep-12	11	164	138
28-Aug-12	19-Sep-12	22	-165	138
08-Sep-12	19-Sep-12	11	-329	138

Appendix D: Overview of StaMPS PS and SB methods

The StaMPS Persistent Scatterers (PS) method is outlined in detail in Hooper et al., 2007. This involves loading the single master interferograms into MATLAB (http://www.mathworks.co.uk/), estimating the phase noise for each pixel in each interferogram and selecting PS pixels based on their noise characteristics. Initial PS candidates are identified based on amplitude analysis using the amplitude dispersion index (D_A). This is defined as the ratio between the standard deviation and the mean of a series of amplitude values (Ferretti et al., 2001). The phase stability of each of the PS candidates is then estimated using phase analysis and a threshold criterion (referred to as the weed standard deviation) is used for the final PS selection (Hooper et al., 2007). A phase correction is applied to the remaining pixels to compensate for spatially-uncorrelated look angle (DEM) error. The phase is filtered to reduce noise and the final interferograms are unwrapped using the statistical cost flow algorithm. The final processing step is the estimation of the residual spatially-correlated look angle (SCLA) error, which results primarily from spatially correlated DEM error and phase contributions from atmospheric delay on the master image and residual orbital errors (Hooper et al., 2007; Hooper, 2013).

The StaMPS small baseline (SB) method is founded on the method outlined by Berardino et al. (2002) and Schmidt and Bürgmann (2003), but uses single-look rather than multi-looked images to identify the slowly-decorrelating filtered phase (SDFP) pixels (Hooper et al., 2007; Hooper, 2008; Karimzadeh et al., 2013). This improves the overall resolution. Interferograms are formed using spectrally filtered single-look-complex images from the initial StaMPS processing. Those image pairs that minimise the perpendicular, temporal and Doppler baselines are selected to reduce decorrelation (Hooper, 2008). As with the PS approach, the initial SDFP pixel selection is undertaken using amplitude analysis, but this time using amplitude difference dispersion ($D_{\Delta A}$). This is the ratio of the difference in amplitude between the master and slave (the first and second images used to form the interferogram) to the mean amplitude, which is a superior indicator of phase stability when utilising spectrally filtered data (Hooper, 2008). The remainder of the SB processing workflow undertaken in StaMPS is the same as that described previously for the PS method (Hooper et al., 2007).

Following the initial selection of SDFP candidates, the wrapped phase of the selected pixels was corrected for spatially-uncorrelated look angle (SULA) error, interferograms were unwrapped and the residual SCLA error estimated. We compared the original unwrapped interferograms (corrected for SULA error) with those corrected for SCLA and master atmospheric and orbital errors (AOE), to check for an improvement in signal to noise ratio between the two. Where no improvement was evident, individual interferograms were examined for unwrapping errors and atmospheric artefacts. Typically, the unwrapping and SCLA correction was only performed once, with the exception of interferograms formed using data from ENVISAT Track 93, in which two scenes were identified containing significant processing/atmospheric artefacts. These scenes were subsequently dropped from the SCLA calculation and the unwrapping was rerun. This resulted in a substantial improvement in the volumetric time series analysis (section 4.6.1).

Appendix E: Interferometric phase-elevation plots used in the analysis at Santorini volcano

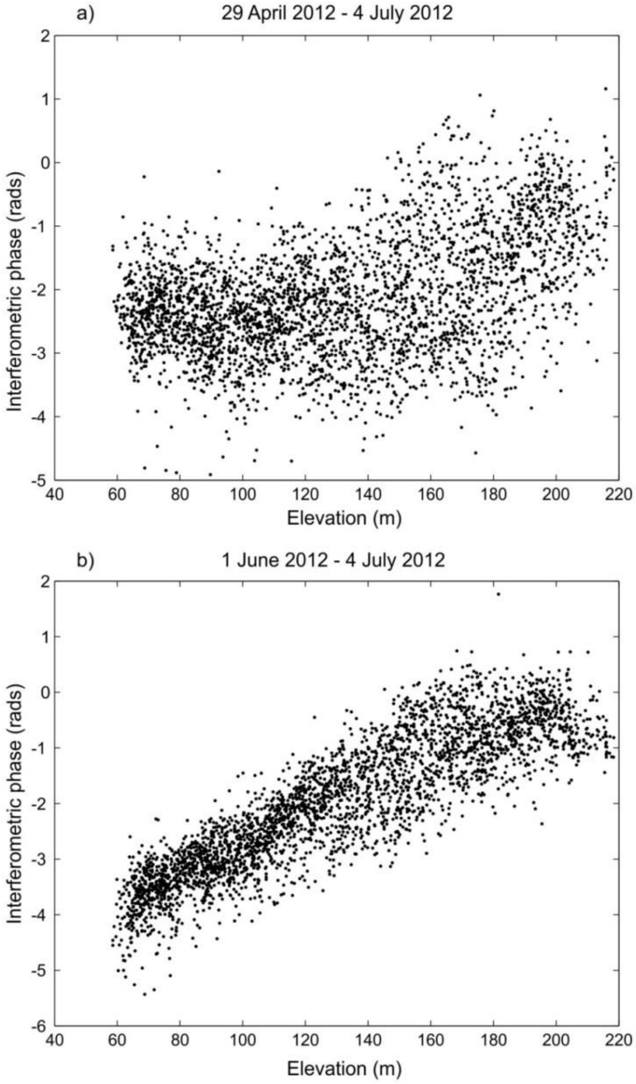

Supplementary Figure 4: *Interferometric phase-elevation plots for a non-deforming area on the east of Thera.* ***(a)*** *Interferogram from TSX track 138, covering the period 29 April 2012-4 Jul 2012 shows no correlation between phase and elevation.* ***(b)*** *Interferogram from TSX track 138, covering the period 1 June 2012-4 Jul 2012 shows a strong correlation between phase and elevation. As such this interferogram was not included in the analysis.*

Appendix F: Comparison of ^{222}Rn measurements obtained from soil gas studies at various volcanoes

Volcano	**References**	**^{222}Rn (Bq m^{-3}) (mean)**	**^{222}Rn (Bq m^{-3}) (range)**
Santorini	This study	2,187	31 to 10,469
Etna	Giammanco et al. (2007)	10,446	232 to 104,300
	Neri et al. (2011)	10,133	266 to 52,000
Stromboli	Laiolo et al. (2012)	1,800 (NE flank)	-
		12,600 (summit)	
El Teide Volcano Complex	Soler et al. (2004)	~17,000	~10,000 to ~22,000
Merapi	Zimmer and Erzinger (2003)	-	4,000 to 15,000
Popocatépetl	Segovia et al. (2001)	-	~250 to ~3,250 (1998 and 1999 surveys)

Appendix G: Mixing equations

When mixing two endmember gases (A, B), where we mix a fraction ϕ_A of gas A into gas B, the hybrid isotopic compositions will be:

$$\left(\delta^{13}C\right)_{hybrid} = \frac{C_A^{CO_2}\phi_A\left(\delta^{13}C\right)_A + C_B^{CO_2}\left(1-\phi_A\right)\left(\delta^{13}C\right)_B}{C_A^{CO_2}\phi_A + C_B^{CO_2}\left(1-\phi_A\right)}$$ and

(6B.1)

$$\left(\frac{(^{222}Rn)}{CO_2}\right)_{hybrid} = \frac{C_A^{CO_2}\phi_A\left(\frac{(^{222}Rn)}{CO_2}\right)_A + C_B^{CO_2}\left(1-\phi_A\right)\left(\frac{(^{222}Rn)}{CO_2}\right)_B}{C_A^{CO_2}\phi_A + C_B^{CO_2}\left(1-\phi_A\right)}$$

(6B.2)

Where:

$C_X^{CO_2}$ = concentration of carbon dioxide in ppm in gas X

$(\delta^{13}C)_X$ = isotopic composition of carbon in units of per mil in gas X

$\left(\frac{(^{222}Rn)}{CO_2}\right)_X$ = radon to carbon dioxide ratio in Bq kg^{-1} in gas X

Bibliography

Alfaro, C. M. & Zapata G, J. (1997). Acid gas emissions from Galeras volcano, Colombia, 1989–1994. *Journal of Volcanology and Geothermal Research*, *77*(1), 209-228.

Allard, P. (2010). A CO_2-rich gas trigger of explosive paroxysms at Stromboli basaltic volcano, Italy. *Journal of Volcanology and Geothermal Research*, *189*(3), 363-374.

Amelung, F., Jónsson, S., Zebker, H. & Segall, P. (2000). Widespread uplift and ‘trapdoor’faulting on Galapagos volcanoes observed with radar interferometry. *Nature*, *407*(6807), 993-996.

Amelung, F. & Bell, J. W. (2003). Interferometric synthetic aperture radar observations of the 1994 Double Spring Flat, Nevada, earthquake (M5. 9): Main shock accompanied by triggered slip on a conjugate fault. *Journal of Geophysical Research: Solid Earth (1978–2012)*, *108*(B9).

Andújar, J., Scaillet, B., Pichavant, M. & Druitt, T. H. (2010). Differentiation conditions of a basaltic magma from Santorini and its bearing on andesitic/dacitic magma production. In *AGU Fall Meeting Abstracts* (Vol. 1, p. 2354).

Archbold, M. J., Mckee, C. O., Talai, B., Mori, J. & De Saint Ours, P. (1988). Electronic distance measuring network monitoring during the Rabaul seismicity/deformational crisis of 1983–1985. *Journal of Geophysical Research: Solid Earth (1978–2012)*, *93*(B10), 12123-12136.

Aristotle University of Thessaloniki. (2005-). *Seismicity Catalogs.* Available: http://geophysics.geo.auth.gr/the_seisnet/WEBSITE_2005/station_index_en.html. Last accessed 20th May 2013.

Baker, S. & Amelung, F. (2012). Top-down inflation and deflation at the summit of Kīlauea Volcano, Hawai‘i observed with InSAR. *Journal of Geophysical Research: Solid Earth (1978–2012)*, *117*(B12).

Baltsavias, E. P. (1999). Airborne laser scanning: basic relations and formulas. *ISPRS Journal of Photogrammetry and Remote Sensing*, *54*(2), 199-214.

Banks, N. G., Carvajal, C., Mora, H. & Tryggvason, E. (1990). Deformation monitoring at Nevado del Ruiz, Colombia-October 1985-March 1988. *Journal of Volcanology and Geothermal Research*, *41*(1), 269-295.

Barton, M. & Huijsmans, J. P. (1986). Post-caldera dacites from the Santorini volcanic complex, Aegean Sea, Greece: an example of the eruption of lavas of near-constant composition over a 2,200 year period. *Contributions to Mineralogy and Petrology*, *94*(4), 472-495.

Bathke, H., Shirzaei, M. & Walter, T. R. (2011). Inflation and deflation at the steep-sided Llaima stratovolcano (Chile) detected by using InSAR. *Geophysical Research Letters*, *38*(10).

Battaglia, M., Roberts, C. & Segall, P. (1999). Magma intrusion beneath Long Valley caldera confirmed by temporal changes in gravity. *Science*, *285*(5436), 2119-2122.

Baubron, J. C., Allard, P., Sabroux, J. C., Tedesco, D. & Toutaln, J. P. (1991). Soil gas emanations as precursory indicators of volcanic eruptions. *Journal of the Geological Society*, *148*(3), 571-576.

Baxter, P. J. & Gresham, A. (1997). Deaths and injuries in the eruption of Galeras Volcano, Colombia, 14 January 1993. *Journal of Volcanology and Geothermal Research*, *77*(1), 325-338.

Bechon, F. & Monsalve, M. L. (1991). Activité récente préhistorique du volcan Azufral (SW de la Colombie). *Comptes rendus de l'Académie des sciences. Série 2, Mécanique, Physique, Chimie, Sciences de l'univers, Sciences de la Terre*, *313*(1), 99-104.

Benz, H. M., Chouet, B. A., Dawson, P. B., Lahr, J. C., Page, R. A. & Hole, J. A. (1996). Three-dimensional P and S wave velocity structure of Redoubt Volcano, Alaska. *Journal of Geophysical Research: Solid Earth (1978–2012)*, *101*(B4), 8111-8128.

Berardino, P., Fornaro, G., Lanari, R. & Sansosti, E. (2002). A new algorithm for surface deformation monitoring based on small baseline differential SAR interferograms. *Geoscience and Remote Sensing, IEEE Transactions on*, *40*(11), 2375-2383.

Berrino, G., Rymer, H., Brown, G. C. & Corrado, G. (1992). Gravity-height correlations for unrest at calderas. *Journal of Volcanology and Geothermal Research*, *53*(1), 11-26.

Beutler, G., Rothacher, M., Schaer, S., Springer, T. A., Kouba, J., & Neilan, R. E. (1999). The International GPS Service (IGS): an interdisciplinary service in support of earth sciences. *Advances in Space Research*, *23*(4), 631-653.

Biggs, J., Wright, T., Lu, Z. & Parsons, B. (2007). Multi-interferogram method for measuring interseismic deformation: Denali fault, Alaska. *Geophysical Journal International*, *170*(3), 1165-1179.

Biggs, J., Anthony, E. Y. & Ebinger, C. J. (2009). Multiple inflation and deflation events at Kenyan volcanoes, East African Rift. *Geology*, *37*(11), 979-982.

Biggs, J., Mothes, P., Ruiz, M., Amelung, F., Dixon, T. H., Baker, S. & Hong, S. H. (2010a). Stratovolcano growth by co-eruptive intrusion: The 2008 eruption of Tungurahua Ecuador. *Geophysical Research Letters*, *37*(21).

Biggs, J., Lu, Z., Fournier, T. & Freymueller, J. T. (2010b). Magma flux at Okmok Volcano, Alaska, from a joint inversion of continuous GPS, campaign GPS, and interferometric synthetic aperture radar. *Journal of Geophysical Research: Solid Earth (1978–2012), 115*(B12).

Bloomer, S. H., Stern, R. J. & Smoot, N. C. (1989). Physical volcanology of the submarine Mariana and Volcano Arcs. *Bulletin of Volcanology, 51*(3), 210-224.

Bohnhoff, M., Rische, M., Meier, T., Becker, D., Stavrakakis, G. & Harjes, H. P. (2006). Microseismic activity in the Hellenic Volcanic Arc, Greece, with emphasis on the seismotectonic setting of the Santorini–Amorgos zone. *Tectonophysics, 423*(1), 17-33.

Boichu, M., Villemant, B. & Boudon, G. (2008). A model for episodic degassing of an andesitic magma intrusion. *Journal of Geophysical Research: Solid Earth (1978–2012), 113*(B7).

Bomford, G. (1980) *Geodesy 4th edn* (Oxford Univ. Press).

Bonaccorso, A., Aloisi, M. & Mattia, M. (2002). Dike emplacement forerunning the Etna July 2001 eruption modeled through continuous tilt and GPS data. *Geophysical Research Letters*, *29*(13), 2-1–2-4.

Bonaccorso, A., Sansosti, E. & Berardino, P. (2004). Comparison of integrated geodetic data models and satellite radar interferograms to infer magma storage during the 1991–1993 Mt. Etna eruption. In *Geodetic and Geophysical Effects Associated with Seismic and Volcanic Hazards* (pp. 1345-1357). Birkhäuser Basel.

Bonforte, A., Federico, C., Giammanco, S., Guglielmino, F., Liuzzo, M. & Neri, M. (2013). Soil gases and SAR measurements reveal hidden faults on the sliding flank of Mt. Etna (Italy). *Journal of Volcanology and Geothermal Research*, 251, 27-40.

Borsa, A., & Minster, J. B. (2012). Rapid Determination of Near-Fault Earthquake Deformation Using Differential LiDAR. *Bulletin of the Seismological Society of America*, *102*(4), 1335-1347.

Boström, K., Ingri, J., Boström, B., Andersson, P. & Löfvendahl, R. (1990). Metallogenesis at Santorini; a subduction-zone related process; II, Geochemistry and origin of hydrothermal solutions on Nea Kameni, Santorini, Greece. *Thera and the Aegean World III. The Thera Foundation. London, 291,* 299.

Bottinga, Y. & Javoy, M. (1989). MORB degassing: evolution of CO_2. *Earth and planetary science letters, 95*(3), 215-225.

Botz, R., Stüben, D., Winckler, G., Bayer, R., Schmitt, M. & Faber, E. (1996). Hydrothermal gases offshore Milos Island, Greece. *Chemical Geology, 130*(3), 161-173.

Briole, P., Massonnet, D. & Delacourt, C. (1997). Post-eruptive deformation associated with the 1986–87 and 1989 lava flows of Etna detected by radar interferometry. *Geophysical Research Letters*, *24*(1), 37-40.

Brombach, T., Caliro, S., Chiodini, G., Fiebig, J., Hunziker, J. C. & Raco, B. (2003). Geochemical evidence for mixing of magmatic fluids with seawater, Nisyros hydrothermal system, Greece. *Bulletin of Volcanology*, *65*(7), 505-516.

Budetta, G. & Carbone, D. (1997). Potential application of the Scintrex CG-3M gravimeter for monitoring volcanic activity: results of field trials on Mt. Etna, Sicily. *Journal of Volcanology and Geothermal Research*, *76*(3), 199-214.

Budetta, G., Carbone, D. & Greco, F. (1999). Subsurface mass redistributions at Mount Etna (Italy) during the 1995–1996 explosive activity detected by microgravity studies. *Geophysical Journal International*, *138*(1), 77-88.

Bürgmann, R., Rosen, P. A. & Fielding, E. J. (2000). Synthetic aperture radar interferometry to measure Earth's surface topography and its deformation. *Annual Review of Earth and Planetary Sciences, 28*(1), 169-209.

Burton, M., Neri, M. & Condarelli, D. (2004). High spatial resolution radon measurements reveal hidden active faults on Mt. Etna. *Geophysical Research Letters, 31*(7).

Butz, A., Guerlet, S., Hasekamp, O., Schepers, D., Galli, A., Aben, I., Frankenberg, C., Hartmann, J.M., Tran, H., Kuze, A., Keppel-Aleks, G., Toon, G., Wunch, D., Wennberg, P., Deutscher, N., Griffith, D., Macatangay, R., Messerschmidt, J., Notholt, J. & Warneke, T. (2011). Toward accurate CO2 and CH4 observations from GOSAT. *Geophysical Research Letters*, *38*(14).

Buurman, H., West, M. E. & Roman, D. C. (2013). Using repeating volcano-tectonic earthquakes to track post-eruptive activity in the conduit system at Redoubt Volcano, Alaska. *Geology*, *41*(4), 511-514.

Caliro, S., Chiodini, G., Galluzzo, D., Granieri, D., La Rocca, M., Saccorotti, G. & Ventura, G. (2005). Recent activity of Nisyros volcano (Greece) inferred from structural, geochemical and seismological data. *Bulletin of Volcanology*, *67*(4), 358-369.

Calvache V, M. L., Cortés J, G. P. & Williams, S. N. (1997). Stratigraphy and chronology of the Galeras volcanic complex, Colombia. *Journal of Volcanology and Geothermal Research*, *77*(1), 5-19.

Calvache V, M. L. & Williams, S. N. (1997). Geochemistry and petrology of the Galeras Volcanic complex, Colombia. *Journal of Volcanology and Geothermal Research*, *77*(1), 21-38.

Capasso, G., Favara, R. & Inguaggiato, S. (1997). Chemical features and isotopic composition of gaseous manifestations on Vulcano Island, Aeolian Islands, Italy: an interpretative model of fluid circulation. *Geochimica et Cosmochimica Acta*, *61*(16), 3425-3440.

Carbone, D., Budetta, G., Greco, F. & Rymer, H. (2003). Combined discrete and continuous gravity observations at Mount Etna. *Journal of Volcanology and Geothermal Research*, *123*(1), 123-135.

Carcolé, E., Ugalde, A. & Vargas, C. A. (2006). Three-dimensional spatial distribution of scatterers in Galeras volcano, Colombia. *Geophysical Research Letters*, *33*(8).

Cardellini, C., Chiodini, G. & Frondini, F. (2003). Application of stochastic simulation to CO_2 flux from soil: mapping and quantification of gas release. *Journal of Geophysical Research: Solid Earth (1978–2012)*, *108*(B9).

Caress, D.W., Thomas, H., Kirkwood, W.J., McEwen, R., Henthorn, R., Clague, D.A., Paull, C.K., Paduan, J. & Maier, K.L. (2008). High-Resolution Multibeam, Sidescan, and Subbottom Surveys Using the MBARI AUV D. Allan B. *Marine habitat mapping technology for Alaska*, 47-69.

Carn, S. A., Krueger, A. J., Bluth, G. J. S., Schaefer, S. J., Krotkov, N. A., Watson, I. M. & Datta, S. (2003). Volcanic eruption detection by the Total Ozone Mapping Spectrometer (TOMS) instruments: a 22-year record of sulphur dioxide and ash emissions. *Geological Society, London, Special Publications*, *213*(1), 177-202.

Carslaw, H. S. & Jaeger, J. C. (1959). Conduction of heat in solids. *Oxford: Clarendon Press, 2nd ed.*, *1*.

Cervelli, P., Segall, P., Johnson, K., Lisowski, M., & Miklius, A. (2002a). Sudden aseismic fault slip on the south flank of Kilauea volcano. *Nature*, *415*(6875), 1014-1018.

Cervelli, P., Segall, P., Amelung, F., Garbeil, H., Meertens, C., Owen, S., Miklius, A. & Lisowski, M. (2002b). The 12 September 1999 upper east rift zone dike intrusion at Kilauea volcano, Hawaii. *Journal of Geophysical Research*, 107(B7), 2150.

Chacko, T., Mayeda, T. K., Clayton, R. N. & Goldsmith, J. R. (1991). Oxygen and carbon isotope fractionations between CO_2 and calcite. *Geochimica et Cosmochimica Acta*, *55*(10), 2867-2882.

Chang, W. L., Smith, R. B., Farrell, J. & Puskas, C. M. (2010). An extraordinary episode of Yellowstone caldera uplift, 2004–2010, from GPS and InSAR observations. *Geophysical Research Letters*, *37*(23).

Chiarabba, C., Amato, A., Boschi, E. & Barberi, F. (2000). Recent seismicity and tomographic modeling of the Mount Etna plumbing system. *Journal of Geophysical Research: Solid Earth (1978–2012)*, *105*(B5), 10923-10938.

Chiodini, G. & Marini, L. (1998). Hydrothermal gas equilibria: the H_2O – H_2 – CO_2 – CO – CH_4 system. *Geochimica et Cosmochimica Acta*, *62*(15), 2673-2687.

Chiodini, G., Cioni, R., Guidi, M., Raco, B. & Marini, L. (1998). Soil CO_2 flux measurements in volcanic and geothermal areas. *Applied Geochemistry*, *13*(5), 543-552.

Chiodini, G., Frondini, F., Cardellini, C., Granieri, D., Marini, L. & Ventura, G. (2001). CO_2 degassing and energy release at Solfatara volcano, Campi Flegrei, Italy. *Journal of Geophysical Research: Solid Earth (1978–2012)*, *106*(B8), 16213-16221.

Chiodini, G., Caliro, S., Cardellini, C., Avino, R., Granieri, D. & Schmidt, A. (2008). Carbon isotopic composition of soil CO_2 efflux, a powerful method to discriminate different sources feeding soil CO_2 degassing in volcanic-hydrothermal areas. *Earth and Planetary Science Letters*, *274*(3), 372-379.

Chiodini, G., Caliro, S., Aiuppa, A., Avino, R., Granieri, D., Moretti, R. & Parello, F. (2011). First $^{13}C/^{12}C$ isotopic characterisation of volcanic plume CO_2. *Bulletin of Volcanology*, *73*(5), 531-542.

Chiodini, G., Caliro, S., De Martino, P., Avino, R. & Gherardi, F. (2012). Early signals of new volcanic unrest at Campi Flegrei caldera? Insights from geochemical data and physical simulations. *Geology*, *40*(10), 943-946.

Chouet, B. (1992). A seismic model for the source of long-period events and harmonic tremor. In *Volcanic seismology* (pp. 133-156). Springer Berlin Heidelberg.

Chouet, B. A., Page, R. A., Stephens, C. D., Lahr, J. C. & Power, J. A. (1994). Precursory swarms of long-period events at Redoubt Volcano (1989–1990), Alaska: Their origin and use as a forecasting tool. *Journal of Volcanology and Geothermal Research*, *62*(1), 95-135.

Chouet, B. A. & Matoza, R. S. (2013). A multi-decadal view of seismic methods for detecting precursors of magma movement and eruption. *Journal of Volcanology and Geothermal Research*, *252*, 108-175.

Cigolini, C., Borgia, A., Cassertano, L. (1983). Intracrateric activity, aa-block lava, viscosity and flow dynamics: Arenal Volcano, Costa Rica. *Journal of Volcanology and Geothermal Research*, *20*, 155-176.

Clark, J. F. & Turekian, K. K. (1990). Time scale of hydrothermal water-rock reactions in Yellowstone National Park based on radium isotopes and radon. *Journal of Volcanology and Geothermal Research*, *40*(2), 169-180.

Coltelli, M., Proietti, C., Branca, S., Marsella, M., Andronico, D. & Lodato, L. (2007). Analysis of the 2001 lava flow eruption of Mt. Etna from three-dimensional mapping. *Journal of Geophysical Research: Earth Surface (2003–2012)*, *112*(F2).

Cornelius, R. R. & Voight, B. (1994). Seismological aspects of the 1989–1990 eruption at Redoubt Volcano, Alaska: The materials failure forecast method (Ffm) with RSAM and SSAM seismic data. *Journal of Volcanology and Geothermal Research, 62*(1), 469-498.

Cortés J, G. P. & Raigosa A, J. (1997). A synthesis of the recent activity of Galeras volcano, Colombia: Seven years of continuous surveillance, 1989–1995. *Journal of Volcanology and Geothermal Research, 77*(1), 101-114.

Cottrell, E., Gardner, J. E. & Rutherford, M. J. (1999). Petrologic and experimental evidence for the movement and heating of the pre-eruptive Minoan rhyodacite (Santorini, Greece). *Contributions to Mineralogy and Petrology*, *135*(4), 315-331.

Crider, J. G., Hill Johnsen, K. & Williams-Jones, G. (2008). Thirty-year gravity change at Mount Baker Volcano, Washington, USA: Extracting the signal from under the ice. *Geophysical Research Letters*, *35*(20).

Cruz, F. G. & Chouet, B. A. (1997). Long-period events, the most characteristic seismicity accompanying the emplacement and extrusion of a lava dome in Galeras Volcano, Colombia, in 1991. *Journal of Volcanology and Geothermal Research, 77*(1), 121-158.

Dach, R., Hugentobler, U., Fridez, P. & Meindl, M. (2007) Bernese GPS Software Version 5.0, User Manual, Tech. Rep., (Astronomical Institute, Univ. Bern).

da Corogna, L. (1867). *De l'influence des émanations volcaniques sur les êtres organisés: particuliérement étudiée à Santorin pendant l'éruption de 1866*. A. Delahaye.

D'Alessandro, W., Brusca, L., Kyriakopoulos, K., Michas, G. & Papadakis, G. (2008). Methana, the westernmost active volcanic system of the south Aegean arc (Greece): Insight from fluids geochemistry. *Journal of Volcanology and Geothermal Research, 178*(4), 818-828.

Dana, P. H. (1997). Global Positioning System (GPS) time dissemination for real-time applications. *Real-Time Systems, 12*(1), 9-40.

D'Auria, L., Giudicepietro, F., Aquino, I., Borriello, G., Del Gaudio, C., Lo Bascio, D., Martini, M., Ricciardi, G. P., Ricciolino, P., & Ricco, C. (2011). Repeated fluid-transfer episodes as a mechanism for the recent dynamics of Campi Flegrei caldera (1989–2010). *Journal of Geophysical Research: Solid Earth (1978–2012), 116*(B4).

Davis, P. M. (1986). Surface deformation due to inflation of an arbitrarily oriented triaxial ellipsoidal cavity in an elastic half-space, with reference to Kilauea volcano, Hawaii. *Journal of Geophysical Research: Solid Earth (1978–2012), 91*(B7), 7429-7438.

Dawson, P. B., Chouet, B. A., Okubo, P. G., Villaseñor, A. & Benz, H. M. (1999). Three-dimensional velocity structure of the Kilauea Caldera, Hawaii. *Geophysical research letters, 26*(18), 2805-2808.

Deardorff, N. D. & Cashman, K. V. (2012). Emplacement conditions of the c. 1,600-year bp Collier Cone lava flow, Oregon: a LiDAR investigation. *Bulletin of Volcanology*, *74*(9), 2051-2066.

Deegan, F. M., Troll, V. R., Freda, C., Misiti, V., Chadwick, J. P., McLeod, C. L. & Davidson, J. P. (2010). Magma–carbonate interaction processes and associated CO_2 release at Merapi Volcano, Indonesia: insights from experimental petrology. *Journal of Petrology*, *51*(5), 1027-1051.

Delaney, P. T. & McTigue, D. F. (1994). Volume of magma accumulation or withdrawal estimated from surface uplift or subsidence, with application to the 1960 collapse of Kilauea Volcano. *Bulletin of Volcanology*, *56*(6-7), 417-424.

Del Gaudio, C., Aquino, I., Ricciardi, G. P., Ricco, C., & Scandone, R. (2010). Unrest episodes at Campi Flegrei: A reconstruction of vertical ground movements during 1905–2009. *Journal of Volcanology and Geothermal Research*, *195*(1), 48-56.

Deutsch, C. V. & Journel, A. G. (1998). GSLIB: Geostatistical software library and user’s guide (GSLIB).

de Zeeuw-van Dalfsen, E., Rymer, H., Sturkell, E., Pedersen, R., Hooper, A., Sigmundsson, F., & Ófeigsson, B. (2013). Geodetic data shed light on ongoing caldera subsidence at Askja, Iceland. *Bulletin of Volcanology*, *75*(5), 1-13.

Dimitriadis, I., Karagianni, E., Panagiotopoulos, D., Papazachos, C., Hatzidimitriou, P., Bohnhoff, M., Rische, M. & Meier, T. (2009). Seismicity and active tectonics at Coloumbo Reef (Aegean Sea, Greece): Monitoring an active volcano at Santorini Volcanic Center using a temporary seismic network. *Tectonophysics*, *465*(1), 136-149.

Di Rocco, T., Freda, C., Gaeta, M., Mollo, S. & Dallai, L. (2012). Magma Chambers Emplaced in Carbonate Substrate: Petrogenesis of Skarn and Cumulate Rocks and Implications for CO_2 Degassing in Volcanic Areas. *Journal of Petrology*, *53*(11), 2307-2332.

d’Oreye, N., González, P. J., Shuler, A., Oth, A., Bagalwa, L., Ekström, G., Kavotha D., Kervyn, F., Lucas, C., Lukaya, F., Osodundu, E., Wauthier, C. & Fernández, J. (2011). Source parameters of the 2008 Bukavu-Cyangugu earthquake estimated from InSAR and teleseismic data. *Geophysical Journal International*, *184*(2), 934-948.

Dotsika, E., Poutoukis, D., Michelot, J. L. & Raco, B. (2009). Natural tracers for identifying the origin of the thermal fluids emerging along the Aegean Volcanic arc (Greece): Evidence of Arc-Type Magmatic Water (ATMW) participation. *Journal of Volcanology and Geothermal Research*, *179*(1), 19-32.

Dow, J. M., Neilan, R. E. & Rizos, C. (2009). The international GNSS service in a changing landscape of global navigation satellite systems. *Journal of Geodesy*, *83*(3-4), 191-198.

Dragoni, M. & Magnanensi, C. (1989). Displacement and stress produced by a pressurized, spherical magma chamber, surrounded by a viscoelastic shell. *Physics of the Earth and Planetary Interiors*, *56*(3), 316-328.

Druitt, T. H., Mellors, R. A., Pyle, D. M. & Sparks, R. S. J. (1989). Explosive volcanism on Santorini, Greece. *Geological Magazine*, *126*(2), 95-126.

Druitt, T.H., Edwards, L., Mellors, R.M., Pyle, D.M., Sparks, R.S.J., Lanphere, M., Davies, M., Barreiro, B. (1999). Santorini volcano. *Geological Society, London, Memoirs*, 19.

Druitt, T. H., Costa, F., Deloule, E., Dungan, M. & Scaillet, B. (2012). Decadal to monthly timescales of magma transfer and reservoir growth at a caldera volcano. *Nature*, *482*(7383), 77-80.

Dvorak, J. J. & Dzurisin, D. (1997). Volcano geodesy: The search for magma reservoirs and the formation of eruptive vents. *Reviews of Geophysics*, *35*(3), 343-384.

Dymond, J., Cobler, R., Gordon, L., Biscaye, P. & Mathieu, G. (1983). ^{226}Ra and ^{222}Rn content of Galapagos Rift hydrothermal waters – the importance of low-temperature interactions with crustal rocks. *Earth and Planetary Science Letters*, *64*(3), 417-429.

Dzurisin, D., Poland, M. P. & Bürgmann, R. (2002). Steady subsidence of Medicine Lake volcano, northern California, revealed by repeated leveling surveys. *Journal of Geophysical Research*, *107*(B12), 2372.

Dzurisin, D., Lisowski, M., Wicks, C. W., Poland, M. P. & Endo, E. T. (2006). Geodetic observations and modeling of magmatic inflation at the Three Sisters volcanic center, central Oregon Cascade Range, USA. *Journal of Volcanology and Geothermal Research*, *150*(1), 35-54.

Ebmeier, S. K., Biggs, J., Mather, T. A., Wadge, G. & Amelung, F. (2010). Steady downslope movement on the western flank of Arenal volcano, Costa Rica. *Geochemistry, Geophysics, Geosystems*, *11*(12).

Ebmeier, S. K., Biggs, J., Mather, T. A., Elliott, J. R., Wadge, G. & Amelung, F. (2012). Measuring large topographic change with InSAR: Lava thicknesses, extrusion rate and subsidence rate at Santiaguito volcano, Guatemala. *Earth and Planetary Science Letters*, *335*, 216-225.

Eggers, A. A. (1983). Temporal gravity and elevation changes at Pacaya volcano, Guatemala. *Journal of Volcanology and Geothermal Research*, *19*(3), 223-237.

Elsworth, D., Mattioli, G., Taron, J., Voight, B. & Herd, R. (2008). Implications of magma transfer between multiple reservoirs on eruption cycling. *Science*, *322*(5899), 246-248.

Endo, E. T. & Murray, T. (1991). Real-time seismic amplitude measurement (RSAM): a volcano monitoring and prediction tool. *Bulletin of Volcanology*, *53*(7), 533-545.

England, P. C., Walker, R. T., Fu, B., & Floyd, M. A. (2013). A bound on the viscosity of the Tibetan crust from the horizontality of palaeolake shorelines. *Earth and Planetary Science Letters*, *375*, 44-56.

Farrar, C. D., Sorey, M. L., Evans, W. C., Howle, J. F., Kerr, B. D., Kennedy, B. M., King, Y. & Southon, J. R. (1995). Forest-killing diffuse CO_2 emission at Mammoth Mountain as a sign of magmatic unrest. *Nature*, *376*(6542), 675-678.

Ferretti, A., Prati, C. & Rocca, F. (2001). Permanent scatterers in SAR interferometry. *Geoscience and Remote Sensing, IEEE Transactions on*, *39*(1), 8-20.

Feuillet, N. (2013). The 2011-2012 unrest at Santorini rift: Stress interaction between active faulting and volcanism. *Geophysical Research Letters*.

Fews, A. P. & Henshaw, D. L. (1982). High resolution alpha particle spectroscopy using CR-39 plastic track detector. *Nuclear Instruments and Methods in Physics Research*, *197*(2), 517-529.

Fiebig, J., Chiodini, G., Caliro, S., Rizzo, A., Spangenberg, J. & Hunziker, J. C. (2004). and isotopic equilibrium between CO_2 and CH_4 in fumarolic gas discharges: generation of CH_4 in arc magmatic-hydrothermal systems. *Geochimica et cosmochimica acta*, *68*(10), 2321-2334.

Fischer, T. P., Morrissey, M. M., Calvache, V. M. L., Gómez, M. D., Torres, C. R., Stix, J. & Williams, S. N. (1994). Correlations between SO_2 flux and long-period seismicity at Galeras volcano. *Nature*, *368*(6467), 135-137.

Fischer, T. P., Arehart, G. B., Sturchio, N. C. & Williams, S. N. (1996). The relationship between fumarole gas composition and eruptive activity at Galeras Volcano, Colombia. *Geology*, *24*(6), 531-534.

Fischer, T. P., Sturchio, N. C., Stix, J., Arehart, G. B., Counce, D. & Williams, S. N. (1997). The chemical and isotopic composition of fumarolic gases and spring discharges from Galeras Volcano, Colombia. *Journal of Volcanology and Geothermal Research*, *77*(1), 229-253.

Flentje, H., Claude, H., Elste, T., Gilge, S., Köhler, U., Plass-Dülmer, C., Steinbrecht, W., Thomas, W., Werner, A. & Fricke, W. (2010). The Eyjafjallajökull eruption in April 2010–detection of volcanic plume using in-situ measurements, ozone sondes and lidar-ceilometer profiles. *Atmospheric Chemistry and Physics*, *10*(20), 10085-10092.

Fornaciai, A., Bisson, M., Landi, P., Mazzarini, F. & Pareschi, M. T. (2010). A LiDAR survey of Stromboli volcano (Italy): Digital elevation model-based geomorphology and intensity analysis. *International Journal of Remote Sensing*, *31*(12), 3177-3194.

Foumelis, M., Trasatti, E., Papageorgiou, E., Stramondo, S. & Parcharidis, I. (2013). Monitoring Santorini volcano (Greece) breathing from space. *Geophysical Journal International*, *193*(1), 161-170.

Fouqué, F. (1879). *Santorin et ses éruptions*. G. Masson.) (Translation: McBirney, A. R. *Santorini and Its Eruptions by Ferdinand Fouqué* (Johns Hopkins Univ. Press 1998).

Fournier, T. J., Pritchard, M. E. & Riddick, S. N. (2010). Duration, magnitude, and frequency of subaerial volcano deformation events: New results from Latin America using InSAR and a global synthesis. *Geochemistry, Geophysics, Geosystems*, *11*(1).

Friedrich, W. L., Kromer, B., Friedrich, M., Heinemeier, J., Pfeiffer, T. & Talamo, S. (2006). Santorini eruption radiocarbon dated to 1627-1600 BC. *Science*, *312*(5773), 548-548.

Fukushima, Y., Cayol, V. & Durand, P. (2005). Finding realistic dike models from interferometric synthetic aperture radar data: The February 2000 eruption at Piton de la Fournaise. *Journal of Geophysical Research: Solid Earth (1978–2012)*, *110*(B3).

Fytikas, M., Kolios, N., Vougioukalakis, G. (1990). Post-Minoan activity of the Santorini volcano: Volcanic hazard and risk, forecasting possibilities. In: Hardy, D.A., Keller, J., Galanopoulos, V.P., Flemming, N.C., Druitt, T.H. (eds), *Thera and the Aegean world III, vol. 2.* The Thera Foundation, London, 183-198.

Gärtner, C., Bröcker, M., Strauss, H., Farber, K., (2011). Strontium-, carbon- and oxygen-isotope compositions of marbles from the Cycladic blueschist belt, Greece. *Geological Magazine* 148, 511-528.

Gasparini, P., Mantovani, M. S. M. & Scandone, R. (1981). A thermal model of the magma reservoir feeding Plinian eruptions at Mt. Vesuvius (Italy). *Bulletin Volcanologique, 44*(3), 317-326.

Georgalas, G. C. (1953). L'éruption du volcan de Santorin en 1950. *Bulletin of Volcanology*, *13*(1), 39-55.

Gertisser, R., Preece, K. & Keller, J. (2009). The Plinian lower pumice 2 eruption, Santorini, Greece: magma evolution and volatile behaviour. *Journal of Volcanology and Geothermal Research*, *186*(3), 387-406.

Gesch, D. B., Muller, J. & Farr, T. G. (2006). The shuttle radar topography mission-Data validation and applications. *Photogrammetric Engineering and Remote Sensing, 72*(3), 233-235.

Giammanco, S., Sims, K. W. & Neri, M. (2007). Measurements of ^{220}Rn and ^{222}Rn and CO_2 emissions in soil and fumarole gases on Mt. Etna volcano (Italy): implications for gas transport and shallow ground fracture. *Geochemistry, Geophysics, Geosystems, 8*(10).

Giammanco, S., Bellotti, F., Groppelli, G. & Pinton, A. (2010). Statistical analysis reveals spatial and temporal anomalies of soil CO_2 efflux on Mount Etna volcano (Italy). *Journal of Volcanology and Geothermal Research*, *194*(1), 1-14.

Giggenbach, W. F. (1987). Redox processes governing the chemistry of fumarolic gas discharges from White Island, New Zealand. *Applied Geochemistry*, *2*(2), 143-161.

Glennie, C. (2007). Rigorous 3D error analysis of kinematic scanning LIDAR systems. *Journal of Applied Geodesy*, *1*(3), 147.

Goldstein, R. M., Zebker, H. A. & Werner, C. L. (1988). Satellite radar interferometry: Two-dimensional phase unwrapping. *Radio Science*, *23*(4), 713-720.

González, P. J., Tiampo, K. F., Camacho, A. G. & Fernández, J. (2010). Shallow flank deformation at Cumbre Vieja volcano (Canary Islands): Implications on the stability of steep-sided volcano flanks at oceanic islands. *Earth and Planetary Science Letters*, *297*(3), 545-557.

Goree, F. (1710). A Relation of a New Island, Which Was Raised up from the Bottom of the Sea, on the 23d of May 1707, in the Bay of Santorini, in the Archipelago. Written by Father Goree (a Jesuit) an Eye-Witness. *Philosophical Transactions*, *27*(325-336), 354-375.

Gottsmann, J., Rymer, H. & Wooller, L. K. (2005). On the interpretation of gravity variations in the presence of active hydrothermal systems: Insights from the Nisyros Caldera, Greece. *Geophysical Research Letters*, *32*(23).

Gottsmann, J., Rymer, H., & Berrino, G. (2006). Unrest at the Campi Flegrei caldera (Italy): A critical evaluation of source parameters from geodetic data inversion. *Journal of Volcanology and Geothermal Research*, *150*(1), 132-145.

Grassa, F., Capasso, G., Favara, R. & Inguaggiato, S. (2006). Chemical and isotopic composition of waters and dissolved gases in some thermal springs of Sicily and adjacent volcanic islands, Italy. *Pure and Applied Geophysics*, *163*(4), 781-807.

Gray, A. L., Mattar, K. E. & Sofko, G. (2000). Influence of ionospheric electron density fluctuations on satellite radar interferometry. *Geophysical Research Letters*, *27*(10), 1451-1454.

GVPa - Smithsonian Institution, Global Volcanism Program (1994-). Volcanoes of South America (Colombia) [online]. Available: http://www.volcano.si.edu/world/region.cfm?rnum=1501. Last accessed 1 February 2011.

GVPb - Smithsonian Institution, Global Volcanism Program (1994-). Galeras [online]. Available: http://www.volcano.si.edu/world/volcano.cfm?vnum=1501-08=&volpage=erupt. Last accessed 1 February 2011.

GVPc - Smithsonian Institution, Global Volcanism Program (1994-). Galeras (Index of Monthly Reports) [online]. Available: http://www.volcano.si.edu/world/volcano.cfm?vnum=1501-08=&volpage=var#bgvn_2412. Last accessed 1 February 2011.

GVPd - Smithsonian Institution, Global Volcanism Program (1994-). Nevado del Huila [online]. Available: http://www.volcano.si.edu/world/volcano.cfm?vnum=1501-05=&volpage=weekly#Jul2010. Last accessed 1 February 2011.

GVPe - Smithsonian Institution, Global Volcanism Program (1994-). Nevado del Huila [online]. Available: http://www.volcano.si.edu/world/volcano.cfm?vnum=1501-05=&volpage=erupt. Last accessed 1 February 2011.

Hanssen, R. F. (2001). *Radar interferometry: data interpretation and error analysis* (Vol. 2). Springer.

Harris, A. J., Flynn, L. P., Rothery, D. A., Oppenheimer, C. & Sherman, S. B. (1999). Mass flux measurements at active lava lakes: Implications for magma recycling. *Journal of Geophysical Research: Solid Earth (1978–2012), 104*(B4), 7117-7136.

Heleno, S. I. N., Frischknecht, C., d'Oreye, N., Lima, J. N. P., Faria, B., Wall, R. & Kervyn, F. (2010). Seasonal tropospheric influence on SAR interferograms near the ITCZ–The case of Fogo Volcano and Mount Cameroon. *Journal of African Earth Sciences*, *58*(5), 833-856.

Hernández, P. A., Notsu, K., Salazar, J. M., Mori, T., Natale, G., Okada, H., Virgili, G., Shimoike, Y., Sato, M. & Pérez, N. M. (2001). Carbon dioxide degassing by advective flow from Usu volcano, Japan. *Science*, *292*(5514), 83-86.

Hickey, J., Gottsmann, J. & Potro, R. (2013). The large-scale surface uplift in the Altiplano-Puna region of Bolivia: A parametric study of source characteristics and crustal rheology using finite element analysis. *Geochemistry, Geophysics, Geosystems*, 14, 540–555.

Higgins, M. D. (1996). Magma dynamics beneath Kameni volcano, Thera, Greece, as revealed by crystal size and shape measurements. *Journal of Volcanology and Geothermal Research*, *70*(1), 37-48.

Hill, D. P. (2006). Unrest in Long Valley Caldera, California, 1978–2004. *Geological Society, London, Special Publications*, *269*(1), 1-24.

Hill, D. P. & Prejean, S. (2005). Magmatic unrest beneath mammoth mountain, California. *Journal of Volcanology and Geothermal Research*, *146*(4), 257-283.

Hill, D. P., Pollitz, F. & Newhall, C. (2002). Earthquake-volcano interactions. *Physics Today*, *55*(11), 41-47.

Hodge, D.S. (1974). Thermal model for origin of granitic batholiths. *Nature, 251*, 297-299.

Hooper, A. (2008). A multi-temporal InSAR method incorporating both persistent scatterer and small baseline approaches. *Geophysical Research Letters*, *35*(16).

Hooper, A. (2010). A statistical-cost approach to unwrapping the phase of InSAR time series. In *Proceedings 'Fringe 2009 Workshop'* (ESA SP-677, European Space Agency, 2010).

Hooper, A. (2013). *StaMPS/MTI Manual Version 3.3b1*. Available: http://homepages.see.leeds.ac.uk/~earahoo/stamps/StaMPS_Manual_v3.3b1.pdf. Last accessed 26th Sept 2013.

Hooper, A., Zebker, H., Segall, P. & Kampes, B. (2004). A new method for measuring deformation on volcanoes and other natural terrains using InSAR persistent scatterers. *Geophysical research letters*, *31*(23).

Hooper, A., Segall, P. & Zebker, H. (2007). Persistent scatterer interferometric synthetic aperture radar for crustal deformation analysis, with application to Volcán Alcedo, Galápagos. *Journal of Geophysical Research: Solid Earth (1978–2012)*, *112*(B7).

Hooper, A., Prata, F. & Sigmundsson, F. (2012). Remote Sensing of Volcanic Hazards and Their Precursors. *Proceedings of the IEEE*, *100*(10), 2908-2930.

Huggel, C., Ceballos, J. L., Pulgarín, B., Ramírez, J. & Thouret, J. C. (2007). Review and reassessment of hazards owing to volcano-glacier interactions in Colombia. *Annals of Glaciology*, *45*(1), 128-136.

Hulme, G. (1974). The interpretation of lava flow morphology. *Geophysical Journal International*, *39*(2), 361-383.

Hulme, G. & Fielder, G. (1977). Effusion rates and rheology of lunar lavas. *Philosophical Transactions of the Royal Society of London. Series A, Mathematical and Physical Sciences*, *285*(1327), 227-234.

Hurwitz, S., Christiansen, L. B. & Hsieh, P. A. (2007). Hydrothermal fluid flow and deformation in large calderas: inferences from numerical simulations. *Journal of Geophysical Research: Solid Earth (1978–2012)*, *112*(B2).

Ingebritsen, S. E., Galloway, D. L., Colvard, E. M., Sorey, M. L., & Mariner, R. H. (2001). Time-variation of hydrothermal discharge at selected sites in the western United States: implications for monitoring. *Journal of Volcanology and Geothermal Research*, *111*(1), 1-23.

INGEOMINAS (2008). Instituto Colombiano de Geologia y Mineria - Observatorio Vulcanologico y Sismologico de Pasto [online]. Available: http://intranet.INGEOMINAS.gov.co/pasto/images/a/a2/Resumen_actividad_Galeras_ene_14_2008_ene_20_2008.pdf. Last accessed 1 February 2011.

INGEOMINAS (2009). Subdireccion de Amenazas Geologicas y entorno ambiental. Observatorio Vulcanológico y Sismológico de Pasto [online]. Available: http://intranet.ingeominas.gov.co/pasto/images/d/da/Informe_visita_may_2009_volcan_Dona_Juana.pdf. Last accessed 1 February 2011.

INGEOMINAS (2010a). Principales volcanes de Colombia [online]. Available: http://intranet.ingeominas.gov.co/pasto/Principales_volcanes_de_Colombia. Last accessed 1 February 2011.

INGEOMINAS (2010b). Instituto Colombiano de Geologia y Mineria - Informes_Tecnicos_del_Complejo_Volcanico [online]. Available: http://intranet.INGEOMINAS.gov.co/manizales/Informes_Tecnicos_del_Complejo_Volcanico. Last accessed 1 February 2011.

Inguaggiato, S., Vita, F., Rouwet, D., Bobrowski, N., Morici, S. & Sollami, A. (2011). Geochemical evidence of the renewal of volcanic activity inferred from CO_2 soil and SO_2 plume fluxes: the 2007 Stromboli eruption (Italy). *Bulletin of Volcanology*, *73*(4), 443-456.

INGV (2013). *Luigi Palmieri.* Available: http://www.ov.ingv.it/ov/storia-dellosservatorio/luigi-palmieri.html. Last accessed 27 Oct 2013.

Jachens, R. C. & Roberts, C. W. (1985). Temporal and areal gravity investigations at Long Valley Caldera, California. *Journal of Geophysical Research: Solid Earth (1978–2012)*, *90*(B13), 11210-11218.

James, M. R. & Varley, N. (2012). Identification of structural controls in an active lava dome with high resolution DEMs: Volcán de Colima, Mexico. *Geophysical Research Letters*, *39*(22).

Javoy, M. & Pineau, F. (1991). The volatiles record of a “popping” rock from the Mid-Atlantic Ridge at 14 N: Chemical and isotopic composition of gas trapped in the vesicles. *Earth and Planetary Science Letters*, *107*(3), 598-611.

JAXA EORC (2009). About ALOS - Overview and Objectives [online]. Available: http://www.eorc.jaxa.jp/ALOS/en/about/about_index.htm Last accessed 1 February 2011.

Jentzsch, G., Weise, A., Rey, C. & Gerstenecker, C. (2004). Gravity changes and internal processes: Some results obtained from observations at three volcanoes. *Pure and applied Geophysics*, *161*(7), 1415-1431.

Jiménez, M. J., García-Fernández, M. & Romero, J. (2009). 1989–1995 Earthquake sequences in the Galeras volcano region, SW Colombia, and possible volcano–earthquake interactions. *Tectonophysics*, *463*(1), 47-59.

Johnson, J. B., Aster, R. C. & Kyle, P. R. (2004). Volcanic eruptions observed with infrasound. *Geophysical Research Letters*, *31*(14), L14604.

Johnson, D. J., Eggers, A. A., Bagnardi, M., Battaglia, M., Poland, M. P. & Miklius, A. (2010). Shallow magma accumulation at Kīlauea Volcano, Hawai ‘i, revealed by microgravity surveys. *Geology*, *38*(12), 1139-1142.

Johnston, M. J. S., Byerlee, J. D. & Lockner, D. (2001). Rapid fluid disruption: A source for self-potential anomalies on volcanoes. *Journal of Geophysical Research: Solid Earth (1978–2012)*, *106*(B3), 4327-4335.

Jolivet, R., Grandin, R., Lasserre, C., Doin, M. P. & Peltzer, G. (2011). Systematic InSAR tropospheric phase delay corrections from global meteorological reanalysis data. *Geophysical Research Letters*, *38*(17).

Jónsson, S., Segall, P., Pedersen, R. & Björnsson, G. (2003). Post-earthquake ground movements correlated to pore-pressure transients. *Nature*, *424*(6945), 179-183.

Kadko, D. & Moore, W. (1988). Radiochemical constraints on the crustal residence time of submarine hydrothermal fluids: Endeavour Ridge. *Geochimica et Cosmochimica Acta*, *52*(3), 659-668.

Kaneko, T., Wooster, M. J. & Nakada, S. (2002). Exogenous and endogenous growth of the Unzen lava dome examined by satellite infrared image analysis. *Journal of Volcanology and Geothermal Research*, *116*(1), 151-160.

Karimzadeh, S., Cakir, Z., Osmanoğlu, B., Schmalzle, G., Miyajima, M., Amiraslanzadeh, R. & Djamour, Y. (2013). Interseismic strain accumulation across the North Tabriz Fault (NW Iran) deduced from InSAR time series. *Journal of Geodynamics*, *66*, 53-58.

Kerle, N. & Van Wyk De Vries, B. (2001). The 1998 debris avalanche at Casita volcano, Nicaragua - investigation of structural deformation as the cause of slope instability using remote sensing. *Journal of Volcanology and Geothermal Research*, *105*(1), 49-63.

Kilburn, C. R. & Lopes, R. (1991). General patterns of flow field growth: aa and blocky lavas. *Journal of Geophysical Research: Solid Earth (1978–2012)*, *96*(B12), 19721-19732.

Kilburn, C. R. & Voight, B. (1998). Slow rock fracture as eruption precursor at Soufriere Hills volcano, Montserrat. *Geophysical Research Letters*, *25*(19), 3665-3668.

Kilburn, C. R. (2003). Multiscale fracturing as a key to forecasting volcanic eruptions. *Journal of Volcanology and Geothermal Research*, *125*(3), 271-289.

Konstantinou, K. I., Evangelidis, C. P., Liang, W. T., Melis, N. S., & Kalogeras, I. (2013). Seismicity, Vp/Vs and shear wave anisotropy variations during the 2011 unrest at Santorini caldera, southern Aegean. *Journal of Volcanology and Geothermal Research*, *267*, 57-67.

Krueger, A.J. (1983). Sighting of El Chichón sulphur dioxide clouds with the nimbus 7 total ozone mapping spectrometer. *Science*, *220*(4604), 1377-1379.

Kténas, C. A. (1926). L’éruption du volcan des Kaménis (Santorin) en 1925 -1. *Bulletin Volcanologique*, *3*(1), 3-64.

Kténas, C. A. (1927). L’éruption du volcan des Kaménis (Santorin) en 1925 -II. *Bulletin Volcanologique*, *4*(1), 7-49.

KWare (1999). KWare Magma – Geological software developed by Ken Wohletz [online]. Available:http://geodynamics.lanl.gov/Wohletz/Magma.htm Last accessed 1 February 2011.

Kwoun, O. I., Lu, Z., Neal, C. & Wicks, C. (2006). Quiescent deformation of the Aniakchak Caldera, Alaska, mapped by InSAR. *Geology*, *34*(1), 5-8.

Lacruz, J., Ugalde, A., Vargas, C.A. & Carcole, E. (2009). Coda-Wave Attenuation Imaging of Galeras Volcano, Colombia. *Bulletin of the Seismological Society of America*, *99*(6), 3510-3515.

Lagios, E., Parcharidis, I., Foumelis, M. & Sakkas, V. (2005). Ground deformation monitoring of the Santorini volcano using satellite radar interferometry. In *Recent Advances in Space Technologies, 2005. RAST 2005. Proceedings of 2nd International Conference on* (pp. 667-672). IEEE.

Lagios E., Sakkas V., Novali F., Bellotti F., Ferretti A., Vlachou K. & Dietrich V. (2013). SqueeSARTM and GPS Ground Deformation Monitoring of Santorini Volcano (1992-2012): Tectonic Implications. *Tectonophysics*, *594*, 38-59, doi:10.1016/j.tecto.2013.03.012.

Laiolo, M., Cigolini, C., Coppola, D. & Piscopo, D. (2012). Developments in real-time radon monitoring at Stromboli volcano. *Journal of environmental radioactivity*, *105*, 21-29.

Lewicki, J. L., Fischer, T. & Williams, S. N. (2000). Chemical and isotopic compositions of fluids at Cumbal Volcano, Colombia: evidence for magmatic contribution. *Bulletin of Volcanology*, *62*(4-5), 347-361.

Lewicki, J. L., Bergfeld, D., Cardellini, C., Chiodini, G., Granieri, D., Varley, N. & Werner, C. (2005). Comparative soil CO_2 flux measurements and geostatistical estimation methods on Masaya volcano, Nicaragua. *Bulletin of Volcanology*, *68*(1), 76-90.

Lipman, P. W. & Mullineaux, D. R. (Eds.). (1981). *The 1980 eruptions of Mount St. Helens, Washington* (No. 1250). US Dept. of the Interior, US Geological Survey.

Lipman, P. W., Moore, J. G. & Swanson, D. A. (1981). Bulging of the north flank before the May 18 eruption: geodetic data. *US Geological Survey Professional Paper*, *1250*, 143-156.

Liu, Z., Dong, D. & Lundgren, P. (2011). Constraints on time-dependent volcanic source models at Long Valley Caldera from 1996 to 2009 using InSAR and geodetic measurements. *Geophysical Journal International*, *187*(3), 1283-1300.

Loboguerrero, A. and Gilboa, Y. (1987). Groundwater in Colombia. *Hydrological Sciences Journal* *32*(2), 161-178.

Londoño, J.M. and Ospina, L.F. (2008). Estructura tridimensional de velocidad de onda P para el volcán Galeras. *Boletín Geológico* *42*(1-2), 7-23.

López, C., Blanco, M. J., Abella, R., Brenes, B., Cabrera Rodríguez, V. M., Casas, B., Domínguez Cerdeña, I. et al (2012). Monitoring the volcanic unrest of El Hierro (Canary Islands) before the onset of the 2011–2012 submarine eruption. *Geophysical Research Letters*, *39*(13).

Lowrie, W. (1997). *Fundamentals of geophysics*. Cambridge University Press.

Lu, Z. and Dzurisin, D., 2010. Ground surface deformation patterns, magma supply, and magma storage at Okmok volcano, Alaska, from InSAR analysis: 2. Coeruptive deflation, July–August 2008. *Journal of Geophysical Research: Solid Earth (1978–2012)*, *115*(B5).

Macpherson, C. & Mattey, D. (1994). Carbon isotope variations of CO_2 in Central Lau Basin basalts and ferrobasalts. *Earth and planetary science letters*, *121*(3-4), 263-276.

Macpherson, C. G., Hilton, D. R., Newman, S. & Mattey, D. P. (1999). CO_2, $^{13}C/^{12}C$ and H_2O variability in natural basaltic glasses: a study comparing stepped heating and ftir spectroscopic techniques-An infrared spectroscopic study. *Geochimica et cosmochimica acta*, *63*(11), 1805-1813.

Macpherson, C. G., Hilton, D. R. & Hammerschmidt, K. (2010). No slab-derived CO_2 in Mariana Trough back-arc basalts: implications for carbon subduction and for temporary storage of CO_2 beneath slow spreading ridges. *Geochemistry, Geophysics, Geosystems*, *11*(11).

Mann, A. C. (1983). Trace element geochemistry of high alumina basalt-andesite-dacite-rhyodacite lavas of the Main Volcanic Series of Santorini Volcano, Greece. *Contributions to Mineralogy and Petrology*, *84*(1), 43-57.

Marsh, B. D. (1981). On the crystallinity, probability of occurrence, and rheology of lava and magma. *Contributions to Mineralogy and Petrology*, *78*(1), 85-98.

Martelli, M., Caracausi, A., Paonita, A. & Rizzo, A. (2008). Geochemical variations of air-free crater fumaroles at Mt Etna: new inferences for forecasting shallow volcanic activity. *Geophysical Research Letters*, *35*(21).

Martens, H. R., & White, R. S. (2013). Triggering of microearthquakes in Iceland by volatiles released from a dyke intrusion. *Geophysical Journal International*, *194*(3), 1738-1754.

Martin, V. M., Holness, M. B. & Pyle, D. M. (2006). Textural analysis of magmatic enclaves from the Kameni Islands, Santorini, Greece. *Journal of Volcanology and Geothermal Research*, *154*(1), 89-102.

Martin, V. M., Morgan, D. J., Jerram, D. A., Caddick, M. J., Prior, D. J. & Davidson, J. P. (2008). Bang! Month-scale eruption triggering at Santorini volcano. *Science*, *321*(5893), 1178-1178.

Massimo, F., Baldi, P., Anzidei, M., Pesci, F., Bortoluzzi, G. and Aliani, S. (2010). High resolution topographic model of Panarea Island by fusion of photogrammetric, lidar and bathymetric digital terrain models. *The Photogrammetric Record,* 25(132), 382–401.

Massonnet, D. & Feigl, K. L. (1998). Radar interferometry and its application to changes in the Earth's surface. *Reviews of Geophysics, 36*(4), 441-500.

Massonnet, D. and Sigmundsson, F. (2000). Remote Sensing of Active Volcanism, *AGU 116,* 207-221.

Masterlark, T., Haney, M., Dickinson, H., Fournier, T. & Searcy, C. (2010). Rheologic and structural controls on the deformation of Okmok volcano, Alaska: FEMs, InSAR, and ambient noise tomography. *Journal of Geophysical Research: Solid Earth (1978–2012)*, *115*(B2).

Mattioli, G. S., Herd, R. A., Strutt, M. H., Ryan, G., Widiwijayanti, C. & Voight, B. (2010). Long term surface deformation of Soufrière Hills Volcano, Montserrat from GPS geodesy: Inferences from simple elastic inverse models. *Geophysical Research Letters*, *37*(19).

McBirney, A. R. & Murase, T. (1984). Rheological properties of magmas. *Annual Review of Earth and Planetary Sciences*, *12,* 337-357.

McGee, K. A., Gerlach, T. M., Kessler, R., & Doukas, M. P. (2000). Geochemical evidence for a magmatic CO2 degassing event at Mammoth Mountain, California, September–December 1997. *Journal of geophysical research*, *105*(B4), 8447-8456.

McKee, C. O., Johnson, R. W., Lowenstein, P. L., Riley, S. J., Blong, R. J., de Saint Ours, P. & Talai, B. (1985). Rabaul caldera, Papua New Guinea: Volcanic hazards, surveillance, and eruption contingency planning. *Journal of Volcanology and Geothermal Research*, *23*(3), 195-237.

McNutt, S. R. (2005). Volcanic seismology. *Annual Review of Earth and Planetary Sciences*, *32*, 461-491.

McTigue, D. F. (1987). Elastic stress and deformation near a finite spherical magma body: Resolution of the point source paradox. *Journal of Geophysical Research: Solid Earth (1978–2012), 92*(B12), 12931-12940.

Meindl, M., Schaer, S., Hugentobler, U. & Beutler, G. (2004). Tropospheric Gradient Estimation at CODE: Results from Global Solutions. *Journal of the Meteorological Society of Japan, 82*(1B), 331–338.

Melnik, O. & Sparks, R. S. J. (2005). Controls on conduit magma flow dynamics during lava dome building eruptions. *Journal of Geophysical Research: Solid Earth (1978–2012)*, *110*(B2).

Menke, W. (1989). *Geophysical Data Analysis: Discrete Inverse Theory.* Academic, San Diego, Calif.

MIMIC Wiki, 2008. GeodMod [online]. Available: http://mscserver.cox.miami.edu/divs/mgg/insar/mimicwiki/index.php?n=GeodMod.GeodMod. Last accessed 10 February 2011.

Mogi, K. (1958). Relations between the eruptions of various volcanoes and the deformations of the ground sources around them. *Bulletin of the Earthquake Research Institute*, ***36,*** 99-134.

Moore, H. J., Arthur, D. W. G. & Schaber, G. G. (1978). Yield strengths of flows on the Earth, Mars, and Moon. In *Lunar and Planetary Science Conference Proceedings, 9,* 3351-3378.

Moran, S. C., Kwoun, O., Masterlark, T. & Lu, Z. (2006). On the absence of InSAR-detected volcano deformation spanning the 1995–1996 and 1999 eruptions of Shishaldin Volcano, Alaska. *Journal of Volcanology and Geothermal Research*, *150*(1), 119-131.

Murase, T., McBirney, A. R. & Melson, W. G. (1985). Viscosity of the dome of Mount St. Helens. *Journal of Volcanology and Geothermal Research*, *24*(1), 193-204.

Murcia, H. F., Sheridan, M. F., Macías, J. L. & Cortés, G. P. (2010). TITAN2D simulations of pyroclastic flows at Cerro Machín Volcano, Colombia: Hazard implications. *Journal of South American Earth Sciences*, *29*(2), 161-170.

Nakiboglu, S. M. & Lambeck, K. (1982). A study of the Earth's response to surface loading with application to Lake Bonneville. *Geophysical Journal International*, *70*(3), 577-620.

Naranjo, J. L., Sigurdsson, H., Carey, S. N. & Fritz, W. (1986). Eruption of the Nevado del Ruiz volcano, Colombia, on 13 November 1985: tephra fall and lahars. *Science*, *233*(4767), 961-963.

Narváez M, L., Torres C, R. A., Gómez M, D. M., Cortés J, G. P., Cepeda V, H. & Stix, J. (1997). 'Tornillo'-type seismic signals at Galeras volcano, Colombia, 1992–1993. *Journal of Volcanology and Geothermal Research*, *77*(1), 159-171.

Neri, M., Mazzarini, F., Tarquini, S., Bisson, M., Isola, I., Behncke, B. & Pareschi, M. T. (2008). The changing face of Mount Etna's summit area documented with Lidar technology. *Geophysical Research Letters*, *35*(9), L09305.

Neri, M., Giammanco, S., Ferrera, E., Patanè, G. & Zanon, V. (2011). Spatial distribution of soil radon as a tool to recognize active faulting on an active volcano: the example of Mt. Etna (Italy). *Journal of environmental radioactivity*, *102*(9), 863-870.

Newman, A. V., Dixon, T. H., Ofoegbu, G. I. & Dixon, J. E. (2001). Geodetic and seismic constraints on recent activity at Long Valley Caldera, California: evidence for viscoelastic rheology. *Journal of Volcanology and Geothermal Research*, *105*(3), 183-206.

Newman, A. V., Dixon, T. H. & Gourmelen, N. (2006). A four-dimensional viscoelastic deformation model for Long Valley Caldera, California, between 1995 and 2000. *Journal of volcanology and geothermal research*, *150*(1), 244-269.

Newman, A.V., Stiros, S., Feng, L., Psimoulis, P., Moschas, F., Saltogianni, V., Jiang, Y., Papazachos, C., Panagiotopoulos, D.G., Karagianni, E. & Vamvakaris, D. (2012). Recent geodetic unrest at Santorini Caldera, Greece. *Geophysical Research Letters*, *39*(6).

Nicholls, I. A. (1971a). Petrology of Santorini Volcano, Cyclades, Greece. *Journal of Petrology*, *12*(1), 67-119.

Nicholls, I. A. (1971b). Calcareous inclusions in lavas and agglomerates of Santorini volcano. *Contributions to Mineralogy and Petrology*, *30*(4), 261-276.

Niell, A. E. (1996). Global mapping functions for the atmosphere delay at radio wavelengths. *Journal of Geophysical Research: Solid Earth (1978–2012)*, *101*(B1), 3227-3246.

Nissen, E., Krishnan, A. K., Arrowsmith, J. R., & Saripalli, S. (2012). Three-dimensional surface displacements and rotations from differencing pre-and post-earthquake LiDAR point clouds. *Geophysical Research Letters*, *39*(16).

NOA (2001). Seismicity Catalogs. Available: http://www.gein.noa.gr/services/info-en.html. Last accessed 7th June 2013.

Nomikou, P., Papanikolaou, D., Alexandri, M., Sakellariou, D. & Rousakis, G. (2012a). Submarine volcanoes along the Aegean volcanic arc. *Tectonophysics*, 597-598, 123-146.

Nomikou, P., Carey, S., Papanikolaou, D., Croff Bell, K., Sakellariou, D., Alexandri, M., & Bejelou, K. (2012b). Submarine volcanoes of the Kolumbo volcanic zone NE of Santorini Caldera, Greece. *Global and Planetary Change*, *90*, 135-151.

Nomikou, P., Carey, S., Croff Bell, K. L., Papanikolaou, D., Bejelou, K., Alexandri, M., Cantner, K. & Martin, J. F. (2013). Morphological analysis and related volcanic features of the Kolumbo submarine volcanic chain (NE of Santorini Island, Aegean Volcanic Arc). *Zeitschrift für Geomorphologie, Supplementary Issues*, *57*(3), 29-47.

Okada, Y. (1985). Surface deformation due to shear and tensile faults in a half-space. *Bulletin of the seismological society of America*, *75*(4), 1135-1154.

Oppenheimer, C. (1991). Lava flow cooling estimated from Landsat Thematic Mapper infrared data: the Lonquimay eruption (Chile, 1989). *Journal of Geophysical Research: Solid Earth (1978–2012)*, *96*(B13), 21865-21878.

Ordóñez V.,M.I. & Rey G.,C.A. (1997). Deformation associated with the extrusion of a dome at Galeras volcano, 1990–1991. *Journal of Volcanology and Geothermal Research*, *77*(1), 115-120.

Orsi, G., Civetta, L., Del Gaudio, C., De Vita, S., Di Vito, M. A., Isaia, R., Petrazzuoli, S.M., Ricciardi, G.P. & Ricco, C. (1999). Short-term ground deformations and seismicity in the resurgent Campi Flegrei caldera (Italy): an example of active block-resurgence in a densely populated area. *Journal of Volcanology and Geothermal Research*, *91*(2), 415-451.

Padrón, E., Pérez, N.M., Hernández, P.A., Sumino, H., Meklián, G.V., Barrancos, J., Nolasco, D., Padilla, G., Dionis, S., Rodríguez, F., Hernández, I., Calvo, D., Peraza, M.D., Nagao, K. (2013). Diffusive helium emissions as a precursory sign of volcanic unrest. *Geology*, *41*(5), 539-542.

Pagli, C., Sigmundsson, F., Árnadóttir, T., Einarsson, P. & Sturkell, E., (2006). Deflation of the Askja volcanic system: Constraints on the deformation source from combined inversion of satellite radar interferograms and GPS measurements. *Journal of Volcanology and Geothermal Research*, *152,* 97-108.

Palano, M., Puglisi, G. & Gresta, S. (2008). Ground deformation patterns at Mt. Etna from 1993 to 2000 from joint use of InSAR and GPS techniques. *Journal of Volcanology and Geothermal Research*, *169*(3), 99-120.

Papageorgiou, E., Lagios, E., Vassilopoulou, S. and Sakkas, V. (2007). Vertical & horizontal ground deformation on Santorini island deduced by DGPS measurements. *Bulletin of the Geological Society of Greece, 37,* 1219-1225.

Papageorgiou, E., Tzanis, A., Sotiropoulos, P. & Lagios, E. (2010). DGPS and magnetotelluric constraints on the contemporary tectonics of the Santorini volcanic complex, Greece. *Bulletin of the Geological Society of Greece*, *43*(1), 344-356.

Papageorgiou E., Foumelis M. & Parcharidis I. (2012). Long- and short-term deformation monitoring of Santorini Volcano: unrest evidence by DInSAR analysis. *IEEE Journal of Selected Topics in Applied Earth Observations and Remote Sensing, 5*(5), 1531-1537.

Papavassiliou, C., Boström, K., Paritsis, S., Galanopoulos, V., Arvanitides, N., Kalogeropoulos, S. (1990). Drilling of an ore-forming shallow hydrothermal system. In Hardy, D.A., et al. (eds), *Thera and The Aegean World III, 2*, 250-256, The Thera Foundation, London.

Papoutsis, I., Papanikolaou, X., Floyd, M., Ji, K. H., Kontoes, C., Paradissis, D. & Zacharis, V. (2013). Mapping inflation at Santorini volcano, Greece, using GPS and InSAR. *Geophysical Research Letters*, 40(2), 267-272.

Paritsis, S., Liati, A., Galanopoulos, V., Arvanitides, N., Boström, K. (1990). Petrology of the GPK-1 drill hole lavas, Palaea Kameni hot springs, Santorini volcano, Greece: constraints on the low-T lava fluid interaction. In: Hardy, D.A., et al. (eds), *Thera and The Aegean World III, 2*, 261-265, The Thera Foundation, London.

Parks, M. M., Biggs, J., Mather, T. A., Pyle, D. M., Amelung, F., Monsalve, M. L. & Medina, L. N. (2011). Co-eruptive subsidence at Galeras identified during an InSAR survey of Colombian volcanoes (2006–2009). *Journal of Volcanology and Geothermal Research*, *202*(3), 228-240.

Parks M. M., Biggs J., England P., Mather T. A., Nomikou P., Palamartchouk K., Papanikolaou X., Paradissis D., Parsons B., Pyle D. M., Raptakis C. & Zacharis V. (2012). Evolution of Santorini Volcano dominated by episodic and rapid fluxes of melt from depth. *Nature Geoscience*, *5*(10), 749-754.

Parks, M.M., Caliro, S., Chiodini, G., Pyle, D.M., Mather, T.A., Berlo, K., Edmonds, M., Biggs, J., Nomikou, P. & Raptakis, C. (2013). Distinguishing contributions to diffuse CO_2 emissions in volcanic areas from magmatic degassing and thermal decarbonation using soil-gas ^{222}Rn-$\delta^{13}C$ systematics: applications to Santorini volcano, Greece. *Earth and Planetary Science Letters*, *377-378*, 180-190.

Pavez, A., Remy, D., Bonvalot, S., Diament, M., Gabalda, G., Froger, J. L., Julien, P., Legrand, D. & Moisset, D. (2006). Insight into ground deformations at Lascar volcano (Chile) from SAR interferometry, photogrammetry and GPS data: Implications on volcano dynamics and future space monitoring. *Remote sensing of environment*, *100*(3), 307-320.

Pavlis, N., Holmes, S., Kenyon, S. & Factor, J. (2008). *EGM2008: An Earth Gravitational Model to Degree 2160* (General Assembly of the European Geosciences Union).

Pedersen, R. & Sigmundsson, F. (2004). InSAR based sill model links spatially offset areas of deformation and seismicity for the 1994 unrest episode at Eyjafjallajökull volcano, Iceland. *Geophysical Research Letters*, *31*(14), L14610.

Pedersen, R. & Sigmundsson, F. (2006). Temporal development of the 1999 intrusive episode in the Eyjafjallajökull volcano, Iceland, derived from InSAR images. *Bulletin of Volcanology*, *68*(4), 377-393.

Peterson, D. W. & Tilling, R. I. (1980). Transition of basaltic lava from pahoehoe to aa, Kilauea Volcano, Hawaii: field observations and key factors. *Journal of Volcanology and Geothermal Research*, *7*(3), 271-293.

Prata, A. J. (1989). Observations of volcanic ash clouds in the 10-12 μm window using AVHRR/2 data. *International Journal of Remote Sensing*, *10*(4-5), 751-761.

Pritchard, M. E. & Simons, M. (2004). An InSAR-based survey of volcanic deformation in the central Andes. *Geochemistry, Geophysics, Geosystems*, *5*(2).

Pulgarín, B., Correa, A., Cepeda, H. & Ancochea, E. (2001). Aspectos geológicos del Complejo Volcánico Nevado del Huila (CVNH). In *VIII Congreso Colombiano de Geología y V Conferencia Colombiana de Geología Ambiental (Memorias Digitales). Manizales Colombia*.

Pyle, D. M. & Elliott, J. R. (2006). Quantitative morphology, recent evolution, and future activity of the Kameni Islands volcano, Santorini, Greece. *Geosphere*, *2*(5), 253-268.

Pyle, D.M., Mather, T.A. & Biggs, J. (2013). Remote Sensing of Volcanoes and Volcanic Processes: Integrating Observation and Modelling - Introduction, in *Geological Society Special Publication*, 380, Remote-sensing of volcanoes and volcanic processes: integrating observation and modelling, (Edited by D.M. Pyle, T.A. Mather and J. Biggs), in press.

Radetco (2005). TASLIMAGE Neutron Dosimetry System Technical Notes. Available: http://www.radetco.com/folders/TASL/CR39/Spec%20Sheets/TASLTechnical%20Notes.pdf. Last accessed 11th Apr 2012.

Raus, T. (1988). Vascular plant colonization and vegetation development on sea-born volcanic islands in the Aegean (Greece). *Temporal and Spatial Patterns of Vegetation Dynamics, Advances in vegetation science*, 9, 139-147.

Reck, H., ed., 1936a, Santorin. Das Werdegang eines Inselvulkans und sein Ausbruch, 1925–1928. Ergebnisse einer Deutsch-Grieschischen Arbeitgemeinschaft: Berlin, Dietrich Reimer, 3 vol. (in German).

Reck, H., 1936b, Dynamik und morphogenese des Dafni-Ausbruches als beispiel einer Staukuppenbildung mit Stromerguss, in Reck, H., ed., Santorin, v. II: Berlin, Dietrich Reimer, p. 114–207 (in German).

Reck, H., 1936c, Der sekundäre vulkanismus des Dafni-ausbruches, in Reck, H., ed., Santorin, v. II: Berlin, Dietrich Reimer, p. 208–264 (in German). Reiss, W., and Stübel, A., 1868, Geschichte und Beschreibung der vulkanischen Ausbrüche bei Santorin von der ältesten Zeit bis auf die Gegenwart: Heidelberg, F. Bassermann, 201 p. (in German).

Reiss, W., and Stübel, A., 1868, Geschichte und Beschreibung der vulkanischen Ausbrüche bei Santorin von der ältesten Zeit bis auf die Gegenwart: Heidelberg, F. Bassermann, 201 p. (in German).

Reutebuch, S. E., Andersen, H. E., & McGaughey, R. J. (2005). Light detection and ranging (LIDAR): an emerging tool for multiple resource inventory. *Journal of Forestry*, *103*(6), 286-292.

Revil, A., Saracco, G. & Labazuy, P. (2003). The volcano-electric effect. *Journal of Geophysical Research*: *Solid Earth (1978–2012)*, *108*(B5), 2251.

Richter, N., Poland, M. P. & Lundgren, P. R. (2013). TerraSAR-X interferometry reveals small-scale deformation associated with the summit eruption of Kīlauea Volcano, Hawaiʻi. *Geophysical Research Letters*, 1-5.

Riguzzi, F., Pietrantonio, G., Baiocchi, V. & Mazzoni, A (2008). Water level and volume estimations of the Albano and Nemi lakes (central Italy). *Annals of Geophysics*, 51(4), 563-573.

Rivalta, E. & Segall, P. (2008). Magma compressibility and the missing source for some dike intrusions. *Geophysical Research Letters*, *35*(4).

Rivera, J., Lastras, G., Canals, M., Acosta, J., Arrese, B., Hermida, N., Micallef, A., Tello, O. & Amblas, D. (2013). Construction of an oceanic island: Insights from the El Hierro (Canary Islands) 2011–2012 submarine volcanic eruption. *Geology*, *41*(3), 355-358.

Rix, M., Valks, P., Hao, N., Loyola, D., Schlager, H., Huntrieser, H., Flemming, J., Koehler, U., Schumann, U. & Inness, A. (2012). Volcanic SO_2, BrO and plume height estimations using GOME-2 satellite measurements during the eruption of Eyjafjallajökull in May 2010 *Journal of Geophysical Research: Atmospheres (1984–2012)*, *117*(D6).

Robson, G.R. (1967). Thickness of Etnean lavas. *Nature*, 216, 251-252.

Rogie, J. D., Kerrick, D. M., Sorey, M. L., Chiodini, G. & Galloway, D. L. (2001). Dynamics of carbon dioxide emission at Mammoth Mountain, California. *Earth and Planetary Science Letters*, *188*(3), 535-541.

ROI_PAC (2013). *Repeat Orbit Interferometry PACkage (ROI_PAC).* Available: http://www.roipac.org/ROI_PAC. Last accessed 20th May 2013.

Rosen, P. A., Hensley, S., Joughin, I. R., Li, F. K., Madsen, S. N., Rodriguez, E. & Goldstein, R. M. (2000). Synthetic aperture radar interferometry. *Proceedings of the IEEE*, *88*(3), 333-382.

Rosen, P. A., Hensley, S., Peltzer, G. & Simons, M. (2004). Updated repeat orbit interferometry package released. *Eos, Transactions American Geophysical Union*, *85*(5), 47.

Rosenbaum, J. M. (1994). Stable isotope fractionation between carbon dioxide and calcite at 900°C. *Geochimica et Cosmochimica Acta*, *58*(17), 3747-3753.

Roth, R. B. & Thompson, J. (2008). Practical Application of Multiple Pulse in Air (MPIA) Lidar in Large-Area Surveys. *Proceedings of International Archives of the Photogrammetry, Remote Sensing and Spatial Information Sciences*, 37 (Part 1), 183-188.

Rymer, H. (1994). Microgravity change as a precursor to volcanic activity. *Journal of Volcanology and Geothermal Research*, *61*(3), 311-328.

Rymer, H., Cassidy, J., Locke, C. A. & Murray, J. B. (1995). Magma movements in Etna volcano associated with the major 1991–1993 lava eruption: evidence from gravity and deformation. *Bulletin of Volcanology*, *57*(6), 451-461.

Rymer, H., Cassidy, J., Locke, C. A. & Sigmundsson, F. (1998). Post-eruptive gravity changes from 1990 to 1996 at Krafla volcano, Iceland. *Journal of Volcanology and Geothermal Research*, *87*(1), 141-149.

Saltogianni, V. & Stiros, S. C. (2012). Modeling the Mogi magma source centre of the Santorini (Thera) volcano, Aegean Sea, Greece, 1994–1999, based on a numerical-topological approach. *Studia Geophysica et Geodaetica*, *56*(4), 1037-1062.

Savage, J. C., & Clark, M. M. (1982). Magmatic resurgence in Long Valley caldera, California: Possible cause of the 1980 Mammoth Lakes earthquakes. *Science*, *217*(4559), 531-533.

Savage, J. C., & Cockerham, R. S. (1984). Earthquake swarm in Long Valley caldera, California, January 1983: Evidence for dike inflation. *Journal of Geophysical Research: Solid Earth (1978–2012)*, *89*(B10), 8315-8324.

Scheele, N. & Hoefs, J. (1992). Carbon isotope fractionation between calcite, graphite and CO_2: an experimental study. *Contributions to Mineralogy and Petrology*, *112*(1), 35-45.

Schmidt, D. A. & Bürgmann, R. (2003). Time-dependent land uplift and subsidence in the Santa Clara valley, California, from a large interferometric synthetic aperture radar data set. *Journal of Geophysical Research*, *108*(B9), 2416-2428.

Sedze, M., Heggy, E., Bretar, F., Berveiller, D. & Jacquemoud, S. (2012, July). L-band InSAR decorrelation analysis in volcanic terrains using airborne LiDAR data and in situ measurements: The case of the Piton de la Fournaise volcano, France. In *Geoscience and Remote Sensing Symposium (IGARSS), 2012 IEEE International*, 3907-3910.

Segall, P. (2010). *Earthquake and volcano deformation*. Princeton University Press.

Segovia, N., Valdes, C., Peña, P., Mena, M. & Tamez, E. (2001). Soil radon response around an active volcano. *Radiation Measurements*, *34*(1), 433-436.

Seidl, D., Hellweg, M., Calvache V., M.L., Gómez M., D., Ortega, E., A., Torres C., R., Böker, F., Buttkus, B., Faber, E. & Greinwald, S. (2003). The multiparameter station at Galeras Volcano (Colombia): concept and realization. *Journal of Volcanology and Geothermal Research*, *125*(1), 1-12.

SGC (2013). *Servicio Geológico Colombiano.* Available: http://www.sgc.gov.co/. Last accessed 30th Oct 2013.

Siebert, L. & Simkin, T. (2002). Volcanoes of the world: an illustrated catalog of holocene volcanoes and their eruptions. Smithsonian Institution, Global Volcanism Program Digital Information Series, GVP-3. *Ser., GVP-3, Smithsonian Inst., Washington, DC [Available at http://www.volcano.si.edu/world/.].*

Sigmundsson, F., Hreinsdóttir, S., Hooper, A., Árnadóttir, T., Pedersen, R., Roberts, M.J., Óskarsson, N., Auriac, A., Decriem, J., Einarsson, P., Geirsson, H., Hensch, M., Benedikt, G., Ófeigsson, B.G., Erik Sturkell, E., Hjörleifur Sveinbjörnsson, H., Feigl. K.L. (2010). Intrusion triggering of the 2010 Eyjafjallajökull explosive eruption. *Nature*, *468*(7322), 426-430.

Sinclair, A. J. (1974). Selection of threshold values in geochemical data using probability graphs. *Journal of Geochemical Exploration*, *3*(2), 129-149.

Smith, R., Sammonds, P. R. & Kilburn, C. R. (2009). Fracturing of volcanic systems: Experimental insights into pre-eruptive conditions. *Earth and Planetary Science Letters*, *280*(1), 211-219.

Smithsonian Institution (2013). Global Volcanism Program: Worldwide Holocene Volcano and Eruption Information [online]. Available: http://www.volcano.si.edu/index.cfm. Last accessed 12th August 2013.

Solaro, G., Acocella, V., Pepe, S., Ruch, J., Neri, M. & Sansosti, E. (2010). Anatomy of an unstable volcano from InSAR: Multiple processes affecting flank instability at Mt. Etna, 1994–2008. *Journal of Geophysical Research: Solid Earth (1978–2012)*, *115*(B10).

Soler, V., Castro, J.A., Viñas, R.T., Eff-Darwich, A., Sánchez, S., Hillarie-Marcel, C., Farrujia, I., Coello, J., de la Nuez, J., Martín, M.C., Quesada, M.L., Santana, E. (2004). High CO_2 levels in boreholes at El Teide volcano complex (Tenerife, Canary Islands): implications for volcanic activity monitoring. *Pure and Applied Geophysics*, 161 (7), 1519-1532.

Sorey, M. L., Kennedy, B. M., Evans, W. C., Farrar, C. D., & Suemnicht, G. A. (1993). Helium isotope and gas discharge variations associated with crustal unrest in Long Valley caldera, California, 1989–1992. *Journal of Geophysical Research: Solid Earth (1978–2012)*, *98*(B9), 15871-15889.

Spandler, C., Martin, L. H. & Pettke, T. (2012). Carbonate assimilation during magma evolution at Nisyros (Greece), South Aegean Arc: evidence from clinopyroxenite xenoliths. *Lithos*, *146*, 18-33.

Sparks, R.S.J., Pinkerton, H., Hulme, G. (1976). Classification and formation of lava levees on Mount Etna, Sicily. *Geology*, 4(5), 269- 271.

Sparks, S. R. & Sigurdsson, H. (1977). Magma mixing: a mechanism for triggering acid explosive eruptions. *Nature*, *267*, 315-318.

Sparks, R. S. J., Biggs, J. & Neuberg, J. W. (2012). Monitoring volcanoes. *Science*, *335*(6074), 1310-1311.

Stejny, J. & Portwood, T. (1986). A novel "rapid development" plastic track detector. *International Journal of Radiation Applications and Instrumentation. Part D. Nuclear Tracks and Radiation Measurements*, *12*(1), 59-62.

Stern, C. R. (2004). Active Andean volcanism: its geologic and tectonic setting. *Revista geológica de Chile*, *31*(2), 161-206.

Stevens, N. F., Wadge, G., Williams, C. A., Morley, J. G., Muller, J. P., Murray, J. B. & Upton, M. (2001). Surface movements of emplaced lava flows measured by synthetic aperture radar interferometry. *Journal of Geophysical Research*, *106*(B6), 11293-11314.

Stiros, S. C., Psimoulis, P., Vougioukalakis, G., & Fyticas, M. (2010). Geodetic evidence and modeling of a slow, small-scale inflation episode in the Thera (Santorini) volcano caldera, Aegean Sea. *Tectonophysics*, *494*(3), 180-190.

Stix, J., Torres, R. C., Narváez M, L., Cortés J, G. P., Raigosa, J. A., Gómez M, D. & Castonguay, R. (1997). A model of vulcanian eruptions at Galeras volcano, Colombia. *Journal of Volcanology and Geothermal Research*, *77*(1), 285-303.

Sudhaus, H. & Jónsson, S. (2009). Improved source modelling through combined use of InSAR and GPS under consideration of correlated data errors: application to the June 2000 Kleifarvatn earthquake, Iceland. *Geophysical Journal International*, *176*(2), 389-404.

Sun, R. J. (1969). Theoretical size of hydraulically induced horizontal fractures and corresponding surface uplift in an idealized medium. *Journal of Geophysical Research*, *74*(25), 5995-6011.

Tan, K.H. (1998). Principles of Soil Chemistry, 3rd ed. Marcel Dekker Inc., New York.

Tarillon (1715a), Relation en forme de journal de la nouvelle isle sortie de la mer dans le Golfe du Santorin. In Fleurian D'Armenonville, Th.C., ed., Nouveaux memoires des missions de la compagnie de Jesus, dans le Levant, Paris: Paris, Nicolas Le Clerc, p. 126–161 (in French).

Tarillon (1715b), Extrait d'une lettre écrite de Santorin. In Fleurian D'Armenonville, Th.C., ed., Nouveaux memoires des missions de la compagnie de Jesus, dans le Levant, Paris: Paris, Nicolas Le Clerc, p. 162–173 (in French).

TASL (2011). Track Analysis Systems Ltd. Available: http://www.tasl.co.uk/. Last accessed 11th Apr 2012.

Tassi, F., Vaselli, O., Papzachos, C.B., Giannini, L., Chiodini, G., Vougioukalakis, G.E., Karagianni, E., Vamvakaris, D. & Panagiotopoulos, D. (2013). Geochemical and isotopic changes in the fumarolic and submerged gas discharges during the 2011-2012 unrest at Santorini caldera (Greece). *Bulletin of Volcanology*, *75*(4), 1-15.

Theys, N., Van Roozendael, M., Dils, B., Hendrick, F., Hao, N. & De Maziere, M. (2009). First satellite detection of volcanic bromine monoxide emission after the Kasatochi eruption. *Geophysical Research Letters*, *36*(3), L03809.

Thouret, J. C., Cantagrel, J. M., Robin, C., Murcia, A., Salinas, R. & Cepeda, H. (1995). Quaternary eruptive history and hazard-zone model at Nevado del Tolima and Cerro Machin volcanoes, Colombia. *Journal of Volcanology and Geothermal Research*, *66*(1), 397-426.

Tilling, R.I. 1995. The role of monitoring in forecasting volcanic events. *In:* McGuire, W., Kilburn, C.R.J. & Murray, J. (eds) *Monitoring Active Volcanoes: Strategies, Procedures and Techniques*, UCL Press, 369-402.

Tizzani, P., Battaglia, M., Zeni, G., Atzori, S., Berardino, P. & Lanari, R. (2009). Uplift and magma intrusion at Long Valley caldera from InSAR and gravity measurements. *Geology*, *37*(1), 63-66.

Todesco, M., Rinaldi, A. P., & Bonafede, M. (2010). Modeling of unrest signals in heterogeneous hydrothermal systems. *Journal of Geophysical Research: Solid Earth (1978–2012)*, *115*(B9).

Toth, C. K. (2002). Calibrating Airborne LIDAR Systems, *Proceedings of ISPRS Commission II Symposium, Xi'an, China, August 20–23, 2002*, 475–480.

Traglia, F., Ventisette, C., Rosi, M., Mugnai, F., Intrieri, E., Moretti, S. & Casagli, N. (2012). Ground based InSAR reveals conduit pressurization pulses at Stromboli volcano. *Terra Nova*, 25 (2013), pp. 192–198.

Trenkamp, R., Kellogg, J. N., Freymueller, J. T. & Mora, H. P. (2002). Wide plate margin deformation, southern Central America and northwestern South America, CASA GPS observations. *Journal of South American Earth Sciences*, *15*(2), 157-171.

Troise, C., De Natale, G., Pingue, F., Obrizzo, F., De Martino, P., Tammaro, U., & Boschi, E. (2007). Renewed ground uplift at Campi Flegrei caldera (Italy): New insight on magmatic processes and forecast. *Geophysical research letters*, *34*(3), L03301.

Troll, V.R., Hilton, D.R., Jolis, E.M., Chadwick, J.P., Blythe, L.S., Deegan, F.M., Schwarzkopf, L.M. & Zimmer, M. (2012). Crustal CO_2 liberation during the 2006 eruption and earthquake events at Merapi volcano, Indonesia. *Geophysical Research Letters*, *39*(11).

Tu, K. P., Brooks, P. D. & Dawson, T. E. (2001). Using septum-capped vials with continuous-flow isotope ratio mass spectrometric analysis of atmospheric CO_2 for Keeling plot applications. *Rapid Communications in Mass Spectrometry*, *15*(12), 952-956.

TUDelft (2013). *Doris.* Available: http://doris.tudelft.nl/. Last accessed 20th May 2013.

Varnavas, S. P., & Cronan, D. S. (2005). Submarine hydrothermal activity off Santorini and Milos in the Central Hellenic Volcanic Arc: A synthesis. *Chemical geology*, *224*(1), 40-54.

Ventura, G., & Vilardo, G. (2008). Emplacement mechanism of gravity flows inferred from high resolution Lidar data: The 1944 Somma–Vesuvius lava flow (Italy). *Geomorphology*, *95*(3), 223-235.

Vigouroux, N., Williams-Jones, G., Chadwick, W., Geist, D., Ruiz, A. & Johnson, D. (2008). 4D gravity changes associated with the 2005 eruption of Sierra Negra volcano, Galápagos. *Geophysics*, *73*(6), WA29-WA35.

Voight, B. & Cornelius, R. R. (1991). Prospects for eruption prediction in near real-time. *Nature*, *350*(6320), 695-698.

Voight, B., Hoblitt, R. P., Clarke, A. B., Lockhart, A. B., Miller, A., Lynch, L., & McMahon, J. (1998). Remarkable cyclic ground deformation monitored in real-time on Montserrat, and its use in eruption forecasting. *Geophysical Research Letters*, *25*(18), 3405-3408.

von Fritsch, K., Reiss, W. & Stübel, A. (1867). Santorin. The Kameni islands. London, Trübner and Co.

Vougioukalakis, G. E. & Fytikas, M. (2005). Volcanic hazards in the Aegean area, relative risk evaluation, monitoring and present state of the active volcanic centers. *Developments in Volcanology, 7,* 161-183.

Wadge, G. & Lopes, R. M. C. (1991). The lobes of lava flows on Earth and Olympus Mons, Mars. *Bulletin of Volcanology*, *54*(1), 10-24.

Wadge, G., Oramas Dorta, D. & Cole, P. D. (2006). The magma budget of Volcán Arenal, Costa Rica from 1980 to 2004. *Journal of volcanology and geothermal research*, *157*(1), 60-74.

Wadge, G., Macfarlane, D. G., Odbert, H. M., James, M. R., Hole, J. K., Ryan, G., Bass, V. et al (2008). Lava dome growth and mass wasting measured by a time series of ground-based radar and seismicity observations. *Journal of Geophysical Research: Solid Earth (1978–2012)*, *113*(B8).

Wadge, G., Cole, P., Stinton, A., Komorowski, J. C., Stewart, R., Toombs, A. C. & Legendre, Y. (2011). Rapid topographic change measured by high-resolution satellite radar at Soufriere Hills Volcano, Montserrat, 2008–2010. *Journal of Volcanology and Geothermal Research*, *199*(1), 142-152.

Wadge, G., Saunders, S. & Itikarai, I. (2012). Pulsatory andesite lava flow at Bagana Volcano. *Geochemistry, Geophysics, Geosystems*, *13*(11).

Waite, G. P. & Smith, R. B. (2002). Seismic evidence for fluid migration accompanying subsidence of the Yellowstone caldera. *Journal of Geophysical Research*, *107*(B9), 2177.

Waldhauser, F. & Ellsworth, W. L. (2000). A double-difference earthquake location algorithm: Method and application to the northern Hayward fault, California. *Bulletin of the Seismological Society of America*, *90*(6), 1353-1368.

Walter, T. R., Acocella, V., Neri, M. & Amelung, F. (2005). Feedback processes between magmatic events and flank movement at Mount Etna (Italy) during the 2002–2003 eruption. *Journal of Geophysical Research: Solid Earth (1978–2012), 110*(B10), B10205.

Walter, T. R. (2011). Structural architecture of the 1980 Mount St. Helens collapse: An analysis of the Rosenquist photo sequence using digital image correlation. *Geology*, *39*(8), 767-770.

Walter, T. R., Legrand, D., Granados, H. D., Reyes, G. & Arámbula, R. (2013). Volcanic eruption monitoring by thermal image correlation: Pixel offsets show episodic dome growth of the Colima volcano. *Journal of Geophysical Research: Solid Earth*, *118*(4), 1408-1419.

Walters, R. J., Elliott, J. R., Parsons, B., & Li, Z. (2013). Rapid strain accumulation on the Ashkabad fault (Turkmenistan) from atmosphere-corrected InSAR. *Journal of Geophysical Research: Solid Earth*, *118*, 3674-3690.

Washington, H.S. (1926), Santorini eruptions of 1925. *Geological Society of America Bulletin*, 37, 349–384.

Westphal, J. A., Carr, M. A., Miller, W. F., & Dzurisin, D. (1983). Expendable bubble tiltmeter for geophysical monitoring. *Review of Scientific Instruments*, *54*(4), 415-418.

Wicks, C., Thatcher, W., & Dzurisin, D. (1998). Migration of fluids beneath Yellowstone caldera inferred from satellite radar interferometry. *Science*, *282*(5388), 458-462.

Wicks, C. W., Dzurisin, D., Ingebritsen, S., Thatcher, W., Lu, Z. & Iverson, J. (2002). Magmatic activity beneath the quiescent Three Sisters volcanic center, central Oregon Cascade Range, USA. *Geophysical Research Letters*, *29*(7), 261-264.

Wicks, C. W., Thatcher, W., Dzurisin, D., & Svarc, J. (2006). Uplift, thermal unrest and magma intrusion at Yellowstone caldera. *Nature*, *440*(7080), 72-75.

Williams, C. A. & Wadge, G. (1998). The effects of topography on magma chamber deformation models: Application to Mt. Etna and radar interferometry. *Geophysical Research Letters*, *25*(10), 1549-1552.

Williams, S.N. (ed). 1990a. Nevado del Ruiz Volcano, Colombia, I. *Journal of Volcanology and Geothermal Research, 41* (Special Issue).

Williams, S.N. (ed). 1990b. Nevado del Ruiz Volcano, Colombia, II. *Journal of Volcanology and Geothermal Research, 42* (Special Issue).

Williams, S. N., Calvache, V. M. L., Sturchio, N. C., Zapata, G. J. A., Mendez, F. R. A., Calvache, O. B., Londoño, C.A, Gil, C.F. & Sano, Y. (1990). Premonitory geochemical evidence of magmatic reactivation of Galeras volcano, Colombia. *Eos Trans. AGU*, *74*(43), 690.

Witt, M. L. I., Mather, T. A., Pyle, D. M., Aiuppa, A., Bagnato, E. & Tsanev, V. I. (2008). Mercury and halogen emissions from Masaya and Telica volcanoes, Nicaragua. *Journal of Geophysical Research: Solid Earth (1978–2012)*, *113*(B6).

Wright, H., Cashman, K. V., Gottesfeld, E. H. & Roberts, J. J. (2009). Pore structure of volcanic clasts: Measurements of permeability and electrical conductivity. *Earth and Planetary Science Letters*, *280*(1), 93-104.

Wright, R., Flynn, L. P. & Harris, A. J. (2001). Evolution of lava flow-fields at Mount Etna, 27–28 October 1999, observed by Landsat 7 ETM+. *Bulletin of Volcanology*, *63*(1), 1-7.

Wright, R., Flynn, L., Garbeil, H., Harris, A. & Pilger, E. (2002). Automated volcanic eruption detection using MODIS. *Remote Sensing of Environment*, *82*(1), 135-155.

Wright, T. J., Parsons, B. E., Jackson, J. A., Haynes, M., Fielding, E. J., England, P. C. & Clarke, P. J. (1999). Source parameters of the 1 October 1995 Dinar (Turkey) earthquake from SAR interferometry and seismic bodywave modelling. *Earth and Planetary Science Letters*, *172*(1), 23-37.

Wright, T. J., Lu, Z. & Wicks, C. (2003). Source model for the M_w 6.7, 23 October 2002, Nenana Mountain earthquake (Alaska) from InSAR. *Geophysical Research Letters*, *30*(18), 1974.

Yamauchi, T. (2003). Studies on the nuclear tracks in CR-39 plastics. *Radiation Measurements, 36*(1), 73-81.

Yang, T. F., Wen, H.Y., Fu, C.C., Lee, H.F., Lan, T.F., Chen, A.T., Hong, W.L., Lin, S.J. & Walia, V. (2011). Soil radon flux and concentrations in hydrothermal area of the Tatun Volcano Group, Northern Taiwan. *Geochemical Journal*, *45*(6), 483-490.

Yang, X. M., Davis, P. M. & Dieterich, J. H. (1988). Deformation from inflation of a dipping finite prolate spheroid in an elastic half-space as a model for volcanic stressing. *Journal of Geophysical Research*, *93*(B5), 4249-4257.

Yokota, T., Yoshida, Y., Eguchi, N., Ota, Y., Tanaka, T., Watanabe, H. & Maksyutov, S. (2009). Global concentrations of CO_2 and CH_4 retrieved from GOSAT: first preliminary results. S*ola*, *5*(0), 160-163.

Zapata G., J.A., Calvache V., M.L., Cortés J., G.P., Fischer, T.P., Garzon V., G., Gómez M., D., Narváez Medina M., L., Ordóñez V., M., Ortega E., A., Stix, J., Torres C., R. and Williams, S.N. (1997). SO_2 fluxes from Galeras Volcano, Colombia, 1989–1995: Progressive degassing and conduit obstruction of a Decade Volcano. *Journal of Volcanology and Geothermal Research*, *77*(1), 195-208.

Zebker, H. A. & Villasenor, J. (1992). Decorrelation in interferometric radar echoes. *Geoscience and Remote Sensing, IEEE Transactions on*, *30*(5), 950-959.

Zebker, H. A., Amelung, F. and Jonsson, S. (2000). Remote sensing of volcano surface and internal processes using radar interferometry. *AGU Geophysical Monograph*, 116, 179-205.

Zellmer, G. F., Blake, S., Vance, D., Hawkesworth, C. & Turner, S. (1999). Plagioclase residence times at two island arc volcanoes (Kameni Islands, Santorini, and Soufriere, St. Vincent) determined by Sr diffusion systematics. *Contributions to Mineralogy and Petrology*, *136*(4), 345-357.

Zellmer, G., Turner, S. & Hawkesworth, C.J. (2000). Timescales of destructive plate margin magmatism: new insights from Santorini, Aegean volcanic arc. *Earth and Planetary Science Letters*, *174*(3), 265-281.

Zimmer, M., Erzinger, J., (2003). Continuous H_2O, CO_2, ^{222}Rn and temperature measurements on Merapi volcano, Indonesia. *Journal of Volcanology and Geothermal Research*, *125*(1), 25-38.